THE UNIVERSITY *of* EDINBURGH

Towards a High-precision Description of Resonances through Lattice Simulations

Nelson Pitanga Lachini

Doctor of Philosophy
The University of Edinburgh
October 2023

Abstract

Resonances play a significant role in the phenomenology of the Standard Model. For example, many hadronic resonances are found in flavour-physics processes, which can be central to New Physics searches. The realistic determination of resonance parameters is an important step in the direction of understanding such phenomena. First-principles quantum chromodynamics (QCD) computations using lattice approaches have developed in the last two decades to the point where physical quark masses can now be directly employed. In this context, studying the dynamical properties of QCD, such as scattering amplitudes and resonances, has been challenging, but the development of finite-volume and computational techniques has made it feasible.

In this work, we perform the first calculation of $K^*(892)$ and $\rho(770)$ resonance parameters at physical quark masses with a reliable estimate of systematic uncertainties. This is done on a single domain-wall $N_f = 2 + 1$ RBC-UKQCD ensemble at the physical point. We begin by describing the phenomenological aspects of the strong interaction and the underlying quantum field theory. The algorithmic aspect of lattice QCD using the Monte Carlo method and the description of angular momentum on a cubic spatial lattice are reviewed. Next, we cover the formal groundwork of finite-volume quantum field theory that allows the extraction of scattering amplitudes from lattice observables.

Determining the low-energy spectra is a key goal of lattice QCD. Using the developed open-source distillation library based on `Grid` and `Hadrons`, we compute finite-volume correlators on the physical-point ensemble. We construct a basis of operators to study $\pi\pi$ and $K\pi$ scattering in the relevant channels. This involves using a generalised eigenvalue problem to compute optimised hadronic interpolators and obtain finite-volume energy levels. Finally, the optimised correlator data is used to extract scattering phase shifts and model-averaged $\rho(770)$ and $K^*(892)$ resonance parameters via finite-volume effects.

Lay Summary

The Standard Model (SM) of particle physics provides a unified description of the strong, weak and electromagnetic forces of Nature. For many decades, the Standard Model has been extensively confronted with experimental data coming from subatomic particle collisions, and it still stands as one of the most successful endeavors of Physics.

There are still many open questions that challenge our understanding of the constituent theories of the Standard Model. In particular, Quantum Chromodynamics (QCD) is responsible for the description of the strong interaction and still represents a vast uncharted territory in theoretical physics. Its elementary particles, the quarks and gluons, strongly combine to form the observed hadrons at collider experiments.

Among these hadrons are resonances, which decay via the strong force and are intrinsic to QCD's mechanisms. Such particles are produced as intermediate states of critical processes for unveiling New Physics beyond the Standard Model, such as $B \to K^*$ decays. Disentangling their presence from potential New Physics indicators presents a formidable challenge for the next generations of physicists.

We adopt the lattice field theory approach, which allows us to rigorously treat QCD through computer simulations. The price paid is that simplifications are usually needed to restrict the computational cost, for example, by assuming the quark masses to be higher than in Nature.

We describe the K^* and ρ resonances by employing lattice QCD with physical parameters on supercomputers. In particular, the finite spatial box in which we perform the calculations is used as a theory probe of resonance properties. This is a first step towards a Standard Model prediction of processes involving such particles.

Declaration

I declare that this thesis was composed by myself, that the work contained herein is my own except where explicitly stated otherwise in the text, and that this work has not been submitted for any other degree or professional qualification except as specified.

Parts of this work have been published in [1–5].

(*Nelson Pitanga Lachini, October 2023*)

Acknowledgements

The PhD years deeply changed my life for many reasons, but the main ones are the people I met and the ones who continued by my side. First of all, I thank my supervisor Antonin Portelli for first of all making it possible for me to come over to crunch some random numbers on supercomputers and learn theoretical physics. I also thank Felix Erben for being very patient during my supervision and Mike Peardon for the effort to promote interaction regardless of the pandemic. I am also thankful for the members of the Edinburgh lattice group, especially Fabian Joswig, for creating some order in the middle of the PhD chaos, and Max Hansen, from whom I learned a lot about finite-volume effects and how to present physics research to different people. Last but not least, I thank to my previous supervisors, Marco Moriconi, Tereza Mendes and Attilio Cucchieri, and all people in my undergrad and masters universties, who made all this path to the PhD possible in the first place. I deeply acknowledge all the public funds that made my previous education in Brazil viable.

I deeply thank Alessandro, Raoul and Henrique for creating an environment that fostered physics and memes. I would still be a naive student if I had not been inspired by all of you, including all Jeremy's subjects. I also thank my forró people, in particular Shem and Iris, for going to a dark basement club to dance xote, and keeping my heart filled with music and friendship outside physics. I thank my old friends Gabriel, Douglas, Bruno, Mariana, Ingrid, Braian and the new ones, Lígia, Julia, Pia, André, Safi, for insisting on coming back even after long periods of silence.

I thank my family, Ernesto, Márcia and Maria, for unconditionally supporting me all the time, even 10000 km away. I learn from you even without noticing it. I also thank my uncle Jorge, who has been increasingly present in my life in curious ways. My special thanks go to Hannah, for being so supportive with this weird writing period and helping me to be more than my work. It is your turn now, but remember we have many adventures ahead of us!

I thank the organisers of EuroPLEx, in particular Francesco di Renzo, for making it possible for us to be part of a training network even though we had to change plans constantly. I also acknowledge the computer time on the STFC DiRAC Extreme Scaling Service at Edinburgh, which made my PhD results concrete. This project has received funding from the European Research Council (ERC) under the European Union's Horizon 2020 research and innovation programme under grant agreement No 813942.

Contents

List of Figures

List of Tables

Introduction

There are four elementary interactions in the current paradigm of physics. From the 17^{th} to the 19^{th} centuries, the gravitational and electromagnetic ones were largely developed in their classical framework, ranging from Newton's laws to Maxwell's equations and Eistein's theory of relativity. Alongside the discovery of the atomic nucleus and the development of relativity and quantum mechanics, the weak and strong interactions had their first formulations in the 20^{th} century. The first two interactions have important implications for long-range physics, while the last two could only be observed at subatomic scales, making necessary the advancement of quantum field theory for a quantitative understanding of its properties.

The Standard Model (SM) of particle physics is a set of quantum field theories involving the strong, weak and electromagnetic forces, the latter two unified into the electroweak interaction. The SM is backed up by extensive phenomenological evidence demonstrated in the Review of Particle Physics, with the detection of the Higgs boson announced in 2012 as its most recent milestone.[6] The piece of the SM describing the strong force is the so-called *quantum chromodynamics* (QCD), which originated around the $1970's$ with the discovery of *asymptotic freedom* and the observation of *confinement*. *Hadrons* are the particles emerging from QCD's strong coupling behaviour and were observed by the dozens already in the first particle scattering experiments.

Since before QCD was proposed, the study of hadrons has been guided by the *quark model*, a set of phenomenological models of the low-energy hadronic states.[7] It incorporates QCD features, such as gauge symmetry and confinement, but also adds the quark *flavour* structure present on the strong sector of the Standard Model through a global $SU(N_f)$ symmetry. Such symmetry is only approximate for $N_f \leq 3$, *i.e.* , for the up (u), down (d) and strange (s) quarks, and is quite broken for the charm (c), bottom (b) and top (t) quarks. Nevertheless, it provides a very useful way of cataloguing hadrons into multiplets of $SU(N_f)$, resulting in the so-called *mesons*, particles with a constituent (valence) quark-antiquark pair, and *baryons*, composed of

three quarks. For nearly 40 years, this generated the essential context for discussing the experimentally observed particles under the light of QCD, whose properties are otherwise challenging to study.

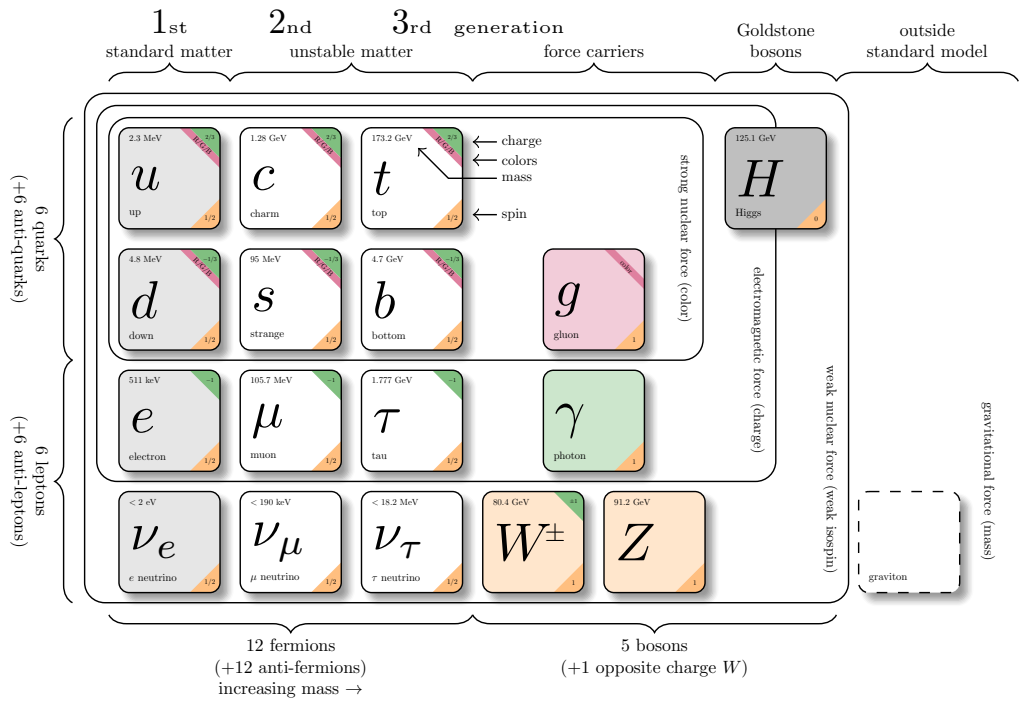

Figure 1 *The Standard Model and the graviton.*[8]

The presence of the QCD-unstable particles called *resonances* is one of the topics where the quark model can provide useful insight. Most observed hadrons are resonances,[9] which decay via the strong force and manifest the "*physics of binding and decay*"[10] in QCD. A typical value for a hadronic resonance "lifetime" is of $\sim 10^{-23} s$, one of the fastest phenomena in physics. Even though they are not *directly* detectable in experiments, resonances are expected to produce a typical *bump* on the cross-section of a process in which they act as an intermediate state. For example, the $\rho(770)$ is a mesonic resonance which is constituted by a light quark-antiquark pair (up or down), according to a vector representation of $SU(N_f = 2)$ in the quark model. It appears in the historically important process of electron-positron scattering, *cf.* Fig. 2, still important nowadays.[11] This particle also features in processes such as the B-*meson decays*,[12] which can potentially constrain new physics *beyond* the Standard Model.[13] The study of the underlying QCD dynamics can give a precise description of hadronic resonances, whose properties need to be identified and distinguished from potential signs of new physics. This is one of the reasons why it is paramount that

the theoretical description of resonances reaches a cutting-edge level.

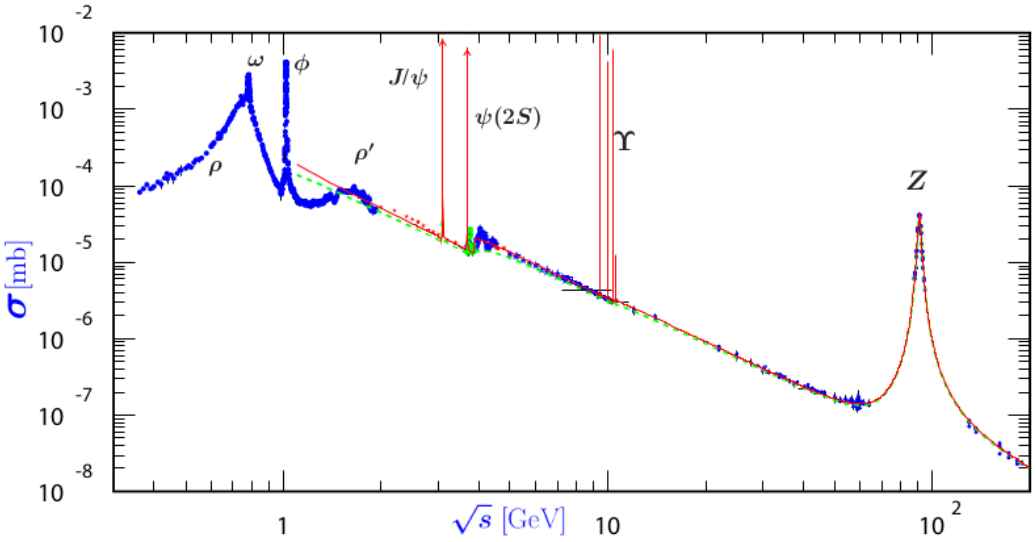

Figure 2 *Total cross-section from e^-e^+ (electron-positron) collisions and related resonances.[6] The $\rho(770)$ is an intermediate state in this historically important process.*

Lattice quantum chromodynamics is one of the most prominent methods for producing first-principle predictions (and postdictions) from QCD, achieved through systematically improvable calculations.[14–16] It consists of discretising spacetime with a Euclidean signature, which eventually leads to a numerically tractable problem. Therefore, the most impactful lattice QCD calculations are numerical by nature and leverage from the synergy with algorithmic and computational developments.[17,18] A showcase of the importance of lattice QCD in the current landscape of particle physics is its role in the ongoing debate on the anomalous magnetic momentum of the muon $g-2$.[11,19–21]

In the context of this work, the extraction of light hadron masses from full QCD is one of the landmarks of spectroscopy on the lattice.[22–24] The study of more complicated dynamical properties of QCD, such as resonances, is considerably hindered on the lattice due to the absence of an explicit Minkowski metric.[25] Nevertheless, the understanding of finite-volume effects[26,27] allied to the creation of novel algorithms in lattice QCD[28,29] allowed for the first rigorous theoretical determinations of resonances in the last decade.[10,30]

Until now, most of the lattice determinations of resonances were performed in unphysical approximations, namely higher than physical quark masses. These calculations rely on effective methods, *e.g.* chiral perturbation theory, to extrapolate

quantities to the physical limit.[31–33] Due to the difficulty of rigorously treating resonances in such methods, the direct implementation of physical quark masses is essential for lifting the uncontrolled systematical uncertainty from that extrapolation. This work presents the first determination of the $K^*(892)$ resonance using lattice QCD with physical quark masses and (nearly-)exact chiral symmetry. We also present the first physical-quark determination of the $\rho(770)$ resonance with a $N_f = 2 + 1$ lattice QCD action where, besides the two degenerate lighter quarks ($N_f = 2$), the strange quark is also allowed to be created from the vacuum fluctuations.

Our resulting statistical precision ("stat") reaches the per cent level, and the systematics uncertainties inherent to our analysis method ("dd") are reliably propagated, which is also novel in the lattice QCD literature. Our results for the mass and width parameters are

$$K^*(892) \begin{cases} M_P &= 892.5(1.7)_{\text{stat}}(6.5)_{\text{dd}} \text{ MeV} \\ \Gamma_P &= 49.5(1.9)_{\text{stat}}(7.2)_{\text{dd}} \text{ MeV} \end{cases}$$

and

$$\rho(770) \begin{cases} M_P &= 788(6)_{\text{stat}}(10)_{\text{dd}} \text{ MeV} \\ \Gamma_P &= 186(16)_{\text{stat}}(41)_{\text{dd}} \text{ MeV} \end{cases}.$$

In Chapter 5, other sources of uncontrolled systematics are identified and future work is suggested to fully control them. From these, we point out our elastic approximation to $K\pi \to K^* \to K\pi$ and $\pi\pi \to \rho \to \pi\pi$ scattering [I], which neglects the decay of the resonances into the suppressed but non-zero $K\pi\pi$ and $\pi\pi\pi\pi$ channels, respectively.[6] Another major systematic is the use of a single lattice spacing and therefore the lack of an extrapolation to the continuum physics, one of the main challenges for scattering determinations on the lattice.[34] This work is also a first step towards a controlled theoretical description of key processes featuring $\rho(770)$ and $K^*(892)$[35,36] in experiments such as LHCb, BaBar and Belle.

We first overview the continuum formulation of QCD and the relevant phenomenological aspects of scattering and resonances. In Chapter 2, we describe the lattice approach to QCD and some of its techniques used here. Then, we present the Lüscher formalism used to extract the scattering information in Chapter 3. The distillation method and the variational problem are presented in Chapter 4. Finally, the data analysis procedure and results are shown in Chapter 5, where model-averaging

[I] We will frequently use the K^* and ρ shorthand notation instead of $K^*(892)$ and $\rho(770)$.

techniques are used in a Lüscher-scattering calculation of the K^* and ρ resonances.

1 Strong Interaction

1.1 Standard Model

The core of the Standard Model is composed of quantum field theories with local gauge invariance. With the discovery of hundreds of subatomic particles, ideas such as the Eightfold Way and the quark model used representations of *global* symmetries to categorise the observed spectrum.[37,38] Yang and Mills inaugurated the era of non-Abelian theories with *local* gauge invariance.[39] These were initially not given much attention due to the absence of massive mediators characteristic of the observed short-ranged interactions. This obstacle was overcome through important theoretical developments. In the electroweak sector of the Standard Model,[40,41] the W^+, W^- and Z bosons acquire their masses via the Higgs mechanism.[42–44] In the strong sector, however, the interactions between *quarks* are mediated via self-interacting massless bosons called *gluons*, a process encoded in *quantum chromodynamics* (QCD).

QCD is the theory of *colour charge* exchange based on local $SU(3)$ invariance, initially proposed to cure the quark model inconsistencies.[45] *Quarks* are the fermionic degrees of freedom in QCD and they acquire mass in the Standard Model via coupling to the Higgs fields. Neither quarks nor gluons are observed in experiments. Instead, through *confinement*, colourless states of quarks called *hadrons* emerge as QCD states. Confinement was extensively observed in experiments and probed by lattice simulations,[46] though it is still not precisely understood how it emerges from QCD.[47]

The hadron masses are way higher than the sum of its constituent (valence) quarks, meaning that most of it is produced by the strong-coupled field excitations binding them via a *dynamical mass generation* mechanism. The deep-inelastic scattering experiments showed a near-free behaviour between the constituents of hadrons at high energies, which is described by the *asymptotic freedom* property of QCD.[48,49] At low energies, the observed pseudoscalar light hadron masses can be reasonably understood on a theory effectively mediated by *pions*. The Standard Model has a clear

hierarchy of masses separating the u, d, s from the c, b, t quarks up to three orders of magnitude. In this work, we focus on the lightest ones as the heaviest essentially decouple from the light-quark physics that we study.

Despite not being amenable to analytical treatment, much of the strong coupling regime of QCD can be learned from its symmetries and their breaking. QCD has an intricate breaking pattern based on a

$$U(N_f)_L \times U(N_f)_R = SU(N_f)_V \times SU(N_f)_A \times U(1)_V \times U(1)_A \tag{1.1}$$

global structure, in which we consider only the lightest three quark flavours, *i.e.* $N_f \leq 3$. The singlet $U(1)_A$ chiral symmetry is broken by a quantum anomaly which can be understood at the level of the path integral measure.[50,51] The non-singlet $SU(N_f)_A$ symmetry is spontaneously broken via the dynamical formation of a non-zero quark condensate $\langle 0|\,\bar{\psi}\psi\,|0\rangle \neq 0$. The non-zero quark masses explicitly break $SU(N_f)_V$ but, for $N_f = 2$, it turns out that the *isospin symmetry* $SU(2)_V$ is a very good approximation up to the small mass difference between the up and $down$ quark (≈ 3 MeV).[6] In this work, we work with exact isospin symmetry, *i.e.* $m_u = m_d$. The only exact global symmetry of QCD is $U(1)_V$ and its associated conserved quantum number is the baryonic number. These are all non-perturbative features that make QCD be referred to as a *vector-like theory*.

1.2 Gauge Theories

QCD is a theory with local gauge invariance based on the non-Abelian Lie group $SU(3)$. Lie groups can be locally mapped onto Euclidean space. For example, the defining group of electromagnetism $U(1)$ can be mapped onto a circle and depends on a single real parameter.

If we go beyond $U(1)$ phase transformations, we have the unitary matrix group $U(N_c)$, which has N_c^2 real parameters and its group elements obey $\Omega_i^{-1} = \Omega_i^\dagger$. By imposing $\det \Omega_i = 1$, we reach at the $SU(N_c)$ group, which depends on $N_c^2 - 1$ real independent parameters. The group elements of $SU(N_c)$, as well as for any Lie group, can be written through an exponential map of its algebra $\mathfrak{su}(N_c)$

$$\Omega = e^{i\theta} = \sum_{k=0}^{\infty} \frac{(i\theta)^k}{k!}. \tag{1.2}$$

The real parameter vector $\theta \in \mathfrak{su}(N_c)$ is written in terms of the generators T^a as

$$\theta = \theta^a T^a, \tag{1.3}$$

where $a = 1, \ldots, N_c^2 - 1$, and

$$\operatorname{tr} T^a T^b = \frac{1}{2}\delta^{ab}. \tag{1.4}$$

Non-Abelian Lie groups also have the property that their group elements do not commute, reflected in the commutation relations of the group generators

$$[T^a, T^b] = i f^{abc} T^c, \tag{1.5}$$

where the structure constants f^{abc} is a defining property of the group. At the end of the day, this non-commutativity results in the high nonlinearity of the equations of motion, which is partly responsible for the non-perturbative effects we are interested in here.

In analogy to electromagnetism, the non-interacting non-Abelian action in the presence of matter is

$$S_{\text{free}}[A, \bar{\psi}, \psi] = \int d^4x \left[-\frac{1}{2g^2} \operatorname{tr} G_{\mu\nu}(x) G^{\mu\nu}(x) + \bar{\psi}(x)(i\gamma_\mu \partial_\mu - m_f)\psi(x) \right], \tag{1.6}$$

where $\bar{\psi}, \psi$ belong to some representation of the Lie group $SU(N_c)$, while A_μ belongs to its algebra. The gamma matrices γ^μ obey the Clifford algebra

$$\{\gamma_\mu, \gamma_\nu\} = 2\eta_{\mu\nu}, \tag{1.7}$$

where $\eta_{\mu\nu}$ is the Minkowski metric. Such action is proposed to be invariant under global $SU(N_c)$ transformations, which is readily achieved by the form $G_{\mu\nu} = \partial_\mu A_\nu - \partial_\nu A_\mu$. A straightforward way of inducing interactions is by promoting ("gauging") such transformations from global to local, which leads to

$$\psi(x) \to \psi' = \Omega(x)\psi(x), \tag{1.8}$$

$$A_\mu(x) \to A_\mu(x)' = \Omega(x) A_\mu(x) \Omega(x)^\dagger - i\Omega(x)\partial_\mu(x)\Omega(x)^\dagger. \tag{1.9}$$

Requiring the $G_{\mu\nu}$ term to be locally gauge-invariant leads to the non-Abelian field-

strength tensor

$$G_{\mu\nu}(x) \equiv \partial_\mu A_\nu(x) - \partial_\nu A_\mu(x) + i[A_\mu(x), A_\nu(x)], \tag{1.10}$$

which also belongs to the algebra and transforms as

$$G_{\mu\nu}(x) \to \Omega(x) G_{\mu\nu}(x) \Omega^\dagger(x). \tag{1.11}$$

Further requiring that the fermionic action stays invariant will lead to a gauge-matter coupling term $\bar{\psi}\gamma_\mu A_\mu \psi$ absorbed into the definition of the covariant derivative

$$D_\mu(x) \equiv \partial_\mu + iA_\mu(x), \tag{1.12}$$

which, acting on the spinor field, transforms as

$$\not{D}\psi(x) \to \not{D}'\psi'(x) = \Omega(x)\not{D}\psi(x). \tag{1.13}$$

Here, A_μ acts as a *parallel transport*, taking into account the $SU(N_c)$ gauge freedom on each space-time point. Observe that the gauge transformations now have a much more complicated mathematical structure as its non-Abelian "phases" are arbitrary *at each* spacetime point.

In QCD, $N_c = 3$ corresponds to the number of *colour* charges. In the context of the Standard Model, the theory also acquires a specific global structure due to the $SU_L(N_f) \times SU_R(N_f)$ *flavour* symmetry and its breaking. The "classical action" of QCD is

$$S_{QCD}[A, \bar{\psi}, \psi] = \int d^4x \left[-\frac{1}{2g^2} \operatorname{tr} G_{\mu\nu}(x) G^{\mu\nu}(x) + \bar{\psi}(x)(i\not{D}(x) - M_f)\psi(x) \right], \tag{1.14}$$

where M_f is a $N_f \times N_f$ diagonal mass matrix and thus all fields have flavour indices. The current Standard Model has $N_f = 6$ but, for our purposes, it is sufficient to consider two degenerate light quarks ($m_u = m_d$) and one strange quark, denoted as $N_f = 2 + 1$.

1.3 Path Integral

The path integral formulation is a concise way of formally defining constrained quantum field theories such as QCD. This formulation also provides the intuitive

idea that a quantum amplitude is composed of a sum of "stories", or in our case, a sum of trajectories or field configurations. Originally, the Lagrangian path integral was derived by discretizing time and taking the continuum limit at the end. In quantum mechanics, this can be done explicitly for some cases, such as the free particle and the harmonic oscillator.[52] In quantum field theory (QFT), analogous steps can be performed to reach a similar result, even though it encodes a more complicated mechanism at a higher dimensionality and is more difficult to rigorously define.

For a generic collection of fields ϕ, the path integral representation of a transition amplitude is

$$\langle \phi_f | \, e^{-2it\hat{H}} \, | \phi_i \rangle = \int_{\phi(-t,\mathbf{x})=\phi_i(\mathbf{x})}^{\phi(+t,\mathbf{x})=\phi_f(\mathbf{x})} \mathcal{D}\phi(x) \; e^{iS[\phi]}, \tag{1.15}$$

where $|\phi_f\rangle$, $|\phi_i\rangle$ are arbitrary states in the Heisenberg (time-independent) picture and the evolution operator $e^{-it\hat{H}}$ brings them to $+t$, $-t$, respectively. Note that the fields ϕ appearing on the right-hand side of (1.15) are not operator-valued objects, instead they are functionals of the field operators which will be loosely defined here by

$$\hat{\phi}(x) \, |\phi\rangle = \phi(x) \, |\phi\rangle \, , \tag{1.16}$$

with integration measure

$$\mathcal{D}\phi(x) = \prod_x d\phi(x). \tag{1.17}$$

The action S is a functional of the fields and their derivatives. The expressions in this section are only formal and a regularisation procedure is needed to make them well-defined (Ch. 2).

The QCD path integral can be written as in (1.15) using the action (1.14) integrated over gauge and fermion fields. In perturbative calculations, it is necessary to further add an effective gauge-fixing term through the Faddeev-Popov procedure to make the saddle-point expansion well-defined.[53] We will be interested in performing non-perturbative calculations of gauge-invariant quantities by directly evaluating QCD's path integral (Ch. 2 and 4), which does not require gauge fixing. We will also omit a possible θ-term in the QCD path integral as it will have negligible influence on the phenomenology dealt with in this work.[54]

There is no need to write a path integral expression in terms of QCD fields here, as the reasoning of this section can be made with a generic field ϕ. This will correspond either to a shortcut for QCD fields or to a low-energy effective degree of freedom,

e.g. a pion, emerging from it.

In QFT, it is often useful to interpolate the amplitude (1.15) with field operators at different times t_1, t_2. Supposing $t > t_2 > t_1 > -t$ and inserting two resolutions of the identity in position space and simplifying, we eventually reach at

$$\langle \phi_f | \, e^{-it\hat{H}} \hat{\phi}(x_2)\hat{\phi}(x_1) e^{-it\hat{H}} \, | \phi_i \rangle = \int_{\phi(-t,\mathbf{x})=\phi_i(\mathbf{x})}^{\phi(+t,\mathbf{x})=\phi_f(\mathbf{x})} \mathcal{D}\phi(x) \; \phi(x_1)\phi(x_2) \; e^{iS[\phi]}, \tag{1.18}$$

where the hatted fields are operator-valued and time-dependent. Note that we get the same result for $t > t_1 > t_2 > -t$, meaning that the path integration automatically encodes the time ordering. We will be frequently interested in *vacuum expectation values* instead. Assuming non-zero overlap of the interacting vacuum $|0\rangle$ with an arbitrary state and with the noninteracting vacuum, we can perform an infinitesimal rotation of time into the complex plane and, asymptotically, get the 2-point Green function

$$\langle 0 | \, T\hat{\phi}(x_1)\hat{\phi}(x_2) \, | 0 \rangle = \lim_{t \to \infty(1-i\epsilon)} \frac{\int \mathcal{D}\phi(x) \; \phi(x_1)\phi(x_2) \; e^{iS[\phi]}}{\int \mathcal{D}\phi(x) \; e^{iS[\phi]}}, \tag{1.19}$$

where we have hidden the integral boundary conditions. From an axiomatic point of view, the set of all (non-time-ordered) n-point functions of a suitably defined QFT contains all the information necessary to reconstruct the whole theory.[55]

One way of recovering the physical information contained in a Green function is through its spectral decomposition. For example, the spectral representation of a 2-point function exposes the 1-particle and bound states of the theory. For example, for the momentum-space 2-point function we have

$$\int d^4x \; e^{-ip\cdot x} \, \langle 0 | \, T\hat{\phi}(x)\hat{\phi}(0) \, | 0 \rangle = \int dq^2 \rho(q^2) \frac{i}{p^2 - q^2 + i\varepsilon}, \tag{1.20}$$

and such states manifest as isolated peaks in the spectral density below the lowest multiparticle threshold (Fig. 1.1). This is also valid for states that do not correspond to fundamental fields appearing in the Lagrangian, which is very important for studying a confining theory such as QCD.

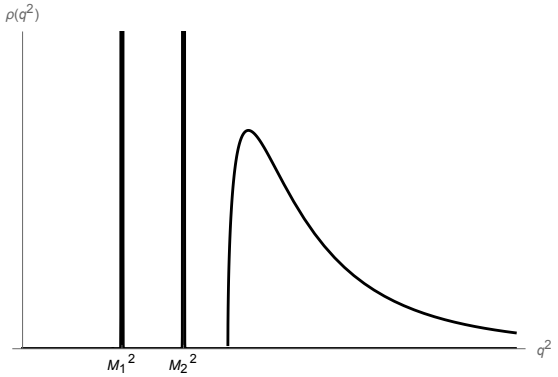

Figure 1.1 *Simple spectral density function with 1-particle state peaks and the multiparticle threshold.*

In QCD, resonances are unstable particles with rest mass above scattering thresholds and thus cannot be represented as spikes in $\rho(q^2)$, but instead as "bumps". The observation of resonances in experiments will be more directly connected to the analytic structure of the S-matrix in the following section.

1.4 Scattering

1.4.1 S-matrix

The main application of QFT in this work is the computation of scattering amplitudes. In this context, it is commonly assumed that interactions have a small finite duration and that the scattered particles are sufficiently far apart at asymptotic times. Then, in/out states can be built as narrow wavepackets asymptotically peaked at certain spatial momenta.[56] At $t \to \pm\infty$, the map

$$\langle p_1 p_2 \ldots ; out \,|\, q_1 q_2 \ldots ; in \rangle \equiv \langle p_1 p_2 \ldots \,|\, S \,|\, q_1 q_2 \ldots \rangle \tag{1.21}$$

defines the so-called S-matrix. We can isolate the case of no scattering by writing it as

$$S \equiv \mathbb{1} + i\mathcal{T} \equiv \mathbb{1} + (2\pi)^4 \delta(\textstyle\sum_j p_j^{out} - \sum_j q_j^{in})\; i\mathcal{M}, \tag{1.22}$$

where the $\mathcal{T}$-matrix and the *scattering amplitude* $\mathcal{M}$ are defined implicitly. It is often useful to split the real and imaginary parts of the inverse $\mathcal{T}$-matrix as

$$\mathcal{T}^{-1} = \mathcal{K}^{-1} - \mathbb{1}i, \tag{1.23}$$

where $\mathcal{K}$ is real and symmetric due to unitarity and time-reversal invariance of S.[57]

If we focus on elastic $2 \to 2$ scattering in the s-channel, it is natural to parametrise the S-matrix as[58]

$$S(s,t) = e^{2i\boldsymbol{\delta}(s,t)}, \tag{1.24}$$

where s, t are Mandelstam variables and $\boldsymbol{\delta}$ is the so-called *phase shift*, which in this case, is a matrix in the angular momentum basis. In phenomenology, one is interested in the partial-wave components of the quantities above, labeled by the angular momentum quantum number l. Partial-wave decomposition yields the energy-dependent phase shifts $\delta_l(s)$, reducing the $\mathcal{K}$-matrix to a single function

$$\mathcal{K}_l(s) = \tan \delta_l(s). \tag{1.25}$$

The phase shift can be connected to the usual one from quantum mechanics by constructing an appropriate asymptotic scattering wave, which allows us to interpret δ_l as the phase difference due to a local interaction.[59] For general coupled-channel scattering, $\mathcal{K}$ contains phase shifts for the other channels and inelasticity parameters η between them.[57]

The usual relation between Green functions and the S-matrix is expressed by the *LSZ formula*[56]

$$\begin{aligned}\langle p_1 \dots | \, S \, | \, q_1 \dots \rangle = \int d^4 y_1 e^{i p_1 \cdot x_1} K(x_1) \dots \\ \int d^4 y_1 e^{i y_1 \cdot q_1} K(y_1) \dots \, \langle 0 | \, T \hat{\phi}(x_1) \dots \hat{\phi}(y_1) \dots | 0 \rangle \, ,\end{aligned} \tag{1.26}$$

where K are the kinematic operators of the theory written in terms of renormalised action parameters. Thus, S-matrix elements are residues of the corresponding Green functions, when all external legs go on-shell. The LSZ formula can be analogously written in terms of vacuum expectation values of operators, encoding scattering of particles not directly featuring in the Lagrangian and enabling the use of effective field theories to study hadronic scattering in QCD.[53]

Perturbation theory methods can provide estimations of the Green functions going on the right-hand side of (1.26). However, in an asymptotic-free theory like QCD, this only yields a good description of physics at high energies, *e.g.* in deep-inelastic scattering. At $\simeq 1$ GeV though, hadron scattering and the appearance of *resonances* are highly non-perturbative phenomena.

1.4.2 Resonances

Resonances are unstable particles featuring in numerous scattering processes but that decay through the strong force. We can observe a resonance, say $K^*(892)$, as an intermediate state in processes such as $K\pi \to K^*(892) \to K\pi$, typically displaying an enhancement of the total cross-section around the resonance mass. They can also appear in formation experiments together with other spectator particles.[60] The width of a resonance is directly related to its lifetime and is also called *decay rate*, the broadest resonances being the shortest-lived ones.

The characterisation of unstable states is a long-standing problem in physics, dating back to the origins of quantum mechanics and the problem of the capture of neutrons.[61] In quantum mechanics, unstable states are usually treated as dissipative systems with complex Hamiltonian eigenvalues, which gives rise to an exponential decay of the wave function.[62–64] The definition of resonances in quantum field theory is also problematic because they do *not* correspond to an eigenstate of the Hamiltonian.

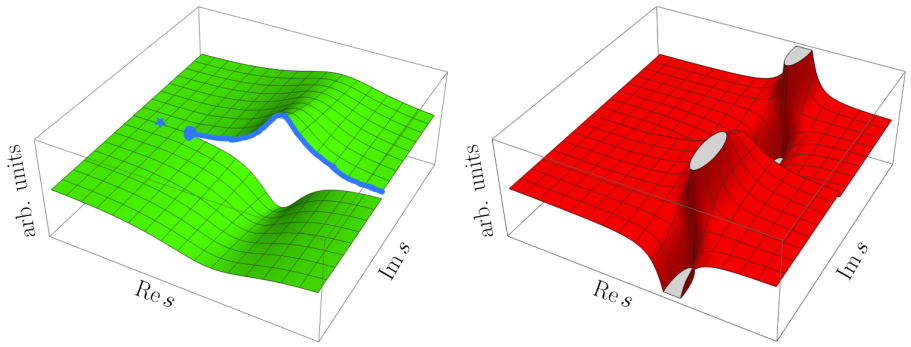

Figure 1.2 *Imaginary parts of the multi-valued amplitude.[60] The resonance poles appear on the unphysical sheet (red), affecting observables on the real-s line (blue) at the physical sheet.*

To study a resonance, one can parametrise the scattering phase shift through some kind of Breit-Wigner distribution with a mass M_{BW} and width Γ_{BW} (see (1.31)). In more sophisticated forms, one uses extra parameters, such as the branching fraction, as well as an energy-dependent width.[6] Another approach is to use pole parameters, which relate the presence of resonances to poles in the complex-energy plane of scattering amplitudes.[60,62] The pole characterisation is comprised of the pole position and residues, which can be written in terms of a mass M_P, a width Γ_P, and couplings

to different channels.

The Breit-Wigner parametrisations were traditionally used to describe specific experimental cross-sections, while the pole parameters are more closely related to the analytic structure of the underlying theory.[62,65,66] From the unitary and causal structure of the theory, resonances are associated with poles on the unphysical sheets of partial-wave scattering amplitudes under analytical continuation. In Figure 1.2, we can see that the $i\varepsilon$ prescription tilts the real s-axis into the physical sheet (green), and the unphysical sheet (red) is accessible from the branch cut.

For the sake of intuition, take a scalar particle in Minkowski space. Following Ref. [56], we can write the "intermediate $1 \to 1$ scattering amplitude" as

$$\mathcal{M}(s) \propto \frac{1}{s - M^2 - \Sigma(s) + i\varepsilon}, \tag{1.27}$$

where s is the (squared) invariant mass and Σ is the sum of all appropriate 1PI (one-particle irreducible) diagrams. If the particle is stable, unitarity through the optical theorem implies that this amplitude is real.[56] In this case, the mass of the particle is identified by the pole position on the real energy axis, *i.e.* $M_P^2 = M^2 + \Sigma(M_P^2)$.

However, if the particle is unstable and kinematically allowed to decay to lighter states, the amplitude will acquire an imaginary part through $\Sigma(s)$ and the pole will shift into the complex plane. We then define the mass and width of the resonance as being, respectively, the real and imaginary parts of the pole position[60]

$$\sqrt{s_R} = M_P - \frac{i}{2}\Gamma_P. \tag{1.28}$$

For $\Gamma_P \ll M_P$, then $\Sigma(s) \approx \Sigma(M_P^2)$ and so

$$M_P^2 \approx M^2 + \operatorname{Re}\Sigma(M_P^2), \qquad \Gamma_P \approx -\frac{1}{M_P}\operatorname{Im}\Sigma(M_P^2). \tag{1.29}$$

Hence, the amplitude will be

$$\mathcal{M}(s) \propto= \frac{1}{s - M_P^2 + i\Gamma_P M_P}, \tag{1.30}$$

and we can also identify the Breit-Wigner distribution in the cross-section

$$\sigma \propto |\mathcal{M}|^2 \propto \frac{1}{(s - M_P^2)^2 + \Gamma_P^2 M_P^2}. \tag{1.31}$$

Notice that this is a pictorial view of what would happen if an intermediate unstable state goes on-shell. For a more explicit example in perturbation theory for $2 \to 2$ scattering, see Ref. [67].

We assumed $\Gamma_P \ll M_P$ above, known as the *narrow-width approximation*. As soon as different channels open and resonances overlap in the same region, finite-width and threshold effects make the actual distribution deviate from Breit-Wigner and be process dependent, which can be accounted for by enhancing the parametrisation. Nevertheless, the pole position (1.28) and its residue are taken to be model-independent quantities, in the sense that resonances are the poles in the S-matrix manifesting in experiments in different ways.[6] When far from the narrow-width approximation, the Breit-Wigner parameters do not necessarily coincide with the pole parameters and the connection between them is lost.

2 Lattice Quantum Chromodynamics

The reliable computation of observables in QCD relies on the development of nonperturbative approaches, especially at low energies where the coupling constant is high. Lattice field theory provides a systematically improvable tool for computing QCD observables. Its main applications are based on numerical calculations using Monte Carlo methods to evaluate a *discretised Euclidean* path integral on a finite volume, a procedure that is frequently called *simulation* [I].

2.1 Formulation

Wick rotation

The QFT path integral formulas presented in Sec. 1.3 are complex-valued and highly oscillatory. Despite being useful for formal manipulations in Minkowski spacetime, they are not only extremely hard to provide a well-defined mathematical framework but also not easy to treat numerically.

We define *correlation functions* computable from a suitably defined Euclidean path integral as

$$\langle \varphi(x_1) \dots \varphi(x_2) \rangle = \mathcal{Z}^{-1} \int \mathcal{D}\varphi(x)\ \varphi(x_1) \dots \varphi(x_n)\ e^{-S[\varphi]}, \tag{2.1}$$

where

$$\mathcal{Z} = \int \mathcal{D}\varphi(x)\ e^{-S[\varphi]} \tag{2.2}$$

is the *partition function*. Under certain conditions of the theory, such as reflection-

[I] Even though it is standard, the term "simulation" might be misleading in lattice QCD as it does not include real-time evolution but a stochastic estimation of the observables, *cf.* Sec. 2.4.

positivity,[68] the Minkowski QFT can be recovered via an analytic continuation of the n-point functions that coincide with (2.1) at the imaginary time axis. The time-ordered functions in (1.19) can be recovered with a *Wick rotation*. From now on, we will use the words *correlators* or n-point functions to refer to Euclidean expectation values computed from expressions such as (2.1), which can also include composite operators of the fields (Ch. 4).

In practice, the spectral observables we will compute from an Euclidean version of QCD do not carry a metric label. This means that we can perform the change of coordinates [II]

$$x_0 \to -ix_4 \tag{2.3}$$

and the analogous changes for all fields in (1.14) to get our imaginary-time version of QCD

$$\begin{aligned} iS_{QCD}[A,\bar{\psi},\psi] \to -S_{QCD}[A,\bar{\psi},\psi] = \\ -\int d^4x \left[\frac{1}{2g^2}\,\mathrm{tr}\, G_{\mu\nu}(x)G^{\mu\nu}(x) + \bar{\psi}(x)(\not{D}(x) + M_f)\psi(x)\right], \end{aligned} \tag{2.4}$$

where all fields are now in Euclidean space. The metric and γ-matrices are changed accordingly to obey the algebra $\{\gamma_\mu, \gamma_\nu\} = 2\delta_{\mu\nu}$, which can be achieved by the choice

$$\gamma^4 = \gamma^0, \qquad \gamma^j \to -i\gamma^j. \tag{2.5}$$

Note that the oscillatory exponential term in the original path integral now turns into a Boltzmann-like probability weight. The provided exponential damping of large field fluctuations will be fundamental for the numerical convergence of our calculations (Ch.4). This also connects (2.2) to a partition function from statistical mechanics, whose techniques are fundamental to lattice QCD simulations (Sec. 2.4).

Lattice Regulator

It is still hard to give precise meaning to an Euclidean path integral without a regularisation procedure. In QCD at high energies, it is possible to regulate the integrals appearing on the perturbative expansion.[56] We instead use a lattice regulator[69] which corresponds to defining the Euclidean theory on a spacetime grid

$$\Lambda = \{x; x/a \in \mathbb{Z}^4\}, \qquad x = (x_1, x_2, x_3, x_4), \tag{2.6}$$

[II] We will keep using t now as the imaginary time x_4.

where a is called the *lattice spacing*. This defines a nonperturbative cutoff for the ultraviolet modes with $p \gtrsim \pi/a$. In practical computations, we will also need an infrared cutoff introduced by limiting the coordinates above to

$$x_{i=1,2,3} = 1, \dots N, \quad L = aN, \qquad \text{and} \qquad x_4 = 1, \dots N_T, \quad T = aN_T. \tag{2.7}$$

In this work, a finite spatial volume will be also important for the extraction of dynamical quantities (Ch. 3).

It is worth mentioning that one can build a lattice Hamiltonian $\hat{H}$ via[70]

$$\hat{\mathrm{T}}_{t+1,t} = e^{-a\hat{H}_{t+1,t}}, \tag{2.8}$$

where the *transfer matrix* $\hat{\mathrm{T}}$ is a discretised time evolution operator, the Euclidean analogous to the one in (1.18). Fundamental proofs of unitarity and positivity of lattice theories are more directly shown in such formalism, guaranteeing a well-defined quantum theory. The partition function is recovered through

$$\mathcal{Z} = \mathrm{tr}\, e^{-a\hat{H}}, \tag{2.9}$$

and observables as well in a similar way. Even though we will directly estimate the path integral in this work, we assume the existence of such Hamiltonian when dealing with spectral observables in Ch.4.

The ultimate goal of typical lattice calculations is to reach the *physical* limits:

- $L, T \to \infty$ (thermodynamical limit)
- $m_{\mathsf{quarks}} \to m_{\mathsf{quarks}}^{\mathsf{phys}}$ (chiral limit)
- $a \to 0$ (continuum limit)

The thermodynamical limit requires simulations at different temporal and spatial extensions so that finite-volume and finite-T (thermal) effects are under control. Regarding the spatial box size, we note that such effects are actually what allows us to compute resonance parameters in infinite volume up to exponentially suppressed volume corrections (Ch.3). Even though they are small for an appropriate choice of parameters, one would ideally have multiple volumes (in physical units) so that such effects can be carefully extrapolated away.

The chiral limit is usually necessary because simulations at physical pion masses are

expensive and difficult. We take advantage of having the lightest pseudoscalar state tuned to have mass very close to the pion one, using a discretised version of QCD with approximate chiral symmetry, *cf.* Sec.2.3.

The continuum limit is taken by repeating the calculation at different values of a on an asymptotic regime where something is known about the small-a behaviour of the desired quantities. For that, one first requires that a minimal set of observables remain invariant as the regulator a is removed. This fixes the free parameters present in QCD (quark masses and strong coupling). Using renormalisation group equations, it can be shown that[71]

$$a = \frac{1}{\Lambda_{\mathsf{lat}}} \exp\left(-C/g^2\right)(1 + \mathcal{O}(g^2)), \tag{2.10}$$

where C is a known constant and Λ_{lat} is fixed by the scale-setting procedure. The continuum limit thus corresponds to the asymptotic freedom regime, *i.e.* $g \to 0$. From a statistical mechanics perspective, in the continuum limit one approaches a critical point in the phase diagram of the inverse coupling $\beta = 6/g^2$, where the correlation length diverges and the physics does not depend anymore on local fluctuations. In this work, we focus on a single value of $a \approx 0.1$ fm due to the high cost of our spectroscopy calculation (Ch.4).

Due to such high computational cost, we only have a single volume at a single lattice spacing and thus their respective limits are not directly treated here. Ideally, one would have to take $a \to 0$ at several values of L to extrapolate the discretisation and residual finite-volume volume effects away, respectively.

2.2 Gauge Sector

We still need a discretised form of (2.4) in order to compute path integrals on a computer. It turns out that defining a non-Abelian theory by discretising the algebra-valued gauge potential A_μ would need a high amount of fine-tuning due to the lack of exact gauge invariance.[72] Instead, lattice gauge theory is built from elements of the compact $SU(3)$ gauge group

$$U_\mu(x) \in SU(3), \qquad x \in \Lambda, \tag{2.11}$$

living in-between sites $x, x+\hat{\mu}$, known as *link* variables. They can be viewed as an approximation of the elementary parallel transporter between x and $x+\hat{\mu}$

$$\mathfrak{U}(x \to x+\hat{\mu}) = \mathcal{P} \exp\left[i \int_{x \to x+\hat{\mu}} \mathrm{d}x' \cdot A(x') \right] \approx e^{iaA_\mu(x)} \tag{2.12}$$

for small enough $|\hat{\mu}| = a$, where A is the continuum gauge field [III]. Note that the link variables are dimensionless fields.

Under gauge transformations $\Omega(x) \in SU(3)$, the link variables transform as

$$U_\mu(x) \to U_\mu(x)' = \Omega(x) U_\mu(x) \Omega^\dagger(x+\hat{\mu}). \tag{2.13}$$

This allows the construction of gauge-invariant quantities by taking the trace of closed paths of links

$$\mathcal{W}(\mathcal{C}) = \frac{1}{3} \operatorname{tr} \prod_{U^{(i)} \in \text{closed } \mathcal{C}} U^{(i)}, \tag{2.14}$$

the so-called Wilson loops. A strong coupling expansion ($\beta \to 0$) of Wilson loops exhibits an area law characteristic of a confining theory.[69] The full confining behaviour was evidenced in various numerical simulations of the quark-antiquark static potential.[46]

A minimal closed loop of link variables

$$U_{\mu\nu}(x) = U_\mu(x)\, U_\nu(x+\hat{\mu})\, U_\mu^\dagger(x+\hat{\nu})\, U_\nu^\dagger(x) \tag{2.15}$$

is called a *plaquette*. Originally, the discretised $SU(3)$ action was proposed as a sum over all plaquettes[69]

$$S_{\mathrm{W}}[U] = \frac{2}{g^2} \sum_{x \in \Lambda} \sum_{\mu > \nu} \operatorname{Re}\ \operatorname{tr}\left[\mathbb{1} - U_{\mu\nu}(x) \right], \tag{2.16}$$

which is gauge invariant by (2.13). Given equation (2.12), one can make the connection to the continuum for small a via (2.12), which can be used to expand the plaquette operator to leading order

$$U_{\mu\nu}(x) = \exp\left[i a^2 G_{\mu\nu}(x) + \mathcal{O}(a^3) \right]. \tag{2.17}$$

[III] Even though not explicitly needed here, one can also define a lattice representation of the gauge field through an algebra projection of the link variables.[73]

By substituting this into (2.16), we have

$$S_{\mathsf{W}}[U] = \frac{a^4}{2g^2} \sum_{x\in\Lambda} \sum_{\mu,\nu=1}^{4} \left[\text{tr}\, G_{\mu\nu}(x)^2 + \mathcal{O}(a^2)\right] \tag{2.18}$$

and formally taking $a \to 0$ and $a^4 \sum_{x\in\Lambda} \to \int d^4x$ shows the correct *naive continuum limit* of the gauge Wilson action.

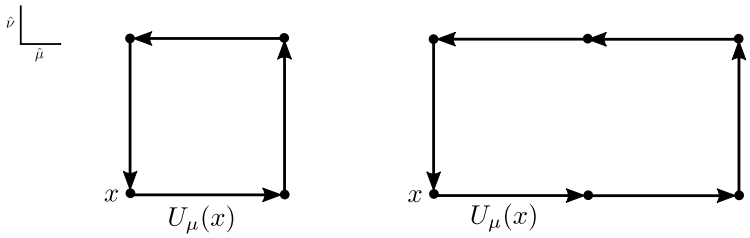

Figure 2.1 *Left: plaquette. Right: rectangular loop.*

The approach to the continuum corresponds to a second-order phase transition in statistical mechanics, which has a universal character. This means that one is free to define different lattice actions that approach the critical point from different trajectories. This can be done by proposing an improved lattice action

$$S_{\mathsf{G}}[U] = \frac{2}{g^2}\left[c \sum_{x\in\Lambda} \sum_{\mu>\nu} \text{Re}\ \text{tr}\,(\mathbb{1} - U_{\mu\nu}(x)) + \sum_{\text{type}-k\ \text{loops}} c_k\, \text{Re}\ \text{tr}\,(\mathbb{1} - R_k(x))\right], \tag{2.19}$$

where R_k are link-variable loops different from the plaquette. We use an RBC-UKQCD ensemble with the Iwasaki gauge action[74] where only the additional 1×2 $(k = 1)$ rectangular loop with coefficients

$$c_1 = -0.331, \qquad c = 1 - 8c_1 \tag{2.20}$$

are non-zero, as it was observed to improve topological tunneling and chiral properties on the fermion sector.[75] Originally, through a block-spin renormalisation procedure such action was found to lie close to the renormalized trajectory thus leading to the critical point faster than other choices.[76]

We finally write down the discretised gauge path integral used in this work

$$\mathcal{Z}_G = \int \mathcal{D}U e^{-S_{\mathsf{G}}[U]}, \tag{2.21}$$

where

$$\mathcal{D}U = \prod_{x\in\Lambda}\prod_{\mu=1}^{4} dU_\mu(x) \tag{2.22}$$

is the spacetime Haar measure of $SU(3)$ defined through its algebra.[77,78] Note the integrations in (2.21) are over the $SU(3)$ group in a finite number of lattice points, which is finite and numerically well-defined.

2.3 Quark Sector

2.3.1 Naive and Wilson fermions

Differently from gauge fields, fermions are put directly on the lattice sites. A naive way of discretising the interacting fermionic action in (2.4) is to introduce a "gauged" symmetric finite difference

$$\frac{\gamma_\mu}{2a}\sum_{\mu=1}^{4} U_\mu(x)\psi(x+\hat{\mu}) - U_{-\mu}(x)\psi(x-\hat{\mu}), \tag{2.23}$$

resulting in

$$\begin{aligned} S_{\mathsf{F}}^{\mathsf{naive}}[\bar{\psi},\psi,U] &= a^4\sum_x \bar{\psi}(x)\left[\frac{1}{2a}\sum_{\mu=\pm1}^{\pm4}\gamma_\mu U_\mu(x)\delta_{x+\hat{\mu},y} + m_f\right]\psi(y) \\ &\equiv a^4\sum_x \bar{\psi}(x) D_{\mathsf{naive}}(x,y;m_f)\psi(y), \end{aligned} \tag{2.24}$$

where the link variables make this term gauge-invariant under (1.13), (1.8).

In momentum space, the naive fermion propagator $D^{-1}_{\mathsf{naive}}(x,y)$ corresponds to its continuum

$$D^{-1}_{\mathsf{naive}}(p;m_f) = \left(i\sum_\mu \gamma_\mu a^{-1}\sin(ap_\mu) + m_f\right)^{-1} \xrightarrow{a\to 0} (i\not{p} + m_f)^{-1}, \tag{2.25}$$

where the lattice momentum is in the Brillouin zone $p_\mu \in (-\pi/a, \pi/a]$. The naive Dirac propagator has poles at[79]

$$p_0 = \pm i\omega(\mathbf{p}),\ \pm i\omega(\mathbf{p}) \pm \pi/a, \tag{2.26}$$

with

$$\omega(\mathbf{p}) = a^{-1}\text{arcsinh}\sqrt{\sum_i \sin(ap_i)^2 + m_f^2} \xrightarrow{a\to 0} \sqrt{\mathbf{p}^2 + m_f^2}. \tag{2.27}$$

Besides the proliferation of poles in (2.26), the dispersion relation (2.27) displays identical behaviour at the boundaries of the Brillouin zone on each direction ($p_i \sim \pi/a$). Translated to Minkowski spacetime, these are interpreted as different (anti) particles of equal mass that survive in the continuum limit. Such spurious modes are called *doublers* and, in four spacetime dimensions, they sum up to 16 fermions interacting with each other and with the gauge fields.

Discretising fermions is a general problem in physics that, in one way or another, leads to some penalty. The *Nielsen-Ninomiya no-go theorem* implies that one cannot have a *local* lattice theory with the "correct" naive continuum limit and still

- be doubler-free *and*
- have exact chiral symmetry.

In general, locality is a desirable property in quantum field theories and one would expect the lattice action to match the continuum classical one when $a \to 0$. Exact chiral symmetry means that the Dirac operator obeys

$$\{\gamma_5, D\} = 0, \tag{2.28}$$

implying that the action is invariant under infinitesimal chiral transformations, *e.g.* in

$$\delta\psi = i\alpha\gamma^5\psi, \tag{2.29}$$

in the limit $m_f \to 0$.

The so-called *Wilson fermions* are a widely employed solution for fermion doubling.[69] They are achieved by adding a term proportional to the discretised covariant Laplacian to the action, resulting in the Dirac operator [IV]

$$D_{\text{W}}(x, y; m_f) = \frac{4}{a} + m_f - \frac{1}{2a}\sum_{\mu=\pm 1}^{\pm 4}(1 - \gamma_\mu)U_\mu(x)\delta_{x+\hat{\mu},y}, \tag{2.30}$$

which decouples the doublers through the UV-divergent mass term in the continuum limit. This comes at the cost of *explicitly* breaking chiral symmetry. Besides obscuring

[IV] $\gamma_{-\mu} = -\gamma_\mu$.

the role of *spontaneous* chiral symmetry breaking in lattice QCD simulations, it also adds mixing to operators of lower dimension in various processes, *e.g.* $K \to \pi\pi$, otherwise forbidden by chiral symmetry.[80]

Note that the naive lattice fermions from (2.24) do have the exact continuum chiral symmetry at $m_f \to 0$. This is not necessarily desirable, as it means that in the continuum limit the quantum theory will *not* display a well-known property of QCD, the $U_A(1)$ chiral anomaly.[80] The *Ginsparg-Wilson* relation

$$\{D, \gamma^5\} = aD\gamma^5 D \tag{2.31}$$

implies a form of exact chiral transformation on the lattice

$$\delta\psi = i\gamma^5 \left(1 - aD/2\right)\psi \tag{2.32}$$

that leads to the chiral anomaly in the continuum limit. The explicit solution of the Ginsparg-Wilson relation is the *overlap* Dirac operator

$$D_{\mathsf{ov}} = \frac{1}{2}(a^{-1} + m_f)\left[1 + \gamma^5 \operatorname{sgn}(H)\right], \tag{2.33}$$

which involves the sign function of a Hermitian kernel, *e.g.* $H = \gamma^5 D_{\mathsf{W}}$,[81] challenging to be directly used in large-scale simulations.

2.3.2 Domain wall fermions

In this work, we use an RBC-UKQCD ensemble[74] (Sec. 4.4) with *domain wall fermions*. The main idea is that the mass of Ψ would vary along a fifth auxiliary dimension and introduce a localised defect at the 5-coordinate $s = 0$. Under these conditions, a solution of the associated $5d$ Dirac equation corresponding to a chiral fermion in $4d$ is found at such defect.

On a lattice, this fermion formulation has doublers that can be avoided with a $5d$ Wilson term. Using periodic boundary conditions introduces an anti-wall and a second $4d$ chiral fermion of opposite chirality attached to it. These modes mix, implying a residual breaking of the chiral symmetry suppressed exponentially with the size L_s of the fifth dimension.[82]

To include interactions to gauge fields, these are embedded in $5d$ so that

$$U_5(x,s) = 1 \quad \text{and} \quad U_\mu(x,s) = U_\mu(x), \quad \mu = 1,2,3,4. \tag{2.34}$$

To introduce a non-zero quark mass, one uses specific boundary terms to couple the wall and anti-wall proportionally to m_f.[83] This is encoded in the $5d$ Dirac operator

$$D_{5d}(x,s,y,r;m_f) = \delta_{s,r} D_{\mathsf{W}}(x,y;-M_5) + \delta_{x,y} D^{\perp}(s,r;m_f) \tag{2.35}$$

with

$$\begin{aligned} D^{\perp}(s,r;m_f) =& P_L \delta_{s+1,r} + P_R \delta_{s-1,r} - \delta_{sr} \\ & - m_f \left[P_L \delta_{s,L_s-1} \delta_{0,r} + P_R \delta_{s,0} \delta_{L_s-1,r} \right], \end{aligned} \tag{2.36}$$

where $P_{R/L} = (1 \pm \gamma^5)/2$. The choice of *domain wall height* in the interval $0 < M_5 < 2$ localises the two chiral modes at $s = 0, L_s - 1$, which can be projected out as

$$\begin{aligned} \psi(x) &= P_R \Psi(x,0) + P_L \Psi(x, L_s - 1), \\ \bar{\psi}(x) &= \bar{\Psi}(x, L_s - 1) P_R + \bar{\Psi}(x,0) P_L \end{aligned} \tag{2.37}$$

to yield the $4d$ fermions of mass m_f. Furthermore, $5d$ scalars known as Pauli-Villars fields are needed to cancel out the heavy-mode contributions coming from the bulk of the fifth dimension.[83] The spurious breaking of chiral symmetry exponentially suppressed with L_s can be measured in simulations by a *residual mass*.[84] For infinite L_s, the overlap Dirac operator can be written in terms of a domain wall kernel and for finite L_s it corresponds to an approximation of the sign function in (2.33). The ensemble used in this work further employs a Möbius transformation of (2.35) that exploits the extension of the fifth dimension to effectively decrease the value of L_s needed for a sufficiently small residual mass.[85,86]

This defines a controlled way of achieving a simulation with physical pion masses and chiral fermions.[74] For continuations of this work, where weak decays are included, having access to exact chiral symmetry on the lattice will be important to obtaining the continuum physics.

Overall path integral

Putting together the gauge and fermionic degrees of freedom, the discretised path integral used in this work has in principle the form

$$\mathcal{Z} = \int \mathcal{D}U \mathcal{D}\bar{\Psi} \mathcal{D}\Psi \; e^{-S_{5d}[U,\bar{\Psi},\Psi]} \; e^{-S_{\mathsf{G}}[U]}, \tag{2.38}$$

where, after a Möbius transformation, S_{5d} contains bilinear terms of the type

$$\int d^4x ds \; \bar{\Psi}(x,s) D_{5d}(x,s,y,r;m_f) \Psi(y,r). \tag{2.39}$$

The Grassmann-valued fields $\bar{\Psi}, \Psi$ can thus be explicitly rewritten using *fermionic* Gaussian integrals,[78] resulting in

$$\mathcal{Z} = \int \mathcal{D}U \left[\det D_{5d}(m_l)\right]^2 \left[\det D_{5d}(m_s)\right] e^{-S_{\mathsf{G}}[U]} \tag{2.40}$$

for a $N_f = 2 + 1$ theory.

To numerically simulate the fermionic degrees of freedom, anticommuting by nature, one lifts the determinants in (2.40) to the exponential weight using complex *bosonic* Gaussian integrals,

$$|\det D|^2 = \det(DD^\dagger) = \int \mathcal{D}\phi^\dagger \mathcal{D}\phi \; e^{-\int d^5x \; \phi^\dagger (DD^\dagger)^{-1} \phi}, \tag{2.41}$$

where $\phi^\dagger, \phi$ are called *pseudofermion* fields. The combination $DD^\dagger$ must be used to ensure the positive-definiteness of the Gaussian integral kernel. The effective fermion action is then

$$S_{\mathsf{F}}^{\mathsf{eff}}[U,\phi^\dagger,\phi] = \int d^5x \; \phi_l^\dagger (D_l D_l^\dagger)^{-1} \phi_l + \phi_s^\dagger (D_s D_s^\dagger)^{-1/2} \phi_s, \tag{2.42}$$

where $\phi^\dagger, \phi$ are tuples of $2 + 1$ bosonic fields. In the ensemble we use, a rational approximation was originally employed for computing the (inverse) fractional exponentials of the strange Dirac operator.[74]

The introduction of Pauli-Villars fields for canceling out the domain-wall bulk modes corresponds to dividing them out at the determinant level (2.40) as

$$\det D_{5d}(m_f) \to \det D_{5d}(m_f) / \det D_{pv}(1), \tag{2.43}$$

where D_{pv} is constructed from D_{5q} with appropriate choices of L_s and boundary conditions. These are then included in the effective action again through a bosonic Gaussian integral (2.41) over fields $\Phi^\dagger, \Phi$, resulting in bilinear terms involving $D_{pv}(1)D_{pv}(1)^\dagger$ in the regulated effective action $S_{\mathsf{F}}^{\text{eff}}[U, \phi^\dagger, \phi, \Phi^\dagger, \Phi]$.

In summary, the lattice path integral formally involves $2+1$ domain wall fermion $\bar{\Psi}, \Psi$ and bosonic Pauli-Villars fields $\Phi^\dagger, \Phi$

$$\mathcal{Z} = \int \mathcal{D}U\mathcal{D}\bar{\Psi}\mathcal{D}\Psi\mathcal{D}\Phi^\dagger\mathcal{D}\Phi \; e^{-S_{\mathsf{F}}[U,\bar{\Psi},\Psi,\Phi^\dagger,\Phi]} \; e^{-S_{\mathsf{G}}[U]}. \tag{2.44}$$

At the end of the day, one replaces the fermionic contribution with pseudofermion fields $\phi^\dagger, \phi$ for numerical evaluation

$$\mathcal{Z} = \int \mathcal{D}U\mathcal{D}\phi^\dagger\mathcal{D}\phi\mathcal{D}\Phi^\dagger\mathcal{D}\Phi \; e^{-S^{\text{eff}}[U,\phi^\dagger,\phi,\Phi^\dagger,\Phi]}, \tag{2.45}$$

where the overall effective action includes the gauge field contribution. In this work, we do not implement these formulas and thus refer to the ensemble generation paper for details on the Pauli-Villars fields, Möbius transformation as well as determinant pre-conditionings used in the actual simulation.[74]

2.4 Simulations

2.4.1 Monte Carlo method

Our main goal is to numerically compute the expectation values of observables from a discretised path integral, which for simplicity we write in terms of φ containing all lattice QCD degrees of freedom

$$\langle Y \rangle = \mathcal{Z}^{-1} \int \mathcal{D}\varphi \; e^{-S[\varphi]} Y[\varphi], \tag{2.46}$$

where Y can range from Wilson loops (2.14) to correlation functions of hadron interpolators that we will compute later. Counting only the gauge fields on a small 8^4 lattice, we already end up with $\mathcal{O}(10^5)$ degrees of freedom. Using a simple approximation to one-dimensional integrals leads to a sum over $\sim 10^{10^5}$ possible field configurations, which is virtually impossible to compute directly. This situation is considerably worsened when dynamical fermion effects are considered.

We circumvent the problem above by using Monte Carlo methods to estimate $\langle Y \rangle$ as the sample average

$$\langle Y \rangle \approx \frac{1}{n} \sum_{i=1}^{n} Y[\varphi^{(i)}] \equiv \bar{Y}, \tag{2.47}$$

where $Y[\varphi^{(i)}]$ is the observable *measured* on the field configuration $\varphi^{(i)}$. Such configurations are products from a stochastic process that approximates the desired distribution $\mathcal{D}\varphi\, e^{-S[\varphi]}$ after an equilibration phase. The error associated with this estimation will scale as $\sim 1/\sqrt{n}$ for large n, which for a system with a high number of degrees of freedom is a reasonable compromise.

The stochastic process commonly used in lattice field theory is a *Markov chain*, schematically represented by

$$(\varphi^{(1)}, u_1) \;\to\; (\varphi^{(2)}, u_2) \ldots \;\to \to\; (\varphi^{(n)}, u_n). \tag{2.48}$$

Here, $\varphi^{(i)}$ is viewed as a random variable drawn from the distribution u_i over the space of possible configurations. The two main ingredients of Markov chains are the initial distribution u^{init} from where the initial configuration is sampled, and the transition probability T_{ij} of going from some $\varphi^{(i)}$ to $\varphi^{(j)}$. In a Markov chain, T_{ij} can depend only on the state $\varphi^{(i)}$ and does not hold the memory of previous states [V].

Usually, we are interested in Markov chains that are

$$\textit{aperiodic:} \sum_{\{k\}} T_{ik_1} T_{k_1 k_2} \ldots T_{k_{m-1} i} > 0, \qquad \text{for all } i, m, \tag{2.49}$$

meaning that there is always the chance of hopping back to $\varphi^{(i)}$ in any number of steps, and also

$$\textit{irreducible:}\ \exists m \geq 0,\ \sum_{\{k\}} T_{ik_1} T_{k_1 k_2} \ldots T_{k_{m-1} j} > 0, \qquad \text{for all } i, j, \tag{2.50}$$

so that we can always go from any $\varphi^{(i)}$ to any $\varphi^{(j)}$ in a finite number of steps. These two features compose *strong ergodicity*, which intuitively means that all regions of the configuration space are accessible by the chain. This guarantees that a unique distribution $\tilde{u}$ is reached after a sufficient number m of transitions[87]

$$\sum_{\{k\}} T_{ik_1} T_{k_1 k_2} \ldots T_{k_{m-1} j} \sim \tilde{u}_j \tag{2.51}$$

[V] This does not mean that the generated set of states $\{\varphi\}$ are uncorrelated (Sec.2.4.3).

and that it is *stationary* under further transitions. A sufficient condition for a chain to be stationary is

$$\tilde{u}_i T_{ij} = \tilde{u}_j T_{ji}, \tag{2.52}$$

also known as *detailed balance*.

2.4.2 Algorithms

In practice, one needs appropriate algorithms to generate a Markov chain in a numerical computation. Here, we present two fundamental algorithms in lattice QCD which are relevant to this work.

Metropolis

The simplest version of the Metropolis algorithm is given by[88]

$$p_{ij} = \min\left(1, \frac{\tilde{u}_i}{\tilde{u}_j}\right) = \min\left(1, \frac{e^{-S[U_i]}}{e^{-S[U_j]}}\right) = \min\left(1, e^{-\Delta S}\right), \tag{2.53}$$

which obeys detailed balance. Then, given some proposed configuration $\varphi^{(j)}$, the step

$$\text{accept-reject:} \begin{cases} \text{if } \Delta S \leq 0, \text{ accept } \varphi^{(j)} \text{ right away} \\ \text{if } \Delta S \geq 0, \text{ accept } \varphi^{(j)} \text{ with probability } \min(1, e^{-\Delta S}) \end{cases} \tag{2.54}$$

can be used to build a chain of configurations drawn from $\mathcal{D}\varphi\, e^{-S}$ after several iterations.

It is usually optimal to apply such update link by link, where one can recycle part of the ΔS computation to perform several hits. This helps to increase the acceptance rate of the algorithm in certain cases, such as in pure gauge theory, where ΔS depends only on nearest neighbours.

Hybrid Monte Carlo

Metropolis is a working algorithm but not necessarily efficient enough for simulations with dynamical fermions. The main problem is that the Dirac operator determinants in (2.40) depend non-locally on the gauge field. The acceptance rate of a global update using a Metropolis-like step is in practice very low. The alternative idea is to introduce

a procedure that globally updates a configuration along a preferential direction more likely to be accepted.

The conventional algorithm for simulating lattice QCD with dynamical fermions is the so-called *Hybrid Monte Carlo* (HMC).[89] HMC uses a (fictitious) Hamiltonian evolution for a lattice action S

$$\mathcal{H} = \frac{1}{2}\mathcal{P}^2 + S[U] \tag{2.55}$$

to propose a joint candidate configuration $(\mathcal{P}, U)$. In this form, the conjugate momenta $\mathcal{P}$ are sampled from an algebra-valued Gaussian distribution. The action depends on algebra-valued coordinates, directly related to the gauge field U by exponentiation.

This process is a well-known microcanonical evolution used in molecular dynamics (MD) and the fictitious time introduced is referred to as *MD time*. A *MD trajectory* corresponds to a series of evolution steps resulting in a configuration $(\mathcal{P}', U')$. The gauge and pseudofermion fields effectively enter the HMC through the so-called MD forces governing the Hamiltonian evolution. In these forces, the pseudofermion fields are computed via Gaussian-distributed source fields $D^{-1}\phi = \chi$, *cf.* Eq. (2.42).

The numerical integration of the associated Hamilton equations introduces imprecision on the MD evolution, which would otherwise always generate an acceptable configuration U. An accept-reject step as in 2.54, involving the variation of $\mathcal{H}$, is thus needed to be performed on each proposed trajectory. Starting from U, the HMC steps for generating an MD trajectory are, schematically,

1. generate initial pseudofermion fields ϕ through $D^{-1}\phi = \chi$ and conjugate momenta $\mathcal{P}$ from Gaussian distributions
2. evolve the gauge fields and conjugate momenta with the Hamiltonian $\mathcal{H}$ to obtain the $(\mathcal{P}', U')$ after a sequence of MD steps (trajectory)
3. perform an accept-reject step on $\Delta\mathcal{H}$ to ensure "energy conservation" after numerical integration of the Hamilton equations
4. if accepted, one has a new Markov chain state U', if not, one repeats the procedure starting from U' in step 1

The optimal MD time step is not necessarily the smallest one possible in a given computational setup, as they have to be accounted for in step 3 anyway. In fact,

one might even use a quite coarse approximation of the action to accelerate the MD evolution steps. Finally, as the momenta are introduced quadratically, it is possible to write down a path integral in the Hamiltonian representation and show that HMC satisfies ergodicity and converges to the distribution in the lattice QCD path integral.[89]

2.4.3 Statistical errors

We are stochastically estimating vacuum expectation values $\langle Y \rangle$ through a numerical approach. In summary, we produce n configurations from the probability distribution given by the path integral and measure Y on each of them. The estimate $\bar{Y}$ is then obtained through Eq. (2.47), which will thus necessarily carry some variance.

It is unavoidable that a Markov chain algorithm produces correlated configurations, which affects their variance. The autocorrelation function[17]

$$\Gamma_Y(j) = \langle Y_i Y_{i+j} \rangle - \langle Y_i \rangle \langle Y_{i+j} \rangle \tag{2.56}$$

can be estimated from the data[90] and gives the correlation between measurements of Y at different Monte Carlo times j. The integrated autocorrelation time

$$\tau_Y = 1/2 + \sum_{i=1}^{\infty} \Gamma(i)/\Gamma(0) \tag{2.57}$$

is the characteristic relaxation time for an observable Y to become uncorrelated. A related quantity is the exponential autocorrelation function τ_{exp}, which represents the relaxation time of the slowest mode of the Markov chain and controls the convergence to equilibrium.

In a simulation, one would like to estimate the autocorrelation time of typical observables, as well as the rate of convergence to the equilibrium distribution of the implemented algorithm. In the ensemble we use, the integrated autocorrelation time for several quantities was estimated and the value of the slowest observable was used as a reference relaxation time.[74] Based on that, the first 420 MD trajectories are discarded to avoid bias otherwise introduced in the equilibration phase. Furthermore, all the measurements are taken every 20 MD trajectories, resulting in a total of 90 effectively independent configurations.

On top of the intrinsic quantum theory variance $\sigma_0^2 = \Gamma(0)$, the stochastic estimator

$\bar{Y}$ will fluctuate around $\langle Y \rangle$ for each time the simulation is repeated, introducing a *statistical variance* σ^2. The relation between them at large enough n is

$$\sigma = \frac{\sigma_0}{\sqrt{n}} \tag{2.58}$$

if the configurations are uncorrelated, which is approximately our case as we skip 20 MD trajectories between measurements [VI]. In practice, we cannot repeat the simulation multiple times, so we rely on bootstrap resampling for estimating the statistical error, *cf.* A.1.

2.5 Angular Momentum

Rotational symmetry plays an important role in particle physics as it is a fundamental property that can be experimentally probed. The *irreducible representations* of the $SO(3)$ group, or $SU(2)$ for general spin, identify states of the Hamiltonian with the associated angular momentum quantum numbers.

The introduction of both finite *and* discrete space breaks the rotational symmetry of QCD, restricting the spatial rotations that maintain the system invariant.[91] In spectroscopy, the most relevant breaking of rotational symmetry is at large distances, which is governed by the *finite box size* and constrains the allowed momenta carried by hadronic states [VII]. Because such finite-volume states and their corresponding creation operators do not transform irreducibly under the infinite-volume rotation symmetries, we now review the group-theory framework necessary for treating them in our simulation.

Octahedral group

The finite subgroup of $SO(3)$ containing all possible rotations on a $3d$ cubic lattice is known as the *octahedral group* $\mathcal{O}$ and is one of the so-called *point groups* [VIII]. It contains 24 elements corresponding to the symmetries of a $3d$ cube, divided into the

[VI] If we would consider all MD trajectories generated on the HMC run, the statistical error would have to be corrected by a factor of $\sqrt{2\tau_Y}$.

[VII] The rotational symmetry breaking due to the non-zero lattice spacing will be relevant when taking the continuum limit of a lattice simulation.

[VIII] When dealing with half-integer states, one would have to use the double cover $SU(2)$ and its finite subgroup $\mathcal{O}^D$. However, as we are dealing only with meson states, we will only discuss the group $\mathcal{O}$ for simplicity.

5 conjugacy classes depicted in Figure (2.2). The classes represent different kinds of symmetry operations related to each other by a similarity transformation.

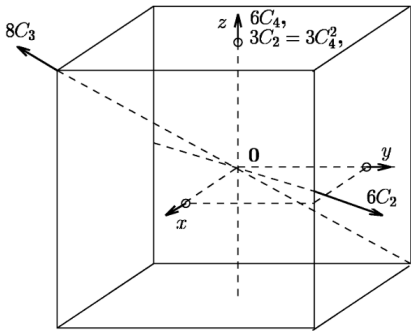

Figure 2.2 *Symmetry operations on a cube, representing the octahedral group* $\mathcal{O}$.*.*[92]

Here, we will be interested in building specific representations that irreducibly define QCD operators and states on a cubic lattice. Representations are maps taking the group elements onto a vector space while preserving the group product rule and the correspondence between e and the identity. Representations that generate an invariant subspace by acting on a vector within that same subspace are called *irreducible* (irrep). Irreducible representations of the cubic group are important in lattice QCD spectroscopy because they are one of the quantum numbers of the states we are studying.

Class	**Symmetries**
e	identity
$3C_2$	3 rotations of π around x, y, z
$6C_4$	6 rotations of $\pi/2$ around x, y, z
$8C_3$	8 rotations of $2\pi/3$ around four body diagonals
$6C_2$	6 rotations of π around six face diagonals

Table 2.1 *Conjugacy classes of* $\mathcal{O}$.

An important concept in representation theory is the *character*, defined as the trace along the rows of an irrep matrix [IX]

$$\chi^{\alpha}(R) = \operatorname{tr} \Gamma^{\alpha}(R), \qquad R \in \mathcal{O}, \tag{2.59}$$

for each of the $n_{\mathcal{O}}$ elements and representation Γ^{α}. Probably the most useful identity

[IX] We will denote an irrep and its representation matrix with the same symbol, *e.g.* Γ^{γ}.

of finite representation theory,

$$\frac{1}{n_{\mathcal{O}}}\sum_{R\in\mathcal{O}}\chi^{\alpha}(R)\chi^{\beta}(R)^{*}=\delta_{\alpha\beta}, \tag{2.60}$$

states the orthogonality between irreps through their characters. Due to the cylic property of the trace, the character is the same for all elements within a class. A generalisation of (2.60) is the orthogonality relation between different rows of an irrep

$$\frac{1}{n_{\mathcal{O}}}\sum_{R\in\mathcal{O}}\Gamma^{\alpha}_{ij}(R)\Gamma^{\beta}_{kl}(R)^{*}=\frac{1}{\dim\Gamma^{\alpha}}\delta_{\alpha\beta}\delta_{ik}\delta_{jl}, \tag{2.61}$$

which reduces to (2.60) by summing over the diagonal elements of the Γ's.

For finite groups, one can always reduce any given representation Γ into a direct sum of a finite number of irreps $\Gamma_1, \Gamma_2, \ldots$ in a unique way. The invariant subspaces generated by the irreps are consequently orthogonal to each other. This reduction can be represented through the block-diagonal form

$$\Gamma=\begin{pmatrix}\Gamma_1 & 0 & 0\\ 0 & \Gamma_2 & 0\\ 0 & 0 & \ddots\end{pmatrix}=\Gamma_1\oplus\Gamma_2\oplus\ldots, \tag{2.62}$$

which can be written in terms of characters as

$$\chi^{\Gamma}(R)=\sum_{\alpha}N^{\alpha}_{\Gamma}\chi^{\alpha}(R), \tag{2.63}$$

where N^{α}_{Γ} is the number of copies of the irrep Γ^{α} in the reduction of Γ.

When the $SO(3)$ rotation group is restricted to the lattice, the irreps Γ^{l} of $SO(3)$ become reducible in $\mathcal{O}$ and so can be reduced as shown above. For pseudoscalar mesons, the spin is zero and l equals the total angular momentum. If one knows the characters of the $SO(3)$ irreps, the orthogonality relation (2.60) can be used to write[93]

$$N^{\alpha}_{\Gamma}=\frac{1}{n_{\mathcal{O}}}\sum_{R\in\mathcal{O}}\chi^{\beta}(R)^{*}\chi^{l}(R) \tag{2.64}$$

where $\chi^{l}(R)$ are the characters of the continuum irrep evaluated at the lattice group elements. For example, in S-wave the character is always $\chi^{l=0}=1$ and (2.64) leads to

$$\Gamma^{l=0}=A_1, \tag{2.65}$$

where A_1 is the trivial irrep of $\mathcal{O}$ (Table 2.2).

Note that until now, we only referred to pure $SO(3)$ rotations embedded into the cubic symmetries. Including parity transformations from the improper $O(3)$ group corresponds to multiplying the cubic group by the spatial inversions

$$\mathcal{O}_h = \mathcal{O} \otimes \{e, -e\}, \tag{2.66}$$

which is trivially realised as they commute with all elements of $\mathcal{O}$. This doubles the number of elements to 48 and each irrep will gain a parity descriptor, either g, for positive, or u, for negative, parity. This will correspond to states that at rest have definite parity transformations.

States of non-zero total momentum are conceptually more difficult to treat, as one needs to consider a larger subgroup of the Poincarè group. The main difficulty comes from the fact that translations do not commute with rotations.[94] At the end of the day, it is enough to consider certain subgroups of $\mathcal{O}_h$ corresponding to the restricted symmetry operations of a box contracted along the direction of a boost to the CM frame. Such subgroups will contain the elements of $\mathcal{O}_h$ that keep the total momentum $\mathbf{d} = \mathbf{P}L/(2\pi)$ unchanged, *i.e.* [X]

$$\{R \mid R\mathbf{d} = \mathbf{d}, \quad R \in \mathcal{O}_h\}, \tag{2.67}$$

which we conventionally call the *little group* of the momentum $\mathbf{d}$. The little groups can be labeled by a representative $\mathbf{d}_{\text{ref}}$ obeying (2.67). Furthermore, we often refer to the "star" of a given momentum $\mathbf{d}$, given by[94,95]

$$\{\mathbf{d}\}^* = \{\mathbf{d}' \mid R\mathbf{d}' = \mathbf{d}, \quad R \in \mathcal{O}_h\}, \tag{2.68}$$

which comprises all momenta related to $\mathbf{d}$ by $\mathcal{O}_h$ rotations. The "star" of a little group momentum $\{\mathbf{d}_{\text{ref}}\}^*$ is useful to identify subgroups equivalent to $\mathbf{d}_{\text{ref}}$ in the infinite-volume limit, *cf.* Sec. 2.5. We summarise the irreps for each of the subgroups of $\mathcal{O}$ used in this work in Table 2.2. Their embedding, or *subduction*, into the first few continuum partial-wave irreps is shown in Table 2.3. We focus on P-wave scattering ($l = 1$) as this will lead to our practical application later.

[X] In general, we will reserve the letter $\mathbf{d}$ to refer to momenta in units of $2\pi/L$.

Group	Order	$\mathbf{d}_{\text{ref}}$	Irrep(dim)	Crystal
$\mathcal{O}$	24	[000]	$A_{1,2}(1), E(2), T_{1,2}(3)$	cubic
C_{4v}	8	[001], [002]	$A_{1,2}(1), B_{1,2}(1), E(2)$	tetragonal
C_{2v}	4	[110]	$A_{1,2}(1), B_{1,2}(1)$	orthorhombic
C_{3v}	6	[111]	$A_{1,2}(1), E(1)$	trigonal

Table 2.2 *Subgroups relevant in this work, together with all their irreps. Including parity further labels the irreps into g (gerade) and u (ungerade) in the case the system is invariant under spatial inversions.*

l	$\mathcal{O}$	C_{4v}	C_{2v}	C_{3v}
0	A_1	A_1	A_1	A_1
1	T_1	$A_1 \oplus E$	$A_1 \oplus B_1 \oplus B_2$	$A_1 \oplus E$
2	$T_2 \oplus E$	$A_1 \oplus B_1 \oplus B_2 \oplus E$	$2A_1 \oplus A_2 \oplus B_1 \oplus B_2$	$A_1 \oplus 2E$

Table 2.3 *Subductions of irreps into each angular momenta up to $l = 2$. For states with non-zero momentum, l corresponds to the angular momentum of the system boosted back to the CM frame.*

Operator projection

As indicated in Sec. 2.1, we discretised and compacted a theory with continuum rotational symmetry. In particular, due to the way fermions are discretised, we naturally carry over operators with a bilinear form, for example

$$O(\mathbf{p}, t) = \int d^3x \, e^{-i\mathbf{x}\cdot\mathbf{p}} \bar{\psi}(\mathbf{x}, t)\gamma^5\psi(\mathbf{x}, t) \tag{2.69}$$

on the pseudoscalar channel. In the language of the previous section, the space spanned by the operators of type (2.69) is reducible with respect to the lattice symmetry groups and will thus contain mixed contributions from lattice Hamiltonian states.

To construct operators overlapping optimally with lattice states we need to find combinations of continuum-like operators O that form a basis for the various irreducible spaces corresponding to a certain irrep and momenta assignments. One way of projecting a given continuum-like operator into the row r of an irrep Λ is to

perform a group average in the form[96]

$$\mathcal{P}^{\Lambda r} = \frac{\dim \Lambda}{n_G} \sum_{R \in G} \Gamma^{\Lambda}_{rr}(R)^* \, \Gamma(R), \tag{2.70}$$

where $\Gamma(R)$ is the unitary operator corresponding to the group element R transforming O. By applying the orthogonality relation (2.61) one can show that it obeys the usual projector property $P^2 = P$. Furthermore, the operator components orthogonal to the row r of the irrep Λ vanish while the parallel component is left intact. Due to the way the rotations act on the momenta, applying (2.70) to an operator with an arbitrary number of momentum projections, $O(\mathbf{p}_1, \mathbf{p}_2, ...)$, leads to

$$O^{\Lambda r}(\mathbf{p}_1, \mathbf{p}_2, ..., t) \equiv \frac{\dim \Lambda}{n_G} \sum_{R \in G} \Gamma^{\Lambda}_{rr}(R)^* \, \hat{R} O(\mathbf{p}_1, \mathbf{p}_2, ..., t) \hat{R}^\dagger \tag{2.71}$$

where $\hat{R}$ is the unitary transformation associated to $R \in G$ in the Hilbert space of O.

Note that for multidimensional irreps, operators obtained by substituting different values of r in (2.70) are not guaranteed to form a basis for the irrep Λ.[96] This happens because the continuum-like O is not guaranteed to have non-zero components on all of the irreps of a certain symmetry group. One can build, given an initial $O^{\Lambda r_0}$, a basis for Λ by applying a "transfer" operator[97]

$$O^{\Lambda r}(\mathbf{p}_1, \mathbf{p}_2, ..., t) = \frac{\dim \Lambda}{n_G} \sum_{i=1}^{n_G} \Gamma^{\Lambda}_{rr_0}(R) \, \hat{R} O^{\Lambda r_0}(\mathbf{p}_1, \mathbf{p}_2, ..., t) \hat{R}^\dagger, \tag{2.72}$$

for fixed r_0. The transfer operator is not a projector, but it contains a projection followed by a transformation of the operator to another irrep row.[96] Each row-projected operator will be a linearly independent basis vector of the invariant space generated by the irrep. Nevertheless, the lattice QCD Lagrangian is symmetrical under swapping of irrep rows, such that operators projected along different rows are equivalent under the gauge-average and we can combine them to improve the statistical signal of our correlators (Sec. 4.4.2).

We can also generate copies of operators with non-zero total momenta $\mathbf{d}$ via projections onto irreps of the momenta contained in its "star" $\{\mathbf{d}\}^*$, *cf.* Eq. (2.68). Operators defined like that will be equivalent in the infinite-volume limit. To implement that, one chooses a reference $\mathbf{d}_{\text{ref}}$ and rotations $R_{\text{ref}} \in \mathcal{O}_h$ which transform the elements of $\{\mathbf{d}_{\text{ref}}\}^*$ back to $\mathbf{d}_{\text{ref}}$. Then, we perform a "group rotation" by replacing

$$R \to R_{\text{ref}}\, R\, R_{\text{ref}}^{-1} \tag{2.73}$$

and applying the projection formula (2.70) for each $\mathbf{d}$. Because the system does not prefer any specific boost direction, it will be useful to average equivalent momenta to improve statistics. For example, the "star" of $\mathbf{d} = [001]$ will be

$$\{[001]\}^* = \{[001], [010], [100], [00-1], [0-10], [-100]\}, \tag{2.74}$$

and thus corresponds to an overall factor of 6 in the number of operators projected into the irreps of the little group C_{4v}. The correlators computed from each $\mathbf{d}$ can then be averaged before further analysis is performed to improve statistics.

In the case of operators with multiple bilinear components, there will be extra arbitrariness on how to choose their initial momentum assignments. For example, in operators with two bilinears, this will happen because the product representation of both projected bilinears will reduce to potentially multiple copies of the target irrep Λ, *i.e.*

$$\Lambda_1 \otimes \Lambda_2 \xrightarrow{\mathcal{P}} \Lambda^{N(\Lambda_1 \otimes \Lambda_2, \Lambda)}, \tag{2.75}$$

where $N(\Lambda_1 \otimes \Lambda_2, \Lambda)$ are the number of copies of Λ in the reduction of $\Lambda_1 \otimes \Lambda_2$. Finding this explicit reduction and its basis-changing (generalised Clebsch-Gordan) coefficients is necessary to systematically build multi-particle interpolators from single-particle ones.[91,98,99] In this work, all we need can be obtained from Eq. (2.70) because the single-bilinear operators we use to compose two-bilinear operators will *uniquely* map into the A_{1u} and A_2 irreps for the rest and moving frames, respectively.

3 Finite Volume Methods

Lattice QCD simulations are done on finite volumes, modifying extracted observables away from the infinite-volume behaviour. In general, one is interested in the latter as they correspond directly to the physics we are studying. From that perspective, finite-volume effects are estimated as a systematic error and can also be used to control infinite-volume extrapolations.[22] However, this is not the only way lattice field theory can make use of volume corrections, as one can infer *scattering* information from them. We will use such a connection to compute resonance parameters from lattice QCD data.

The extraction of scattering parameters from lattice simulations is not straightforward though. Because of the Euclidean signature, mapping lattice correlators back to Minkowski spacetime, where LSZ can be used, is a tough task. The analytical continuation of a finite set of noisy data points is an ill-posed numerical problem,[100,101] even though it is in principle guaranteed on a suitably defined lattice theory, *e.g.* with reflection-positivity.[68] Taking a different approach, Maiani and Testa have shown that only scattering parameters *at* the production threshold can be computed from the large imaginary time behaviour of Euclidean correlators, which is also quite limiting.[25]

At this point, restricting an Euclidean theory to a finite spatial box does not seem to be particularly helpful, instead bringing us even further from the physics. For example, a three-dimensional spatial box of size L with a field obeying periodic boundary conditions

$$\varphi(t, \mathbf{x}) = \varphi(t, \mathbf{x} + \hat{\mathbf{x}}_i L), \quad i = 1, 2, 3, \tag{3.1}$$

restricts the allowed momenta to

$$\mathbf{p} = \frac{2\pi}{L}\mathbf{n}, \quad \mathbf{n} \in \mathbb{Z}_3, \tag{3.2}$$

and thus also the energies. Other typical features of Euclidean correlators on the complex plane are also affected, *e.g.* threshold branch cuts which in Euclidean finite

volume emerge as poles on the imaginary time axis, as depicted in Fig. 3.1. However, the details of these structures vary as one changes L, and it turns out that one can analytically relate such dependency to infinite-volume scattering observables.

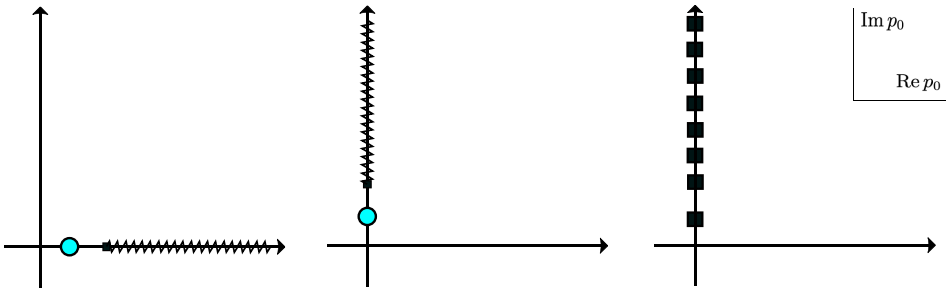

Figure 3.1 *Scheme of amplitude's complex energy plane: Left: infinite-volume ($i\varepsilon$ prescription implicit). Middle: after Euclidean rotation. Right: after compactification in space.*

In the context of quantum mechanics scattering, the modifications introduced on the spectrum of a theory due to a finite spatial volume were studied at least since the 1950's.[102,103] After a series of works estimating the size of finite-volume effects,[104,105] their relation to the two-particle scattering amplitude was systematically established with the so-called *Lüscher formalism*.[106,107] The advancement of lattice field theory simulations created the prospect of studying scattering phase shifts and resonance parameters through lattice data, which is a challenging problem in low-energy QCD.[30]

3.1 Exponentially Suppressed Effects

We first overview the finite-volume effects on a single particle represented by a scalar field φ with bare mass m_0. We use a standard Lagrangian with a kinetical term and a potential V encoding arbitrary self-interactions. In the spirit of effective field theories, one can view such field as the lightest particle of QCD, the pion, which will contribute to the leading finite volume corrections.

3.1.1 Mass shift

Leading order φ^4

As an illustration, we can compute the mass shift for the $V = \lambda_4\varphi^4/4!$ interaction at leading order in perturbation theory. In a finite box, the integrals over spatial momentum turn into sums, *e.g.* as in the momentum representation of the 2-point Green function

$$\langle 0|\, T\hat{\varphi}(x)\hat{\varphi}(0)\,|0\rangle_L = \frac{1}{L^3}\sum_{\mathbf{k}}\int\frac{dk^0}{2\pi}G_L(p)e^{ip\cdot x}, \tag{3.3}$$

which is also reflected in the Feynman rules by the replacement

$$\int d^4k \to \sum_{\mathbf{k}}\int dk^0 \equiv \sum\!\!\!\!\!\!\int_k . \tag{3.4}$$

We assume an infinite time extension and work directly in Minkowski space, as spectral observables will be agnostic to the signature. Whenever we do not specify the sum $\mathbf{k}$, it will take place over the $\frac{2\pi}{L}\mathbb{Z}_3$. We omit the $i\varepsilon$ unless it is explicitly needed.

From the spectral representation of the 2-point Green function, we have

$$G(p) \sim \frac{-i|Z|^2}{p^2 - m^2} \tag{3.5}$$

up to analytic pieces at the pole that we will be able to discard later, *cf.* Eq. (3.12) below. At order $\mathcal{O}(\lambda_4)$, there are corrections δm^2 to the squared mass but not to the field-strength renormalisation (overlap Z)[53]

$$|Z|^2 = 1, \qquad m^2 = m_0^2 + \delta m^2, \tag{3.6}$$

where m is the physical (renormalised) mass. The term in (3.5) can then be expanded

$$G(p) \sim -i(p^2 - m_0^2)^{-1} + (-i)^2(p^2 - m_0^2)^{-2}(-i\delta m^2), \tag{3.7}$$

and comparing to the infinite-volume Feynman series at same order leads to

$$\delta m^2 = i \quad \text{ 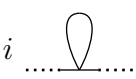 } \quad = \frac{-i\lambda_4}{2}\int\frac{d^3k}{(2\pi)^3}\frac{dk^0}{2\pi}\frac{1}{(k^0)^2 - \omega_{\mathbf{k}}^2 + i\varepsilon} = \frac{\lambda_4}{2}\int\frac{d^3k}{(2\pi)^3}\frac{1}{2\omega_{\mathbf{k}}}, \tag{3.8}$$

where we performed the contour integral in p_0. Repeating this calculation in a finite volume, the physical mass m_L will differ from the bare mass at order $\mathcal{O}(\lambda_4)$ by an analogous quantity

$$\delta m_L^2 = \frac{\lambda_4}{2}\frac{1}{L^3}\sum_{\mathbf{k}}\frac{1}{2\omega_{\mathbf{k}}}, \tag{3.9}$$

where we picked the rest-frame ($\mathbf{p} = 0$) for simplicity.

The finite-volume correction to the physical mass at order $\mathcal{O}(\lambda_4)$ is then

$$\Delta m^2 = \delta m_L^2 - \delta m^2 = \frac{\lambda_4}{2}\left[\frac{1}{L^3}\sum_{\mathbf{k}} - \int\frac{d^3k}{(2\pi)^3}\right]\frac{1}{2\omega_{\mathbf{k}}}. \tag{3.10}$$

We introduce now the so-called Poisson summation formula in three dimensions

$$\sum_{\mathbf{n}\in\mathbb{Z}_3} e^{2\pi i\mathbf{z}\cdot\mathbf{n}} = \sum_{\mathbf{n}\in\mathbb{Z}_3}\delta^{(3)}(\mathbf{z}+\mathbf{n}), \tag{3.11}$$

where formally $\delta^{(3)}(\mathbf{x}) = \prod_{i=1}^3\delta(x_i)$. Setting $\mathbf{z} = \frac{2\pi}{L}\mathbf{k}$ and integrating both sides over $\mathbf{k}$ with a test function $f(\mathbf{k})$ leads to an useful form of the integral-sum difference

$$\left[\frac{1}{L^3}\sum_{\mathbf{k}} - \int\frac{d^3k}{(2\pi)^3}\right]f(\mathbf{k}) = \sum_{\mathbf{n}\neq 0}\int\frac{d^3k}{(2\pi)^3}f(\mathbf{k})e^{iL\mathbf{n}\cdot\mathbf{k}}, \tag{3.12}$$

where the zero mode is conveniently isolated. Using this in (3.10), we observe that, for each Poisson mode $|\mathbf{n}|$, the resulting integral behaves as a scalar field propagating over a spacelike interval of length $|\mathbf{n}|L$, and thus[56]

$$\Delta m^2 = \frac{\lambda_4}{2}\sum_{\mathbf{n}\neq 0}\int\frac{d^3k}{(2\pi)^3}\frac{e^{iL\mathbf{n}\cdot\mathbf{k}}}{2\sqrt{\mathbf{k}^2+m^2}} \sim \lambda_4 e^{-mL} \tag{3.13}$$

decays exponentially for large L. This exemplifies how the finite volume effects on the polarisation cloud are exponentially suppressed via virtual particles wrapping around the box.

Arbitrary interactions at all orders

The result above was generalised by Lüscher in its seminal paper,[106] where it was found that the mass shift at all orders for an anbitrary V can be summarised by 3 diagrams up to $\mathcal{O}(e^{-\sqrt{3/2}mL})$ corrections. Instead of normalizing with Z as in (3.5), we equivalently write the propagator with contributions from all orders resummed

into the self-energy Σ

$$G(p) = \frac{-i}{p^2 - m_0^2 - \Sigma(p)}, \tag{3.14}$$

with $\Sigma(p)$ chosen so that $\Sigma(p) = \partial\Sigma(p)/\partial p^0 = 0$ at the physical mass $p^2 = m^2$. In finite volume, the full propagator is written in an analogous way and the pole condition at vanishing spatial momentum

$$G_L(m_L, \mathbf{p} = 0)^{-1} = 0 \tag{3.15}$$

defines the finite-volume physical mass. For large L, $\Sigma_L(p) \to \Sigma(p)$ and $\Delta m \equiv m_L - m$ is small.

The crucial point is to compute the leading behaviour of Σ at large L, which involves writing it as an all-order perturbative series over 1PI diagrams

$$\Sigma_L(m, 0) = \sum_{\text{1PI}} \mathcal{J}_L^{\text{1PI}}. \tag{3.16}$$

Each free propagator in a diagram can be written in terms of its infinite-volume counterpart as a sum over all Poisson modes

$$\Delta_L(x) = \sum_{\boldsymbol{n} \in \mathbb{Z}^3} \Delta(x + \mathbf{n}L). \tag{3.17}$$

The contribution of a certain diagram will be classified according to the way its propagators Δ wrap around the box. For that, when substituting (3.17) into (3.16) one can identify equivalency classes $[\mathbf{n}]$ in the space of all possible wrapping topologies of a diagram. The diagrams contained in the same $[\mathbf{n}]$ will contribute equally to the sum so that it can be split into a sum over the equivalency classes

$$\Sigma_L(m, 0) = \sum_{\text{1PI}} \sum_{[\mathbf{n}]} \mathcal{J}_L^{\text{1PI},[\mathbf{n}]}, \tag{3.18}$$

in a similar fashion to the Faddeev-Popov gauge-fixing procedure but for abstract gauge fields $\mathbf{n}$.

After considerable effort, it can be shown that all diagrams with a non-trivial wrapping (not equivalent to $\mathbf{n} = 0$ in all propagators) have exponentially suppressed volume effects of order $\mathcal{O}(e^{-mL\sqrt{3}/2})$ in the large-L limit. Furthermore, it is shown that the leading behaviour comes from the equivalency class of diagrams containing *only one loop propagator* wrapping the box with $\mathbf{n} = \hat{\mathbf{x}}, \hat{\mathbf{y}}, \hat{\mathbf{z}}$, also called *simple* class. In view of (3.17) and (3.4), such propagator will be the only one with a momentum

integral replaced by a sum, and the corresponding diagrams are

$$\Sigma_L(\hat{p}) =$$ 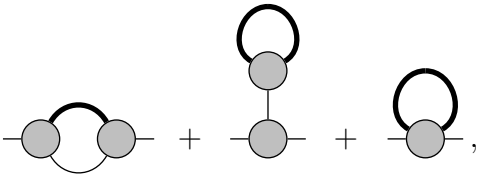 (3.19)

where the shaded blobs are 1PI diagrams and the lines are full finite- (thick) and infinite- volume (thin) propagators. Solving the associated integrals and expanding $\Sigma_L(m_L, 0)$ in (3.15) around m in powers of Δm will lead to[106]

$$\begin{aligned}\Delta m &= -\frac{1}{2m}\Sigma_L(m,0) \\ &= -\frac{3}{16\pi m^2 L}\left[\lambda_3^2 e^{-mL\sqrt{3}/2} + \frac{m}{\pi}\int dy e^{-\sqrt{m^2+y^2}L} F(iy)\right]\end{aligned} \tag{3.20}$$

up to $\mathcal{O}(e^{-mL\sqrt{3/2}})$ corrections from non-simple diagrams. Here, the first term contains the 3-point interaction coupling constant λ_3 coming from the first and second diagrams in (3.19). On the other hand, the third diagram gives rise to a dependence on $F(\nu)$, which is the 2-to-2 forward scattering amplitude $T(\mathbf{p}, \mathbf{q}; \mathbf{p}, \mathbf{q})$ written in terms of the crossing variable $\nu = (\omega_{\mathbf{p}}\omega_{\mathbf{q}} - \mathbf{p}\cdot\mathbf{q})/m$.

In an effective description of low-energy QCD, *e.g.* chiral perturbation theory, the first and second diagrams in (3.19) are forbidden due to exact G-parity, the generalisation of charge conjugation to isospin multiplets. This means that in the effective description of $\pi\pi$ scattering, diagrams such as $\pi\pi \to \pi\pi\pi$ will vanish and thus $\lambda_3 = 0$ [I]. Therefore, the exponentially suppressed effects only depend the scattering amplitude, which on the threshold limit $\mathbf{p}, \mathbf{q} \to 0$ ($\nu \to m$) corresponds to the 4-point interaction coupling constant λ_4. We see that the result estimated in Sec. 3.1.1 through the tadpole diagram is contained in the third diagram of (3.19), as expected. This is the first hint at how the finite-volume spectrum indirectly relates to the scattering amplitude.

[I] In the Standard Model, electromagnetic effects and isospin breaking render these contributions non-zero but still highly suppressed.[6] On the other hand, the consideration of exact $SU(3)_f$ symmetry extends G-parity constraints to kaons as well, which hints at the suppression of the analogous $K\pi \to K\pi\pi$ contributions achieved by the addition of an anomalous term to the chiral Lagrangian, *cf.* Sec.5.4.3.

3.1.2 Bethe-Salpeter kernel

When we directly study the elastic 2-to-2 scattering amplitude in the next section, we will expand a correlation function and the scattering amplitude in terms of the Bethe-Salpeter kernel

$$iK(k_1,k_2) = \quad = \quad + \quad + \quad + \ \ldots, \tag{3.21}$$

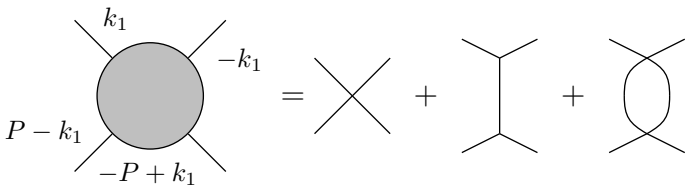

defined as the sum over all amputated 4-point 2PI s-channel diagrams. Thus, all 4-point diagrams which *cannot* be reduced by a *vertical cut* of 2 lines are included in K. [II]

It is possible to show that the Bethe-Salpeter kernel is analytic in the low-energy regime.[107] This can be schematically seen by contour-integrating the temporal part of any of the diagrams in (3.21) in the centre-of-momentum (CM) frame, which will lead to a form

$$\int d^3k_1 \int d^3k_2 \ldots \int d^3k_n \frac{h(k_1,k_2,\ldots,k_n)}{E-\omega_{\mathbf{k}_1}-\omega_{\mathbf{k}_2}\ldots-\omega_{\mathbf{P}-\mathbf{k}_1-\mathbf{k}_2\ldots-\mathbf{k}_n}} \tag{3.22}$$

that will not hit a pole unless $E > nm$, for the scattering of n identical particles of mass m. For the elastic scattering of two pions, it is sufficient to consider $E < 4m$, so that none of the diagrams contained in (3.21) will feature a pole in the loop integrals. That can easily be extended to $K\pi$ scattering, so that the condition turns into $E < 2m_\pi + m_K$. Later in this work, we employ an elastic approximation of $\pi\pi$ and $K\pi$ scattering where the expansion (3.21) is used at energies above $4m_\pi$ and $2m_\pi + m_K$, respectively. We thus neglect the effects of $\pi\pi \to \pi\pi\pi\pi$ and $K\pi \to K\pi\pi$-type diagrams, which we safely expect to be small, *cf.* Sec.5.4.3.

In Sec. 3.1.1, we exemplified how the sum-integral difference was exponentially volume-suppressed in the presence of the analytic integrand coming from the tadpole diagram. It turns out that this will happen in general when there are no poles which will not be canceled out by the infinite-volume loop. This corresponds to the condition that the loop propagators in (3.22) cannot go *on-shell* simultaneously.

[II] The verticality of the cut corresponds to the restriction of the Lüscher formalism to only s-channel contributions to the partial-wave scattering amplitudes, which is enough for us. Extensions of the formalism including u,t-channels recently appeared in the literature.[108,109]

The finite-volume Bethe-Salpeter kernel K_L will then be equal to its infinite-volume version K[107]

$$K_L(k_1, k_2) = K(k_1, k_2), \tag{3.23}$$

up to exponentially suppressed volume corrections. This will be important in the next section, as we will ignore all corrections decaying faster than powers of L.

3.2 Two-particle Formalism

We now consider the scattering of two particles with different masses in an arbitrary moving frame. As we already mentioned, even at large times, the most one can obtain from Euclidean correlators is scattering information at the production threshold.[25] This is worsened by the fact that in a finite box, the particles and their polarisation clouds cannot be placed arbitrarily far from each other so as to create asymptotic states.

We will instead rely on the indirect relation between the *finite-volume spectrum* and the infinite-volume *scattering amplitude*, closely following the approach of Kim, Sachrajda and Sharpe[110] for a relativistic field theory of scalar particles in a general moving frame. The main product is the so-called *quantisation condition*, which relates *power-like* finite-volume corrections on the spectrum to the elastic two-particle scattering amplitude. Such relation was originally developed in an effective Schrödinger equation approach for the scattering of identical particles in the rest frame,[107,111] later extended to general moving frames[112] and non-identical particles.[113,114]

3.2.1 Power-like effects

Skeleton expansion

We start by considering a finite-volume correlator projected into momentum space

$$C_L(P) = \int dx^0 \int_L d^3\mathbf{x}\, e^{-iP\cdot x} \langle 0 \,|\, \sigma(x)\bar{\sigma}(0) \,|\, 0\rangle = \langle 0 \,|\, \sigma(E, \mathbf{P})\bar{\sigma}(E, -\mathbf{P}) \,|\, 0\rangle \,, \tag{3.24}$$

where $\sigma, \bar{\sigma}$ are operators interpolating two-particle states we are interested in. The total (Minkowski) 4-momentum $P = (E, \mathbf{P})$ has its components expressed through

$$E = \sqrt{m_1^2 + \mathbf{p}_1^2} + \sqrt{m_2^2 + \mathbf{p}_2^2}, \qquad \mathbf{p}_1 + \mathbf{p}_2 = \mathbf{P}. \tag{3.25}$$

The effects observed in Sec. 3.1.2 related to the squeezing of the vacuum polarisation clouds of self-interactive particles can be safely ignored for large enough $m_\pi L$. The value $m_\pi L \approx 4$ is usually taken as a safe choice in the context of lattice simulations.[10,115] Up to exponentially volume-suppressed corrections, we can thus use the Bethe-Salpeter kernel (3.21) to write down the correlator as the skeleton expansion[110]

$$C_L(P) = \quad + \quad + \ \ldots \tag{3.26}$$

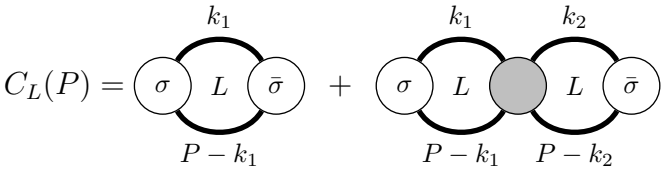

in the elastic regime $0 < E^* < 2m_1 + m_2$, where E^* is the CM energy, and assuming $m_1 < m_2$ when 3-particles interactions are allowed on the underlying theory (QCD). Rearranging the integration symbols, the N-th term of (3.26) has the form

$$\begin{aligned} &\sum\!\!\!\!\!\!\int_{k_1} \sigma(k_1) G_2(k_1) \sum\!\!\!\!\!\!\int_{k_2} iK(k_1, k_2) G_2(k_2) \\ &\quad \ldots \sum\!\!\!\!\!\!\int_{k_j} iK(k_{j-1}, k_j) G_2(k_j) \sum\!\!\!\!\!\!\int_{k_{j+1}} iK(k_j, k_{j+1}) G_2(k_{j+1}) \\ &\quad \ldots \sum\!\!\!\!\!\!\int_{k_N} iK(k_{N-1}, k_N) G_2(k_N) \bar{\sigma}(k_N), \qquad N > 1, \end{aligned} \tag{3.27}$$

where we defined the "two-particle full propagator" $G_2(k) = G_L(k; m_1) G_L(P - k; m_2)$ for convenience, represented by the thick lines, *cf.* Ref [116, Eqs. (7)]. The smooth functions $\sigma, \bar{\sigma}$ are matrix elements of the corresponding interpolators involving in/out states, but their explicit form is not important here.

As we have seen in Sec. 3.1.1, the finite-volume self-energy differs from the infinite-volume version by exponentially suppressed corrections, such that we use the corresponding full propagators equivalently here. For all N, we can identify the finite-

volume loop function

$$\mathcal{L}_L \equiv \sum\!\!\!\!\!\!\int_k l(k;v)G_2(k)r(k;u) = \frac{1}{L^3}\sum\!\!\!\!\!\!\int_k h(k)G_2(k), \tag{3.28}$$

where $h(k) \equiv l(k;v)r(k;u)$ and the functions l, r are defined in terms of iK, σ or $\bar{\sigma}$ coming from the left or right of G_2 in (3.27), with fixed momenta v, u and total momentum $P = (E, \mathbf{P})$.

The crucial difference between the skeleton expansion above and the corresponding one in infinite volume is that the loops (3.28) introduce power-like finite-volume corrections when the propagators in G_2 go *on-shell* simultaneously. On the other hand, the functions l, r are analytic and thus do not contribute to such corrections. We concentrate on such corrections and neglect all corrections decaying exponentially with the volume, such as in the Bethe-Salpeter kernel and the full propagators.

Loop function

Closely following Ref. [110, Eqs. $(31)-(42)$], the strategy is to perform the k^0 integral by closing the contour on the lower half plane, thus picking up contributions from the poles

$$k^0 = +\omega_{\mathbf{k}1} - i\varepsilon, \; +\omega_{\mathbf{k}2} + E - i\varepsilon, \tag{3.29}$$

where $\omega_{\mathbf{k}1} = \sqrt{\mathbf{k}^2 + m_1^2}$ and $\omega_{\mathbf{k}2} = \sqrt{(\mathbf{P}-\mathbf{k})^2 + m_2^2}$, leading to

$$\begin{aligned}
\mathcal{L}_L &= -\frac{1}{L^3}\sum_{\mathbf{k}}\int\frac{dx^0}{2\pi}\frac{h(k)}{\left[(k^0)^2 - \omega_{\mathbf{k}1}^2 + i\varepsilon\right]\left[(E-k^0)^2 - \omega_{\mathbf{k}2}^2 + i\varepsilon\right]} \\
&= \frac{i}{L^3}\sum_{\mathbf{k}}\left[\frac{h(\omega_{\mathbf{k}1},\mathbf{k})}{2\omega_{\mathbf{k}1}\left((E-\omega_{\mathbf{k}1})^2 - \omega_{\mathbf{k}2}^2\right)} + \frac{h(E+\omega_{\mathbf{k}2},\mathbf{k})}{2\omega_{\mathbf{k}2}\left((E+\omega_{\mathbf{k}2})^2 - \omega_{\mathbf{k}1}^2\right)}\right] \\
&\equiv \mathcal{L}_L^1 + \mathcal{L}_L^2.
\end{aligned} \tag{3.30}$$

Here, $\mathcal{L}_L^2$ does not contain poles in the elastic region and so we focus on $\mathcal{L}_L^1$, which can be written in terms of CM quantities through the Lorentz boost

$$\mathbf{k}_\parallel^* = \gamma(\mathbf{k}_\parallel - \boldsymbol{\beta}\omega_{\mathbf{k}1}), \qquad \mathbf{k}_\perp^* = \mathbf{k}_\perp, \quad \omega_{\mathbf{k}i}^* = \gamma(\omega_{\mathbf{k}i} + \boldsymbol{\beta}\cdot\mathbf{k}_\parallel), \tag{3.31}$$

taking an on-shell particle of momentum $\mathbf{k}$ and energy $\omega_{\mathbf{k}1}$ to the CM frame [III]. Observing the relation between the CM energy and back-to-back momenta

$$q^{*2} = \frac{1}{4}\left(E^{*2} - 2(m_1^2 + m_2^2) + \frac{(m_1^2 - m_2^2)^2}{E^{*2}}\right) \tag{3.32}$$

we can simplify the first term of the loop function as

$$\mathcal{L}_L^1 = \frac{i}{2L^3E^*}\sum_{\mathbf{k}}\frac{\omega^*_{\mathbf{k}1}}{\omega_{\mathbf{k}1}}\frac{h^*(\omega^*_{\mathbf{k}1},\mathbf{k}^*)}{\mathbf{q}^{*2}-\mathbf{k}^{*2}}\frac{E^* + \frac{\omega^{*2}_{\mathbf{k}1}-\omega^{*2}_{\mathbf{k}2}}{E^*} + 2\omega^*_{\mathbf{k}1}}{4\omega^*_{\mathbf{k}1}}, \tag{3.33}$$

where $h^*(\omega^*_{\mathbf{k}1},\mathbf{k}^*) \equiv h\big(\omega_{\mathbf{k}1}(\mathbf{k}^*),\mathbf{k}(\mathbf{k}^*)\big)$. This expression is worked out so that the Jacobian of the transformation (3.31) and the pole at $\mathbf{q}^{*2} = \mathbf{k}^{*2}$ are explicit.

Now we note that, in the large-L asymptotic regime, the Poisson formula (3.12) gives

$$\frac{1}{L^3}\sum_{\mathbf{k}} f(\mathbf{k}) \approx \int \frac{d^3k}{(2\pi)^3} f(\mathbf{k}), \tag{3.34}$$

up to exponentially suppressed corrections in volume for analytic f. Going back to (3.33), we rewrite it in the form

$$\mathcal{L}_L^1 = \frac{1}{L^3}\sum_{\mathbf{k}}\frac{\omega^*_{\mathbf{k}1}}{\omega_{\mathbf{k}1}}\frac{f^*(\mathbf{k}^*)}{q^{*2}-k^{*2}}, \tag{3.35}$$

where $q^* = |\mathbf{q}^*|$, $k^* = |\mathbf{k}^*|$ and we defined for convenience

$$f^*(\mathbf{k}^*) \equiv \frac{ih^*(\omega^*_{\mathbf{k}1},\mathbf{k}^*)}{2E^*}\left(\frac{E^* + \frac{\omega^{*2}_{\mathbf{k}1}-\omega^{*2}_{\mathbf{k}2}}{E^*} + 2\omega^*_{\mathbf{k}1}}{4\omega^*_{\mathbf{k}1}}\right). \tag{3.36}$$

The Poisson formula as written in (3.34) cannot be used without first removing the pole at $q^{*2} = k^{*2}$, which is achieved through $f^*(\mathbf{k}^*) \to f^*(\mathbf{k}^*) - f^*(\mathbf{q}^*)$ as in Ref. [110, Eq. (11)]. Using (3.34) then yields

$$\mathcal{L}_L^1 = \text{p. v.}\int \frac{d^3\mathbf{k}^*}{(2\pi)^3}\frac{f^*(\mathbf{k}^*)}{q^{*2}-k^{*2}} + \sum_{lm} f^*_{lm}(q^*)c^{\mathbf{d}}_{lm}(q^*) \tag{3.37}$$

up to exponentially volume-suppressed terms and where l, m indexes the spherical

[III] Here, $\mathbf{k}_{\parallel} = \mathbf{k}\cdot\boldsymbol{\beta}/\beta$, $\mathbf{k}_{\perp} = \mathbf{k} - \mathbf{k}_{\parallel}$ and $\gamma = (1-\beta^2)^{-1} = E/E^*$ is the relativistic factor.

components from the partial-wave decomposition

$$f^*(\mathbf{k}^*) = \sum_{l=0}^{\infty} \sum_{m=-l}^{l} f^*_{lm}(k^*) k^{*l} \sqrt{4\pi} Y_{lm}(\hat{\mathbf{k}}^*). \tag{3.38}$$

The kinematical functions $c^{\mathbf{d}}_{lm}$ are

$$c^{\mathbf{d}}_{lm}(q^*) = \left(\frac{1}{L^3} \sum_{\mathbf{k}} \frac{\omega^*_{\mathbf{k}1}}{\omega_{\mathbf{k}1}} - \text{p. v.} \int \frac{d^3k^*}{(2\pi)^3} \right) \frac{1}{q^{*2} - k^{*2}} k^{*l} Y_{lm}(\hat{\mathbf{k}}^*), \tag{3.39}$$

and $\mathbf{d} = \mathbf{P}L/2\pi$ is the dimensionless total spatial momentum. Observe that a principal-value prescription was introduced to isolate the pole-subtraction term into $c^{\mathbf{d}}_{lm}$, *cf.* Ref. [110, Eqs. (21), (23)].

We note that one should also introduce a UV regulator either in the pole subtraction (3.35),(3.37) or when splitting the loop function $\mathcal{L}_L$ in (3.30), to make sure each term is itself convergent, *cf.* Ref. [110, Eq. (11)]. It is sufficient to consider a cutoff function H such that, *e.g.* $f^*(\mathbf{k}^*) \to f^*(\mathbf{q}^*)H(\mathbf{q}^*, \mathbf{k}^*)$ in (3.35). This will have the desired effect and not modify the leading finite volume corrections as long as $H = 1$ is satisfied *at the pole*. We do not explicitly introduce the UV regulator as we will not study the effects of the regulator on the finite-volume corrections[110] and will instead later introduce an analytic regularisation, *cf.* Sec. 3.3.

Cutting rule

Using the Dirac-delta representation of the principal-value integral

$$\int \frac{\xi(A)}{A + i\varepsilon} \xrightarrow{\varepsilon \to 0^+} \text{p. v.} \int \frac{\xi(A)}{A} - i\pi \int \delta(A)\xi(A) \tag{3.40}$$

in (3.37), we recover an integral with the $i\varepsilon$ prescription

$$\mathcal{L}^1_L = \int \frac{d^3k^*}{(2\pi)^3} \frac{f^*(\mathbf{k}^*)}{q^{*2} - k^{*2} + i\varepsilon} + \sum_{lm} f^*_{lm}(q^*) c^{\mathbf{d}}_{lm}(q^*) + \frac{iq^*}{4\pi} f^*_{00}(q^*), \tag{3.41}$$

in addition to a finite term evaluated on-shell but with unfixed direction, *cf.* Ref [110, Eqs. (40) − (42)]. Undoing the k^0 contour integration on both terms in (3.41) and (3.30), we recover the infinite-volume volume version of $\mathcal{L}_L$ from the $i\varepsilon$ prescriptions, i.e. a loop function that matches the one we would obtain by skeleton-expanding the infinite-volume correlator as in (3.26). Observing that the bracketed term in (3.36)

equals 1 at the pole, the finite-volume correction on $\mathcal{L}_L$ in terms of the original function h is

$$\mathcal{L}_\Delta \equiv \mathcal{L}_\infty - \mathcal{L}_L \equiv -\frac{i}{2E^*}\sum_{lm} h^*_{lm}(q^*)c^{\mathbf{d}}_{lm}(q^*) + \frac{q^*}{8\pi E^*}h^*_{00}(q^*). \tag{3.42}$$

In order to use the result (3.42) to evaluate the expansion (3.26), we formally define a *geometrical function* F such that

$$\begin{aligned}\int \frac{d^2\hat{\mathbf{q}}^*}{(2\pi)^2}\frac{d^2\hat{\mathbf{q}}^{*'}}{(2\pi)^2} l^*(\mathbf{q}^*)F(\mathbf{q}^*,\mathbf{q}^{*'})r^*(\mathbf{q}^{*'}) = \\ -\frac{i}{2E^*}\sum_{lm} h^*_{lm}(q^*)c^{\mathbf{d}}_{lm}(q^*) + \frac{q^*}{8\pi E^*}h^*_{00}(q^*),\end{aligned} \tag{3.43}$$

cf. Ref [116, Eqs. (14)]. Based on (3.42), we can then finally write down the cutting rule

$$\begin{aligned}&\sum\!\!\!\!\!\!\int_k l(k;v)G_2(k)r(k;u) = \\ &\int \frac{d^4k}{(2\pi)^4} l(k;v)G_2(k)r(k;u) - \int \frac{d^2\hat{\mathbf{q}}^*}{(2\pi)^2}\frac{d^2\hat{\mathbf{q}}^{*'}}{(2\pi)^2} l^*(\mathbf{q}^*)F(\mathbf{q}^*,\mathbf{q}^{*'})r^*(\mathbf{q}^{*'}),\end{aligned} \tag{3.44}$$

diagrammatically represented by

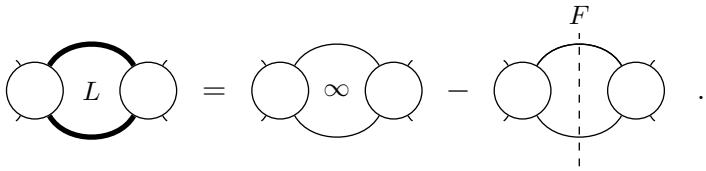

(3.45)

3.2.2 Quantisation condition

Following Ref [110, Eq. (44), Fig. (2)], we iteratively substitute the cutting rule into the expansion terms in (3.27), and the integrating from right to left, we get

$$\begin{aligned}C_L(P) = &\left(\sigma G_2^{i\varepsilon}\bar{\sigma} - \sigma F\bar{\sigma}\right) + \\ &\left(\sigma G_2^{i\varepsilon} iK G_2^{i\varepsilon}\bar{\sigma} - \sigma G_2^{i\varepsilon} iKF\bar{\sigma} - \sigma F iK G_2^{i\varepsilon}\bar{\sigma} + \sigma F iKF\bar{\sigma}\right) + \mathcal{O}(K^2),\end{aligned} \tag{3.46}$$

where we schematically denoted the infinite-volume loops with an $i\varepsilon$ in G_2. At all orders, we can identify the infinite-volume propagator C_∞ expansion with the sum of the terms having no F insertions. Subtracting it and reorganising the series in

powers of F leads to

$$\begin{aligned} C_\Delta(P) &\equiv C_L(P) - C_\infty(P) \\ &= \left(-\sigma F\bar{\sigma} - \sigma G_2^{i\varepsilon} iKF\bar{\sigma} - \sigma FiKG_2^{i\varepsilon}\bar{\sigma} + \mathcal{O}(K^2, F^1)\right) + \mathcal{O}(F^2) \\ &= -\left[\sigma + \sigma G_2^{i\varepsilon} iK + \mathcal{O}(K^3)\right] F \left[\bar{\sigma} + iKG_2^{i\varepsilon}\bar{\sigma} + \mathcal{O}(K^3)\right] + \mathcal{O}(F^2). \end{aligned} \tag{3.47}$$

We can further define the sum between square brackets as the generic endcaps $A, \bar{A}$ to explicitly write down

$$\begin{aligned} C_\Delta(P) &= -AF\bar{A} + AFiKF\bar{A} + AFiKG_2^{i\varepsilon}iKF\bar{A} + \dots \\ &= -AF\bar{A} + AFiK\sum_{n=0}^{\infty}(G_2^{i\varepsilon}iK)^n F\bar{A} + \dots \\ &= -AF\bar{A} + AFi\mathcal{M}F\bar{A} - AFi\mathcal{M}Fi\mathcal{M}F\bar{A}\dots \\ &= -AF\sum_{n=0}^{\infty}(-i\mathcal{M}F)^n\bar{A} = -AF(1+i\mathcal{M}F)^{-1}\bar{A}, \end{aligned} \tag{3.48}$$

where the skeleton expansion of the (infinite-volume) scattering amplitude was used

$$\mathcal{M} = \sum_{n=0}^{\infty}(G_2^{i\varepsilon}iK)^n =$$

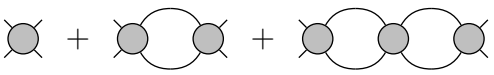

, (3.49)

with the external legs amputated. This follows from considering the LSZ formula (1.26) for a 2-to-2 process and skeleton-expanding the 4-point function in the elastic region using the Bethe-Salpeter kernel.

Our goal is to find the power-like finite-volume corrections in C_L expressed as poles of C_Δ, which in view of (3.48) translates into the condition that $(1 + i\mathcal{M}F)^{-1}$ is singular. Because F was defined through a partial-wave decomposition, (3.38) and (3.44), we can explicitly write it down as a matrix in angular momentum space

$$\begin{aligned} F_{l_1m_1,l_2m_2}(E^*) &= \frac{q^*}{8\pi E^*}\delta_{l_1m_1,l_2m_2} \\ &- \frac{i}{2E^*}\sum_{l=0}^{\infty}\sum_{m=-l}^{l}\sqrt{4\pi}q^{*l}c_{lm}^{\mathbf{d}}(q^*)\int\frac{d^2\hat{\mathbf{k}}^*}{(2\pi)^2}Y_{l_1m_1}^*(\hat{\mathbf{k}}^*)Y_{lm}^*(\hat{\mathbf{k}}^*)Y_{l_2m_2}(\hat{\mathbf{q}}), \end{aligned} \tag{3.50}$$

where we left implicit the dependence on the moving frame specified by $\mathbf{d}$, *cf.* Ref [110, Eqs. (48), (49)]. Using the same partial-wave basis, note that all the other quantities can be deemed as matrices (*e.g.* $K, \mathcal{M}$) or vectors (*e.g.* $A, \bar{A}$). This leads to the so-called determinant form of the *quantisation condition* for 2 particles with different

masses [IV]

$$\det\left[1 + i\mathcal{M}F(L)\right] = 0, \tag{3.51}$$

where we made the L-dependence encoding the finite-volume corrections explicit on F, *cf.* Ref [110, Eqs. (50)]. Note that both F and $\mathcal{M}$ depend on E^* and satisfy (3.51) precisely *at the finite-volume energies*. This will be the point of contact between the lattice spectral data and the infinite-volume scattering amplitude used in this work.

Even though we restrict ourselves to the relation (3.51), finite-volume methods, including or not field theory methods, have considerably advanced over the last years.[10,26] The main developments regard the inclusion of coupled-channel scattering,[116] three-particle effects,[117–119] particles of general spin,[120] as well as decay and transition amplitudes.[121–123] The addition of left-hand cut effects in the finite-volume formalism, important for studying resonances such as the doubly-charmed tetraquark,[124] is also underway.[108,109] Furthermore, besides the relativistic field theoretic (RFT) method reviewed here[110,117] other approaches, the non-relativistic effective field theory (NREFT)[119] and the finite-volume unitarity (FVU)[118] have been developed to a great extent. To a certain degree, an equivalence between the three formalisms seems to exist.[125] A completely different direction is taken by the HALQCD method, which seeks to directly extract a non-relativistic nuclear potential from lattice QCD data.[126]

3.3 Applications

Generalised Zeta Regularisation

Originally, a specific limit of (3.51) in the case of *elastic scattering* was derived through an effective Schrödinger equation.[111,112] These were shown to be equivalent to the quantisation condition (3.51) derived in relativistic field theory up to exponentially suppressed volume effects,[107,111] but involving different quantities. The quantisation condition obtained is of the form[111]

$$\det\left[S + (M+i)(M-i)^{-1}\right] = 0, \tag{3.52}$$

[IV] The case of identical particles is achieved by making $m_1 = m_2$ and adding the symmetrisation factor via $\mathcal{M} \to \mathcal{M}/2$.

where the *elastic* S-matrix is parametrised by energy-dependent phase shifts

$$S_{lm,l'm'} = \delta_{ll'}\delta_{mm'}e^{2i\delta_l} \tag{3.53}$$

and the geometrical function

$$M^{\mathbf{d}}_{lm,l'm'}(q^*) = \frac{(-1)^l}{\gamma\pi^{3/2}} \sum_{j=|l-l'|}^{l+l'} \sum_{s=-j}^{j} \frac{i^j}{q^{*j+1}} \mathcal{Z}^{\mathbf{d}}_{js}(1;q^{*2}) C_{lm,js,l'm'} \tag{3.54}$$

encodes the finite volume effects. We can write (3.52) in terms of the elastic $\mathcal{K}$-matrix (Sec. 1.4.1)

$$\det\left[M_{lm,l'm'} - \delta_{ll'}\delta_{mm'}\mathcal{K}_l^{-1}\right] = \det\left[M_{lm,l'm'} - \delta_{ll'}\delta_{mm'}\cot\delta_l\right] = 0 \tag{3.55}$$

which is the quantisation condition explicitly in terms of elastic phase shifts. The $C_{lm,js,l'm'}$ are proportional to Clebsch-Gordan coefficients and also to the triple angular integral featuring in the geometrical function F (3.50) [V]. In fact, we can again rewrite (3.52) using $\mathcal{T}_l\delta_{ll'}\delta_{mm'} \equiv \mathcal{T}_{lm,l'm'}$ (Sec. 1.4.1) as

$$\det\left[1 + 2i\mathcal{T}(1+iM)\right] = 0, \tag{3.56}$$

which is essentially (3.51) up to a phase-space factor going into the amplitude $\mathcal{M}$. This suggests a connection between the F function and the M above, which relies on the connection between the so-called *generalised zeta function* $\mathcal{Z}^{\mathbf{d}}_{lm}$ and the $c^{\mathbf{P}}_{lm}$.

The definition of the generalised zeta function is[111,112]

$$\mathcal{Z}^{\mathbf{d}}_{lm}(s;q^{*2}) = \sum_{\mathbf{n}\in\mathcal{P}_{\mathbf{d}}} \frac{Y_{lm}(\hat{\mathbf{n}})n^l}{(n^2-q^{*2})^s}, \tag{3.57}$$

with $n = |\mathbf{n}|$ for $\mathbf{n} \in \mathbb{Z}$. The $\mathbf{n}$-momentum sum is over the Lorentz-distorted grid

$$\mathcal{P}_{\mathbf{d}} = \left\{\mathbf{r} \mid \mathbf{r} = \boldsymbol{\gamma}^{-1}(\mathbf{x} - \frac{1}{2}A\mathbf{d})\right\}, \qquad A = 1 + \frac{m_1^2 - m_2^2}{E^{*2}}, \qquad \mathbf{x},\mathbf{d} \in \mathbb{Z}^3, \tag{3.58}$$

where $\boldsymbol{\gamma}^{-1}$ is a shorthand for the inverse of the Lorentz boost (3.31). Following Ref. [110], this zeta function can be connected to the kinematical functions $c^{\mathbf{d}}_{lm}$ (3.39) by first showing that, at the pole $k^{*2} = q^{*2}$, the momentum variable obeys $\mathbf{n} = \mathbf{k}^*$.

[V] The Clebsch-Gordan coefficients (or $3j$-Wigner symbols) are related to the spherical harmonics integral contraction in (3.50) by an identity, *e.g.* Ref. [127, Eq. (3.8.73)].

Given that, one can show that

$$q^{*2} - k^{*2} = \frac{\gamma\omega^*_{\mathbf{k}1}}{\omega_{\mathbf{k}1}}(q^{*2} - n^{*2}) \tag{3.59}$$

up to higher orders in $q^{*2} - k^{*2}$, and it follows that the Jacobian $\omega^*_{\mathbf{k}1}/\omega_{\mathbf{k}1}$ in (3.39) can be absorbed into $q^{*2} - n^{*2}$ up to an analytic function. As we have observed before, analytic pieces yield exponentially suppressed volume effects through the Poisson formula and thus the equivalence is established, which we write down here for completeness[110]

$$c^{\mathbf{d}}_{lm}(q^{*2}) = -\frac{\sqrt{4\pi}}{\gamma L^3}\left(\frac{2\pi}{L}\right)^{l-2} \mathcal{Z}^{\mathbf{d}}_{lm}\big(1; (q^*L/2\pi)^2\big). \tag{3.60}$$

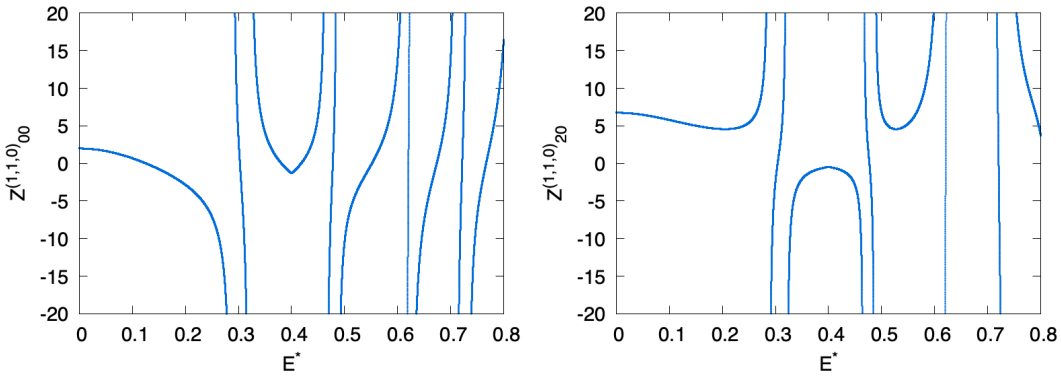

(a) $\mathcal{Z}^{(\mathbf{110})}_{00}(1; q^{*2}(E^*))$ **(b)** $\mathcal{Z}^{(\mathbf{110})}_{20}(1; q^{*2}(E^*))$

Figure 3.2 *Numerical evaluation generalised zeta function against the CM energy $E*$ for $L = 32$ and $m_1 = m_2 = 0.2$ in arbitrary units.*

Note that, the singular term at $l = 0$, treated in the field-theoretic method of the last section by the p.v. prescription together with a UV regulator,[110] is approached in the zeta framework by defining a suitable analytical continuation of $\mathcal{Z}^{\mathbf{d}}_{lm}(s; q^{*2})$ through a heat-kernel representation, such that $\mathcal{Z}^{\mathbf{d}}_{lm}(s = 1; q^{*2})$ is finite[111] for all l. This also indirectly corresponds to the ultraviolet regularisation present in $c^{\mathbf{d}}_{lm}$. Both $\mathcal{Z}^{\mathbf{d}}_{lm}$ and $c^{\mathbf{d}}_{lm}$ versions are equivalent up to exponentially suppressed volume effects and are suitable to numerical computations. In particular, we implement $\mathcal{Z}^{\mathbf{d}}_{lm}(s = 1; q^{*2})$ under such "analytic regularisation" and use it to evaluate the quantisation conditions in this work,[112,113] *cf.* Fig. 3.2.

Partial-wave truncation

The quantisation condition in matrix form (3.51) is still a bit opaque to direct applications, as it involves infinitely many partial waves. In particular, we are interested only in the low-energy scattering, where higher partial waves tend to be suppressed by threshold barriers and only a few lower ones are effectively non-zero.

The scattering amplitude can be decomposed in the angular momentum basis as in (3.38). This translates into a diagonal matrix $\mathcal{M}_{l_1 m_1, l_2 m_2} \propto \delta_{l_1 l_2} \delta_{m_1 m_2}$ in terms of its phase shifts or, in general, of its $\mathcal{K}$-matrix components (Sec. 1.4.1). Supposing only the first l_{max} components are non-zero, one can define a projector $\mathcal{P}$ onto the angular momenta $l \leq l_{max}$ such that[110]

$$F_{\mathcal{P}} = \mathcal{P} F \mathcal{P} \quad \text{and} \quad \mathcal{M} = \mathcal{P} \mathcal{M} \mathcal{P}, \tag{3.61}$$

where $F_{\mathcal{P}}$ and $\mathcal{M}$ vanish outside the l_{max}-block. Using that in (3.51) leads to

$$\det(\mathcal{P} + i F_{\mathcal{P}} \mathcal{M}) = 0, \tag{3.62}$$

which is equivalent to using the original quantisation condition with F restricted to the l_{max}-block in the angular momentum basis.

Calculations of S-wave scattering have been serving as a laboratory for exploring the finite-volume formalism since its inception,[111,112] in particular for the computation of scattering lengths.[128] More recent calculations using lattice QCD data typically featured $\pi\pi$[129,130] S-wave scattering at large pion masses. Other works also study the contamination of higher partial waves on the scattering length extracted via the Lüscher formalism.[131]

Block diagonalisation

As mentioned in Sec. 2.5, the rotational and parity symmetries at rest are broken into a smaller set of symmetries dictated by the cubic group when we put QCD on a finite volume lattice. An analogous effect occurs in moving frame systems.

The quantisation conditions (3.51) and (3.52) were expressed using a continuum angular momentum basis. We thus expect such formulas to reduce under the

symmetries of a cube, corresponding to a change of basis

$$|lm\rangle \in \mathcal{H}^l \to |\Lambda r\rangle \in \mathcal{H}^\Lambda, \quad m = -l, \ldots, j, \; r = 1, \ldots, \dim \Lambda, \tag{3.63}$$

whose target vectors are labeled by the irreps Λ of the cubic subgroups and its rows i. The irreducible subspaces $\mathcal{H}^l$ of the $SO(3)$ continuum irreps are spanned by the spherical harmonics

$$Y_{lm}(R\hat{\mathbf{r}}) = \sum_{m'=-l}^{l} \mathcal{D}^l_{mm'}(R) Y_{lm'}(\hat{\mathbf{r}}), \quad R \in SO(3), \tag{3.64}$$

which in addition of parity behave as $Y_{lm}(\hat{\mathbf{r}}) \to (-1)^l Y_{lm}(\hat{\mathbf{r}})$. The unitary $(2l+1)$-dimensional representation matrices $\mathcal{D}^l$ are the Wigner D-matrices,[127] reducible with respect to the cubic subgroups.

For exposing the breakdown properties of the quantisation condition, we use the property of the M matrix[111]

$$\mathcal{D}(R) M = M \mathcal{D}(R) \tag{3.65}$$

for all elements R of a lattice group. Under the general orthogonality property of irreps (Schur's lemma), the commutativity with a representation implies that there is a change of basis which reduces D into cubic irreps and block-diagonalises M, such that in the new basis[132,133]

$${}_{l_1 n_1}\langle \Lambda_1 r | \, M \, |\Lambda_2 s\rangle_{l_2 n_2} = M_{l_1 n_1, l_2 n_2} \delta_{\Lambda_1 \Lambda_2} \delta_{r,s}, \tag{3.66}$$

where $n_{1,2}$ were added to label which copy of Λ is being subduced into the irreps $\mathcal{D}^{l_{1,2}}$. The new basis is obtained from the old by transformations

$$|\Lambda r\rangle_{ln} = \sum_{m=-l}^{l} \mathcal{S}^{\Lambda r(n)}_{lm} \, |lm\rangle \,, \tag{3.67}$$

where

$$\mathcal{S}^{\Lambda r(n)}_{lm} = \langle lm \, | \, \Lambda r\rangle_{ln} \tag{3.68}$$

are the reduction (or subduction) coefficients. One can proceed analogously with the F and c_{lm} functions from (3.50), but we stick to the zeta notation as that is the one we implement directly.

The block-diagonalisation of M enables one to decompose (3.55) into individual

quantisation conditions on each lattice irrep

$$\det\left[M^{\Lambda} - \mathcal{K}^{-1}\right] = 0, \tag{3.69}$$

where $(\mathcal{K}^{-1})_{l_1 l_2, n_1 n_2} = \delta_{l_1 l_2}\delta_{n_1 n_2}\cot\delta_{l_1}$ and we left the total momentum $\mathbf{d}$ implicit. Due to (3.66), the relations for each row in the same irrep are equivalent. When performing the partial-wave truncation from 3.3, the matrix $M^{\Lambda} - \mathcal{K}^{-1}$ becomes finite and

$$\dim M^{\Lambda} = \sum_{l \in \mathrm{sub}(\Lambda)} N(\Lambda, l), \tag{3.70}$$

where the reduction of the angular momentum irrep l results in $\mathsf{sub}(\Lambda)$, and so the sum (3.70) is finite.

In this work, we are interested in $K\pi^{(I=1/2)}$ and $\pi\pi^{(I=1)}$ scattering in the $l = 1$ partial-wave (P-wave) under an elastic approximation. In that case, a projector along the lines of (3.61) can be used to define quantisation conditions in terms of the so-called pseudophases

$$M^{\Lambda}(q^*; L) = \cot\phi^{\Lambda}(q^* L/2\pi; L), \tag{3.71}$$

cf. B and Sec. 4.4.2. In our case, the phase shift δ_1 will typically behave as a Breit-Wigner parametrisation due to the presence of the $K^*(892)$ and $\rho(770)$ resonances. This is one of the most explored applications of the two-particle formalism, especially for the ρ, with several independent contributions to the literature,[134–141] including studies of their quark-mass dependence.[142,143]

Given (3.71), we can take an explicit example of $K\pi$ scattering in the rest frame. In this case, the $l = 1$ partial wave is subduced only by the T_{1u} irrep of $\mathcal{O}_h$, leading to the so-called pseudophase form of the quantisation condition, *cf.* B.1,

$$\cot\phi^{T_{1u}[000]}(q^* L/2\pi) = \frac{\mathcal{Z}_{00}^{(000)}(1; q^* L/2\pi)}{\pi^{3/2}} = \cot\delta_1(q^*). \tag{3.72}$$

One can visualise the dependency of the spectrum by using some model for δ_1 and numerically solving the equation above for q^*. It is then straightforward to compute the finite-volume energies E^* through (3.32) and their dependence on the box size L.

In Fig. 3.3, we substituted physical values for the π and ρ masses into a Breit-Wigner model, *cf.* Sec. 5.2. For a relatively low value of g, representing stronger coupling of the resonance to the $\pi\pi$ states, the shift from the non-interacting energies caused by the box is quite small and we can easily associate a level to the resonance state for a considerable range of L. This identification fails close to the

level avoidances, where the resonance mass and the free energies cross. When the coupling of the resonant and the two-particle states increases, the mixing of the finite-volume spectrum makes the labeling of the levels based on the non-interacting energy even more discrepant. This illustrates the qualitative behaviour of the finite-volume spectrum under different two-particle interactions which we use to determine scattering amplitudes.

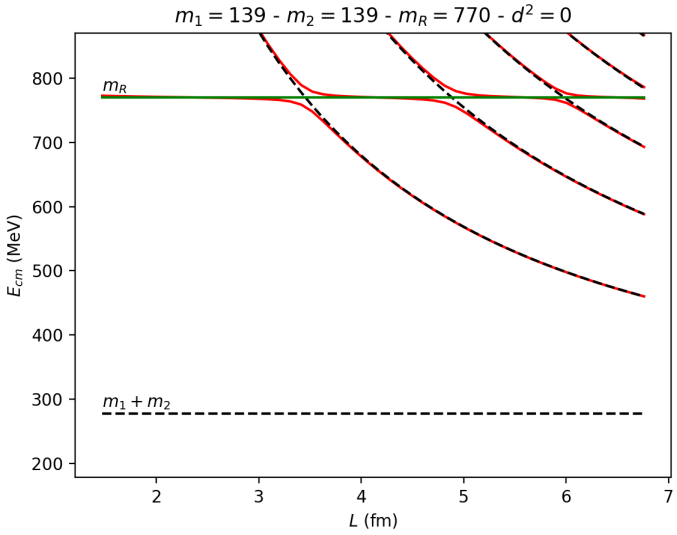

(a) *Low coupling* ($g = 1$)

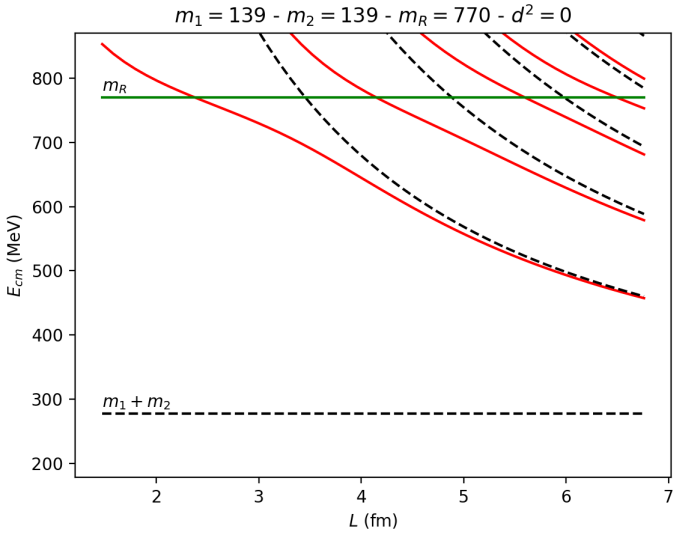

(b) *High coupling* ($g = 5.9$)

Figure 3.3 *Inverse Lüscher problem from Eq.(3.72) for a Breit-Wigner model with physical ρ and π masses. The crossing between non-interacting levels (dashed lines) and resonance mass (green line) indicates a level avoidance.*

4 Hadron Spectroscopy

Hadron spectroscopy is a well-established topic in lattice QCD.[30,144–146] Besides the early success in computing light hadron masses,[22–24] lattice simulations of heavy[147] and heavy-light[148] systems, containing c or b quarks, also attained a good level of maturity by now. Furthermore, the study of states outside the quark model has undergone considerable development, including hybrid mesons (mesons with some gluon content),[149] glueballs (only gluon content),[150] and exotic hadrons,[151–153] the latter featuring the so-called *tetraquark* states. This translates into the advancement of a range of techniques for numerically computing Euclidean correlation functions, or *correlators*. Despite being simple, the idea behind using correlators to extract finite-volume energy levels from lattice QCD faces many obstacles.

Firstly, the direct observables (correlators) computed in lattice simulations come with a *statistical uncertainty* inherent to the stochastic character of Monte Carlo techniques, *cf.* Sec. 2.4.3. Similarly to any data-driven method, *systematic uncertainties* will also appear due to limited knowledge of some underlying properties of the data. These uncertainties need to be controlled and methodically propagated down to the derived quantities in order for a lattice determination to be meaningful.

Secondly, correlators potentially have much more information, *e.g. excited states*, than just the specific energies we want to compute. Such contributions were historically hard to treat and represent a classical systematical uncertainty in lattice calculations.[154] Nowadays, there is a significant collection of techniques used to control them, mainly surrounding the construction of a large set of hadronic *interpolators*.[28,29,91,99,155–159]

Thirdly, the measurement of correlators is in practice computationally very expensive and often the dominant cost of lattice QCD simulations, especially when close to the *physical point*. This is especially true in the case of this work, where domain-wall fermions are combined with the spectroscopy techniques of this chapter. While the domain-wall action possesses good chiral symmetry properties, the price is that its

cost is roughly at least *ten* times the cost of the next cheaper action. Moreover, we analyse a lattice ensemble that was generated almost ten years ago but with current computational resources, which allows us to perform a large number of operations on this ensemble that would not be possible at the time of its creation and thus becomes the main accumulated cost of this work. [I]

All the factors above combined amount to a formidable task. They summed up to one year of continuous running at two major supercomputing facilities in the United Kingdom [II], plus another year of theoretical and data analysis. We now describe and implement the well-established techniques necessary to compute the low-lying spectrum associated with the $\pi\pi$ and $K\pi$ states relevant to us at good statistical precision, with emphasis on the *distillation method*.[28]

4.1 Basics

Spectral Decomposition and Smearing

The main direct products of our lattice simulations are correlation functions, *i.e.* the expected values of interpolators between states of interest. The *interpolators* are chosen according to the quantum numbers, *i.e.* symmetries, of the state. For instance, a suitable interpolator for a pion state is

$$O(x) = -\bar{d}(x)\gamma^5 u(x), \tag{4.1}$$

where u and d are quark fields. This operator transforms as a pseudoscalar under Lorentz symmetries and lives in a flavour representation corresponding to the π^+.[6] Inserting O and $O^\dagger$ in a correlator at two different times, we can simplify the spin-colour sums and write down the single Wick contraction, *cf.* Sec. 4.3.2,

$$\begin{aligned} C(x,y) &= \langle O(x)O(y)^\dagger \rangle_{\mathsf{F}} = \langle \bar{d}(x)\gamma^5 u(x)\ \bar{u}(y)\gamma^5 d(y) \rangle_{\mathsf{F}} \\ &= -\operatorname{tr}\left[\gamma^5 D^{-1}_{(d)}(y,x)\gamma^5 D^{-1}_{(u)}(x,y)\right] \end{aligned} \tag{4.2}$$

[I] Due to the organisation of the lattice QCD community into collaborations with extensive long-term plans, the *ensemble generation* phase (HMC) is potentially separated from the *measurement* phase by many years, when the landscape of computational resources is completely different, and thus the simulations more costly.

[II] The *Tesseract* and *Tursa* machines within the STFC DiRAC Extreme Scaling service (www.dirac.ac.uk).

in terms of the inverse of the Dirac operator D^{-1}, *i.e.* , the quark propagator involving only the surface fermions (2.37). The notation $\langle\rangle_{\mathsf{F}}$ indicates only the fermionic path integral was evaluated. Note that the quark-content in the operator (4.1) is exactly what one would expect from the quark model, a practice that has been one of the pillars of lattice hadron spectroscopy since its origins.[7]

It is computationally unfeasible to exactly calculate D^{-1}, so what one can do is to solve the linear problem

$$Dz = \chi, \tag{4.3}$$

where χ is some *source* vector. In this way, only columns $z = D^{-1}\chi$ are extracted [III]. The simplest example of this is a *point source*

$$\chi_{a\beta}^{(b,\beta,\mathbf{y})}(\mathbf{x}) = \delta_{ab}\delta_{\alpha\beta}\delta(\mathbf{x}-\mathbf{y}), \tag{4.4}$$

for fixed b, β and $\mathbf{y}$. Solving this system for all 12 combinations of colour and spin yields an *one-to-all* propagator, *i.e.* , it describes the propagation of a quark from the source position $\mathbf{y}$ to all possible *sink* positions at a certain time slice. Due to translation invariance, we do not need to vary the source position and time slice for a simple correlator as (4.2). This will not be possible for more complicated correlators used later.

The spectral decomposition can be used to access the low-energy energies through correlators. Ignoring normalisations, consider projecting a two-point correlator to zero spatial momentum on a system with infinite time extension

$$\begin{aligned}\tilde{C}(\mathbf{P}=0,t) &= \sum_{\mathbf{x},n} \langle 0|e^{tH}\tilde{O}e^{-tH}|n\rangle \langle n|\tilde{O}^\dagger|0\rangle = \sum_n \langle 0|\tilde{O}|n\rangle \langle n|\tilde{O}^\dagger|0\rangle e^{-tE_n} \\ &= \sum_n |A_n|^2 e^{-tE_n} \xrightarrow{t\to\infty} |A_0|^2 e^{-tE_0},\end{aligned} \tag{4.5}$$

where $\tilde{O} = \tilde{O}(\mathbf{x})$ time-independent operator, $t = x_0 - y_0$ and $|n\rangle$ are the energy eigenstates of the lattice QCD Hamiltonian. One can then see that at large imaginary times, the log-mass $\log \tilde{C}(t)/\tilde{C}(t+1)$ tends to the ground state energy. On a lattice calculation where an estimate for $\tilde{C}(\mathbf{P}=0,t)$ is computed, one would be able to isolate E_0 through a fit to a single exponential (Ch. 5).

Note that the choice of interpolator is not unique at all. For instance, we could have used $\gamma^4\gamma^5$ or displaced the quark fields with gauge links[157] instead of γ^5 in

[III] This operation repeated *tens of thousands* of times constitutes our major computational cost.

(4.1). In principle, any form is valid as long as it preserves the symmetries from the original interpolator, *e.g.* flavour or angular momentum quantum numbers, as well as spacetime symmetries, such as translations. We could also change the spatial distribution from a point source to an extended profile. This freedom is also expressed in the fact that a given operator contains contributions from *all* states on its symmetry channel. Although challenging, the arbitrariness of this choice can be explored to obtain interpolators with improved overlapping to the states we wish to study, reducing contributions from highly excited states.

Smeared Links

Link or gauge smearing is used to increase the signal-to-noise ratio when extracting the low-lying energy spectrum from correlators. Methods such as APE and HYP smearing[160] have been long used in interpolator building in order to suppress short-distance fluctuations on the gauge fields.

It corresponds to replacing link variables with a gauge-invariant "fat link". This is usually obtained by left-multiplying the gauge field on each site and direction as

$$U_\mu^{(n_{\text{step}}+1)}(x) = G_\mu^{(n_{\text{step}})}(x) U_\mu^{(n_{\text{step}})}(x), \quad n_{\text{step}} = 0, \ldots, n_{\text{stout}}, \quad U^{(0)} \equiv U, \tag{4.6}$$

where $G_\mu^{(n_{\text{step}})}(x)$ is some suitable group element built from $U_\mu^{(n_{\text{step}})}$ in the neighbourhood of x. In general, either $G_\mu^{(n_{\text{step}})}(x)$ or $U_\mu^{(n+1)}(x)$ need to be projected back into the $SU(3)$ gauge group. The superscript n indicates that this is an iterative process, starting from the unsmeared gauge field U_μ.

We detail a type of link smearing used in the present calculation, called *stout smearing*.[161] It is built from (4.6) by choosing

$$G_\mu^{(n_{\text{step}})}(x) = e^{iQ_\mu^{(n_{\text{step}})}(x)}, \tag{4.7}$$

which is automatically an element of the $SU(3)$ group with the choice of $Q_\mu(x)$ in the algebra

$$Q_\mu(x) = \frac{i}{3}\left[A_\mu(x)^\dagger - A_\mu(x)\right] - \frac{i}{6}\,\text{tr}\left[A_\mu(x)^\dagger - A_\mu(x)\right], \tag{4.8}$$

where the closed "staple" sum is

$$A_\mu(x) = \sum_{\nu \neq \mu} \rho_{\mu\nu} \big[U_\nu(x) U_\mu(x+\nu) U_\nu(x+\mu)^\dagger + U_\nu(x-\nu)^\dagger U_\mu(x-\nu) U_\nu(x-\nu+\mu) \big] U_\mu(x)^\dagger. \tag{4.9}$$

Besides obeying all symmetry properties from the initial gauge field, this construction can be shown to be analytic and differentiable.[161] For the present work, it is sufficient that it reduces the contribution from short-distance modes to the long-distance behaviour we are interested in, translated into an improved signal-to-noise ratio in lattice correlators.

Smeared Sources

At the end of the day, we need to extract low-lying energy levels from correlators using their exponential series form, as indicated in (4.5). In the literature, this was observed to be considerably improved when using *smeared* sources.[28,162,163] It corresponds to modifying an interpolator into a form compatible with the hadronic scale of interest through a convolution operation, a process generally called *quark smearing*.

In the case of (4.2), one is interested in suppressing the overlap factors of the hadron interpolator O with a large number of excited states. It is desirable to choose a smearing operation separable at the quark level, *i.e.*

$$\psi(\mathbf{x}) \to \sum_{\mathbf{x}'} \square(\mathbf{x}, \mathbf{x}') \psi(\mathbf{x}'), \tag{4.10}$$

where $\square$ can depend on the gauge field. The physics extracted from a source-smeared correlator is preserved as long as this operation is linear and leaves the spacetime and discrete symmetries untouched.

Early examples of *gauge-covariant* quark smearing are the Jacobi and Wuppertal methods, which deform point sources into a bell-like shape.[162] These consist of solving a three-dimensional gauge-covariant Klein-Gordon equation representing the effective hadronic degree of freedom in space. In this case, a hopping parameter is used to tune the radial extent of the smeared source. In general, extended gauge-covariant sources can be built by connecting different sites with chains of link variables.[163] On the other hand, methods that directly impose specific spatial

configurations without preserving gauge symmetry, such as Gaussian and wall smearing,[78] are useful in some contexts[164] but require a gauge-fixing step.

One can further combine quark smearing with *stochastic noises*,[165] which potentially decrease local fluctuations and in some cases reduce computational costs, especially if combined with *dilution* techniques[166] (Sec. 4.2).

4.2 Distillation

In many modern lattice QCD calculations, all spacetime entries of the D^{-1} operator are needed to evaluate multi-hadron interpolators, *cf.* (4.4). This is because quark propagations from *all* spacetime positions to *all* spacetime positions appear as soon as more than one interpolator such as $\bar{u}(x)\gamma^5 d(x)$ is employed on a two-point function (Fig. 4.1). The so-called *all-to-all* methods can be used to achieve that,[166] in contrast to the one-to-all sources.

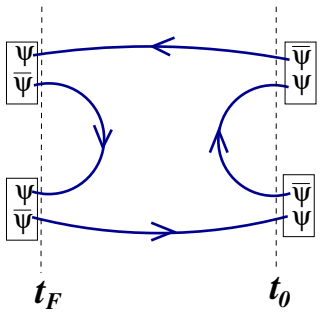

Figure 4.1 *Example of diagram in a multi-hadron correlator.*[29] *The t_f-to-t_f (sink-to-sink) quark lines and the implicit spatial sums introduce the need for all-to-all propagators.*

An efficient way of computing a sizeable number of hadronic correlators involving all-to-all quark propagations is the so-called *distillation method*.[28,29] In its conception, the physics goal of distillation was to make possible the rigorous study of hadronic scattering and, in particular, hadronic resonances on the lattice. In summary, it allows for the computation of a large number of smeared correlation functions by *projecting* the spatial degrees of freedom, reaching $\mathcal{O}(10^5)$ in modern simulations, into the less numerous low-lying modes a suitable operator.

It cannot be overly emphasised the impact that distillation had in the field of lattice QCD spectroscopy and in the following we give a detailed introduction to its

formulation, describing how it is used to compute the correlation functions in this work.

Exact Method

The distillation operator (kernel) is written as

$$\Box_{ab}(\mathbf{x},\mathbf{y};t) = \sum_{k=1}^{N_{\text{vec}}} v_a^{(k)}(\mathbf{x};t) v_b^{(k)}(\mathbf{y};t)^* = (\Box^\dagger)_{ab}(\mathbf{x},\mathbf{y};t), \tag{4.11}$$

where $v^{(k)}$ are the first N_{vec} eigenvectors of the eigenvalue equation

$$-\sum_{b,\mathbf{y}} \nabla^2_{ab}(\mathbf{x},\mathbf{y};t) v_b^{(k)}(\mathbf{y},t) = \xi_k(t) v_a^{(k)}(\mathbf{x};t) \tag{4.12}$$

with $0 \leq \xi^{(1)} \leq \xi^{(2)} \leq \ldots \leq \xi^{(N_{\text{vec}})}$, and where the (negative) *three-dimensional gauge-covariant Laplace* operator is given at each t by

$$-\nabla^2_{ab}(\mathbf{x},\mathbf{y};t) = 6\delta_{\mathbf{x},\mathbf{y}}\delta_{ab} - \sum_{j=1}^{3} (U_j^{ab}(\mathbf{x},t)\delta_{\mathbf{x}+\hat{\mathbf{j}},\mathbf{y}} + U_j^{ba}(\mathbf{y},t)^*\delta_{\mathbf{x}-\hat{\mathbf{j}},\mathbf{y}}) \tag{4.13}$$

from the gauge field U stout-smeared only on the spatial directions, *i.e.* $\rho_{i4} = \rho_{4i} = 0$, *cf.* Sec. 4.1. The operator (4.11) is Hermitian and nilpotent, which also makes it a projector. It effectively acts on the quark fields as in (4.10), projecting the unsmeared field onto the space spanned by the low-lying eigenvectors of $\Box$, referred to as *distillation space*. Another important property of the distillation kernel is that it preserves rotational as well as charge and parity symmetries.[28] We defer the choice of N_{vec} to Sec. 4.4.1.

Given a full quark propagator S, one can express the effect of applying the distillation kernel as

$$\begin{aligned} S_{ab,\alpha\beta}(x,y) &\equiv \left[\Box D^{-1} \Box^\dagger\right]_{ab,\alpha\beta}(x,y) \\ &= \sum_{k,l} v_a^{(k)}(\mathbf{x};x_0) \left[\sum_{\tilde{\mathbf{x}},\tilde{a}} v_{\tilde{a}}^{(k)}(\tilde{\mathbf{x}};x_0)^* \sum_{\tilde{\mathbf{y}},\tilde{b}} D^{-1}_{\alpha\beta,\tilde{a}\tilde{b}}(\tilde{\mathbf{x}},x_0;\tilde{\mathbf{y}},y_0) v_{\tilde{b}}^{(l)}(\tilde{\mathbf{y}};y_0)\right] v_b^{(l)}(\mathbf{y};y_0)^*, \end{aligned} \tag{4.14}$$

where the term between square brackets is called *perambulator*, denoted by $\tau^{kl}_{\alpha\beta}(x_0,y_0)$, and carries information of D^{-1} with space-colour indices summed out. The peram-

bulator can also be seen as a type of all-to-all propagator projected into distillation space.

The number of inversions needed to compute a perambulator is large, but way smaller than the number of inversions for an explicit full propagator (all positions to all positions), namely $N_s\, N_{\text{vec}} \sim \mathcal{O}(10^2)$ against $N_s N_c N^3 \sim \mathcal{O}(10^6)$ per source and sink time slice, quark flavour and configuration (typically for $\mathcal{O}(10)$ time slices and $\mathcal{O}(10^3)$ configurations). This procedure is what we refer to as *exact distillation*.

To illustrate how one can compute correlators using distillation, we use the notation where the $v^{(k)}$ are written as the columns of the $N_c N^3\, N_{\text{vec}} \times N_c N^3\, N_{\text{vec}}$ matrix $V(t)$,

$$\square(t) = V(t)V(t)^\dagger, \tag{4.15}$$

turning (4.14) into

$$S(x_0, y_0) = V(x_0)V(x_0)^\dagger D^{-1}(x_0, y_0)V(y_0)V(y_0)^\dagger, \tag{4.16}$$

where the position dependence was hidden. Then, the pion correlator (4.2) is

$$C(x_0, y_0) = -\operatorname{tr}\left[V(y_0)^\dagger \gamma^5 V(y_0)\, \tau_{(u)}(y_0, x_0)\, V(x_0)^\dagger \gamma^5 V(x_0)\, \tau_{(d)}(x_0, y_0)\right], \tag{4.17}$$

with

$$\tau(x_0, y_0) = V(x_0)^\dagger D^{-1}(x_0, y_0)V(t_0). \tag{4.18}$$

Notice that, for a fixed perambulator, we can vary $V^\dagger \gamma^5 V$ to any structure with quantum numbers of the states we want to study. This takes place with no further inversions $D^{-1}V$, typically the most costly operation on a spectroscopy lattice QCD simulation. In principle, we can additionally project the correlator to arbitrary momenta at this step.

Stochastic and Diluted Sources

Distillation gives us access to all sink and source spatial points through the spin-Laplacian basis. Nevertheless, sink-to-sink propagators require the evaluation of perambulators of the kind $\tau(t_f, t_f)$ for different sink times t_f. Moreover, in,[28,29] it is argued that the number N_{vec} of low-lying eigenvectors scales with the physical volume for a *fixed cutoff* of the three-dimensional Laplacian spectrum.

The extension of the distillation method developed in Ref. [29] is called *stochastic*

distillation. Rather than exactly computing the smeared propagator as in Eq.(4.14), Z_N noise vectors are introduced as inversion sources and S is then evaluated *stochastically*.[160,166] The number of inversions will then scale with the chosen amount of noises N_η, instead of N_{vec}. Of course, one needs to make sure the fluctuations introduced are not greater than the original gauge fluctuations coming from the gauge average (2.47),[29,167] *cf.* Sec. 4.4.1.

One begins by defining the spin-time-Lap noises $\eta = [\eta_{\alpha k}(x_0)]$ obeying

$$\langle \eta^r_{\alpha k}(x_0) \rangle_\eta = 0 \tag{4.19}$$

$$\left\langle \eta^r_{\alpha k}(x_0) \eta^s_{\beta l}(y_0) \right\rangle_\eta = \delta_{rs}\delta_{kl}\delta_{\alpha\beta}\delta(x_0 - y_0), \tag{4.20}$$

where the bracketed index is a noise index and the expectation value is given by the usual definition $\langle\cdot\rangle_\eta = \lim_{N_\eta\to\infty} \frac{1}{N_\eta}\sum_{r=1}^{N_\eta}(\cdot)^r$. We can then evaluate the propagator associated with noise r by inserting (4.20) in (4.14)

$$S^r_{ab,\alpha\beta}(x,y) \equiv \sum_{k,l} v_{ak}(\mathbf{x};x_0) \sum_{\tilde\beta,\tilde y_0,\tilde l} \left[\tau^r_{\alpha\tilde\beta,k\tilde l}(x_0,\tilde y_0)\right] \eta^r_{\beta l}(y_0)^* v_{bl}(\mathbf{y};y_0)^*. \tag{4.21}$$

The Monte Carlo estimator for S will then be

$$\hat S(x_0,y_0) \equiv \frac{1}{N_\eta}\sum_{r=1}^{N_\eta} S^r(x_0,y_0), \tag{4.22}$$

whereas, by construction,

$$\left\langle \hat S(x_0,y_0) \right\rangle_\eta = \langle S^r(x_0,y_0)\rangle_\eta = S(x_0,y_0). \tag{4.23}$$

Typically, the stochastic fluctuations introduced by averaging over a few noise sources are too large.[160] Increasing N_η helps but is costly and not particularly effective, so a variance reduction method dubbed *dilution* was introduced into distillation together with the stochasticity.[160,166,168] Essentially, one imposes exact instead of statistical zeros in the block diagonal structure of the second identity in Eq.(4.20). Dilution can be formalised by dividing the distillation space into subspaces with vanishing overlaps between themselves. We define a single dilution space I as

$$I = \bigcup_{i=1}^{N_i} I^i, \quad i_1 \neq i_2 \Rightarrow I^{i_1} \cap I^{i_2} = \varnothing, \quad I^i \neq \varnothing, \tag{4.24}$$

where I^i is a dilution partition labeled by i, which is a subset of I. There are

no overlaps between different partitions and no partition is empty. Furthermore, when combining different dilution spaces, we wish the overlap between them to be zero. A natural way of specifying dilution partitions and their sparseness is through characteristic functions, *cf.* C.1.

The standard way of projecting different objects onto the various partitions is to define projectors into each distillation subspace, P^S, P^T and P^L, and the collective projector $P^d \equiv P^S P^T P^L$, where d is a compound index containing S, T, L. We do not specify the projectors at first, but they naturally obey

$$(P^d)^2 = P^d = P^{d\dagger}, \tag{4.25}$$

$$\sum_d P^d = \mathbb{1}, \tag{4.26}$$

where $\mathbb{1}$ here is the identity matrix. Using these properties, we can insert a resolution of the identity

$$\delta_{\tilde{\beta}\beta}\delta_{\tilde{l}l}\delta(\tilde{y_0} - y_0) = \sum_d \sum_{\gamma,m,z_0} \sum_{\sigma,n,w_0} P^d_{\tilde{\beta}\gamma,\tilde{l}m}(\tilde{y_0}, z_0) \left\langle \eta^d_{\gamma m}(z_0)\eta^d_{\sigma n}(w_0)^* \right\rangle_\eta P^d_{\sigma\beta,nl}(w_0, y_0) \tag{4.27}$$

in (4.14) and write it as

$$\begin{aligned} S_{ab,\alpha\beta}(\mathbf{x}, x_0; \mathbf{y}, y_0) &= \sum_{k,l} v_{ak}(\mathbf{x}; x_0) \sum_{\tilde{\mathbf{x}},\tilde{a}} v_{\tilde{a}k}(\tilde{\mathbf{x}}; x_0)^* \\ &\times \sum_{\tilde{\mathbf{y}},\tilde{b}} \sum_{\tilde{\beta},\tilde{y_0},\tilde{l}} D^{-1}_{\alpha\beta,\tilde{a}\tilde{b}}(\tilde{\mathbf{x}}, x_0; \tilde{\mathbf{y}}, y_0) v_{\tilde{b}l}(\tilde{\mathbf{y}}; y_0) \delta_{\tilde{\beta}\beta}\delta_{\tilde{l}l}\delta(\tilde{y_0} - y_0) v_{bl}(\mathbf{y}; y_0)^* \\ = \left\langle \sum_d \sum_k v_{ak}(\mathbf{x}; x_0)\tau^d_{\alpha k}(x_0)\varrho^d_{b\beta}(\mathbf{y}, y_0)^* \right\rangle_\eta &= \left\langle \sum_d \varphi^d_{a\alpha}(\mathbf{x}, x_0)\varrho^d_{b\beta}(\mathbf{y}, y_0)^* \right\rangle_\eta , \end{aligned} \tag{4.28}$$

where the "distilled-stochastic-dilluted" perambulator is

$$\tau^d_{\alpha k}(x_0) = \left[\sum_{\tilde{\mathbf{x}},\tilde{a}} v_{\tilde{a}k}(\tilde{\mathbf{x}}; x_0)^* \sum_{\tilde{\beta},\tilde{y_0}} \sum_{\tilde{\mathbf{y}},\tilde{b}} D^{-1}_{\alpha\tilde{\beta},\tilde{a}\tilde{b}}(\tilde{\mathbf{x}}, x_0; \tilde{\mathbf{y}}, \tilde{y_0}) \varrho^d_{\tilde{b}\tilde{\beta}}(\tilde{\mathbf{y}}, \tilde{y_0}) \right]. \tag{4.29}$$

We also implicitly defined the *source* vector

$$\varrho^d_{b\beta}(\mathbf{y}, y_0) \equiv \sum_l v_{bl}(\mathbf{y}; y_0) \sum_{\sigma,n,w_0} P^d_{\beta\sigma,ln}(y_0, w_0)\eta_{\sigma n}(w_0) = \sum_l v_{bl}(\mathbf{y}; y_0) \left(P^d\eta\right)_{\beta l}(y_0) \tag{4.30}$$

and the *sink* (or solution) vector

$$\varphi^d_{a\alpha}(\mathbf{x}, x_0) \equiv \sum_k v_{ak}(\mathbf{x}; x_0) \left[\sum_{\tilde{\beta}, \tilde{y_0}} \sum_{\tilde{\mathbf{x}}, \tilde{a}} v_{\tilde{a}k}(\tilde{\mathbf{x}}; x_0)^* \sum_{\tilde{\mathbf{y}}, \tilde{b}} D^{-1}_{\alpha\tilde{\beta}, \tilde{a}\tilde{b}}(\tilde{\mathbf{x}}, x_0; \tilde{\mathbf{y}}, \tilde{y_0}) \varrho^d_{\tilde{b}\tilde{\beta}}(\tilde{\mathbf{y}}, \tilde{y_0}) \right] \tag{4.31}$$

with noise index omitted in τ, η, ϱ and φ. Notice that now the source indices in τ are taken into account by the action of the P^d. Finally, the Monte Carlo estimator is

$$\hat{S}_{ab,\alpha\beta}(x, y) = \frac{1}{N_\eta} \sum_{r=1}^{N_\eta} \sum_d \varphi^d_{a\alpha}(\mathbf{x}, x_0) \varrho^d_{b\beta}(\mathbf{y}, y_0)^* \tag{4.32}$$

and (4.23) still holds. We can simplify the notation, hiding space-colour-spin indices, so that the propagator is expressed as

$$S(x_0, y_0) = \left\langle \sum_d \varphi^d(x_0) \varrho^d(y_0)^\dagger \right\rangle_\eta . \tag{4.33}$$

Meson Fields

The notation introduced using the source and sink vectors (4.30),(4.31) is the most general form of distillation presented in this work, such that we use it for both exact and stochastic/diluted versions. Exact distillation is recovered from (4.33) by choosing the full-dilution projector of the form

$$P^d = \delta(x_0 - y_0) \delta_{\alpha\beta} \delta_{kl}, \tag{4.34}$$

and using a single pseudo-noise vector

$$\eta_{\alpha k}(x_0) \equiv 1. \tag{4.35}$$

Another useful building block within the distillation method applied to mesonic systems is called *meson field*. To obtain it in a generic distillation notation, we rewrite our trial correlation function (4.2) in terms of source and sink vectors and group them

into distillation space matrices $\mathcal{M}$

$$\begin{aligned} C(x_0, y_0) &= -\sum_{d_1,d_2} \mathrm{tr}\left[\varrho^{d_1}(y_0)^\dagger \Gamma_1 \varphi^{d_2}(y_0)\ \varrho^{d_2}(x_0)^\dagger \Gamma_2 \varphi^{d_1}(x_0)\right] \\ &= -\sum_{d_1,d_2} \mathcal{M}_{\gamma^5}^{d_1 d_2}(\varrho\varphi; y_0)\ \mathcal{M}_{\gamma^5}^{d_2 d_1}(\varrho\varphi; x_0), \end{aligned} \tag{4.36}$$

where eventual averages over noise vectors are omitted. The meson field is

$$\mathcal{M}_\Gamma^{d_1 d_2}(\varrho\varphi; y_0) \equiv \varrho^{d_1}(y_0)^\dagger \Gamma \varphi^{d_2}(y_0) \tag{4.37}$$

and their source-sink structure can be swapped around by using γ^5-Hermiticity at the correlator level, yielding the variations $\mathcal{M}_\Gamma(\varrho\varphi; t)$, $\mathcal{M}_\Gamma(\varphi\varphi; t)$ and $\mathcal{M}_\Gamma(\varrho\varrho; t)$. In this work, we will deal mostly with $\mathcal{M}_\Gamma(\varrho\varphi; t)$ due to our computational setup, *cf.* 4.3.2, C.2.

4.3 Variational Method

Even though we devised smeared interpolators to improve the overlap onto low-lying states, this was demonstrated to not be enough to reliably extract such states,[169] which is fundamental for the computation of hadronic resonances on the lattice. In view of the spectral decomposition (4.5), imagine that one could find N optimal interpolators such that the overlaps

$$\langle 0|O_i|n\rangle \approx a_i^n \delta_{ni}, \qquad i = 1, \ldots, N, \tag{4.38}$$

would provide an approximate one-to-one map between them and the states $|n\rangle$, and thus

$$\langle O_i(t) O_j(0)^\dagger \rangle \approx \delta_{ij} |a_i^i|^2\, e^{-E_i t}. \tag{4.39}$$

It would then be straightforward to extract the energy for the target state $m = 1, \ldots, N$, which is not a simple task if m appears in a subleading term of a noisy exponential series, *e.g.* not the ground state. This can also be phrased as a *variational problem*: given a lattice Hamiltonian, find O_i such that $\langle 0|O_i|n\rangle - a_i^n \delta_{ni}$ is minimised.

This idea can be implemented by the use of a *generalised eigenvalue problem* (GEVP), where the computation of the two-point functions of N operators gives one access to the lowest N states. The GEVP has been in the lattice QCD literature at least since the 1980's,[155,170,171] but it was the invention of methods such as distillation allied

to the increase of sheer computational power that allowed the unlocking of its full potential.[30]

4.3.1 Generalised eigenvalue problem

Using distillation, we have now access to a $N \times N$ correlation matrix [IV]

$$C_{ij}(t) = \langle O_i(t) O_j(0)^\dagger \rangle \,, \tag{4.40}$$

which effectively builds a N-dimensional *variational basis* of operators. The generalised indices i, j collectively label the bilinear content and momentum projections, *cf.* Table 4.3. It can be shown that this problem is asymptotically restricted to the subspace spanned by the low-lying N states of the system.[155] The optimised operators in (4.39) are then obtained through a diagonalisation procedure in which the states above N are treated as a perturbation. More specifically, the eigenvalues $\lambda_n(t)$ of $C(t)$ will behave asymptotically as[155]

$$\lambda_n(t) \xrightarrow[t\to\infty]{} b_n e^{-tE_n}, \qquad n = 1, \ldots, N, \tag{4.41}$$

with corrections exponentially suppressed in time by the smallest energy gap from E_n, *i.e.* of order $\mathcal{O}(e^{-t\Delta E_n})$.

To see how this works by induction in N, consider the simpler eigenvalue problem. Following Ref. [155], the N-truncated spectral sum in matrix notation is [V]

$$C^N(t) = \sum_{n=1}^{N} a^n a^{n\dagger} e^{-E_n t} = A^N \mathcal{E}^N(t) A^{N\dagger}, \tag{4.42}$$

where $\mathcal{E}^N(t) = \mathrm{diag}(e^{-E_1 t}, \ldots, e^{-E_N t})$ and A^N is a matrix whose n^{th} column is the vector a^n. Note that $C^1 \propto e^{-tE_1}$ automatically satisfies (4.41) and thus the base case is established. The inductive step for the property (4.41) is shown by splitting the $N+1$ correlator as

$$C^N(t) = C^{N+1}_{(0)}(t) + C^{N+1}_{(1)}(t) = A^N \mathcal{E}^{N+1}_{(0)}(t) A^{N\dagger} + A^N \mathcal{E}^{N+1}_{(1)}(t) A^{N\dagger}, \tag{4.43}$$

[IV] We drop the ˜ to represent the momentum-projected correlator and abstract its arguments into the indices i, j.

[V] Specifically in this section, we use E_1 as the ground state for simplicity, while elsewhere it will be E_0.

where $\mathcal{E}^{N+1}_{(0)}(t) = \text{diag}(e^{-E_1 t}, \ldots, e^{-E_N t}, 0)$ and $\mathcal{E}^{N+1}_{(1)}(t) = \text{diag}(0, \ldots, 0, e^{-E_{N+1} t})$. Note that the set of vectors composed by the canonical basis of C^N embedded in $N+1$ *and* $v_i = \delta_{i,N+1}$ can be used to write $C^{N+1}_{(0)}$ as

$$C(t) = \begin{pmatrix} & & 0 \\ & (C^N) & \vdots \\ & & 0 \\ 0 & \ldots & 0 \end{pmatrix}, \tag{4.44}$$

in such a way that the N first eigenvalues $\lambda^{(0)}_n$ of $C^{N+1}_{(0)}$ follow from the hypothesis (4.41), and $\lambda^{(0)}_{N+1} = 0$ by construction. The crucial point now is that

$$||C^{N+1}_{(1)}|| = ||a^{(N+1)} a^{(N+1)\dagger}|| e^{-E_{N+1} t} \leq \min_{\forall n \neq m} |\lambda^{(1)}_n(t) - \lambda^{(1)}_m(t)|, \tag{4.45}$$

implying that $||C^{N+1}_{(1)}||$ is asymptotically bounded and can be treated as a perturbation to $C^{N+1}_{(0)}$ for large enough t. Standard non-degenerate perturbation theory yields the property (4.41) for C^{N+1}, as we wanted. This procedure assumes the operators are all linearly independent in order to render the correlator matrices non-singular.

Given the considerations above, we can use the eigenvalues of a $N \times N$ correlator matrix to asymptotically extract the N lowest energies with (4.41). The more used version of this method is the *generalised* eigenvalue problem (GEVP)

$$C(t) u_n(t, t_0) = \lambda_n(t, t_0) C(t_0) u_n(t, t_0), \qquad n = 1, \ldots, N, \tag{4.46}$$

where t_0 is chosen as a fixed value. This can be transformed into a regular eigenvalue problem whose unperturbed eigenvalues obey $\lambda^{(0)}_i = e^{-E_i(t-t_0)}$ and the perturbed ones converge faster to the log-energy E_i for large enough t_0.[155] Through explicit perturbation theory, in Ref. [156] it was shown that the first order correction to the eigenvalues is $\mathcal{O}(e^{-t(E_{N+1}-E_i)})$, *i.e.* controlled by the larger gap to the state $N+1$ and independent of t_0. However, at fixed t_0 and asymptotic t, the second order correction is $\mathcal{O}(e^{-t\Delta E_i})$ and a method was proposed to tackle this, where t_0 is chosen such that this second-order correction is suppressed. In our case, it is observed that the regime in t where the "pessimistic" correction $\mathcal{O}(e^{-t\Delta E_i})$ dominates is not reached before the signal-to-noise becomes an issue, as long as t_0 is chosen appropriately, *cf.* Sec. 4.4.2.

4.3.2 Correlator measurement

The present calculation relies on how well we can extract the correlator matrix used in the GEVP. In particular, the choice of a basis of linearly independent operators is crucial for the variational method. In general, it is not obvious when the addition of a certain type of operator will be beneficial, because controlling the noise introduced and the size of the relative overlaps in the spectral decomposition is a completely non-trivial task. Nevertheless, an almost conventional prescription for the general operator building exists in the literature.[91,169]

Single-bilinear interpolators

The building blocks for our operator basis come from the bilinear operators based on the $SU(3)_f$ quark model. We start from fields corresponding to the u, d, s quarks and, *after* the Wick contractions, take the isospin limit where u, d have the same *light* mass, *cf.* Table 4.1

$$m_u = m_d \equiv m_l. \tag{4.47}$$

We start by choosing a minimal combination of quark fields interpolating the pseudoscalar light-light and light-strange channels corresponding to the pion and kaon. After taking the isospin limit, degeneracies coming from the use of different I_3 will not matter for our lattice calculation, as long as all relevant contractions are taken into account, *cf.* Sec. 4.3.2.

The vector resonances K^* and ρ show up at total isospin $I = 1/2$ and $I = 1$, respectively, and thus we choose

$$O_{K^{*+}}(x) = \bar{s}(x)\gamma^i u(x), \tag{4.48}$$

$$O_{\rho^+}(x) = -\bar{d}(x)\gamma^i u(x) \tag{4.49}$$

as corresponding single-particle interpolators. The γ^i is the simplest choice for meson operators transforming as vectors under the Lorentz group.

As we are working with $K\pi$ and $\pi\pi$ scattering in P-wave, we write down the standard

pseudoscalar bilinears with respectively $I = 1/2$ and $I = 1$,

$$O_{K^+}(x) = \bar{s}(x)\gamma^5 u(x), \tag{4.50}$$

$$O_{K^0}(x) = \bar{s}(x)\gamma^5 d(x), \tag{4.51}$$

$$O_{\pi^+}(x) = -\bar{d}(x)\gamma^5 u(x), \tag{4.52}$$

$$O_{\pi^0}(x) = \frac{1}{\sqrt{2}}\left[\bar{u}(x)\gamma^5 u(x) - \bar{d}(x)\gamma^5 d(x)\right], \tag{4.53}$$

from the appropriate combination of $SU(3)_f$ representations involving u, d and s quarks. These operators will yield the kaon and pion masses but also will be combined into non-local interpolators.

Double-bilinear interpolators

It was shown in several works that the inclusion of only single-bilinear operators is not enough for resolving two-particle states.[91,169] Far from resonant energies, this is due to the volume-suppression of the overlaps, *e.g.* $\langle 0|O_{K^{*+}}|K\pi\rangle$, since (4.48) is a local operator. It was proven necessary to include double-bilinears containing two independent momentum sums over the whole spatial lattice.

The inclusion of double-bilinears is also important for resolving the states around a resonance mass. A heuristic model for this was given in Ref. [134], where a two-particle state located roughly within the width of a resonance will strongly mix with an associated finite-volume state. This happens near the level avoidances in Fig. 3.3 when the spectrum becomes near-degenerate. In that case, without the inclusion of both operators, the log-mass will take an unreasonable amount of time to decay to the lowest energy even after the GEVP.

We implement double-bilinears by combining the pion and kaon operators (4.50) through a standard isospin sum. The K,π are combined into the $I = 1/2$ representation in $1/2 \otimes 1$

$$O_{K\pi^+}(x,y) = -\sqrt{\frac{1}{3}}O_{K^+}(x)O_{\pi^0}(y) + \sqrt{\frac{2}{3}}O_{K^0}(x)O_{\pi^+}(y), \tag{4.54}$$

and the π's into the $I = 1$ representation in $1 \otimes 0$

$$O_{\pi\pi^+}(x,y) = \sqrt{\frac{1}{2}}O_{\pi^+}(x)O_{\pi^0}(y) - \sqrt{\frac{1}{2}}O_{\pi^0}(x)O_{\pi^+}(y). \tag{4.55}$$

In momentum space, these will yield several linearly independent operators with different combinations of individual momenta on each lattice irrep.

Wick contractions

Using the lattice QCD path integral (2.38),

$$\left\langle O(x)O(y)^\dagger \right\rangle = \int \mathcal{D}U\mathcal{D}\bar{\Psi}\mathcal{D}\Psi\mathcal{D}\Phi^\dagger\mathcal{D}\Phi\; O(x)O(y)^\dagger e^{-S_G[U]-S_\mathsf{F}[U,\bar{\Psi},\Psi,\Phi^\dagger,\Phi]}, \tag{4.56}$$

where the interpolators O only involve the near-chiral quarks at the boundaries of the domain wall, *cf.* Sec. 2.3.2. In particular, S_F is bilinear in the fermion fields so that we can explicitly integrate them out using Wick's theorem[78]

$$\left\langle O(x)O(y)^\dagger \right\rangle = \int \mathfrak{D}U e^{-S_\text{eff}[U]} \sum_{i\in\text{Wick}} \left\langle O(x)O(y)^\dagger \right\rangle_\mathsf{F}^i, \tag{4.57}$$

where all possible quark contractions are summed over and S_eff corresponds to an action containing the exponentiated pseudofermion determinants. In a Monte Carlo calculation, the path integral has been taken into account by the HMC in a previous step independently of this work.[74] Once the given gauge configurations are fixed, we measure the Wick contractions $\left\langle O(x)O(y)^\dagger \right\rangle_\mathsf{F}^i$ on each of them and compute the full correlator using the sample average (2.47), usually called *gauge average*.

For a correlation function involving a single bilinear operator such as in (4.48), there is only one possible contraction

$$\langle O_{\rho^+}(x)O_{\rho^+}(z)^\dagger\rangle_\mathsf{F} = -\operatorname{tr}\left[\gamma^i S(x,z)\gamma^i S(z,x)\right], \tag{4.58}$$

where we took the isospin limit.

Using distillation notation for the propagator in (4.33) (hiding the summation and averages)

$$S(x,z) = \varphi(x)\varrho(z)^\dagger, \tag{4.59}$$

we get

$$\langle O_{\rho^+}(x)O_{\rho^+}(z)^\dagger\rangle_\mathsf{F} = -\operatorname{tr}\left[\gamma^i\varphi^{(l)}(x)\varrho(z)^\dagger\gamma^i\varphi^{(l)}(z)\varrho(x)^\dagger\right] = -\operatorname{tr}\left[\mathcal{M}_{\gamma^i}^{(l)}(x)\mathcal{M}_{\gamma^i}^{(l)}(z)\right], \tag{4.60}$$

where the last trace is taken over dilution indices instead of colour and spin. The

meson building block $\mathcal{M}$ is defined in (4.37) and has the dimension of the dilution spaces combined, $N_S N_T N_L$.

We will be interested in correlators in momentum space, such that we use instead

$$\mathcal{M}(\mathbf{p}, t) = \int d^3x \, e^{-i\mathbf{p}\cdot\mathbf{x}} \mathcal{M}(\mathbf{x}, t) \tag{4.61}$$

to compute, for example,

$$\langle O_{\rho^+}(\mathbf{p}, t) O_{\rho^+}(\mathbf{q}, 0)^\dagger \rangle_{\mathsf{F}} = -\operatorname{tr}\left[\mathcal{M}^{(l)}_{\gamma^i}(\mathbf{p}, t)\mathcal{M}^{(l)}_{\gamma^i}(\mathbf{q}, 0)\right] = -$$

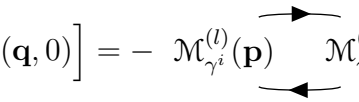

, (4.62)

up to a momentum-conservation delta $\delta(\mathbf{p} + \mathbf{q})$. In the graphical notation, the lines represent matrix products and the closed loops represent a trace over dilution space.

Correlator matrix

In order to build a correlator matrix, we contract all the operators above in each channel of interest. This quickly becomes a tedious bookkeeping task, especially for double-bilinear interpolators. One eventually uses an automated tool to perform algebraic simplifications.[172] In the isospin limit and for total momentum $\mathbf{P}$, the resulting $K\pi^{I=1/2}$ Wick contractions are

$$\langle O_{K^{*+}}(\mathbf{P}, t) O_{K^{*+}}(-\mathbf{P}, 0)^\dagger \rangle_{\mathsf{F}} = -$$

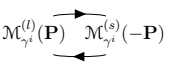

, (4.63)

$$\langle O_{K\pi^+}(\mathbf{p}_1, \mathbf{p}_2, t) O_{K^{*+}}(-\mathbf{P}, 0)^\dagger \rangle_{\mathsf{F}} = \sqrt{\frac{3}{2}} \operatorname{Im}$$

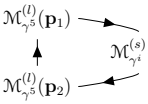

, (4.64)

$$\langle O_{K\pi^+}(\mathbf{p}_1, \mathbf{p}_2, t) O_{K\pi^+}(\mathbf{p}'_1, \mathbf{p}'_2, 0)^\dagger \rangle_{\mathsf{F}} =$$

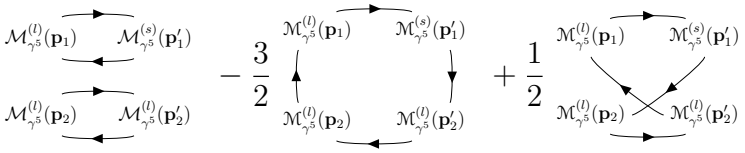

, (4.65)

and the $\pi\pi^{I=1}$ ones are

$$\langle O_{\rho^+}(\mathbf{P},t)O_{\rho^+}(-\mathbf{P},0)^\dagger\rangle_{\mathsf{F}} = -$$ 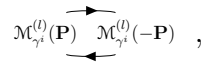 , (4.66)

$$\langle O_{\pi\pi^+}(\mathbf{p}_1,\mathbf{p}_2,t)O_{\rho^+}(-\mathbf{P},0)^\dagger\rangle_{\mathsf{F}} = 2\ \mathrm{Im}$$ 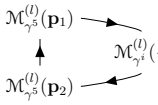 , (4.67)

$$\langle O_{\pi\pi^+}(\mathbf{p}_1,\mathbf{p}_2,t)O_{\pi\pi^+}(\mathbf{p}_1',\mathbf{p}_2',0)^\dagger\rangle_{\mathsf{F}} = -$$ 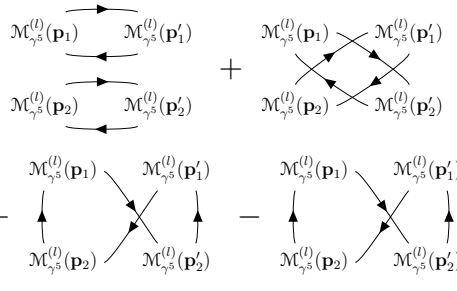 (4.68)

Each term is given on a single gauge configuration and a collection of them is used to form the gauge average and also to estimate errors using the bootstrap method, *cf.* A.1.

We use the freedom of choosing an arbitrary phase to take only the non-zero part of the $\pi\pi$-ρ correlator under gauge average, which can be shown to be purely imaginary using a combination of charge conjugation and γ^5-hermiticity,[173] while all other diagrams are purely real. Some of the $\pi\pi$-$\pi\pi$ diagrams can be further simplified under gauge average via parity,[174] but as we have access to all diagrams with small overhead through distillation, we explicitly compute all of them as above.

The correlators above lead to a triangular correlator matrix. From the time-reversal property of the interpolators, it can be shown that the complete correlator matrix is Hermitian under gauge average. Because we chose the arbitrary global phases of each correlator such that such a matrix is real, we thus symmetrise the triangular component to reach the full matrix used in the GEVP. In the $K\pi^{I=1/2}$ case, for example, it takes the form

$$C_{\mathbf{P}} = \begin{pmatrix} \langle O_{(1)}O_{(1)}^\dagger\rangle & \langle O_{(1)}K\pi_{(1)}^\dagger\rangle & \dots & \langle O_{(1)}K\pi_{(n)}^\dagger\rangle \\ \langle K\pi_{(1)}O_{(1)}^\dagger(1)\rangle & \langle K\pi_{(1)}K\pi_{(1)}^\dagger\rangle & \dots & \dots \\ \vdots & \vdots & \ddots & \langle K\pi_{(n-1)}K\pi_{(n)}^\dagger\rangle \\ \langle K\pi_{(n)}O_{(1)}^\dagger\rangle & \dots & \langle K\pi_{(n)}K\pi_{(n-1)}^\dagger\rangle & \langle K\pi_{(n)}K\pi_{(n)}^\dagger\rangle \end{pmatrix}, \quad (4.69)$$

where the indices stand for the possible momentum assignments.

Finally, notice that we built a correlator matrix using interpolators with continuum

rotational symmetry, which is broken on a finite lattice. Using the techniques described in Sec. 2.5, especially the operator projection formula (2.71), we build operators transforming according to the appropriate irreps of the octahedral symmetry group and subgroups. The allowed irreps and momentum assignments used in this work are detailed in Sec. 4.4.2.

4.4 Data Extraction

We now unveil the extraction of lattice QCD data done in this work. This corresponds to implementing many of the techniques outlined in this chapter, including distillation, operator projection and GEVP. The domain-wall fermion ensemble used throughout is summarised in Table 4.1

$N^3 \times N_t$	a	L	$m_\pi L$	am_π	am_K
$48^3 \times 96$	≈ 0.114 fm	5.476(2) fm	3.863(5)	138.5(2) MeV	498.9(4) MeV

Table 4.1 *Physical point domain wall $N_f = 2 + 1$ ensemble used in this work.*[74]

A scattering calculation at the physical point is quite demanding and it was thus divided into two phases: exploration and production. The exploration (Sec. 4.4.1) contains a study of the smearing radius as well as the first tests of the code developed in this work.

We implemented the distillation method within the workflow management system `Hadrons`[4,175] on top of the `C++` lattice library `Grid`, which efficiently implements domain-wall fermions and other general lattice utilities.[176] In this initial phase, we explored several distillation setups at low statistics (10 gauge configurations) to decide the most appropriate course to take.

In the production phase, we adopted a single distillation setup (exact, $N_{\text{vec}} = 64$) and employed it on all 90 gauge configurations of the ensemble in Table 4.1, where the pion and kaon masses are determined in Ch. 5 and given in physical units through the (inverse) lattice spacing $a^{-1} = 1.7295(38)$ GeV.[74] This amounted to the measurement of perambulators on *every* time slice and corresponds to the maximum number of correlator time translations one can get. The computations were performed daily at the Edinburgh-based STFC DiRAC Extreme Scaling service for one entire year.

4.4.1 Distillation tests

As we mentioned in Sec. 4.1, the goal of smearing is to provide hadronic sources that will interpolate well the low-energy hadron states. The main way of doing this is by shaping it with a characteristic scale.

Smearing profile

Distillation projects the spatial degrees of freedom onto three-dimensional Laplacian space spanned by its N_{vec} low-lying eigenvectors. One can preliminarily study its smearing effects through the norm

$$\Psi(r) = \mathcal{N}^{-1} \sum_{\hat{\mathbf{i}},\mathbf{r},t} \sqrt{\operatorname{tr} \Box(\mathbf{r}, \mathbf{r}+\hat{\mathbf{i}}; t)\Box(\mathbf{r}+\hat{\mathbf{i}}, \mathbf{r}; t)}, \tag{4.70}$$

interpreted as the spatial deformation made by distillation to a point source. The normalisation $\mathcal{N} = \Psi(0)$ is chosen so that $\Psi(0) = 1$ and $|\mathbf{r}| = r$ is given in lattice units. In Fig. 4.2a, we observe that the spatial profile becomes narrower as N_{vec} increases.

This localisation of the smearing profile is expected as we are adding more base functions to the expansion in the three-dimensional Laplacian basis, with the limit of a point source at the maximum value of N_{vec} allowed in this lattice. Intuitively, increasing N_{vec} might be important to efficiently project excited energies only a couple of levels above the ground state, with hadrons at non-zero momenta. On the other hand, the overlap of our smeared operator to highly-excited states will reduce in a non-trivial way as N_{vec} is decreased. At some point, the contribution to states close to the cutoff will be affected as well, eventually resulting in a deterioration of the signal-to-noise ratio.

We assign a characteristic length to each profile by defining the smearing radius R through the 68.3% interval around the origin [VI]

$$\int_0^R \Psi(r)dr = 0.683 \int_0^{L/2a} \Psi(r)dr, \tag{4.71}$$

which can be numerically evaluated with a trapezoidal rule. We observe its dependence on N_{vec} to be approximately described by a power law with exponent $b \approx -0.25$

[VI] Equivalent to one standard deviation (sigma) interval in the case of a Gaussian distribution.

(Fig. 4.2b). We also observe an inflection point around $N_{\text{vec}} \sim 100$ which, in other words, means that the smearing radius reduces less drastically from around this value. Notice the dashed lines in Fig. 4.2a are Gaussian fits, which considerably deviate from the profile at large r. Defining the smearing radius through the Gaussian width does not drastically change the behaviour in Fig. 4.2b and thus the conclusion is not changed in any case.

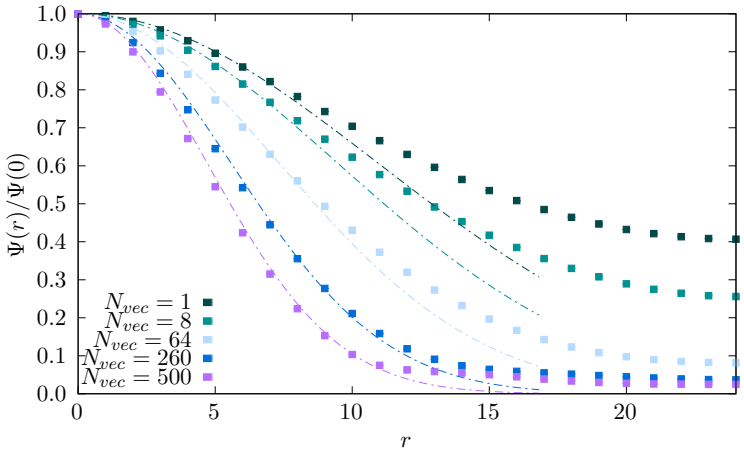

(a) *Smearing profile*

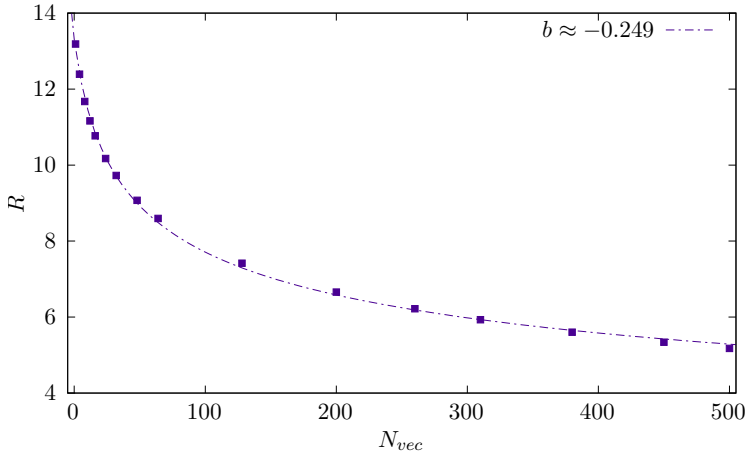

(b) *Smearing radius*

Figure 4.2 *Left: several distillation smearing profiles (negligible error bars omitted) for the various N_{vec} and the lines are Gaussian fits. Right: smearing radius defined in Eq. (4.71) as a function of N_{vec} and the line is the fit to $a(N_{\text{vec}} - c)^b$.*

N_{vec} and Cost Comparison

Given the cost of increasing N_{vec}, the power-law behaviour in (4.2b) motivated the study of simple observables at the region of $N_{\text{vec}} \sim 100$ using various distillation schemes in Table 4.2 at low statistics. Full spin and time dilution were used on the stochastic runs and LI corresponds to the number of diluted Laplacian sources

formed from every N_{vec}/LI eigenvector.[29] For the exact runs, the number of light and strange inversions per configuration per time source is $N_{\text{inv}} = 4\,N_{\text{vec}}$, while for the stochastic ones $N_{\text{inv}} = 2N_\eta LI$ with $N_\eta = 2$ stochastic noises.

In tests both on the smearing radius and here, there was little variation in the observed quantities for different stout-smearing parameters. We thus fixed our choice at a moderate level of link smearing, given by $\rho \equiv \rho_{ij} = 0.2$ with $n_{\text{stout}} = 3$ steps, *cf.* Sec. 4.1.

	$LI = 4$	$LI = 8$	$LI = 16$	$LI = 32$	exact	exact	exact
N_{vec}	64	64	64, 96, 128	64	20	40	64
N_{inv}	32	64	128	256	80	160	256

Table 4.2 *Distillation schemes explored, from exact distillation to stochastic distillation with Laplacian dilution.*

We first used light-strange vector correlators, *i.e.* Eq. (4.63) at several values of N_{vec} without any computational-cost normalisation. In Fig. 4.3a, using a cosh fit function

$$C_{\text{cosh1}}(t) = Z_0 \left(e^{-E_0 t} + e^{-(N_t - t)E_0}\right), \tag{4.72}$$

we tested the effectiveness of the momentum projection (4.61) by comparing E_0 at different moving frames through the continuum dispersion relation (Sec. 5.1). The reference fit ranges were taken from the exact distillation data with $N_{\text{vec}} = 64$.

Due to even-odd partial-wave mixing (Sec. 3.3) and the non-negligible overlap of bilinear operators to nearby $K\pi$ states, it is not expected that cosh effective mass

$$m_{\text{eff}}(t) = \operatorname{arccosh} \frac{C(t-1) + C(t-1)}{2C(t)} \tag{4.73}$$

will plateau to a definite finite-volume level before noise sets in. On top of that, we expect that the finite-volume corrections will be different on each moving frame due to different Lorentz contractions of the spatial box, even though such corrections will be small on our lattice. Nevertheless, at an early stage of the computation, a ground state fit served as a guide to the overall signal-to-noise properties of the data and the effectiveness of momentum projection.

The highlighted data points refer to exact distillation with $N_{\text{vec}} = 64$, where just gauge noise is present. In Fig. 4.3b, we show the cosh effective mass for the exact setup. The 12 time translations on each configuration were treated as independent

samples, which at low statistics was a simple way to estimate errors. Progressive binning of those was performed to check that conclusions did not change dramatically due to correlations.

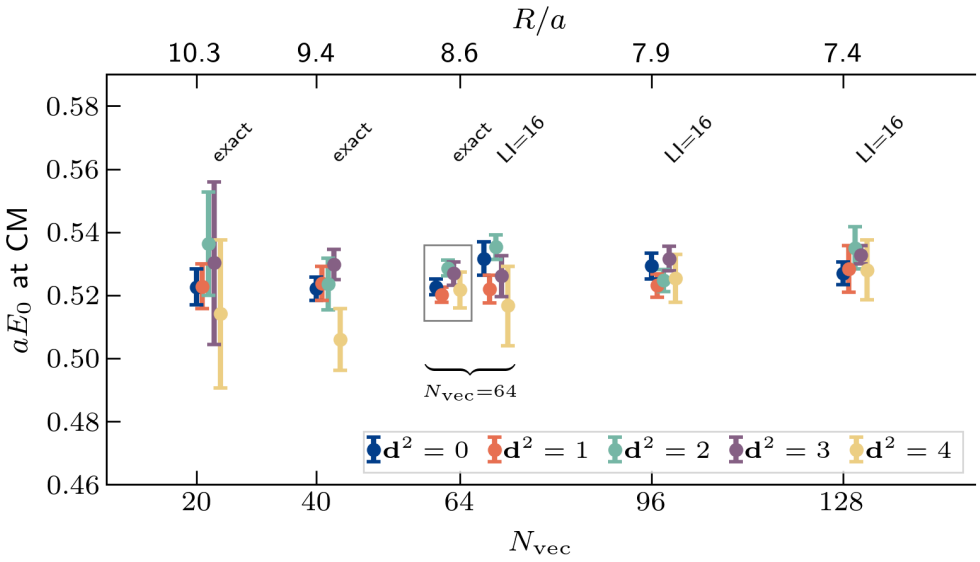

(a) *Fit result from several N_{vec}.*

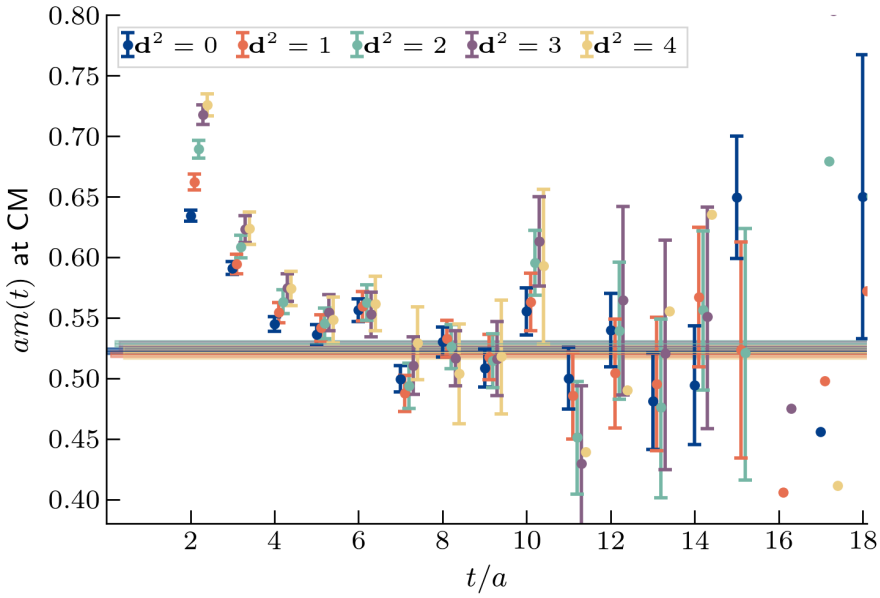

(b) *Effective masses for $N_{\text{vec}} = 64$ and exact distillation.*

Figure 4.3 *Left: fit result E_0 obtained from (4.72) against N_{vec} (or the smearing radius on the upper x-axis). Right: Effective mass for $N_{\text{vec}} = 64$, exact distillation and bands represent the E_0 fit results highlighted in Fig. 4.3a. Different colors represent different moving frames with total momentum $\mathbf{P} = 2\pi\mathbf{d}/L$. Data computed in moving frames (A_1 irreps) was boosted to the CM.*

$N_{\text{vec}} = 64$ - **exact vs. stochastic**

Having some level of confidence around the value $N_{\text{vec}} = 64$, we can also make a cost-comparison study of the exact and stochastic setups, varying the number of Laplacian-interlaced dilution sources LI at fixed N_{vec}.

We compare the cost-normalised error $\tilde{\sigma} = \sigma\sqrt{N_{\text{inv}}}$ between results of stochastic and exact distillation, where in the latter there is only gauge noise. The dashed lines on Fig. 4.4 are a reference for when only gauge noise would be present. As it is expected, lower values of LI tend to be quite above the gauge noise reference.

The noise on a single time slice (Fig. 4.4b) can be inflated by the stochastic noise but still yield overall good fit results when correlations are taken into account. We thus also plot the fit results E_0 in (4.4a). Regardless of the probe, as we increase LI, the convergence to the normalised gauge noise limit is very slow, and at $LI = 32$ the number of inversions is the same as in exact distillation. On a scattering workflow, the number of noises would be increased to at least 4 to avoid bias in multi-particle correlators and the stochastic runs would cost twice as much.

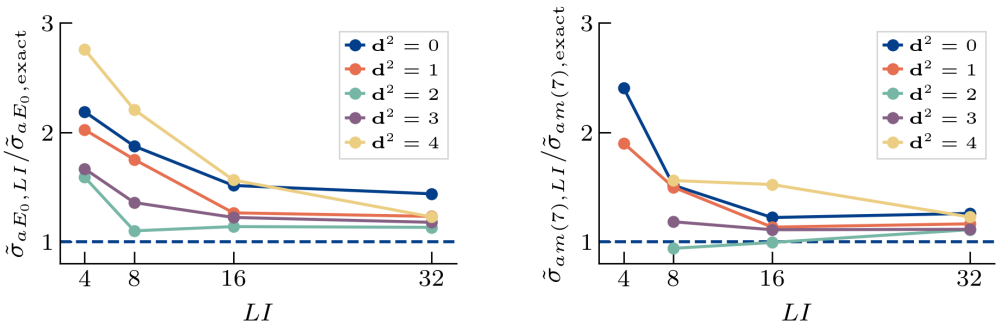

(a) **(b)**

Figure 4.4 *Cost-normalised error ($\tilde{\sigma} = \sigma\sqrt{N_{\text{inv}}}$) ratio between stochastic and exact distillation for $N_{\text{vec}} = 64$. The dashed line represents the gauge-noise limit (exact distillation). Left: fit result E_0. Right: effective mass at source-sink separation $t = 7$.*

In the sections above, we observed that the smearing with $N_{\text{vec}} = 64$ satisfactorily momentum-projects single-particle operators at different moving frames and that increasing value is not particularly beneficial at the correlator level. We also note that the stochastic setups with an increasing number of diluted-interlaced Laplacian sources and $N_\eta = 2$ do not present better cost-signal than on the exact setup at

$N_{\text{vec}} = 64$, in our case. At this point, we further computed a preliminary GEVP which also indicated a sensible extraction of the correlators,[1] later superseded by the results in Sec .4.4.2. A posteriori, we confirm that the value $N_{\text{vec}} = 64$ at full statistics is indeed a good compromise between cost and statistically precise extraction of physics.

4.4.2 Variational spectrum

Based on (4.40) and (4.46), we build correlator matrices $C_{ij}^{\Lambda[\mathbf{d}],r}$ where the operators were projected to the lattice irreps detailed in Table 4.3. The projection is done by combining the correlators in Sec. 4.3.2 in such a way that they contain contributions from operators projected according to (2.71) to a single irrep, row and total momentum.

$K\pi^{I=1/2}$	
$T_{1u}[000]$	[001][00-1], [110][-1-10], [111][-1-1-1], [002][00-2]
$E[001]$	[101][-100], [-100][101], [1-11][-110], [-110][1-11]
$B_1[110]$	[10-1][011], [111][00-1], [00-1][111]
$B_2[110]$	[100][010], [011][10-1], [-110][200], [200][-110]
$E[111]$	[101][010], [010][101], [1-11][020], [020][1-11]
$E[002]$	[011][0-11], [1-11][-111]
$\pi\pi^{I=1}$	
$T_{1u}[000]$	[001][00-1], [110][-1-10], [111][-1-1-1], [002][00-2]
$E[001]$	[101][-100], [1-11][-110]
$B_1[110]$	[10-1][011], [111][00-1]
$B_2[110]$	[100][010], [011][10-1], [-110][200]
$E[111]$	[101][010], [1-11][020]
$E[002]$	[011][0-11], [1-11][-111]
$A_1[001]$	[000][001], [-100][101], [-1-10][111], [00-1][002]
$A_1[110]$	[000][110], [111][00-1], [200][-110]
$A_1[111]$	[111][000], [110][001], [11-1][002]
$A_1[002]$	[000][002], [001][001]

Table 4.3 *Reference momentum assignments of two-bilinear operators in the corresponding lattice irreps they were projected into.*

We computed all possible distillation meson fields with momenta up to $\mathbf{d}^2 = 4$, which gives us access to correlators in the corresponding moving frames. As $\mathbf{d}^2$ increases,

the number of possible combinations of two-particle momenta also increases and allows for a reasonable amount of averaging of equivalent correlators corresponding to different directions $\mathbf{d}$, *cf.* Sec. 2.5. In D.3.4, we show how the signal-to-noise in the effective mass changes with the inclusion of all possible averages.

On the other hand, in some operator bases we have interpolators whose momentum assignments correspond to non-interacting energies,

$$(E^*_{\mathsf{free}})^2 = \left(\sum_i \sqrt{m_i^2 + (2\pi/L)^2 \mathbf{d}_i^2}\right)^2 - \mathbf{P}^2, \quad m_i \in \{m_\pi, m_K\} \tag{4.74}$$

lying higher in the spectrum than other ones including a $\mathbf{d}^2 > 4$ interpolator, as illustrated in Figs. D.3a,D.3b. Additionally, there can also be three- or four-particle non-interacting energies lying lower in the spectrum than the ones corresponding to two-bilinear operators we employ. Our criterion to determine the N^{lev} energies going into the later analysis in Sec. 5.3.1 is that we exclude all the ones lying at or above the lowest non-interacting energy whose operator we do not employ. In this way, we avoid using levels with potentially significant overlaps to such "missing" operators. We also do not use the levels on top or above the inelastic $K\eta$ and $K\bar{K}$ thresholds, respectively in the $K\pi^{I=1/2}$ and $\pi\pi^{I=1}$ channels. This results in $N^{\mathsf{lev}} = 13, 21$, respectively for $K\pi^{I=1/2}, \pi\pi^{I=1}$.

Note that in this first study, we leave out the irreps where odd and even continuum angular momentum ($l = 0, 1$ for us) mix.[113] This happens only for $K\pi$ scattering with $\mathbf{d}^2 > 0$ because in this case parity is not a good symmetry anymore, *i.e.* the subduction of such irreps (the A_1's, *cf.* Table2.3) does not preserve the separation of S and P-wave from the continuum.

We employ the GEVP method where t_0 is kept fixed in (4.46) and the problem is solved on each t. In Ch. 5, we directly use the GEVP eigenvalues to extract energy levels, though it is useful to define the log-mass

$$m_{n,\mathsf{eff}}(t; t_0) = \log \frac{\lambda_n(t; t_0)}{\lambda_n(t+1; t_0)}, \qquad n = 0, \ldots, N-1, \tag{4.75}$$

to get a visualisation of the GEVP data closer to a spectrum representation. In Fig. 4.5, we show particular examples of effective masses, where the plateaux signal saturation of the spectral decomposition (4.5) by a single state.

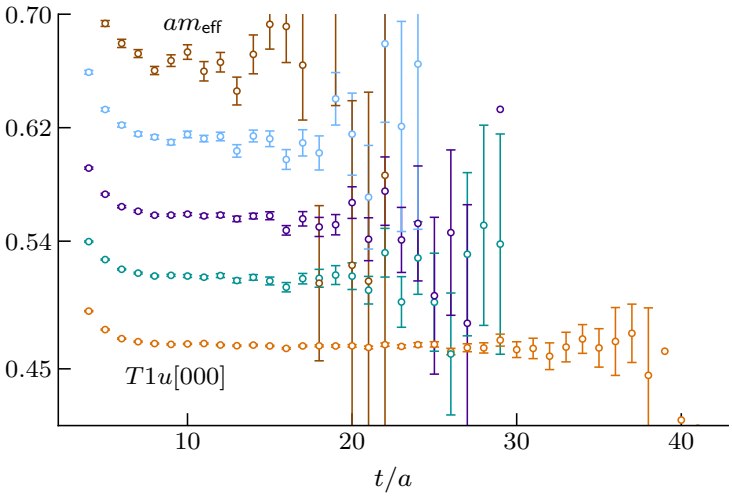

Figure 4.5 *Finite-volume effective masses in the T_{1u} irrep of the $K\pi^{I=1/2}$ channel. The GEVP parameter is fixed at $t_0 = 3$. For detailed $K\pi$ and $\pi\pi$ plots, cf. D.3.1.*

Fixed-t_0 stabilisation

In principle, the asymptotic behaviour (4.41) takes place on the limit of large t, t_0 and thus we must judiciously choose t_0. For a fixed t_0, its value needs to be large enough so that the correlator matrix is not dominated by excited states with $n > N$, meaning that the imposed orthogonality (4.80) is a good approximation for the complete spectrum. However, using too large t_0 will feedback noise from $C(t_0)$ into the solution of the GEVP on every t. In practice, we check that for $t_0 = 3$ the effective spectra and the eigenvalue ordering are consistent.

We confirm this choice by varying t_0 in the interval $2 \leq t_0 \leq 4$ and observing how it affects the relative effective spectrum. In particular, we observe that choosing values close to $t_0 = 3$ cause virtually no change to the ratio of effective masses, *cf.* Fig. 4.6. We also check that this choice of t_0 does not inflict any level crossings in the regions we analyse the GEVP eigenvalues in the next chapter.

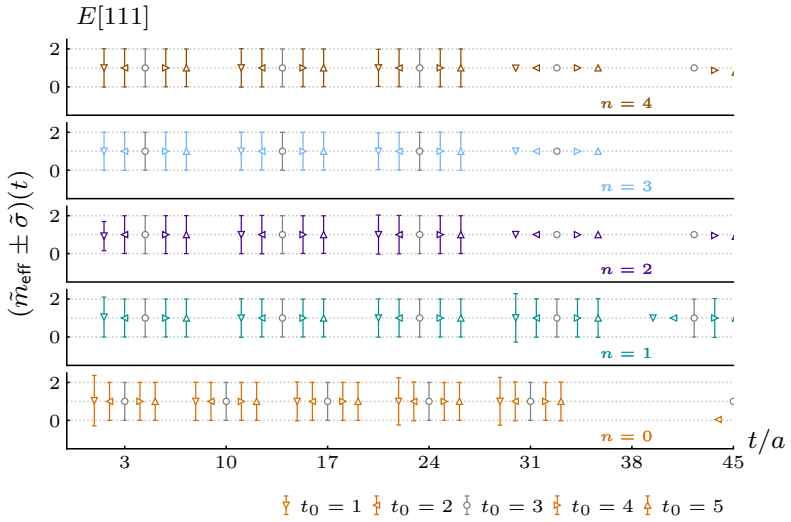

Figure 4.6 *Example of the ratios between $K\pi^{I=1/2}$ GEVP log effective masses $m_{\text{eff}}(t;t_0)$ and $m_{\text{eff}}(t;t_0^{\text{ref}}=3)$, i.e. $\tilde{m}_{\text{eff}}(t) \equiv m_{\text{eff}}(t;t_0)/m_{\text{eff}}(t;3)$. Analogously, the error bars are the ratios of the corresponding standard deviations, i.e. $\tilde{\sigma}(t) \equiv \sigma(t;t_0)/\sigma(t;3)$. We plot only every 7^{th} time slice for a clear but still overall visualisation of the time extension. For the entire spectrum of effective masses, see D.3.3.*

Eigenvector tracking

When we solve the GEVP for each t, the set of labels for the eigenvalues and eigenvectors at different t is not guaranteed to follow any particular order. We use an eigenvector tracking prescription which, for a given eigenvalue labeling on a bootstrap sample and time slice t, proposes a labeling for the next time slice $t+1$.[177] This is done by defining the different-times overlap

$$X_m^{(n)}(t) \equiv |u_n^\dagger(t) C(t_0) u_m(t+1)|, \tag{4.76}$$

where we suppressed the t_0 dependences. In a continuum-time limit, as the $t, t+1$ timeslices approach each other we have $X_\beta^{(\alpha)}(t) \to \delta^{\alpha\beta}$. Assuming a reasonable approximation to smooth time evolution of the eigenvectors, then we can define the relation

$$(n,t) \to (l,t+1) \quad \text{s.t.} \quad X_l^{(n)}(t) = \max_m X_m^{(n)}(t), \qquad n = 1,\ldots,N. \tag{4.77}$$

Defining an early reference time t_{ord} where the eigenvalue ordering by magnitude can be easily done, then the process above leads to a tracking of the eigenvalues by

induction over $t_{\mathsf{ord}}, t_{\mathsf{ord}+1}, \ldots$. We further normalise the correlation matrix as in

$$C_{ij}(t) \to C_{ij}(t)/\sqrt{C_{ii}(t_N)C_{jj}(t_N)} \tag{4.78}$$

at $t_N = 3$ in order to improve the numerical behaviour of the eigenvectors.

Overlap factors

The generalised eigenvalue problem can be transformed into a regular one via the Choleski decomposition $C(t_0) = LL^\dagger$ with $L = C(t_0)$ [VII],

$$[C(t_0)^{-1/2}C(t_0)C(t_0)^{-1/2}][C(t_0)^{1/2}u_n(t)] = \lambda_n(t;t_0)[C(t_0)^{1/2}u_n(t)], \tag{4.79}$$

which implies

$$u^{m\dagger}(t)C(t_0)u^n(t) = \delta^{mn} \tag{4.80}$$

instead of the usual orthogonality between eigenvectors.

Using the matrix notation where $\Lambda_{nm}(t) = \delta_{nm}e^{-E_n t}$ and $(u_n)_i \equiv u_{ni}$, the orthogonality above turns into $u^\dagger(t)C(t_0)u(t) = \mathbb{1}$. Note that we can use the spectral decomposition (4.5) up to state N in the orthogonality relation to get

$$u^\dagger(t)Z^\dagger\Lambda(t_0)Zu(t) = \mathbb{1} \tag{4.81}$$

which has a solution yielding the overlaps

$$Z = \Lambda(t_0)^{-1/2}u^{-1}(t) = \Lambda(t_0)^{-1/2}u^\dagger(t)C(t_0), \tag{4.82}$$

where Z retains a residual time-dependence from u due to the enforced orthogonality at early t. We can then estimate the overlaps $\langle 0 \,|\, O_i \,|\, n\rangle$ for each operator via the GEVP eigenvectors by defining the effective overlap

$$Z_{ni,\mathsf{eff}}(t) \equiv [u_n^\dagger(t)C(t_0)]_i \; e^{E_{n,\mathsf{eff}}(t)t_0/2} \tag{4.83}$$

which should converge to $\langle 0 \,|\, O_i \,|\, n\rangle$ for large enough t. The eigenvectors are assumed to be under a unique phase convention so that they can be resampled together. It is usually enough to pick the values of Z at say $t = 10$ for our case.

[VII] From time-reversal symmetry, C is Hermitian.

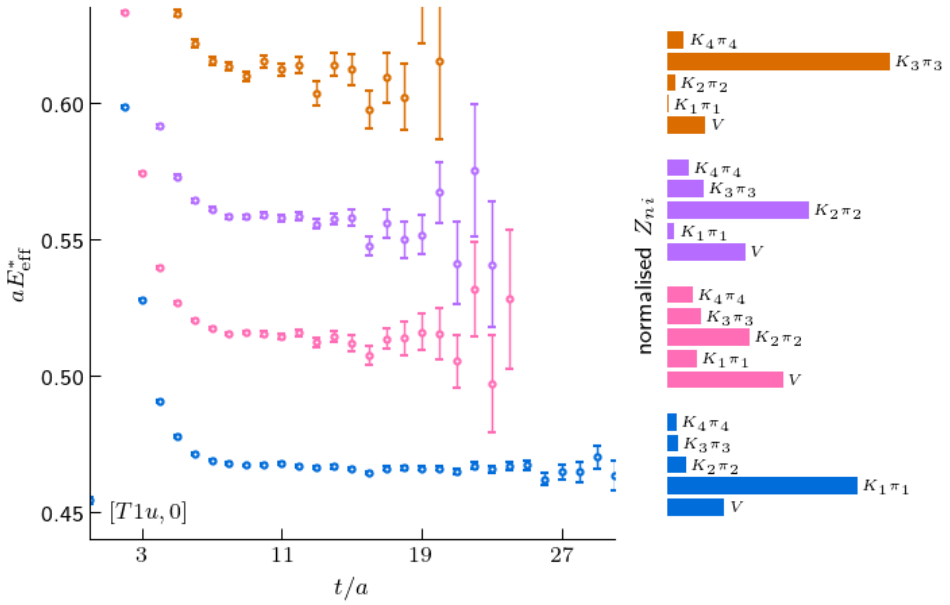

Figure 4.7 *Overlaps from each operator (right) to the states represented by effective masses (left) for the rest-frame irrep in the $K\pi$ channel. We omit the error bars on the overlaps as they are small and do not affect the visualisation.*

In Fig. 4.7, we plot the absolute value of the normalised overlaps $|Z_{ni}|/\sum_j |Z_{nj}|$ for the $K\pi$-like spectrum in the rest frame. Observe how the single-bilinears tend to overlap considerably with all the states, while the two-bilinears do mostly with their "associated" two-particle state, especially when this is isolated. As we anticipated from the discussion in Sec. 4.3.2, the closer a two-particle state is to the expected resonance mass the higher the overlap between the corresponding double-bilinear to the "resonance" level.

Some recent scattering works include the tensor bilinears built from $\gamma_4\gamma_i$,[178,179] besides γ_i, which are essentially free on our setup. The most notable consequence of its inclusion is the appearance of an ill-resolved excited level for P-wave $K\pi^{I=1/2}$ scattering.

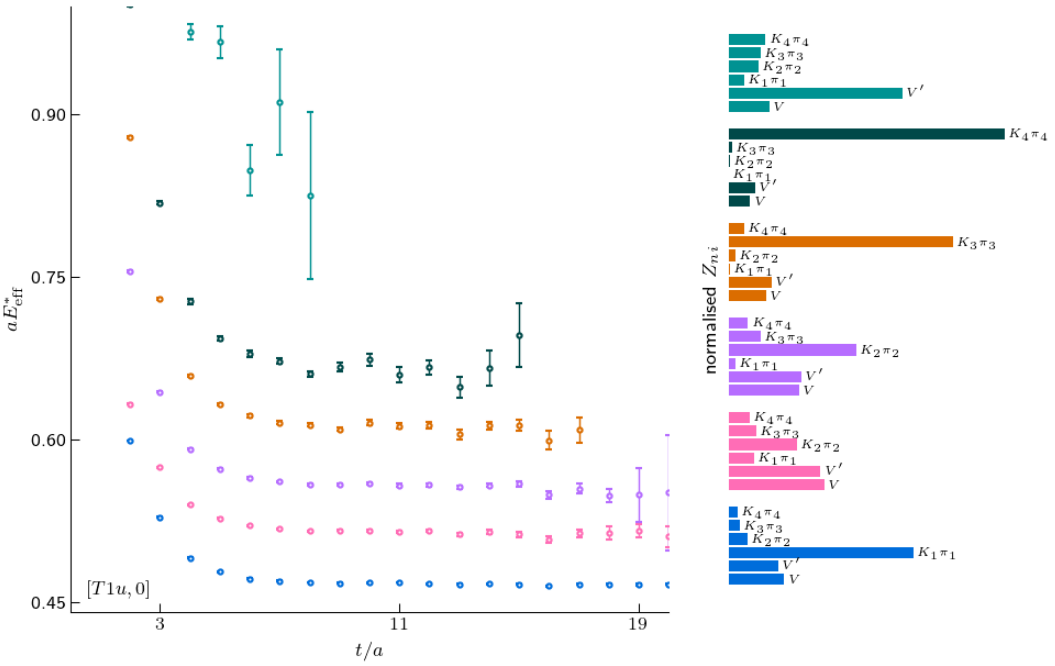

Figure 4.8 *Same as Fig. 4.7 but with the inclusion of* $V' = \bar{s}\gamma^4\gamma^5 u$ *on top of* $V = O_{K^{*+}} = \bar{s}\gamma^5 u$.

However, as one observes in Fig. 4.8, the $\gamma_4\gamma_i$ and γ_i overlap very similarly with all states, apart from the excitation one. Because this last level is quite isolated (so there is not much mixing to states around it happening), it ends up that adding such an operator is not beneficial for our case, at most introducing noise and inconvenient early ordering ambiguities to the GEVP eigenvalues (Sec. 4.4.2). This might indicate that the operators are effectively too similar to each other (in other words, linearly dependent) in order to contribute significantly to the unmixing of the two-particle states.

5 Scattering Analysis

The finite-volume method for computing QCD resonance parameters was introduced in Ch. 3. Such computations were considerably developed in the last decade.[10] This includes determinations of the K^*[140,142,180,181] and ρ[134,135,143,174,178,182–187] parameters. In particular, a few studies were performed at or near the physical point.[141,179,188,189]

We now present the statistical analysis of the $K\pi$ and $\pi\pi$ P-wave scattering taking into account the fit range systematic on our phase-shift determination. Such a technique has not been explored in the literature for Lüscher-type computations. We take inspiration from the model-averaged determinations of the muon $g-2$ HVP and the proton-neutron mass splitting[19,190] and on recent formulations from the Baeysian perspective.[191–193]

5.1 Correlator fit

Our first step towards a high-precision resonance determination was to use a Monte Carlo-generated ensemble where the lightest pseudoscalar particle has its mass equal to the physical one, *cf.* Sec. 4.4.1. This lifts the uncontrolled systematic from using non-QCD information to extrapolate results. However, due to the statistical nature of lattice QCD simulations, many other sources of systematics that are not necessarily understood nor negligible can be introduced *during the data analysis itself*, *i.e.* when computing derived quantities from the main observables (correlators).

The extraction of energies from the asymptotic behaviour of the GEVP eigenvalues, *cf.* (4.41), is usually done through a fit. We opt for fitting directly to the eigenvalue data [I] instead of a derived quantity such as the effective mass. Our main *fit function*

[I] Also called principal correlators or only correlators in this chapter.

(or model) is the N-exponential form

$$C_{\mathsf{expN}}(t;\boldsymbol{\zeta}) = \sum_{n=1}^{N} Z_n e^{-E_n t}, \tag{5.1}$$

from which we frequently adopt the single-state version "exp1". For some cases, such as in the determination of the pion mass, we also utilise "exp2" and "cosh1, cosh2" forms, where the latter is a generalisation of the function in (4.72) incorporating two states. In these models, we denote $\boldsymbol{\zeta} \equiv (Z_i, E_i)$ as the parameters to be determined through the non-linear minimisation of the chi-squared

$$\chi^2_{\mathsf{corr}}(\boldsymbol{\zeta}) \equiv \sum_{t_i,t_j=t_{\mathsf{min}}}^{t_{\mathsf{max}}} \left[C_{\mathsf{lat}}(t_i) - C_{\mathsf{mod}}(t_i;\boldsymbol{\zeta})\right] (\mathbb{C}_{\mathsf{corr}})^{-1}_{ij} \left[C_{\mathsf{lat}}(t_j) - C_{\mathsf{mod}}(t_j;\boldsymbol{\zeta})\right] \tag{5.2}$$

over $\boldsymbol{\zeta}$, where $(\mathbb{C}_{\mathsf{corr}})_{ij}$ is the covariance matrix of the lattice correlators C_{lat} evaluated at time slices t_i, t_j in a given *fit range* $[t_{\mathsf{min}}, t_{\mathsf{max}}]$, *cf.* A.2.

It is clear that (5.1) will not always describe a correlator well enough due to the contribution from residual excited states at small t. Also, the fact that we have a periodic and finite time extension might give rise to significant contributions at large times corresponding to pion matrix elements in the partition function (2.2), known as thermal or around-the-world effects. One way of dealing with this is to restrict the fit range to a region dominated by the ground state, signaled by a plateau in an effective mass plot, *e.g.* Fig. 5.1, which is defined as in (4.73) for a cosh1 model, or as

$$am_{\mathsf{eff}}(t) = \log \frac{C_{\mathsf{exp1}}(t)}{C_{\mathsf{exp1}}(t+1)}, \tag{5.3}$$

for a exp1 model. If one is interested in the lowest state in a correlator, one can visualise the impact of the fit range choice by studying the stability of the fit result E_0 against $t_{\mathsf{min}}, t_{\mathsf{max}}$, *cf.* Fig. 5.1. This can be done either by hand or preferably by a criterion, *e.g.* that E_0 does not change by a threshold value when varying t_{min} by a few units.[179] On top of all that, one can try using different correlator fit functions, for example by accounting for the excited state contributions at small t with a 2-state model.

The potential issue with such approaches is that one needs to make choices at the level of the fit ranges, which leads to uncontrolled systematic errors. This also makes it difficult to give a reasonable interpretation of derived quantities which might depend non-trivially on the energies, *e.g.* resonance parameters. In practice, it is not

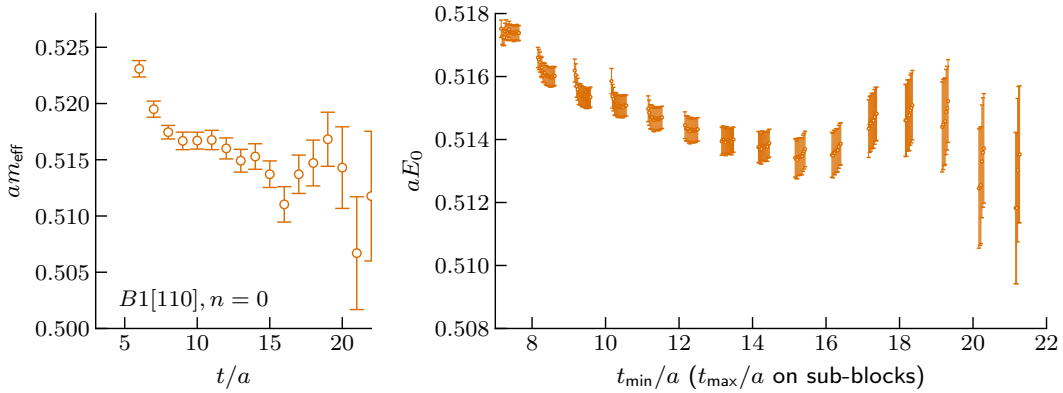

Figure 5.1 *Left: example of (log) effective mass. Right: optimal energy parameter against fit range. Each cluster of points has fixed t_{min} (x-axis) and contains several $t_{\text{max}} > t_{\text{min}} + 3$ in increasing order.*

guaranteed that effective mass plots will have a unique and unanimous plateau. The multiplicity of choices is more prominent in applications such as scattering on the lattice, where one fits the spectrum obtained from fits to several correlators to a model of the scattering amplitude (5.11).

It can be shown that the exclusion of time slices from a correlator fit corresponds to changing the underlying model.[193] Thus, the problem of choosing fit ranges is formally translated into a model selection problem, which has known ways to be approached via *information criteria* and *model averaging* A.3. We first illustrate this in our ensemble for a single-bilinear correlator fitting.

Pion and Kaon masses

We use the pseudoscalar bilinears (4.50) to extract the ground state at zero total momentum, which corresponds to such masses. These will be needed later for computing the geometrical function (3.54) in the quantisation condition. These quantities do not suffer from power-like finite-volume effects, such as the ones in above-threshold two-particle states of channels with resonances and, for that reason, the solution of a GEVP is not needed. Such pseudoscalar-pseudoscalar correlators are the most precise data we have in this analysis, and the result of fitting *directly* to them serves the purpose of demonstrating an ideal model-averaging process at the correlator level without the complication of solving a GEVP.

We approach the fit range selection by the scanning process described as follows. We

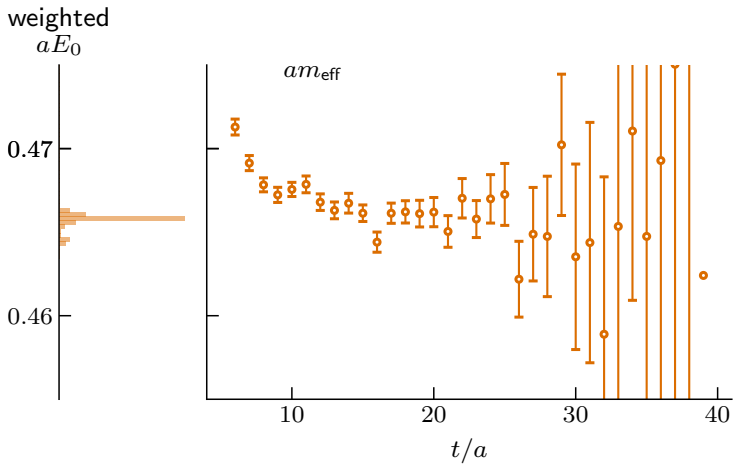

Figure 5.2 *Example of effective mass and weighted histogram of fit results.*

define a region $[t_{\text{start}}, t_{\text{stop}}]$ from which the fit ranges $[t_{\text{min}}, t_{\text{max}}]$ are taken, *i.e.*

$$[t_{\text{min}}, t_{\text{max}}] \in [t_{\text{start}}, t_{\text{stop}}]. \tag{5.4}$$

The upper bound of such scan range is established from a *minimal signal-to-noise criterion*[192] between the correlator central value and its bootstrap variance,

$$\frac{C(t_{\text{stop}})}{\sigma_C(t_{\text{stop}})} < \text{SNR}_{\text{min}}, \tag{5.5}$$

where $t_{\text{stop}} > t_{\text{start}}$ is the earliest timeslice satisfying this condition. For simplicity, we fix $t_{\text{start}} = 4$, justified by the observed invariance of the results under this choice. Given such scan interval, we perform all fits containing at least $\delta t_{\text{min}} + 1$ consecutive timeslices, *i.e.*

$$t_{\text{max}} - t_{\text{min}} \geq \delta t_{\text{min}} \,. \tag{5.6}$$

Under these conditions, we minimise (5.2) on each data bootstrap sample and an extra time on the gauge average. This produces the optimal fit parameters which we refer to as $\boldsymbol{\zeta}^*$, hiding all bootstrap indices for simplicity.

Given a pool of possible fit ranges, we assign the information criterion A.3

$$\text{AIC}_{\text{BMW}} = \chi^2_{\text{corr}}(\boldsymbol{\zeta}^*) + 2n^{\text{par}} - n^{\text{data}}, \tag{5.7}$$

where $n^{\text{data}} = t_{\text{max}} - t_{\text{min}} - 1$ counts how many time slices are included on a specific fit range and the chi-squared is evaluated at the best-fit parameters $\boldsymbol{\zeta}^*$, *i.e.* the minimum chi-squared. In Ref. [193], this formula was rederived by assigning a

"perfect model" to the excluded data points, leading to

$$\mathsf{AIC}_{\mathsf{JN}} = \chi^2_{\mathsf{corr}}(\boldsymbol{\zeta}^*) + 2n^{\mathsf{par}} - 2n^{\mathsf{data}}, \tag{5.8}$$

which should converge to the same results for large enough statistics, *cf.* Fig. 5.3. We weight the fit f using its AIC^f as in

$$w^f = \mathcal{N} \exp\left[-\frac{1}{2}\,\mathsf{AIC}^f\right], \tag{5.9}$$

where the normalisation is $\mathcal{N}^{-1} = \sum_f w^f$, so that w can be treated as a probability. The weights w^f as in (5.9) offer an alternative visualisation of the effective mass in terms of a *weighted histogram* coming from the pool of fit ranges, *cf.* Fig. 5.2. These are also used to compute the *model-averaged parameter* result according to the weighting prescription in A.3. In a Bayesian approach to model averaging, such weights are interpreted as the *posterior* distribution of the model (fit ranges, fit function, etc), given the data.

For statistically precise correlators such as these, we observe a negligible variation from the choices of $\mathsf{SNR}_{\mathsf{min}} = 1, 2, 3$ and thus stick to $\mathsf{SNR}_{\mathsf{min}} = 1$. We also fix $\delta t_{\mathsf{min}} = 3$ to allow for at least one degree of freedom on the chi-squared minimisation. The pair of *hyperparameters* $(\mathsf{SNR}_{\mathsf{min}}, \delta t_{\mathsf{min}}) = (1, 3)$ is thus enough for the results of this section. We also include exp and cosh fit functions with 1 or 2-states in the model averaging. For each choice, we plot in Fig. 5.3 the model-averaged ground state resulting from the AIC weights in (5.9) for each of the models, and then on the overall average. The small circles thus represent the contributions from different model variations going into the larger-circle datapoints. Note that $\mathcal{N}$ needs to be recomputed on each case in order to just include the normalisation from the respective fit results.

We observe that the expN forms give slightly lower values for the pion, indicating thermal contributions are absorbed in the cosh model. The kaon, on the other hand, being much more massive does not suffer as much from such effect.

We also try one level of thinning ("thin $= 2$") on the 1-state fits in order to avoid excessive correlations between consecutive time slices. This corresponds to only including every other time slice within the fit range. When looking at individual results, thinning gives fits with better χ^2 and p-values (A.2), but leads to consistent results with the overall model average. We allow for the variation of this thinning hyperparameter on the pion and kaon correlator fits due to their good statistical

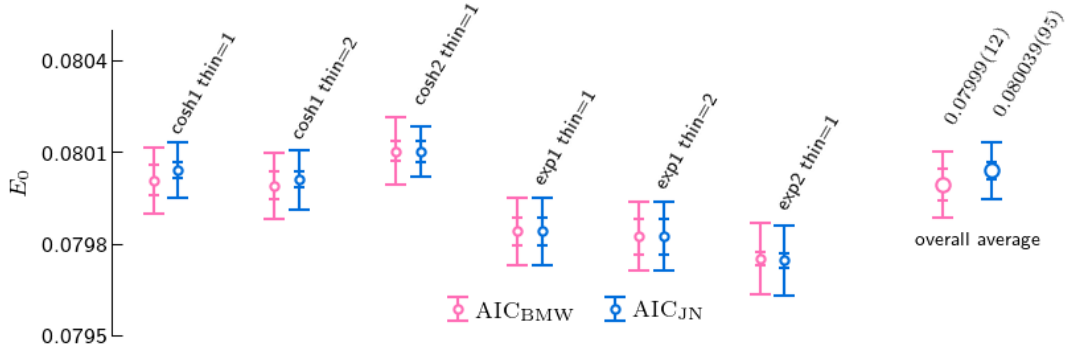

(a) *Pion mass*

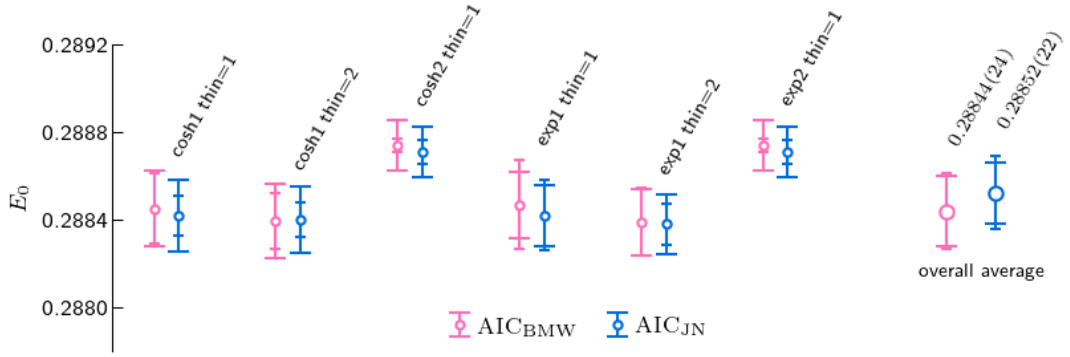

(b) *Kaon mass*

Figure 5.3 *Breakdown of model-averaged ground state results from the variation of fit ranges (small circles) and from the variation of fit ranges, correlator fit functions and thinning levels (larger circles, rightmost points). Different colors compare the different* AIC *definitions* (5.7) *and* (5.8). *Error bars correspond to one standard deviation statistical (large caps) and systematic (small caps) uncertainty intervals, following the definition from* (A.17).

precision across a wide time range, but we will not use it for the later analysis as that reduces the already small amount of data by at least a factor of two.

Dispersion Relation

Another feature of the quantisation condition is that it depends on finite-volume energies boosted to the CM frame. In principle, we do not know which dispersion relation holds for interacting QCD states on the lattice due to discretisation and finite-volume effects. [II]

Fortunately, at our lattice spacing and volume, the continuum dispersion relation

[II] Even though a lattice scalar field dispersion relation[194] should describe weakly-interacting pseudoscalar states fairly well.

holds well, which can be demonstrated by a fit of moving pion and kaon energies to

$$(aE)^2 = (am)^2 + C(a\mathbf{P})^2, \tag{5.10}$$

where the energies were obtained using information criteria similar to the previous section. The good quality of such fit means that lattice discretisation effects are too small to be distinguished within our statistical precision and can be safely neglected on the pion and kaon. In this chapter, we will use this continuum dispersion relation for boosting the interacting two-particle energies into the CM frame.

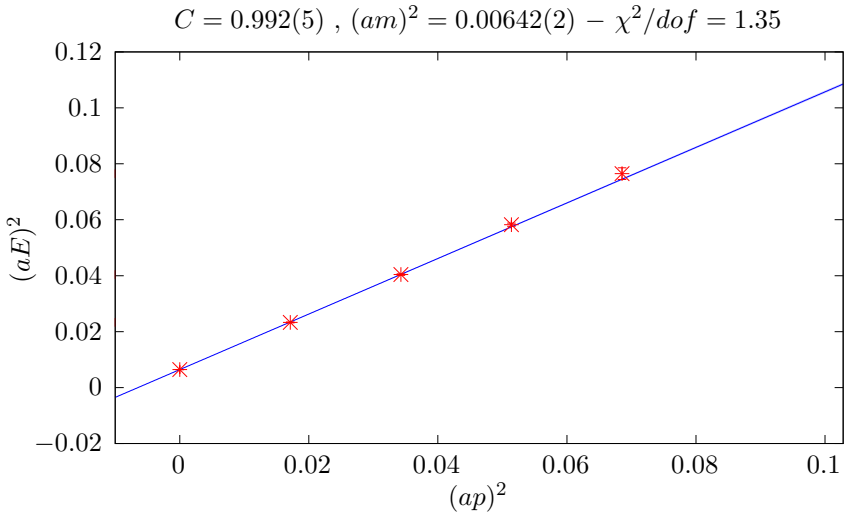

(a) *Pion*

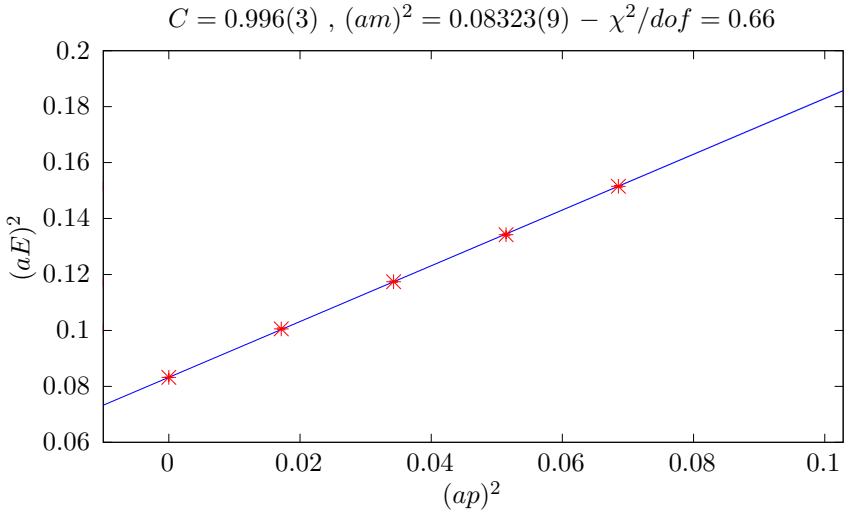

(b) *Kaon*

Figure 5.4 *Fits of single-bilinear correlators to* (5.10).

5.2 Spectrum fit

As detailed in Ch. 3, we use the quantisation condition in the simplified form for elastic P-wave (3.71) to obtain the resonance parameters. In practice, this is done by modeling the associated phase shift and using the lattice data to statistically constrain it. In particular, one needs to take into account the statistical uncertainties intrinsic to the lattice energies, which will be done through least-squares fitting.

Spectrum chi-squared

Given a model for the scattering amplitude, in our case for the elastic phase shift, we employ the *spectrum (or phase-shift) fitting* by minimising the chi-square statistic[133]

$$\chi^2_{\mathsf{PS}}(\boldsymbol{\alpha}) \equiv \sum_{ij} \left[E^{*\mathsf{lat}}_{(i)} - E^{*\mathsf{mod}}_{(i)}(\boldsymbol{\alpha})\right] (\mathbb{C}_E)^{-1}_{ij} \left[E^{*\mathsf{lat}}_{(j)} - E^{*\mathsf{mod}}_{(j)}(\boldsymbol{\alpha})\right], \tag{5.11}$$

where CM energies are identified by the compound labels $(i) = (\Lambda[\mathbf{d}]^2, n)$ and now $(\mathbb{C}_E)_{ij} \equiv \mathrm{Cov}\,(E^{*\mathsf{lat}}_{(i)}, E^{*\mathsf{lat}}_{(j)})$ is the data covariance between the later-extracted energies boosted to the CM frame, *cf.* A.9. On the other hand, $E^{*\mathsf{mod}}_{(i)}(\boldsymbol{\alpha})$ is the solution of the quantisation condition on its respective moving frame and irrep

$$\left[\cot \phi^{\Lambda[\mathbf{d}]}\big(q^* L/2\pi; L\big) - \cot \delta_1^{\mathsf{mod}}(E^*; \boldsymbol{\alpha})\right]_{E^* = E^{*\mathsf{mod}}_{(i)}(\boldsymbol{\alpha})} = 0, \tag{5.12}$$

for a *phase-shift model* δ_1^{mod} parametrised by a vector of *phase-shift parameters* $\boldsymbol{\alpha}$, where the relation between q^* and E^* is given in (3.32). As mentioned in Sec. 3.3, the pseudophases $\phi^{\Lambda[\mathbf{d}]}$ can be computed numerically through the generalised zeta, *cf.* B. The result of this minimisation is exemplified in Fig. 5.5, where the residuals at the minimum, $r_{(i)} \equiv E^{*\mathsf{lat}}_{(i)} - E^{*\mathsf{mod}}_{(i)}(\boldsymbol{\alpha}^*)$ are normalised with a Cholesky decomposition of the inverse covariance, *i.e.* $(\mathbb{C}_E)^{-1} = LL^{\mathsf{T}}$, such that $\bar{r}_{(i)} \equiv \sum_j L_{ji} r_{(j)}$ carries effects of the correlations.

Solving equation (5.12) relies on a root-finding procedure which might depend on an initial guess or bracket for $E^{*\mathsf{mod}}_{(i)}(\boldsymbol{\alpha})$. In our single-channel case, the ambiguity of choosing the brackets and appropriately matching the indices (i) between the data and the model-derived energies in (5.12) is lifted in the specific way we implement this formula, *cf.* B.2. [III] We thus use (5.11) in anticipation of future extensions of this

[III] Another option is to fit the model directly to the phase shifts obtained from (5.12),[135] but such a method does not extend well to advanced cases where more than one phase shift is involved in the

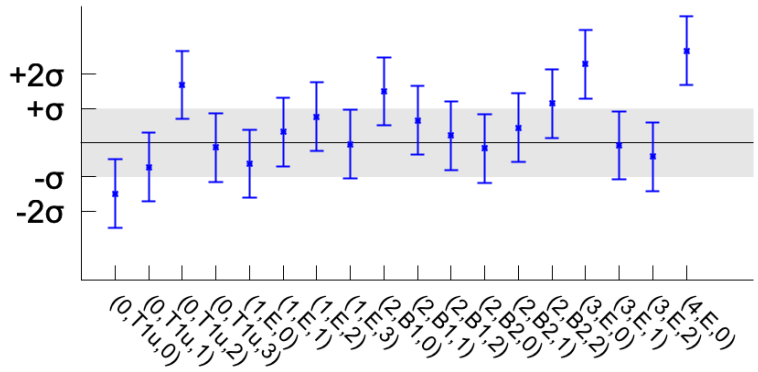

Figure 5.5 *Example of covariance-normalised residuals $\bar{r}_{(i)}$ from the minimisation of (5.11). The y-axis is given in units of standard variations (σ) of the Gaussian probability distribution obtained from χ^2_{PS} at the minimum $\boldsymbol{\alpha}^*$.*

work.

Phase-shift models

We explore more than one phase-shift model in order to study the systematic effect that this choice has on the resonance description:

- Breit-Wigner (BW)

  The Breit-Wigner model has the well-known form for the scattering amplitude[6,61]

  $$\mathcal{T}^{\mathsf{BW}}\left(\sqrt{s}\right) = \frac{\Gamma_{\mathsf{BW}}\sqrt{s}}{M^2_{\mathsf{BW}} - s - i\Gamma_{\mathsf{BW}}\sqrt{s}} \tag{5.13}$$

  in terms of the Breit-Wigner mass M_{BW} and witdh Γ_{BW}. The invariant mass $\sqrt{s} = E^*$ is related to the CM momentum $q^* = q^*(\sqrt{s})$ according to (3.32).

  Restricted to P-wave contributions only, the amplitude above can be expressed in terms of a phase shift as

  $$q^{*3}\cot\delta_1^{\mathsf{BW}}(\sqrt{s}; g, M) = \frac{6\pi}{g^2}(M^2 - s)\sqrt{s}, \tag{5.14}$$

  where we drop the subscript BW on the parameters. The energy-dependent

quantisation condition.[195]

Breit-Wigner width is related to the effective coupling g via

$$\Gamma_{\mathsf{BW}}(s) = \frac{g^2}{6\pi}\frac{q^{*3}}{s} \tag{5.15}$$

and ensures the expected relativistic behavior at the two-particle threshold. The specific form of the width introduces a model dependence that can be relevant for resonances far from the narrow-width approximation.[6]

- Effective range expansion (ERE)

  In the spirit of model variation, we include a model that is not derived from Breit-Wigner. One can expand $q^{*3}\cot\delta_1$ in powers of q^{*2}, *i.e.*

$$q^{*3}\cot\delta_1^{\mathsf{ERE}}(\sqrt{s};a_1,r_1) = \frac{1}{a_1} + \frac{r_1}{2}q^{*2}, \tag{5.16}$$

  which is just the $l=1$ *effective range expansion*[196] to first order in q^{*2}, featuring the *scattering length* a_1. The a_1, r_1 parameters have dimensions of volume and inverse distance, but we inherit the names "length" and "range" coming from the widely used S-wave effective range expansion in nuclear physics. This model is flexible enough to describe resonant, as well as weakly attractive or repulsive scattering.[180]

In general, parametrisations of the partial-wave $\mathcal{K}$-matrix (1.23) can be given by a power series plus a sum of poles to account for phenomenological or theoretical expectations[57,180] *i.e.*

$$q^{*2l+1}\cot\delta_l = \sum_n \frac{(M_n^2-\sqrt{s})}{(\tilde{g}_{n,l})^2} + \sum_n c_{l,2n}(q^{*2})^{2n}. \tag{5.17}$$

In this work, we are examining resonances at the physical point which are phenomenologically well known, and so we stick to the two parametrisations above.

5.3 Model-averaging Strategy

Ideally, one would fit both correlator and phase-shift models simultaneously to all correlator data in order to constrain the scattering phase shifts. However, this is of difficult realisation in practice mainly because the inverse of the global covariance matrix will be badly estimated from limited data. In our case, with only

90 measurements, inverting such a large covariance matrix (size ~ 150) is essentially guaranteed to be an ill-conditioned problem.

Having the pion and kaon masses at hand, we instead split the scattering analysis into two layers

$$\text{fit chaining} \begin{cases} (1).\ \text{Spectrum determination:} \\ \qquad \text{extract a set of energies via exp1 fits to the GEVP eigenvalues} \\ (2).\ \text{Phase-shift determination:} \\ \qquad \text{fit a phase-shift model to the energies obtained in (1)} \end{cases} \tag{5.18}$$

We fix (1) each time (2) is performed and we repeat this fit chain to assess how the phase shifts change across different realisations of (1). The reason we choose to use only exp1 at this step is that they yield statistically well-defined results on a wide range of fit ranges, while more complicated models would only work on a very reduced region. For example, for many of the levels we include, the chi-squared minimisation using the exp2 model converges only for $t_{\mathsf{min}} \lessapprox 8$, as for larger values the statistical signal of excited states becomes very poor. This choice guarantees the stability of the analysis method presented in the following sections.

5.3.1 Spectrum determination

Fit Range Scanning

We *independently* scan *each* GEVP eigenvalue (i) on the range $[t_{\mathsf{start}(i)}, t_{\mathsf{stop}_{(i)}}]$, in analogy to what we did with the pion and kaon correlators in Sec. 5.1. For a given correlator $\lambda^{(i)}$ and each fit range $f \in [t_{\mathsf{start}(i)}, t_{\mathsf{stop}_{(i)}}]$, *cf.* Fig. 5.6a, we assign an $\mathsf{AIC}_{\mathsf{corr},(i)}$ with the same form as (5.7). We adopt only (5.7) for simplicity, as we checked they give results consistent with (5.8) in the scope of our applications.

Due to the orthogonalisation property imposed by the GEVP, the correlator fits are independent of each other for large enough t and t_0. This is enforced by the fact they do not have fit parameters in common. We are then entitled to combine individual fit ranges as

$$\{f_{(i=1)}, f_{(i=2)}, \ldots, f_{(i=N_{\mathsf{lev}})}\}, \tag{5.19}$$

composing a unique set of fit ranges across the N_{lev} levels considered on a given channel.

Given one such fit range combination and the associated energy results, one can fit them using (5.11) to obtain the associated optimal phase-shift parameters. In principle, one could repeat this for all possible combinations to perform the model averaging in the largest model space possible. Of course, performing all such fits is not feasible as the number of combinations scales exponentially with the number of energies $\sim \mathcal{O}(10^{15})$.

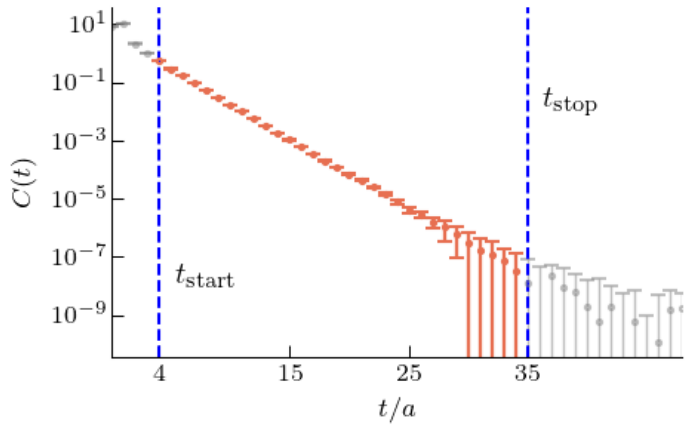

(a) *Eigenvalue*

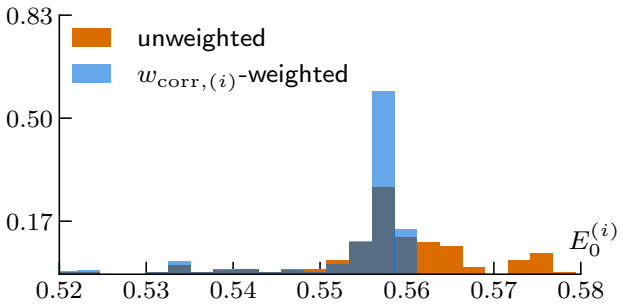

(b) *E_0 fit result histogram*

Figure 5.6 *Top: example of scan range $[t_{\text{start}}, t_{\text{stop}}]$ where all possible single-state exponential fits with $t_{\text{max}} - t_{\text{min}} > 3$ are performed to get the histogram on the right panel. Bottom: example of unweighted and w_{corr}-weighted histogram of the energy fit result.*

Fit Range Sampling

Note that many combinations of correlator fit ranges outlined in the previous section will lead to unreasonable fits which will be eventually weighted out by the AIC weights. So, in order to reduce the number of phase-shift fits performed in practice, we employ a *fit range sampling* on *each* correlator based on the weights $w_{\text{corr},(i)}$. In

this way, the chance that a bad combination of fit ranges will be used in the spectrum fit is exponentially suppressed.

In practice, we first draw N_{scan} fit ranges $\mathsf{s}_{(i)}$ for *each* GEVP eigenvalue (i), with probability given by $w_{\mathsf{corr},(i)}$ [IV]. We then combine the samples across all N_{lev} levels to form an overall *fit range sample*

$$\mathsf{s} \equiv \{\mathsf{s}_{(i=1)}, \mathsf{s}_{(i=2)}, \ldots, \mathsf{s}_{(i=N_{\mathsf{lev}})}\}. \tag{5.20}$$

At this point, we are able to compute the finite-volume spectra in the $\pi\pi$ and $K\pi$ channels by using a similar model-averaging strategy as in Sec. 5.1. The difference is that we average over a set of N_{scan} energy samples

$$E^{\mathsf{s}} \equiv \{E^{\mathsf{s}}_{(i=1)}, E^{\mathsf{s}}_{(i=2)}, \ldots, E^{\mathsf{s}}_{(i=N_{\mathsf{lev}})}\}, \tag{5.21}$$

where each $E^{\mathsf{s}}_{(i)}$ encapsulates all bootstrap samples from the minimisation procedure in A.2. We further boost all obtained energies into the CM frame using (5.10) with the mass replaced by $E^{\mathsf{s}}_{(i)}$, to yield $E^{*\mathsf{s}}_{(i)}$ on all bootstrap samples. We finally depict a subproduct of this work in Fig. 5.7, where the statistical and the *fit-range systematic errors* of each $E^{*}_{(i)}$ were computed using the weighting prescription of A.3.

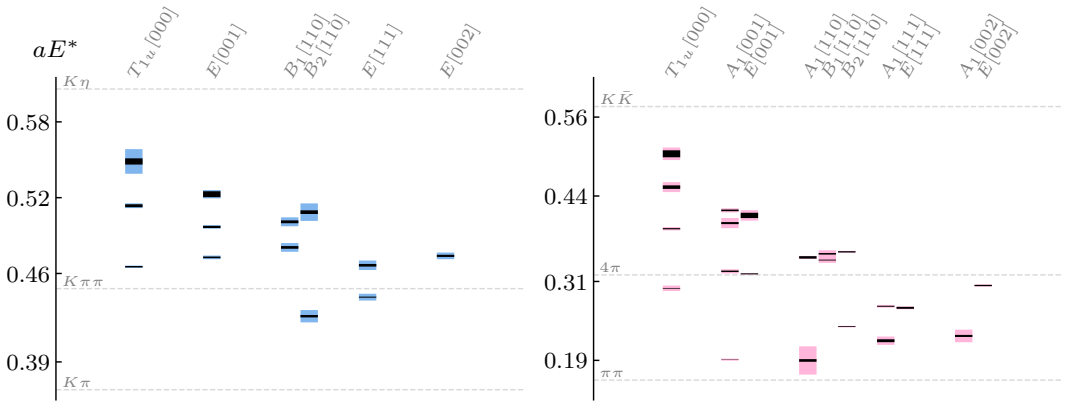

Figure 5.7 *Results for the model-averaged finite-volume spectrum used in our analysis of $K\pi^{I=1/2}$ (left) and $\pi\pi^{I=1}$ (right) quantum numbers. The height of the black rectangles represents statistical uncertainty and that of the colourful lighter ones is a systematic uncertainty determined from the fit range variation with $(\mathsf{SNR}_{\mathsf{min}}, \delta t_{\mathsf{min}}) = (8, 4)$. The lattice irreps are displaced horizontally as indicated.*

[IV] More specifically, we uniformly draw a number between 0 and 1 and use the cumulative sum of the weights to define brackets corresponding to each fit range.

5.3.2 Phase-shift determination

Weighting

The second step of the fit chain (5.18) consists of performing the spectrum fit for each of the fit range combinations obtained in the sampling process above. This chain can be more clearly interpreted from a Bayesian perspective,[191,192] even though in practice we implement a frequentist approach.[197] Following such rationale, a specific choice of fit ranges in (1) can be viewed as a (very sharp) prior to the spectrum fit in (2). This also corresponds to neglecting the off-block-diagonal terms of the global covariance matrix (correlator-spectrum correlations) and adding the $\chi_{\mathsf{corr},(i)}$ to (5.11), which in our case we keep *fixed* during each minimisation of χ^2_{PS}. On that basis, we define the associated total AIC on each fit range sample by

$$\mathsf{AIC}_{\mathsf{t}} = \mathsf{AIC}_{\mathsf{PS}} + \sum_i \mathsf{AIC}_{\mathsf{corr},(i)}, \tag{5.22}$$

yielding the weights w_{t}

$$w_{\mathsf{t}} = \mathcal{N}_{\mathsf{t}} \exp\Big(-\frac{1}{2}\,\mathsf{AIC}_{\mathsf{t}} \Big), \tag{5.23}$$

where $\mathcal{N}_{\mathsf{t}} = \sum_{\mathsf{s}} w^{\mathsf{s}}_{\mathsf{t}}$ is now taken over the fit-range samples defined in (5.20). The model averaging of different phase-shift model parameters, or any other derived quantity, can be done by a straightforward repetition of this process where the set of samples $\{\mathsf{s}\}$ are generalised to include further model variations.

Sampling efficacy

One would like to check that a given fit range sampling is a fair representation of the total space of fit ranges. We first compare its efficacy with a uniform sampling from each correlator, *i.e.* drawing the fits based on the unweighted distribution of the energy fit results, as depicted in Fig. 5.6b. In Fig. 5.8a, we plot the *unweighted* histograms of phase-shift parameter results and compare them to the final histograms *weighted* by the *total* $\mathsf{AIC}_{\mathsf{t}}$ that yield our final results. This demonstrates how the uniform sampling indeed leads to many fits being weighted out at the final phase-shift parameter result. We also note that the uniform sampling draws fit ranges leading to reasonable phase-shift fits at a *much* slower rate than the correlator sampling, *cf.* Fig. 5.8b.

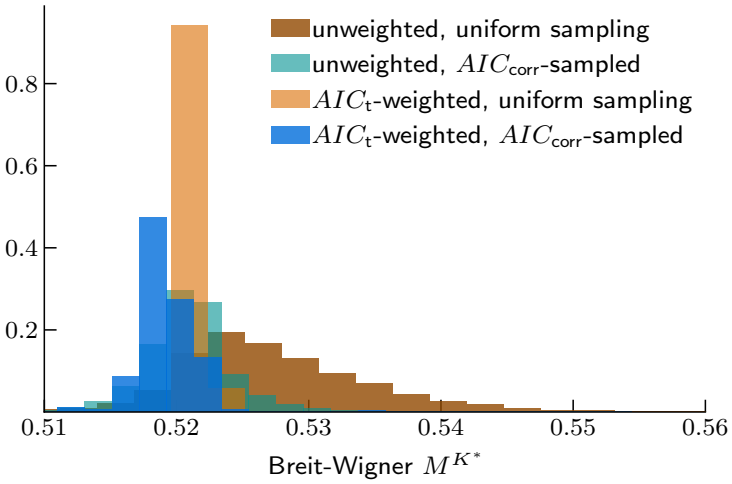

(a) K^* BW *mass from different samplings and weightings*

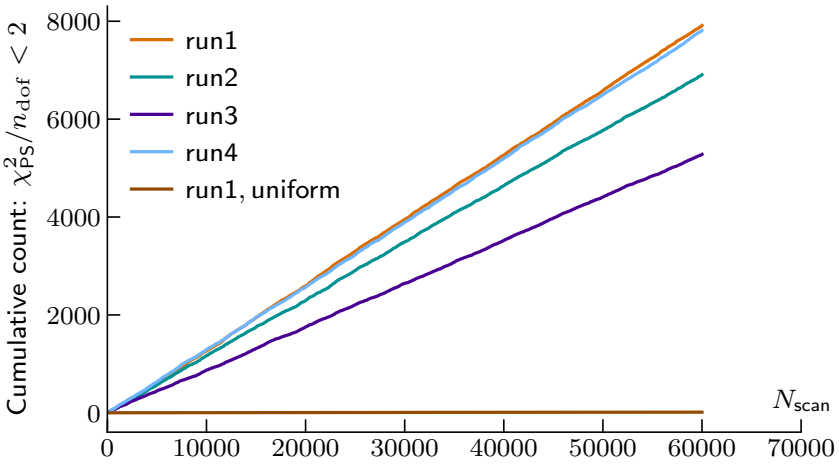

(b) *Accumulation of reasonable phase-shift* $\chi_{\text{PS}}/n^{\text{dof}}$ *with* N_{scan}

Figure 5.8 *Top: example of unweighted and* AIC_{t}*-weighted* BW *mass histograms resulting from uniform and* AIC_{corr} *sampling. Bottom: accumulated number of fits with* $\chi^2_{\text{PS}}/n_{\text{dof}} < 2$ *at a certain* N_{scan} *for the different hyperparameter variations in Table 5.1. The flat line corresponds to the reference choice "*run1*" obtained from uniformly-sampled fit ranges, the others curves come from the* AIC_{corr}*-based sampling.*

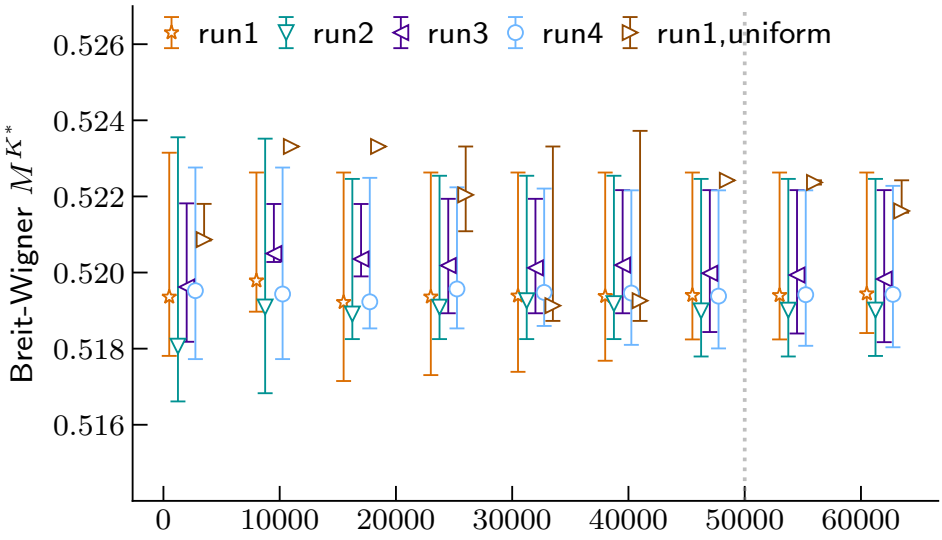

Figure 5.9 *Evolution of the K^* Breit-Wigner mass systematical error with N_{scan} for the different hyperparameter variations in Table 5.1.*

Hyperparameter variation

Even though we do not select fit ranges individually, we still need to choose the scan ranges. The most natural choice would be to use all time ranges available, but this is only true for high enough statistics.[192] We must then decide on ways of cutting the scan range. As in Sec. 5.1, we use a minimum signal-to-noise SNR_{min} and a minimum number of timeslices δt_{min} considered in any given fit to GEVP eigenvalues. In Fig. 5.9, we show the reasonable agreement between a selection of the hyperparameters $(\text{SNR}_{\text{min}}, \delta t_{\text{min}})$, named according to Table. 5.1, for phase-shift parameters at sufficiently large N_{scan}. Based on that, we adopt the choice $N_{\text{scan}} = 50000$ for the main analysis in the next section. Furthermore, we also observe the instability of the uniform sampling for this region of N_{scan}, where the systematic error vanishes and wildly varies because only a few fits dominate the result in that case.

One can still incorporate various choices of hyperparameters by model-averaging them together in the same fashion as we did for the fit ranges. We use the preferred choices in Table. 5.1 for providing individual phase-shift parameters and only model-average pole parameters into a single result in Sec. 5.4.2.

run	$\mathsf{SNR}_{\mathsf{min}}$	δt_{min}
1	8	4
2	5	7
3	7	7
4	6	6

Table 5.1 *Summary of the variation of hyperparameters* $(\mathsf{SNR}_{\mathsf{min}}, \delta t_{\mathsf{min}})$ *used in our resonance determination.*

5.4 Resonance parameters

5.4.1 Phase shift

Using the model averaging procedure described above, we first assess the different phase-shift parametrisations in Sec. 5.2. The results for the phase-shift parameters are visualised through their histograms over $N_{\mathsf{scan}} = 50000$ samples, weighted by the global $\mathsf{AIC}_{\mathsf{t}}$ 5.22. In Fig. 5.10, we give an example of such result for the $K\pi, I = 1/2$ channel with the choice of hyperparameters corresponding to "run1" in Table. 5.1, *i.e.* $(\mathsf{SNR}_{\mathsf{min}}, \delta t_{\mathsf{min}}) = (8, 4)$. In D.1, we give explicit results from individual hyperparameter choices and phase shift models.

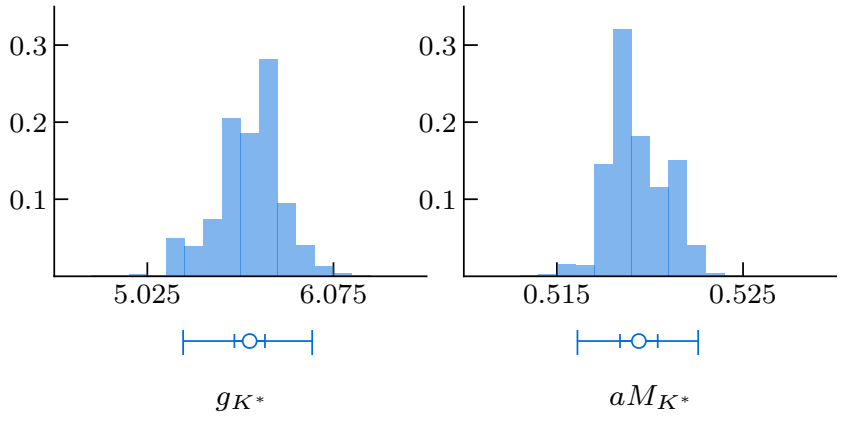

Figure 5.10 *The gauge-average central value (cf. (A.6)) histograms of the optimal* BW *phase-shift parameters for* $(\mathsf{SNR}_{\mathsf{min}}, \delta t_{\mathsf{min}}) = (8, 4)$*, weighted by* $w_{\mathsf{t}} = \mathcal{N}_{\mathsf{t}} \exp -\frac{1}{2} \mathsf{AIC}_{\mathsf{t}}$*. For the other choices of models and hyperparameters, see D.1.*

Numerically, the results obtained for the BW parameters within run1 are

$$\begin{cases} aM_{K^*} &= 0.5193(10)_{\mathsf{stat}}(32)_{\mathsf{fr}} \\ g_{K^*} &= 5.59(9)_{\mathsf{stat}}(36)_{\mathsf{fr}} \end{cases}, \quad \begin{cases} aM_{\rho} &= 0.4685(56)_{\mathsf{stat}}(73)_{\mathsf{fr}} \\ g_{\rho} &= 6.36(22)_{\mathsf{stat}}(48)_{\mathsf{fr}} \end{cases},$$

where the first error is statistical and the second is the conservative symmetrised systematic coming from the fit range variation according to A.3. In the usual interpretation of the BW parameters, the resulting resonance masses M are above the two-particle thresholds as expected for a model in which the unstable character of the particle is built in. The effective coupling g of the resonances to, respectively, the $K\pi$ and $\pi\pi$ channels represents the strength of interaction and was previously noted to be fairly insensitive to the quark mass.[198] Their values are within reasonable agreement with what is expected from experimental data and other lattice works.[6,178,179]

The $K\pi^{I=1/2}$ and $\pi\pi^{I=1}$ P-wave scattering lengths and effective ranges from the ERE model within run1 are

$$\begin{cases} a_{1,K\pi}/a^3 &= -27.2(1.1)_{\mathsf{stat}}(4.5)_{\mathsf{fr}} \\ ar_{1,K\pi} &= 2.64(11)_{\mathsf{stat}}(45)_{\mathsf{fr}} \end{cases}, \quad \begin{cases} a_{1,\pi\pi}/a^3 &= -31.9(1.8)_{\mathsf{stat}}(1.8)_{\mathsf{fr}} \\ ar_{1,\pi\pi} &= 1.231(99)_{\mathsf{stat}}(92)_{\mathsf{fr}} \end{cases}.$$

The interpretation of the minus sign of the scattering length a_1 in the ERE model leads to the conclusion of an attractive interaction on both channels. The (inverse) effective range $r_1^{-1} \sim 0.05$ fm on our lattice is in the scale of the short-range interactions considered for processes of this type.

Even though we do not directly fit to the phase shift data computable from the quantisation condition, its visualisation is still useful from the phenomenological point of view. On each energy bin of Fig. 5.11, we compute the model-averaged optimal phase shift curves coming from BW, ERE and all fit-range and hyperparameter variations, the latter detailed in Table 5.1, weighted by w_{t}. In the next section, we argue that the phase shifts computed in this work are an estimation of the real part of the actual quantity whose, imaginary component we expect to be very small. In the same figure we also show $q^{*3}\cot\delta_1$ featuring in the definitions of the models themselves.

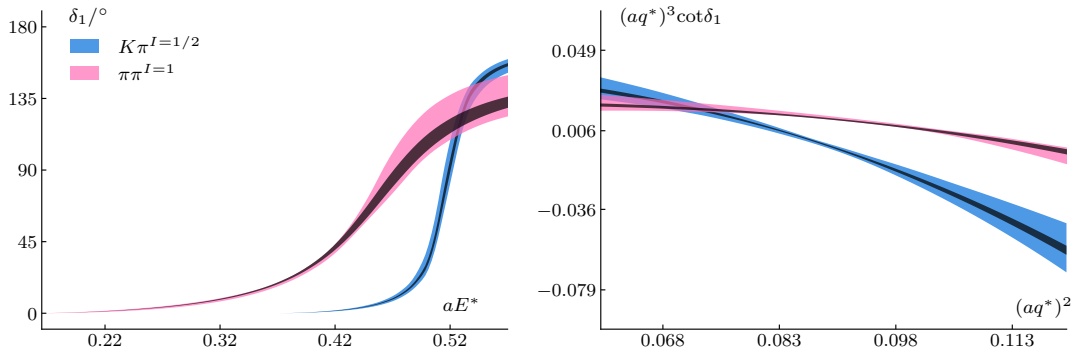

Figure 5.11 *Model average of the (real part of) the phase shifts (left) and* $(aq^*)^3 \cot \delta_1$ *(right) over the* BW, ERE *models and all the hyperparameter choices in Table 5.1, with statistical (black) and data-driven systematical (colourful) bands.*

5.4.2 Pole position

We can substitute the optimal phase shift parametrizations into the elastic scattering amplitude $\mathcal{T}_l \delta_{ll'} \delta_{mm'} \equiv \mathcal{T}_{lm,l'm'}$ as in Eqs. (1.23),(1.25) to get

$$\mathcal{T}_1^{\text{mod}} = \left[\cot \delta_1^{\text{mod}} - i\right]^{-1}, \tag{5.24}$$

which enables us to analytically continue it into the complex-$\sqrt{s}$ plane. Now $\mathcal{T}_1^{\text{mod}}$ is also a function defined on the complex plane and will feature the expected multi-sheet structure encoded by Eq. 3.32. The identification of the poles on the second Riemann (unphysical) sheet provides a model-independent definition of resonances.

We compute the so-called resonance *pole parameters*

$$\sqrt{s_{\text{pole}}} = M_P - \frac{i}{2}\Gamma_P \tag{5.25}$$

located on the unphysical sheet, where $\text{Im } q^* < 0$. This defines the *pole mass* M_P and *pole width* Γ_P of a resonance. In the BW case, we implement the pole-finding by minimizing the quantity [V]

$$\mathcal{F}(q^*) \equiv \left|\mathcal{T}_1\left(\sqrt{s}(q^*)\right)\right|^{-2} \tag{5.26}$$

in the complex-q^* plane restricted to the unphysical sheet. The minimum q^*_{pole} is found to a precision $\epsilon_{\text{pole}} = 10^{-7}$ and then confirmed to be a zero of $\mathcal{T}_1^{-1}$ by checking

[V] We use the *Neldermead* algorithm[199,200] for this minimization step.

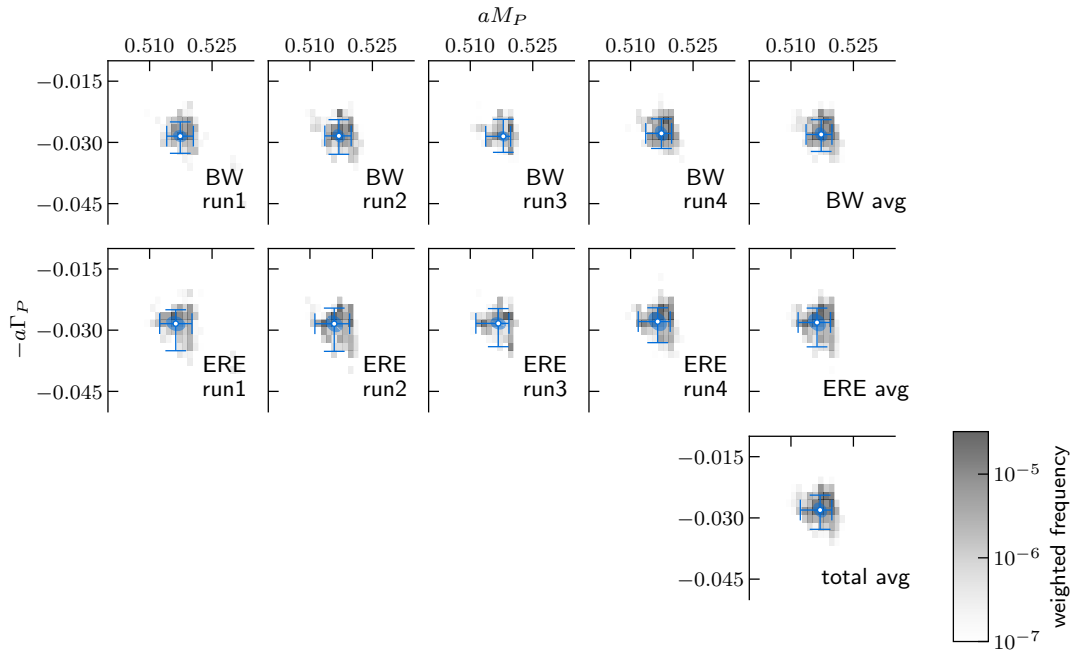

(a) $K^* \to K\pi^{I=1/2}$, *P-wave*

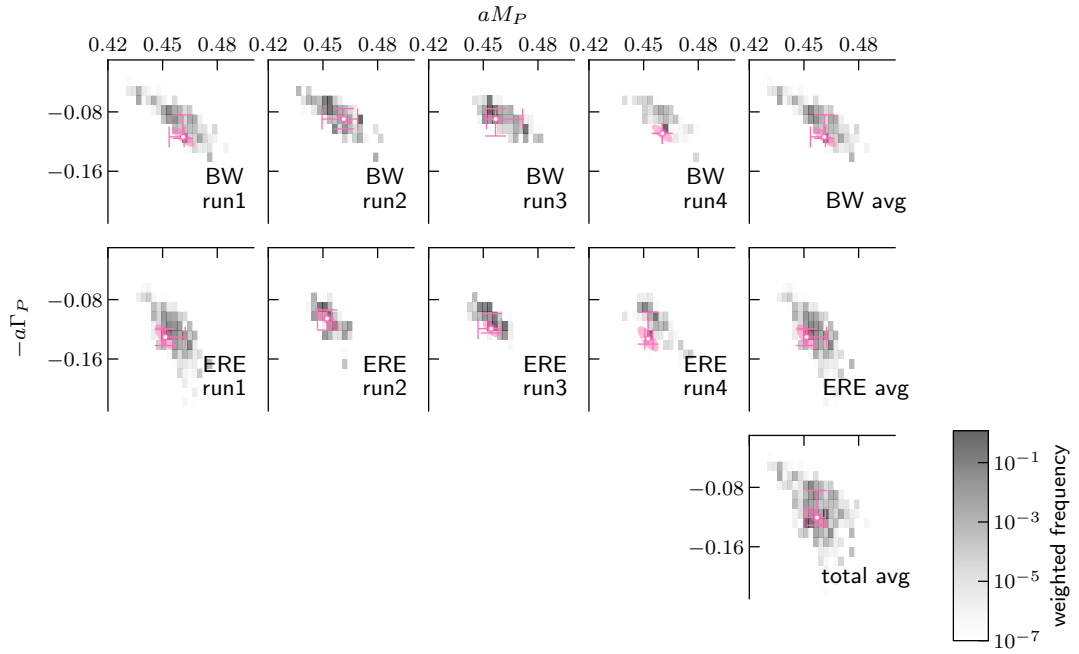

(b) $\rho \to \pi\pi^{I=1}$, *P-wave*

Figure 5.12 *Breakdown of data-driven systematic spread of pole-positions between the* BW, ERE *models and all the hyperparameter choices in Table 5.1, namely* run1 : $(\mathsf{SNR}_{\mathsf{min}} = 8, \delta t_{\mathsf{min}} = 4)$, run2 : $(\mathsf{SNR}_{\mathsf{min}} = 5, \delta t_{\mathsf{min}} = 7)$, run3 : $(\mathsf{SNR}_{\mathsf{min}} = 7, \delta t_{\mathsf{min}} = 7)$, run4 : $(\mathsf{SNR}_{\mathsf{min}} = 6, \delta t_{\mathsf{min}} = 6)$. *The systematic interval is denoted by the cross and the statistical error ellipse shows the correlation between M_P and $-\Gamma_P$. The two-dimensional histogram is the* AIC_t*-weighted frequency over corresponding finite-volume energy samples and it is plotted on a log scale.*

that $\mathrm{Re}\ \mathcal{T}_1^{-1}$ and $\mathrm{Im}\ \mathcal{T}_1^{-1}$ change sign for at least one pair of vertices

$$(\mathrm{Re}\ q^*_{\mathsf{pole}} \pm \epsilon_{\mathsf{pole}}, \mathrm{Im}\ q^*_{\mathsf{pole}} \pm \epsilon_{\mathsf{pole}}) \tag{5.27}$$

around the solution. The ERE model can be written as an order-three polynomial equation that we solve exactly and search for the resonance pole closest to the physical scattering line. In Table 5.2, we report the breakdown of the pole positions for each phase-shift model.

BW	$aM_P^{K^*} = 0.5167(9)_{\mathsf{stat}}(31)_{\mathsf{fr}}$	$aM_P^{\rho} = 0.4577(40)_{\mathsf{stat}}(41)_{\mathsf{fr}}$
	$a\Gamma_P^{K^*} = 0.0283(10)_{\mathsf{stat}}(39)_{\mathsf{fr}}$	$a\Gamma_P^{\rho} = 0.100(8)_{\mathsf{stat}}(16)_{\mathsf{fr}}$
ERE	$aM_P^{K^*} = 0.5156(13)_{\mathsf{stat}}(39)_{\mathsf{fr}}$	$aM_P^{\rho} = 0.4562(34)_{\mathsf{stat}}(62)_{\mathsf{fr}}$
	$a\Gamma_P^{K^*} = 0.0293(13)_{\mathsf{stat}}(47)_{\mathsf{fr}}$	$a\Gamma_P^{\rho} = 0.131(11)_{\mathsf{stat}}(11)_{\mathsf{fr}}$

Table 5.2 *Pole parameters for each individual phase shift model in Sec. 5.2 and* $(\mathsf{SNR}_{\mathsf{min}}, \delta t_{\mathsf{min}}) = (8, 4)$*. The result is symmetrized according to Eq. (A.16). The statistical and fit-range systematics are shown in that order between brackets. See D.1 for other choices of* $(\mathsf{SNR}_{\mathsf{min}}, \delta t_{\mathsf{min}})$*.*

As the pole mass and width (1.28) correspond to the same parameters across different phase-shift models, we can model-average them to find

$$\begin{cases} aM_P^{K^*} &= 0.5160(10)_{\mathsf{stat}}(38)_{\mathsf{dd}} \\ a\Gamma_P^{K^*} &= 0.0286(11)_{\mathsf{stat}}(42)_{\mathsf{dd}} \end{cases}, \quad \begin{cases} aM_P^{\rho} &= 0.4559(7)_{\mathsf{stat}}(11)_{\mathsf{dd}} \\ a\Gamma_P^{\rho} &= 0.108(21)_{\mathsf{stat}}(23)_{\mathsf{dd}} \end{cases}.$$

Note that the *data-driven* systematic uncertainty ("dd") includes not only the variation of the phase shift model but also the variation of the fit range at the correlator level and the variation of the hyperparameters in Table .5.1. The breakdown of the model averaging is illustrated in Fig. 5.12.

5.4.3 Error budget

We do not perform a dedicated scale setting in this work, but instead, use the value of the inverse lattice spacing, $a^{-1} = 1.7295(38)$ GeV, computed in Ref. [74]. We assume this measurement to be statistically uncorrelated from our resonance determination and use it for quoting results in physical units. We indicate the statistical error coming from a^{-1} in the results given in physical units as a separate contribution ("scale").

In the following, we estimate the sources of systematics that are not addressed

directly in this work and quote them in the quoted results in physical units. They are summarized together with the data-driven systematics in Table 5.3. Our largest uncontrolled uncertainty is due to the discretization effects and it composes most of our extra error budget. We add all the systematics discussed below in quadrature and round up the result to an overall 6% uncertainty.

Source	M_P	Γ_P
data-driven	$(0.7\%)_{K\pi}, (1.3\%)_{\pi\pi}$	$(14\%)_{K\pi}, (22\%)_{\pi\pi}$
scale setting	0.2%	0.2%
discretisation	5%	5%
dispersion relation	1%	1%
quark mass	1%	1%
inelastic thresholds	1%	1%
partial-wave truncation	1%	1%
residual finite-volume effects	0.1%	0.1%

Table 5.3 *Error budget used to quote final results on the resonance parameters. We control the data-driven systematic, while all other entries are only estimates. We quote the data-driven (*dd*), scale setting (*scale*) and other systematics separately, where the latter is obtained by rounding the total systematic coming from discretisation and the lines below it to 6% (after quadrature).*

Discretisation and dispersion relation

We work with only one lattice spacing, which means that no continuum limit is possible at this point. We instead assign a discretization systematic of $\mathcal{O}(a^2)$ from naive power counting.[164] Given a conservative estimate of $\Lambda_{QCD} \approx 400$ MeV, this corresponds to $(a\Lambda_{QCD})^2 = 5\%$, which dominates all the other following systematics.

The fit of pseudoscalar-like correlators to the continuum dispersion relation yields an error of $\approx 0.5\%$ on the speed of light. We assume that when boosted to the CM frame using the continuum relation (5.10), the interacting lattice energies used in the quantisation condition will carry a per mil effect.

Quark mass mismatch

The tuning of bare quark masses in the domain-wall action and the exact isospin symmetry inflict a per cent level difference between the pion and kaon masses in our

lattice compared to their physical values.[74] Results from chiral perturbation theory[32] imply the highest deviation on resonance parameters is also at the per cent level on the K^* and ρ widths. For near-physical pions and kaons, the variation in the resonance masses is even milder.

Residual finite-volume effects

The presence of a finite box leads to exponentially suppressed corrections due to virtual pion effects, which are discarded in the Lüscher method.[107,155] For $m_\pi L \approx 3.8$, there is a per cent level error on the asymptotic expansion leading to the quantisation condition.[110] More directly, the associated deviation on resonance parameters was previously reported to be at the per mil level in effective theory studies.[115,198]

Partial-wave truncation

Note that the quantisation condition (5.12) assumes that $\delta_{l>1} = 0$,[110] which is correct up to leading corrections coming from F-waves ($l = 3$). Due to the generic partial-wave suppression $\sim (q^*)^{-4}$ in relation to $l = 1$, we take this as a per cent effect. This is backed up by previous studies on ρ and K^* which observed only small contributions from higher partial waves subducing into lattice irreps.[134,138,180] We assume that such contributions can be neglected and only consider the P-wave component.

Multi-particle thresholds and electromagnetic effects

From unitarity, the scattering amplitude accumulates contributions to its imaginary part above the $K\pi\pi$ and $\pi\pi\pi\pi$ thresholds and the corresponding elastic phase shifts thus become complex-valued. We argue that ignoring such thresholds inflicts an error on the ρ and K^* parameters that can be taken as a systematic, as discussed in the following.

1. *Infinite volume*

In a physical point calculation, the strongest evidence comes from the experimental

branching fractions of resonances[6]

$$\begin{aligned}
&\Gamma_{K^*\to K\gamma} \approx 3\times 10^{-3}\\
&\Gamma_{K^*\to K\pi\pi} < 7\times 10^{-4}\\
&\Gamma_{K^*\to K\pi\pi\pi} \text{ (unknown)}
\end{aligned} \tag{5.28}$$

and

$$\begin{aligned}
&\Gamma_{\rho\to\pi\gamma} \approx 5\times 10^{-3}\\
&\Gamma_{\rho\to\pi\eta} \approx 6\times 10^{-3}\\
&\Gamma_{\rho\to\pi\pi\gamma} \approx 10^{-2}\\
&\Gamma_{\rho\to\pi\pi\pi\pi} < 2\times 10^{-3}.
\end{aligned} \tag{5.29}$$

Through the optical theorem, the imaginary part of the elastic phase shift due to a certain threshold will be of the order of the branching fraction on the corresponding decay channel. From the infinite-volume side, we can argue that the contribution on Γ due to decays into $K\pi\pi$ and $\pi\pi\pi\pi$ is $\lesssim 10^{-3}$ at the threshold energies. This view is reinforced by the theoretically expected chiral and phase-space suppressions of the $K\pi \to K\pi\pi$ and $\pi\pi \to \pi\pi\pi\pi$ amplitudes in comparison to their $2 \to 2$ counterparts. Furthermore, the $K\pi \to K\pi\pi$ process corresponds to an anomalous term of the Wess-Zumino form[201,202]

$$\sim F_\pi^{-5}\varepsilon_{\mu\nu\rho\sigma}\varphi'\partial_\mu\varphi\partial_\nu\varphi'\partial_\rho\varphi\partial_\sigma\varphi \tag{5.30}$$

where φ, φ' are pseudoscalar fields and F_π is the pion decay constant. Besides chirally suppressed with $\sim F_\pi^{-5} \approx (90\ \text{MeV})^{-5}$, such a term depends on very specific external momenta configurations due to a contraction with the Levi-Civita symbol, leading to an additional kinematic suppression [VI]. In fact, due to the larger decay fraction to final states with a photon, one could even argue that the inclusion of electromagnetic effects should be addressed even before multi-pion effects are detectable.

[VI] In an effective field theory of strong interactions, this term comes from the *anomalous* breaking of axial symmetry and thus it is not reducible into other contributions from the usual chiral expansion. In fact, a 3-pion vertex proportional to the λ_3 correction in (3.20) cannot arise from such a term, which can be seen by taking (5.30) into momentum space: $\varepsilon_{\mu\nu\rho\sigma}p_\mu p_\nu p_\rho p_\sigma \varphi'(q)\varphi(p_\mu)\varphi'(p_\nu)\varphi(p_\rho)\varphi(p_\sigma) + \text{perm.}$ Considering φ' as spectator ($q = -p_\nu$), we see that the φ contribution with the relevant conservation of momenta is symmetric under $\rho \leftrightarrow \sigma$ and thus vanishes when contracted with $\varepsilon_{\mu\nu\rho\sigma}$.

We are using the two-particle quantisation condition, which does not take into account finite-volume effects from diagrams where three or more propagators can simultaneously go on-shell in the s-channel.[107,110] The result is that this method ignores the imaginary part attained by the phase shift above $K\pi\pi$ and $\pi\pi\pi\pi$ thresholds, though we expect it to be small at physical quark masses.

On the other hand, due to the small coupling to the K^* and ρ resonances, cf. (5.28) and (5.29), the $K\pi\pi$ and $\pi\pi\pi\pi$ energies in their respective channels will lie very close to their non-interacting energies, except when near level crossings, *cf.* 5.13. In our main analysis, we do not use the states with level-crossings near $L \approx 48$, which we fully specify in Fig. 5.7 and Appendix D.3.1. In principle, the GEVP matrices including $K\pi\pi$ and $\pi\pi\pi\pi$ correlators can be computed numerically to directly estimate the size of off-diagonal terms, which is out of the scope of this work. Nevertheless, we expect the generic volume scaling $\langle 0|O_{K\pi}|K\pi\pi\rangle \sim L^{-3}$ and $\langle 0|O_{\pi\pi}|\pi\pi\pi\pi\rangle \sim L^{-6}$, which suggests that three and four-particle operators would have a small effect on the two-particle levels we do include in the final analysis.

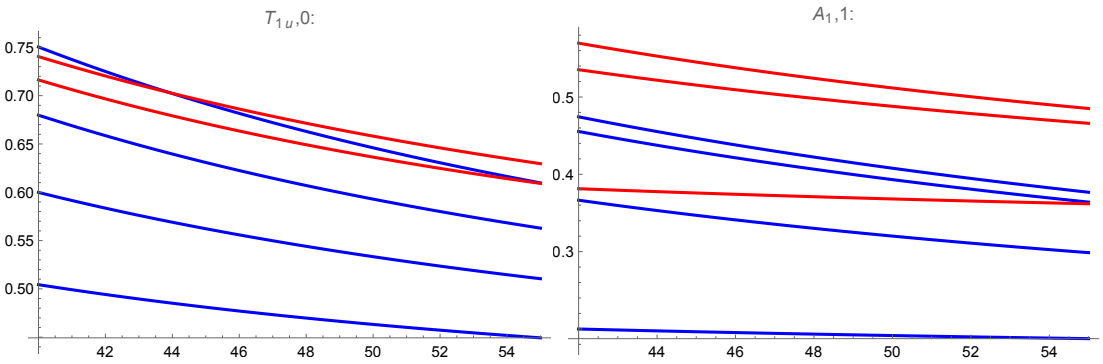

(a) $K\pi$ *and* $K\pi\pi$ **(b)** $\pi\pi$ *and* $\pi\pi\pi\pi$

Figure 5.13 *Example of two-particle (blue) and three or four-particle (red) finite-volume noninteracting energy levels and their crossings crossings as functions of* L*. See D.2 for a full non-interacting spectrum overview.*

Conclusions

In this thesis, we computed resonance parameters corresponding to the physical $K^*(892)$ and $\rho(770)$ particles using first-principles lattice QCD simulations with a physical quark masses. We estimated the associated systematics coming from the correlator fit-range choice by developing and using a data-driven technique applied to Lüscher-type calculations. The pole parameters in physical units read

$$K^*(892)\begin{cases} M_P &= 892.5(1.7)_{\mathsf{stat}}(6.5)_{\mathsf{dd}}(44.6)_{\mathsf{other}}(1.8)_{\mathsf{scale}}\ \text{MeV} \\ \Gamma_P &= 49.5(1.9)_{\mathsf{stat}}(7.2)_{\mathsf{dd}}(2.5)_{\mathsf{other}}(0.1)_{\mathsf{scale}}\ \text{MeV} \end{cases},$$

and

$$\rho(770)\begin{cases} M_P &= 788(6)_{\mathsf{stat}}(10)_{\mathsf{dd}}(39)_{\mathsf{other}}(1.6)_{\mathsf{scale}}\ \text{MeV} \\ \Gamma_P &= 186(16)_{\mathsf{stat}}(41)_{\mathsf{dd}}(9)_{\mathsf{other}}(0.4)_{\mathsf{scale}}\ \text{MeV} \end{cases},$$

where the uncertainties correspond, respectively, to statistical ("stat"), fit range and model variation ("dd") symmetrised via (A.16), other systematics from Table 5.3 ("other"), the latter dominated by the conservative discretisation error estimate, and the scale setting error ("scale"). In Fig. 5.14, we note that our K^* result shows good agreement with the pole positions obtained from experimental data using unitarized chiral perturbation theory.[203,204] The ρ result agrees only within two standard deviations of the total uncertainty [VII], suggestsing that some of the other systematics estimated in Sec. 5.4.3 ("other") might be important in this case. In Fig. 5.15, we compare the experimental phase shifts data[205,206] to our statistical and data-driven uncertainties, which leads to similar conclusions.

In this work, the distillation method was implemented in the `Grid` and `Hadrons` lattice code environment. Such codebase allowed for the large-scale simulations in this work performed at different supercomputer architectures [VIII]. Thus, besides the physics

[VII] Given by quadrature: $\sqrt{\mathsf{stat}^2 + \mathsf{dd}^2}$.

[VIII] The distillation measurements used CPU (Tesseract) and GPU (Tursa) at the Edinburgh-based

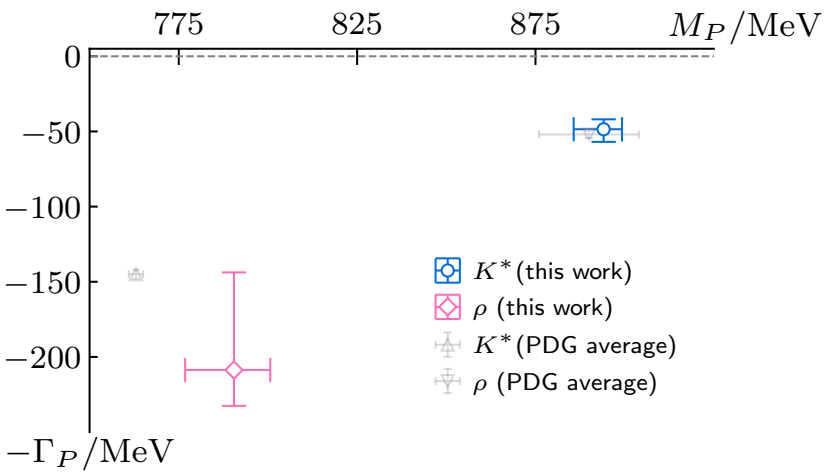

Figure 5.14 *Resonance pole positions extracted from the second Riemann sheet, with only statistical and data-driven systematics added in quadrature (colorful). The PDG estimates (gray) come from unitarized chiral perturbation theory applied to experimental data.*[6]

output presented in Chapter 5, we produced a notable use case of supercomputer facilities using lattice QCD. The effort to make the code open-source means that it can receive further improvements in the future from the community, enabling further applications. At least one separated calculation using this distillation code is already in advanced stages.[3]

We focused on providing a reliable estimate of the systematic error inherent to our analysis, anticipating future computations from realistic lattice QCD simulations featuring resonances. This involved the exploration of a model-averaging technique applied to scattering on the lattice through the importance-sampling of finite-volume energies. The data-driven method allowed us to use the spectral data more inclusively, lifting potentially uncontrolled data cuts to the GEVP eigenvalues. Instead, the choices were concentrated on exploring the potential model space and making the problem numerically well-defined at all steps.

Some improvements to this calculation are possible and also important. Firstly, this work does not provide a continuum limit for the finite-volume spectrum, which in principle is required for utilising the Lüscher method. As a consequence, the continuum limit of the resonance parameters is also not provided. Such a limit is even more important in view of the sizeable discretisation error we assume, cf. Table 5.3. A rigorous continuum limit requires the use of the available RBC-UKQCD ensembles with finer lattice spacing but the same volume and quark masses.[74] Due to

STFC DiRAC Extreme Scaling service (`www.dirac.ac.uk`).

the high cost of the domain-wall action implemented on those ensembles, this limit is particularly challenging and relies on the advancement of dedicated lattice QCD software allied to next-generation supercomputers. Nevertheless, this formulation might prove itself worth the price as recently they have been observed to approach the continuum limit at a better rate than other actions for another spectroscopic quantity.[34]

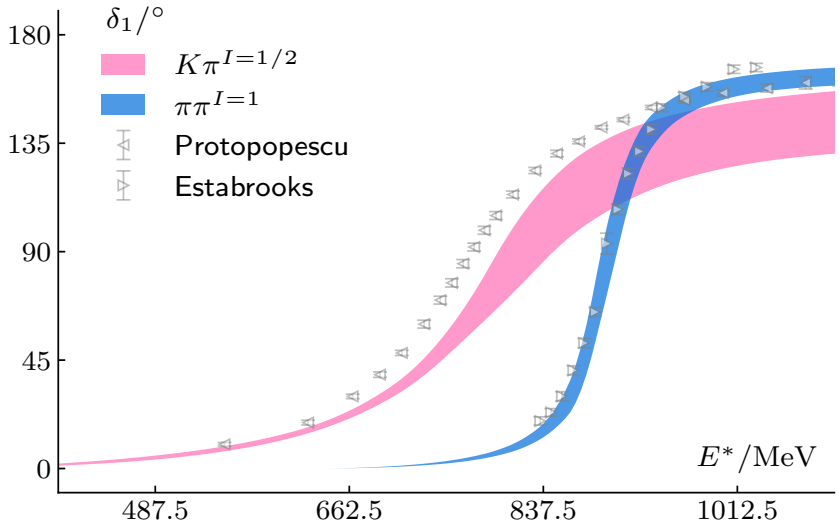

Figure 5.15 *Results for the scattering phase shift for $K\pi \to K\pi$ and $\pi\pi \to \pi\pi$ (colorful) and experimental phase-shift data (gray).*[205,206]

Secondly, even though we argued that we likely cause a small systematic by assuming elastic scattering in the range of our energies, it is theoretically important to account for the effects of $K\pi \to K^* \to K\pi\pi$ and $\pi\pi \to \rho \to \pi\pi\pi\pi$ thresholds directly. An intermediate step could be to estimate the associated diagrams in chiral perturbation theory or, preferably, by using the existing distillation data to compute the related $\langle K\pi \,|\, K\pi\pi\rangle$ and $\langle \pi\pi \,|\, \pi\pi\pi\pi\rangle$ correlators from QCD. This would already give a more quantitative estimation of the error caused by the elastic approximation, but ultimately, it would be preferable to employ the many-particle extensions of the Lüscher method which explicitly include contributions of the relevant diagrams to the quantisation condition. The so-called three-body formalism has been under steady development for the last ten years and should be soon able to approach resonances decaying to three hadrons in general.[26,117–119] Alternative approaches relying on spectrum reconstruction methods are also possible in the long-term but still need to be proven useful for the kind of amplitudes considered in this thesis.[207]

The legacy of this work is based on the use of the distillation data generated (or that was made possible to generate) and the analysis method. The κ and σ

scalar resonances can be soon studied from the same observables projected into the appropriate lattice irreps.[179,181,208,209] Additionally, the inclusion of the odd-even mixed irreps, containing not only κ but also $K^*(892)$ signatures, can be used to improve our determination of the latter. Due mainly to their large decay widths, the κ and σ have long been a theme of debate in which tetraquark and meson-meson molecule models were proposed,[210] but little is known from QCD.

Besides spectroscopic quantities, the extension of the finite-volume formalisms for the computation of transition amplitudes was significantly developed in the last years.[122,211–213] This opens the venue to a physical-mass calculation of the $\gamma \to \pi\pi$ transition amplitude, which leads to the time-like pion form factor and the hadronic corrections to the anomalous muon $g-2$ lattice determination.[138,178,214] Besides that, the radiative $K\gamma \to K\pi$ and $\pi\gamma \to \pi\pi$ transitions are also available within this dataset and would be of invaluable interest both phenomenologically and theoretically.[215–217]

A related longer-term application is to either extend our dataset or use new data at unphysical pion masses to study weak decays such as $B \to K^*$ via the variants of the Lellouch-Lüscher finite-volume methods.[116,121,218,219] The phenomenological value of a first-principles determination of such decays is demonstrated by the recent scrutinising of experimental $B \to K^*$ data in the search of physics beyond the Standard Model.[220,221] The $B \to \rho$ decays are also another possible venue for new physics from violations of lepton universality in the Standard Model,[13,222] and explorations on the lattice community at higher-than-physical quark masses are on their way.[223] Due to the difficulty of incorporating resonances with effective theory methods,[31] the determination of such processes from lattice QCD at physical quark masses is necessary for eliminating uncontrolled systematic uncertainties. In that context, the good chiral properties of domain-wall fermions simplify the renormalisation properties of electroweak currents, which can be another source of systematic.[224] Given all the above, it is clear that the progress of lattice QCD simulations is important for the overall landscape of particle physics, as currently that is the only way to rigorously treat the non-perturbative physics contained in hadronic resonances.

A Statistical Tools

A.1 Bootstrapping

In order to estimate the statistical variance of our measurements, a simulation would have to be in principle repeated many times. In lattice QCD simulations this usually not feasible due to the high computational costs. A common practice to estimate the variance is to use resampling methods such as *bootstrapping* [225].

We begin all our calculations with an initial set of n measurements of a primary quantity Y

$$\{y_1, y_2, \ldots, y_n\}. \tag{A.1}$$

We employ the bootstrap method building the n_b resampled sets of size n

$$\{y\}^{(k)} = \{y_{k_1}, y_{k_2}, \ldots, y_{k_n}\}, \quad (k) = 1, \ldots, n_b, \tag{A.2}$$

by drawing each k_j from $\{1 \ldots, n\}$ with uniform probability. The *bootstrap samples* will be given by the resampled averages

$$y^{(k)} = \frac{1}{n} \sum_{j=1}^{n} y_{k_j}, \tag{A.3}$$

and the variance of Y can be estimated by the bootstrap variance

$$\bar{\sigma}_Y^2 = \mathrm{Var}\left(y^{(k)}\right) = \frac{1}{n_b} \sum_{j=1}^{n_b} \left(y^{(k)} - \bar{y}\right)^2, \tag{A.4}$$

where

$$\bar{y} = \frac{1}{n_b} \sum_{k=1}^{n_b} y^{(k)}. \tag{A.5}$$

We quote the gauge average of the primary measurements of Y

$$Y_{(C)} = \frac{1}{n}\sum_{i=1}^{n} y_i \tag{A.6}$$

as the central value.

To estimate the variance on secondary quantities of Y, *e.g.* for some function h of Y, we compute

$$h^{(k)} = h(y^{(k)}) \tag{A.7}$$

and the variance on h thus follows by using (A.4) on $h^{(k)}$. We are commonly interested in fits to primary quantities through non-linear relations, where bootstrapping can be applied to estimate the variance on the fit parameters.

A.2 Chi-squared Fitting

We estimate the parameters $\boldsymbol{\alpha}$ of a model $\mathcal{Y}$ by minimising the standard chi-squared goodness of fit [I]

$$\chi^2(\boldsymbol{\alpha}) = \left[\boldsymbol{y} - \mathcal{Y}(\boldsymbol{x};\boldsymbol{\alpha})\right]^{\mathrm{T}} \mathbb{C}^{-1} \left[\boldsymbol{y} - \mathcal{Y}(\boldsymbol{x};\boldsymbol{\alpha})\right] \tag{A.8}$$

from $\mathcal{Y}(\boldsymbol{x},\boldsymbol{\alpha})$ to some data vector $\boldsymbol{y}$ dependent on exact $\boldsymbol{x}$. The sample covariance matrix is estimated via bootstrap as $\mathbb{C} \equiv \mathrm{Cov}(\boldsymbol{y},\boldsymbol{y})$, where

$$\mathrm{Cov}(\boldsymbol{u},\boldsymbol{v}) = \frac{1}{N_{\mathsf{boot}}-1}\sum_{k=1}^{N_{\mathsf{boot}}} (\boldsymbol{u}^{(k)} - \bar{\boldsymbol{u}})^T (\boldsymbol{v}^{(k)} - \bar{\boldsymbol{v}}), \tag{A.9}$$

and $\boldsymbol{u},\boldsymbol{v}$ are vectors of arbitrary data, *cf.* (A.5). The result of the minimisation process over the gauge-averaged data Y, *cf.* (A.6), yields the central value parameter vector $\boldsymbol{A}^*$ such that $\chi^2(\boldsymbol{A}^*) = \min_{\boldsymbol{\alpha}} \chi^2(\boldsymbol{\alpha})$ and its variance is estimated by bootstrapping, *i.e.* by repeating the minimisation on every bootstrap sample $\boldsymbol{y}^{(k)}$ and using (A.4) to estimate $\bar{\sigma}^2_{\boldsymbol{A}}$.

We can have an idea of the fit quality by computing the (two-sided) p-value

$$p = 2\min\{P(X > \chi^{2*}), P(X < \chi^{2*})\} \tag{A.10}$$

[I] For the whole data analysis, we use the open-source lattice data analysis package `LatAnalyze`.[226]

where X is a random variable sampled from the associated χ^2 distribution around $\boldsymbol{\alpha}^*$ and the data with n_{dof} degrees of freedom. Here, P is the cumulative χ^2 distribution function and thus the $p-$value represents the probability that the data was sampled from our model.

When the independent variables $\boldsymbol{x}$ are also coming from a random distribution, one should include them in the fit process by extending χ^2 and $\mathbb{C}$ to allow for their fluctuation. In the spectrum fit, the energies populate $\boldsymbol{y}$ and the energy labels are $\boldsymbol{x}$. Even though the pion and kaon masses should enter as independent variables with fluctuations through the zeta function, we fix them to the central value and argue that the difference is negligible at the current level of precision.

In practice, the chi-squared minimisations in this work are carried out on a multi-step procedure where we first perform a preconditioning at a sloppy precision which is then refined on a final step. This is implemented within the open-source library for lattice data analysis *LatAnalyze* [226]. In the preconditioning step, we use the global algorithm *GN_CRS2* [200, 227] followed by *Minuit* [228, 229] to minimise (5.2) *only* at the gauge average of the observable, with a precision of $\epsilon_{\text{precon.}} = 10^{-3}$ and ignoring the off-diagonal components of $\mathbb{C}$. This produces a single initial guess which is then fed into *Minuit* to perform the minimisation on *every* bootstrap sample with a precision $\epsilon_{\text{final}} = 10^{-7}$, now using the full covariance matrix. For the spectrum chi-squared minisation of 5.3.2, a last correlated minimisation step using the local *SLSQP* [200, 230] algorithm is performed after *Minuit* to guarantee numerical stability.

A.3 Model Averaging and AIC

In Chapter 5, we approach the scattering calculation through *model averaging*. This approach is an alternative to the common practice of *model selection*, which might overlook differences between models based on some statistical measure, *e.g.* p-value.

Assume the data is drawn from a "true model" that we wish to approximate within a given space of models $\{M\}$ and some fixed dataset $\mathcal{D}$. Given model parameters α contained in $\{M\}$, model averaging (denoted by hat) is summarised by [191]

$$\hat{\boldsymbol{\alpha}} = \sum_M \boldsymbol{\alpha}^*_M \text{pr}(M|\mathcal{D}) \tag{A.11}$$

where $\text{pr}(M|\mathcal{D})$ is the probability of the model M given the data $\mathcal{D}$, or simply the

model weights w_M. The best-fit parameters $\boldsymbol{\alpha}^*_M$ are estimated through the least-squares minimisation outlined in (A.2).

The model weights are computed from the Akaike information criterion (AIC)

$$w_M = \exp -\frac{1}{2}\mathrm{AIC}_M, \tag{A.12}$$

originally given by[231]

$$\mathrm{AIC}_M = \chi^{2*}_M + 2n_{\mathrm{par},M} \tag{A.13}$$

where χ^{2*} is our estimation of the maximum log-likelihood from least-squares fitting. The AIC approximates a (log) distance between a model and the unknown true distribution, called Kullback-Leibler divergence. The term $2n^{\mathrm{par}}$ corresponds to an asymptotic bias correction to account for finite-sample fluctuations when minimising (A.8).[191] Data exclusion can be accounted for in the AIC by the introduction of the extra terms as in (5.7),(5.8), allowing us to model-average over different data cuts.

Weighting prescription

In the language of weights, the model-averaged central value of a quantity is defined as the weighted mean of the bootstrap central value over scans

$$\hat{\boldsymbol{\alpha}} \equiv \sum_{i=1}^{M} \boldsymbol{\alpha}^i_{(C)} w^i \tag{A.14}$$

and its statistical variance is simply the variance over the bootstrap samples after weighting

$$(\Delta\boldsymbol{\alpha}_{\mathsf{stat}})^2 = \mathrm{Var}[\hat{\boldsymbol{\alpha}}^{(k)}]. \tag{A.15}$$

We take the systematic error interval $[\alpha^-_{\mathsf{syst}}, \alpha^+_{\mathsf{syst}}]$ to be the $[2\%, 98\%]$ confidence interval of the w^i-weighted distribution of the central value $\boldsymbol{\alpha}^i_{(C)}$ over scans i.[II] When explicitly quoting results, we choose to symmetrise it so that the central value is placed in the middle of the interval, *i.e.*

$$\hat{\boldsymbol{\alpha}}^{\mathsf{sym}}_{\mathsf{syst}} \equiv \frac{\boldsymbol{\alpha}^-_{\mathsf{syst}} + \boldsymbol{\alpha}^+_{\mathsf{syst}}}{2}, \tag{A.16}$$

It is pointed out in Ref. [191] that such type of systematic tends to be over-

[II] Around two standard deviations in the case of a Gaussian

conservative in comparison to

$$(\Delta\boldsymbol{\alpha}_{\mathsf{syst}}^{\mathsf{JN}})^2 = \sum_i^M (\boldsymbol{\alpha}_{(C)}^i)^2 w_i - \left(\sum_i^M \boldsymbol{\alpha}_{(C)}^i w_i\right)^2 , \tag{A.17}$$

which we test in the pion and kaon model averaging but stick to the conservative estimate in the rest of the analysis.

B Quantisation Condition Supplement

B.1 P-wave Formulas

For convenience, we define $q^* \to q^* L/2\pi$ and use the shorthand functions[112]

$$w_{lm}^{\mathbf{d}}(q^*) = \frac{\mathcal{Z}_{lm}^{\mathbf{d}}(q^*;1)}{\gamma\pi^{3/2}\sqrt{2l+1}\bar{q}^{*l+1}} \tag{B.1}$$

for the generalised zeta function (3.57), to list the P-wave quantisation conditions of the form

$$\Big[\cot\phi^{\Lambda[\mathbf{d}]}(q^*) - \cot\delta_1(q^*)\Big]_{q^*=q_{(i)}^{*\mathrm{mod}}} = 0 \tag{B.2}$$

used in this work:

Different masses - $K\pi$

$$\cot\phi^{T_{1u}[000]} = w_{00}^{[000]} \tag{B.3}$$
$$\cot\phi^{E[001]} = w_{00}^{[001]} - w_{20}^{[001]} \tag{B.4}$$
$$\cot\phi^{B_1[110]} = w_{00}^{[110]} + 2w_{20}^{[110]} \tag{B.5}$$
$$\cot\phi^{B_2[110]} = w_{00}^{[110]} - w_{20}^{[110]} - \sqrt{6}\,\mathrm{Im}\;w_{22}^{[110]} \tag{B.6}$$
$$\cot\phi^{E[111]} = w_{00}^{[111]} + i\sqrt{6}w_{22}^{[111]} \tag{B.7}$$
$$\cot\phi^{E[002]} = w_{00}^{[002]} - w_{20}^{[002]} \tag{B.8}$$
$$\tag{B.9}$$

$$\cot\phi^{T_{1u}[000]} = w_{00}^{[000]} \tag{B.10}$$

$$\cot\phi^{A_1[001]} = w_{00}^{[001]} + 2w_{20}^{[001]} \tag{B.11}$$

$$\cot\phi^{E[001]} = w_{00}^{[001]} + w_{20}^{[001]} \tag{B.12}$$

$$\cot\phi^{A_1[110]} = w_{00}^{[110]} + \frac{1}{2}w_{20}^{[110]} - \sqrt{6}\,\mathrm{Im}\;w_{21}^{[110]} + \sqrt{\frac{3}{2}}w_{22}^{[110]} \tag{B.13}$$

$$\cot\phi^{B_1[110]} = w_{00}^{[110]} + \frac{1}{2}w_{20}^{[110]} + \sqrt{6}\,\mathrm{Im}\;w_{21}^{[110]} + \sqrt{\frac{3}{2}}w_{22}^{[110]} \tag{B.14}$$

$$\cot\phi^{B_2[110]} = w_{00}^{[110]} - w_{20}^{[110]} + \sqrt{6}\,\mathrm{Im}\;w_{22}^{[110]} \tag{B.15}$$

$$\cot\phi^{A_1[111]} = w_{00}^{[111]} + \sqrt{\frac{8}{3}}\,\mathrm{Im}\;w_{22}^{[111]} + \sqrt{\frac{8}{3}}\left[\mathrm{Re}\;w_{21}^{[111]} - \mathrm{Im}\;w_{21}^{[111]}\right] \tag{B.16}$$

$$\cot\phi^{E[111]} = w_{00}^{[111]} + i\sqrt{6}w_{20}^{[111]} \tag{B.17}$$

$$\cot\phi^{E[002]} = w_{00}^{[002]} + w_{20}^{[002]} \tag{B.18}$$

$$\tag{B.19}$$

B.2 Pseudophase

In the cases where the quantisation condition is reduced to a single equation of the form (B.2), it is possible to separate and take the arccot to get[111]

$$\phi^{\Lambda[\mathbf{d}]}(q^*)\Big|_{q^*=q_n^{*\mathsf{mod}}} + n\pi = \delta(E;\boldsymbol{\alpha})\Big|_{q^*=q_n^{*\mathsf{mod}}}, \tag{B.20}$$

where n labels the n^{th} energy level on the given irrep.

One can enforce the pseudophase to be continuous in the neighbourhood of non-interacting $q^*_{n,\mathsf{free}}$ by doing

$$\phi^{\Lambda[\mathbf{d}]}(q^*) \to \phi^{\Lambda[\mathbf{d}]}(q^*) - n\pi, \quad q^*_{n,\mathsf{free}} < q^* < q^*_{n+1,\mathsf{free}}, \quad n = 0, 1, \ldots. \tag{B.21}$$

and by construction Eq. (B.20) has a unique solution for each n. For quantisation conditions of this type, there will be a unique $E_n^{*\mathsf{mod}}(\boldsymbol{\alpha})$ for a given $\boldsymbol{\alpha}$ and n. In practice, this involves a numerical root-finding procedure which we solve using the Brent-Dekker algorithm[232,233] implemented in the GSL library.[234]

C Distillation in Hadrons

C.1 Meson Field Sparsity

We have essentially three kinds of meson fields, $\varrho\varphi$, $\varphi\varphi$ and $\varrho\varrho$. Notice that in our case, sparsity exists for essentially two reasons. The first is that the action of the projectors ensures exact zeros. The second is due to the practical reason that e.g. in full-time dilution, one often cannot compute inversions on all available time slices, which implies sparsity of objects with source time indices. A characteristic function is defined in terms of the dilution partitions (4.24), for example

$$\chi^i_\alpha = \begin{cases} 1, & \text{if} \quad \alpha \in I^i \\ 0, & \text{else} \end{cases} . \tag{C.1}$$

This enables us to write the source vector 4.30 as

$$\varrho^d_\alpha(x_0) = \sum_k \chi^L_k v_k(\mathbf{x}; x_0)\ \chi^S_\alpha \chi^T_{x_0} \eta_{k\alpha}(x_0) = \chi^S_\alpha \chi^T_{x_0} \sum_k \chi^L_k v_k(\mathbf{x}; x_0) \eta_{k\alpha}(x_0), \tag{C.2}$$

which exposes its sparsity structure factorised in $\chi^S_\alpha \chi^T_{x_0}$. We can write a similar expression for φ and verify that all characteristic function indices are summed over in this case, leading to a completely dense vector.

When combined into meson fields, the distillation vectors can lead to an even larger

number of predictable zeros. For the $\varrho\varphi$ case, we have

$$\begin{aligned}\mathcal{M}_{\Gamma}^{d_1,d_2}(\varrho\varphi;x_0) &= \mathrm{tr}\sum_{\alpha,\beta}\left[\varrho_{\alpha}^{d_1}(x_0)^{\dagger}\Gamma_{\alpha\beta}\varphi_{\beta}^{d_2}(x_0)\right] \\ &= \chi_{x_0}^{T_1}\ \mathrm{tr}\sum_{\alpha,\beta}\left[\sum_{k}\chi_{k}^{L_1}v_k(x_0)^{\dagger}\chi_{\alpha}^{S_1}\eta_{k\alpha}(x_0)^{*}\Gamma_{\alpha\beta}\varphi_{\beta}^{d_2}(x_0)\right] \\ &\begin{cases}\neq 0, & \text{if} \quad x_0\in I^{T_1}\\ = 0, & \text{else}\end{cases},\end{aligned} \tag{C.3}$$

i.e., it will be zero whenever $x_0 \notin I^{T_1}$, which depends on the dilution scheme and the source time slices chosen. For example, if full time-dilution is chosen and inversions are done in every time slice, this meson field will be non-zero when $x_0 = T_1$.

For the $\rho\rho$ case, the situation is similar, i.e.

$$\begin{aligned}\mathcal{M}_{\Gamma}^{d_1,d_2}(\varrho\varrho;x_0) &= \mathrm{tr}\sum_{\alpha,\beta}\left[\varrho_{\alpha}^{d_1}(x_0)^{\dagger}\Gamma_{\alpha\beta}\varrho_{\beta}^{d_2}(x_0)\right] \\ &= \chi_{x_0}^{T_1}\chi_{x_0}^{T_2}\ \mathrm{tr}\sum_{\alpha,\beta}\left[\sum_{k}\chi_{k}^{L_1}v_k(x_0)^{\dagger}\chi_{\alpha}^{S_1}\eta_{k\alpha}(x_0)^{*}\Gamma_{\alpha\beta}\sum_{l}\chi_{l}^{L_2}v_l(x_0)^{\dagger}\chi_{\beta}^{S_2}\eta_{l\beta}(x_0)^{*}\right] \\ &\begin{cases}\neq 0, & \text{if} \quad x_0\in I^{T_1}\cap I^{T_2}\\ = 0, & \text{else}\end{cases},\end{aligned} \tag{C.4}$$

which therefore is zero whenever $x_0 \notin I^{T_1}$ or $x_0 \notin I^{T_2}$. Recalling that no dilution partition overlaps with any other partition, meaning that the $\varrho\varrho$ meson field is block diagonal in time-dilution space. For instance, if full time-dilution is chosen and inversions are done in every time slice, this meson field will be non-zero only when $x_0 = T_1 = T_2$.

We implement the time-dilution sparsity in a file specification of the meson fields in `Hadrons`.[4,175] This helps save disk space crucial for the storage of a variety of meson fields in the medium term and their use in other projects.

C.2 Exact Distillation Workflow

We keep documentation for the distillation module structure and usage within Hadrons.[235] We can schematically build the workflow for meson field production required in this work. Based on the *dataflow program paradigm*, the data gets transformed in the direction of the arrows.

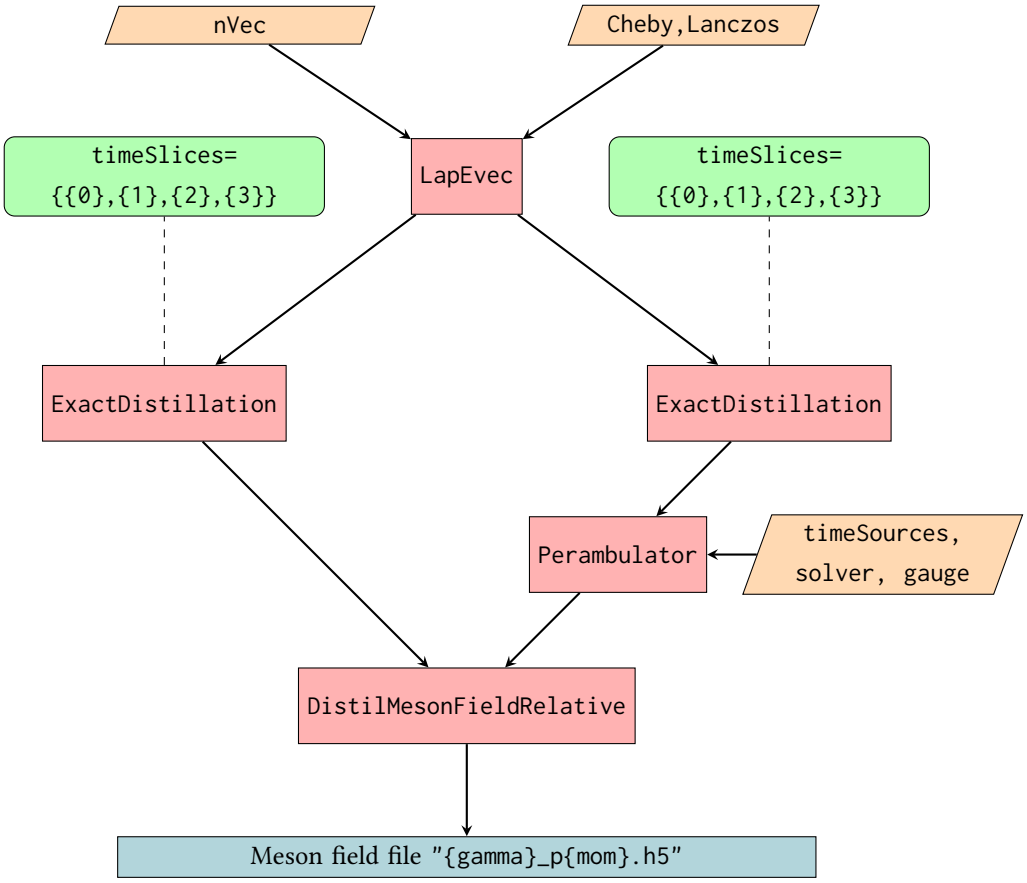

Figure C.1 *Exact distillation workflow for a $\mathcal{M}(\varrho\varphi)$ meson field within* Hadrons.[4]

It starts with input parameters (green) and modules (orange), meets component modules (red) and finishes as a meson field output saved to disk (violet). The perambulator module either computes the necessary inversions (with `solver`) or loads a file from disk. The parameters `timeSources`, `timeSources` specifies the non-zero support of the perambulator in source time. The `DistilMesonFieldRelative` module with standard input computes meson fields $\mathcal{M}^{tt'}(\varrho\varphi;t)$, where quark lines have support only on one sink time slice t'.

D Supplementary Plots

D.1 Phase-shift Parameters

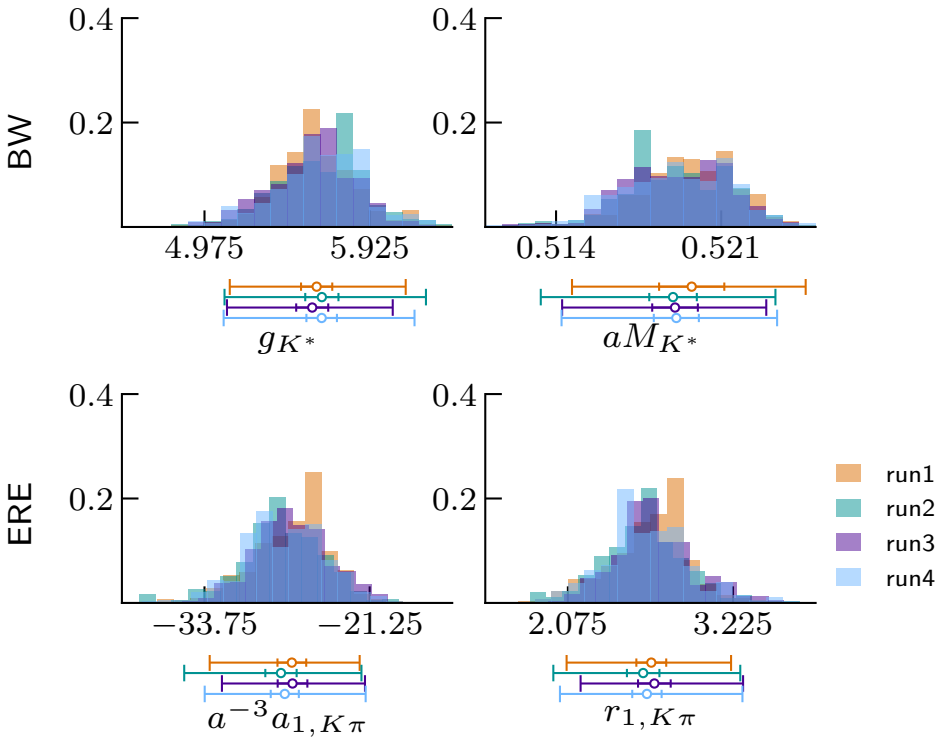

Figure D.1 *Overlaid* $\mathrm{AIC_t}$*-weighted histograms of central phase-shift parameters from fits of* BW, ERE *models to* $K\pi^{I=1/2}$ *data and all hyperparameter variations according to Table 5.1. Corresponding central (circles), statistical (smaller caps) and systematic (larger caps) errors computed according to A.3 are also shown.*

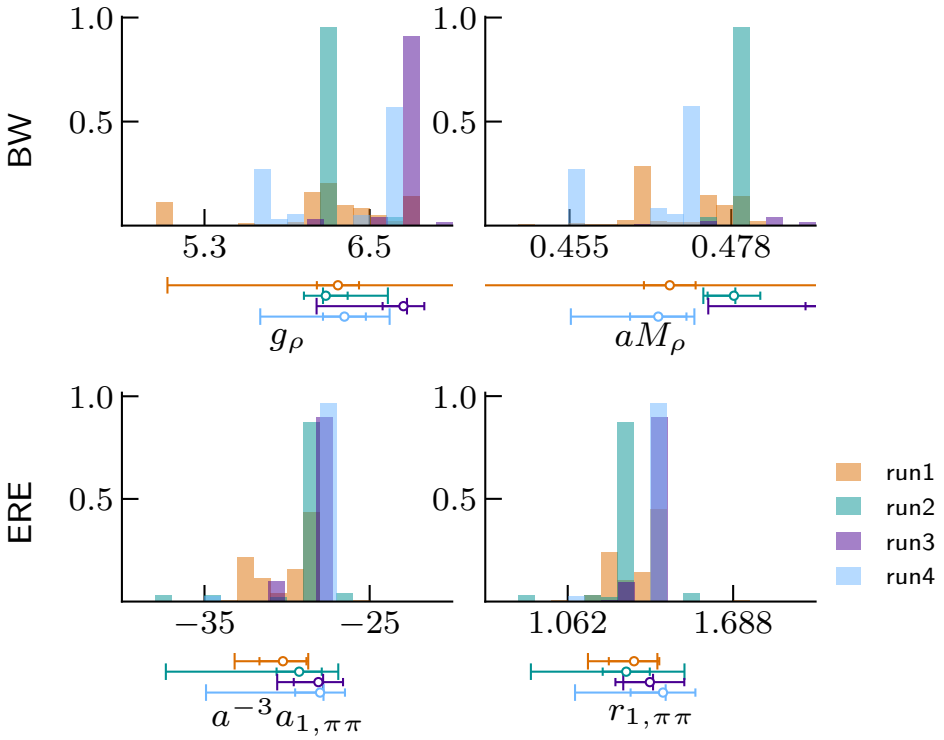

Figure D.2 *Same as Fig. D.1 for* $\pi\pi^{I=1}$.

D.2 Non-interacting Spectra

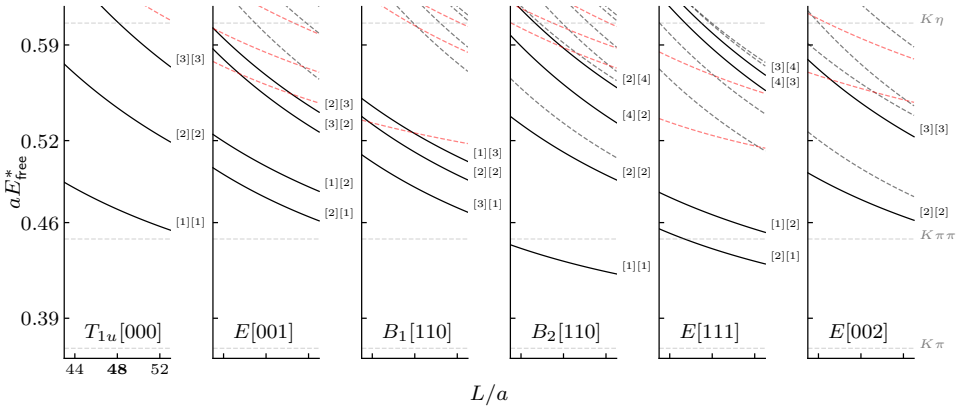

(a) $K\pi^{I=1/2}$

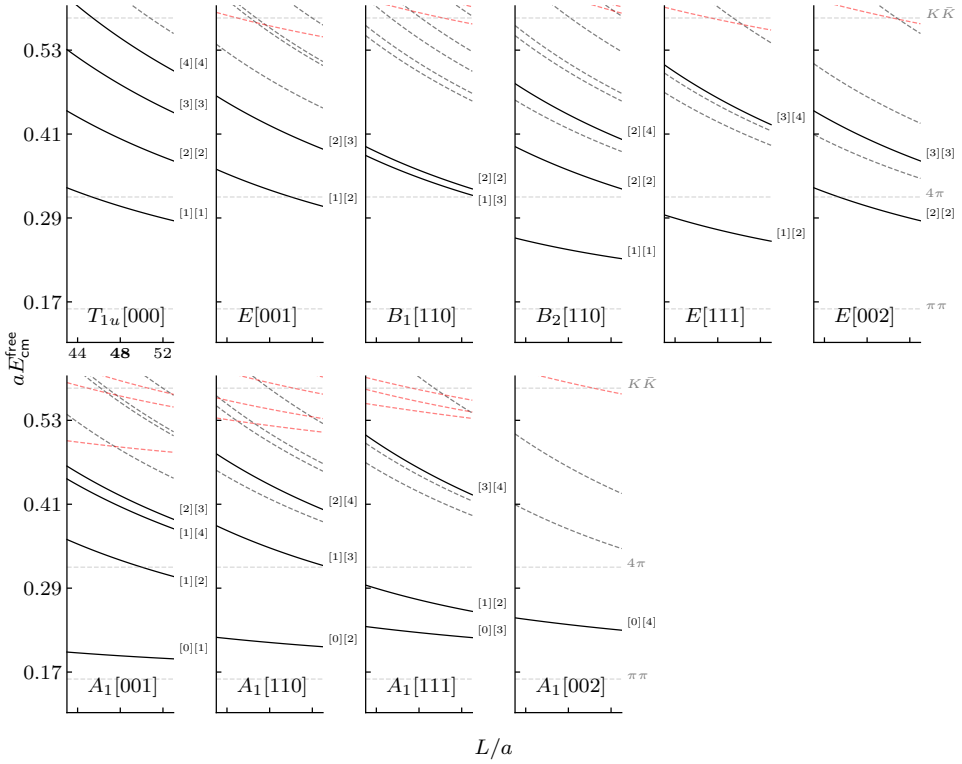

(b) $\pi\pi^{I=1}$

Figure D.3 *Following (4.74), overview of non-interacting two-particle energies in a L^3 box with momenta assignments of the $K\pi^{I=1/2}$ and $\pi\pi^{I=1}$ two-bilinear operators after momentum projection included in the GEVP (full black lines labeled as $[\mathbf{d}_K^2][\mathbf{d}_\pi^2]$ and $[\mathbf{d}_\pi^2][\mathbf{d}_\pi^2]$, respectively). The free energies corresponding to two-bilinear operators not included are also shown (dashed gray lines). The red dashed lines represent the free low-lying $K\pi\pi$ and $\pi\pi\pi\pi$ states in the corresponding irreps.*

D.3 GEVP

D.3.1 Effective spectra

We show here the effective log-mass spectra boosted to the CM frame for fixed $t_0 = 3$, together with the AIC_{corr}-weighted histograms of the associated single-exponential fit result with hyperparameters $(\mathsf{SNR}_{\mathsf{min}}, \delta t_{\mathsf{min}}) = (8, 4)$. We fade out the levels we do not use in the scattering analysis. We also show the two-particle noninteracting energies (horizontal lines) from momentum components corresponding to the two-bilinears we employ in the GEVP.

$\boldsymbol{K\pi^{I=1/2}}$

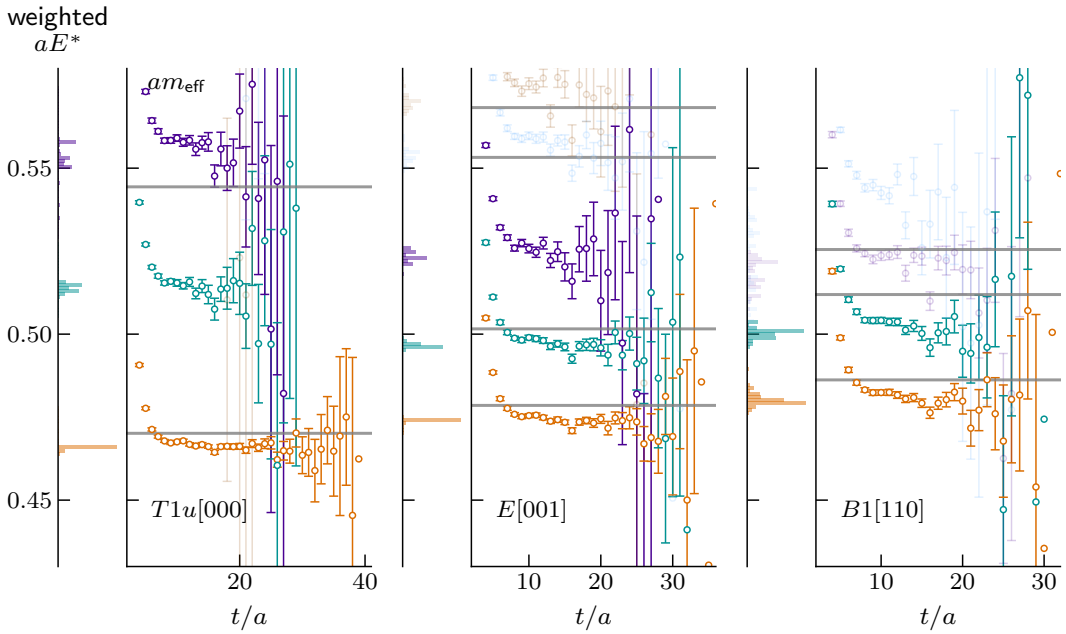

Figure D.4 $\Lambda[\mathbf{d}] = T_{1u}[000], E[001], B_1[110]$

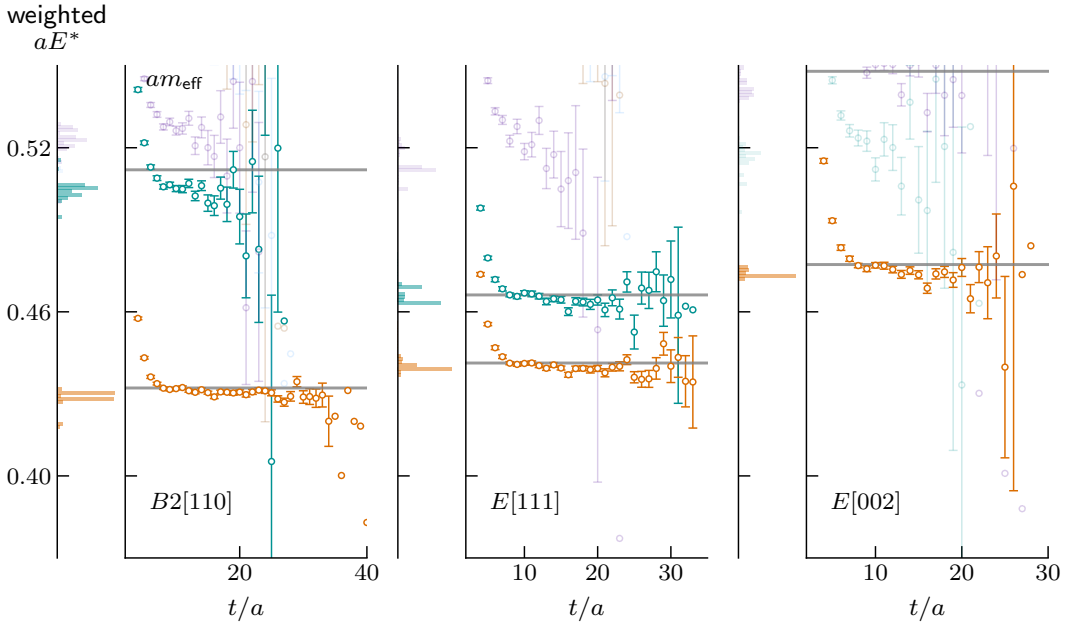

Figure D.5 $\Lambda[\mathbf{d}] = B_2[110], E[111], E[002]$.

$\boldsymbol{\pi\pi}^{I=1}$

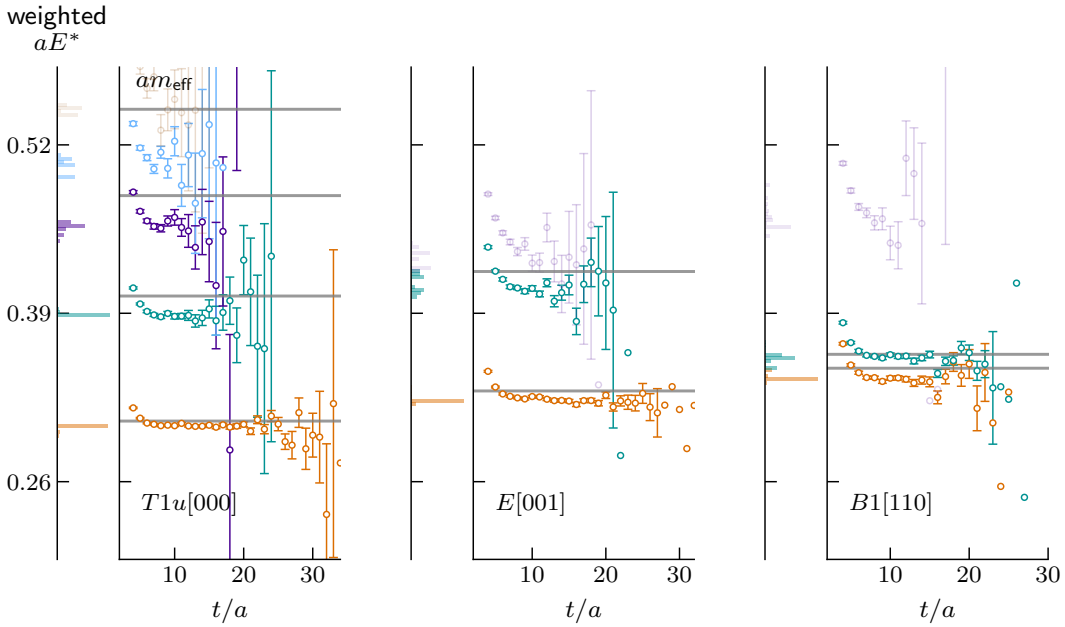

Figure D.6 $\Lambda[\mathbf{d}] = T_{1u}[000], E[001], B_1[110]$.

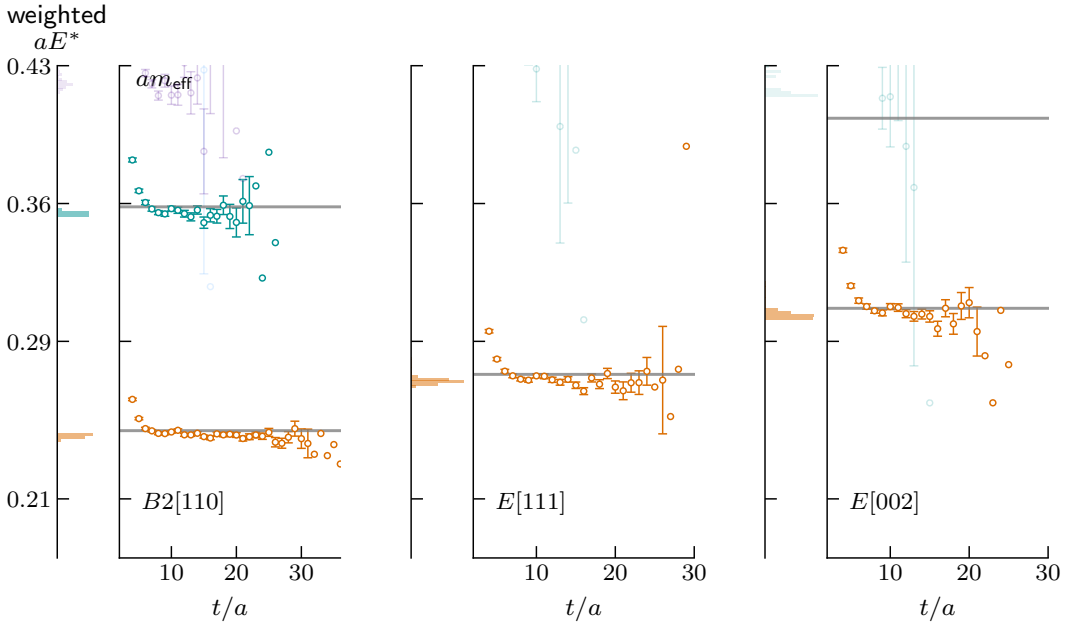

Figure D.7 $\Lambda[\mathbf{d}] = B_2[110], E[111], E[002]$.

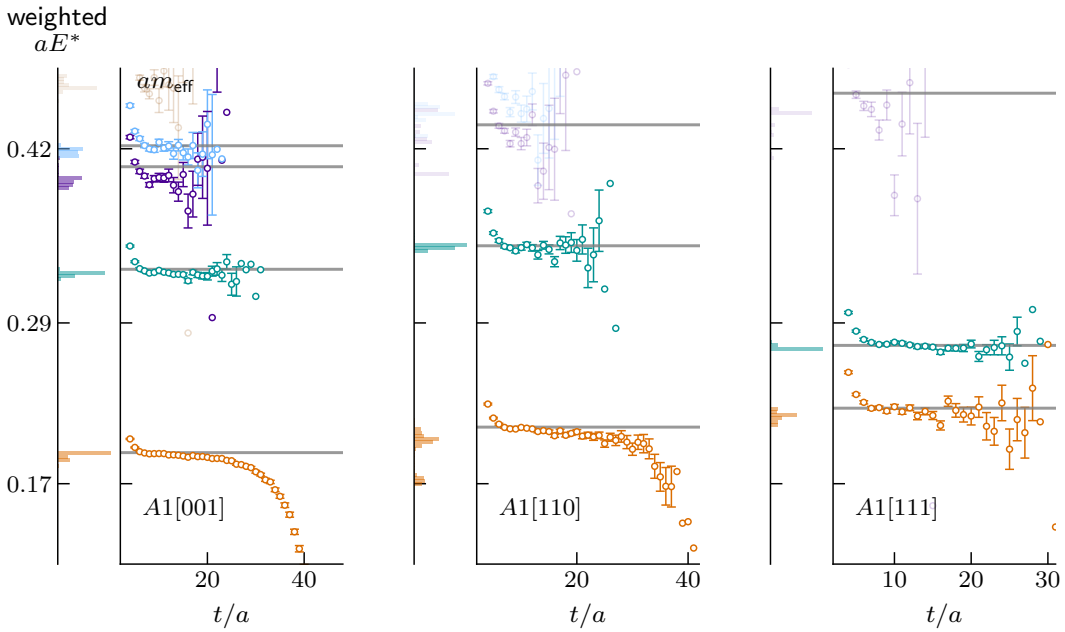

Figure D.8 $\Lambda[\mathbf{d}] = A_1[001], A_1[110], A_1[111]$.

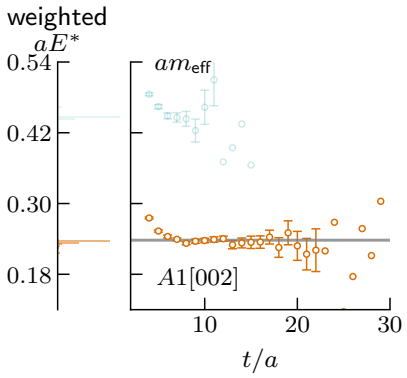

Figure D.9 $\Lambda[\mathbf{d}] = A_1[002]$.

D.3.2 Thermal effects in $A_1[001], A_1[110]$

In the particular case of the ground states of the $\pi\pi, A_1[110]$ and $A_1[001]$ irreps (Fig. D.8), note the downwards trend on the log effective masses. This reflects the propagation of pions through the temporal periodic boundaries, amounting to spurious contributions to the correlator spectral decomposition at large times. In the case of $A_1[001]$, the choice $(\mathsf{SNR}_{\mathsf{min}}, \delta t_{\mathsf{min}}) = (8, 4)$ satisfactorily weights out the fits to this spurious data. However, for $A_1[110]$ this is not the case. In Fig. D.10, we show that different hyperparameters suppress the thermal effects on the $\mathsf{AIC}_{\mathsf{corr}}$-weighted histograms.

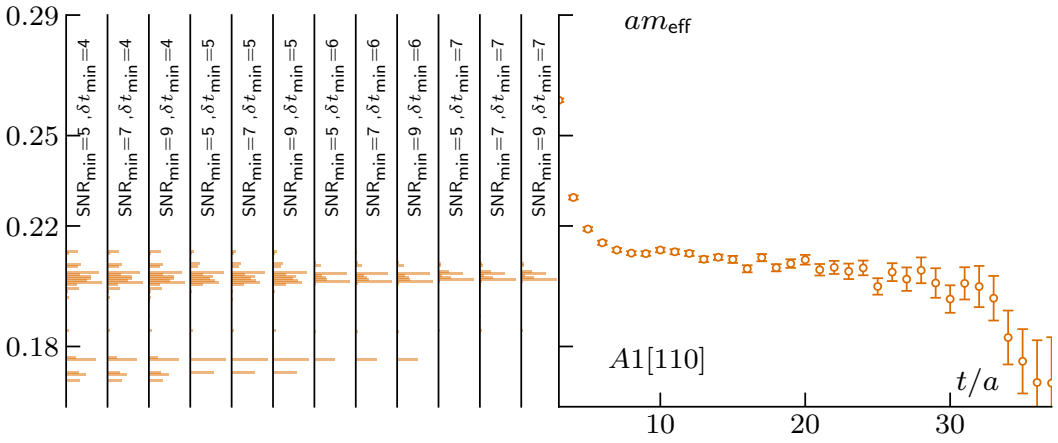

Figure D.10 *Left:* $\mathsf{AIC}_{\mathsf{corr}}$*-weighted histograms of* $\pi\pi, A_1[110]$ *fits for different* $(\mathsf{SNR}_{\mathsf{min}}, \delta t_{\mathsf{min}})$. *Right: corresponding log effective mass. Increasing* δt_{min} *suppresses the tails on the histograms by forbidding small plateau regions.*

D.3.3 Variation of parameter t_0

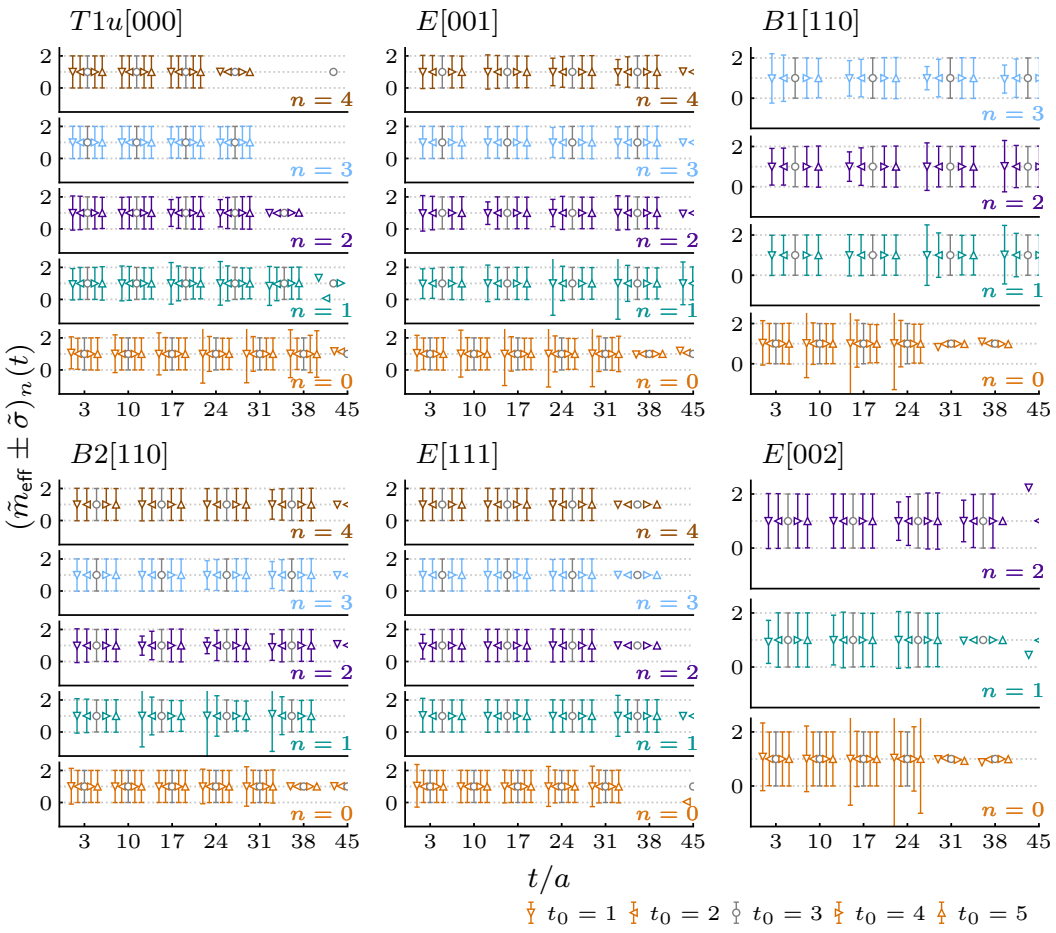

Figure D.11 *$K\pi^{I=1/2}$: ratios between GEVP log effective masses $m_{\text{eff}}(t;t_0)$ and $m_{\text{eff}}(t;t_0^{\text{ref}}=3)$, i.e. $\tilde{m}_{\text{eff}}(t) \equiv m_{\text{eff}}(t;t_0)/m_{\text{eff}}(t;3)$. Analogously, the errorbars are the ratios of the corresponding standard deviations, i.e. $\tilde{\sigma}(t) \equiv \sigma(t;t_0)/\sigma(t;3)$. We plot only every 7^{th} time slice for a clear but still overall visualisation of the time extension.*

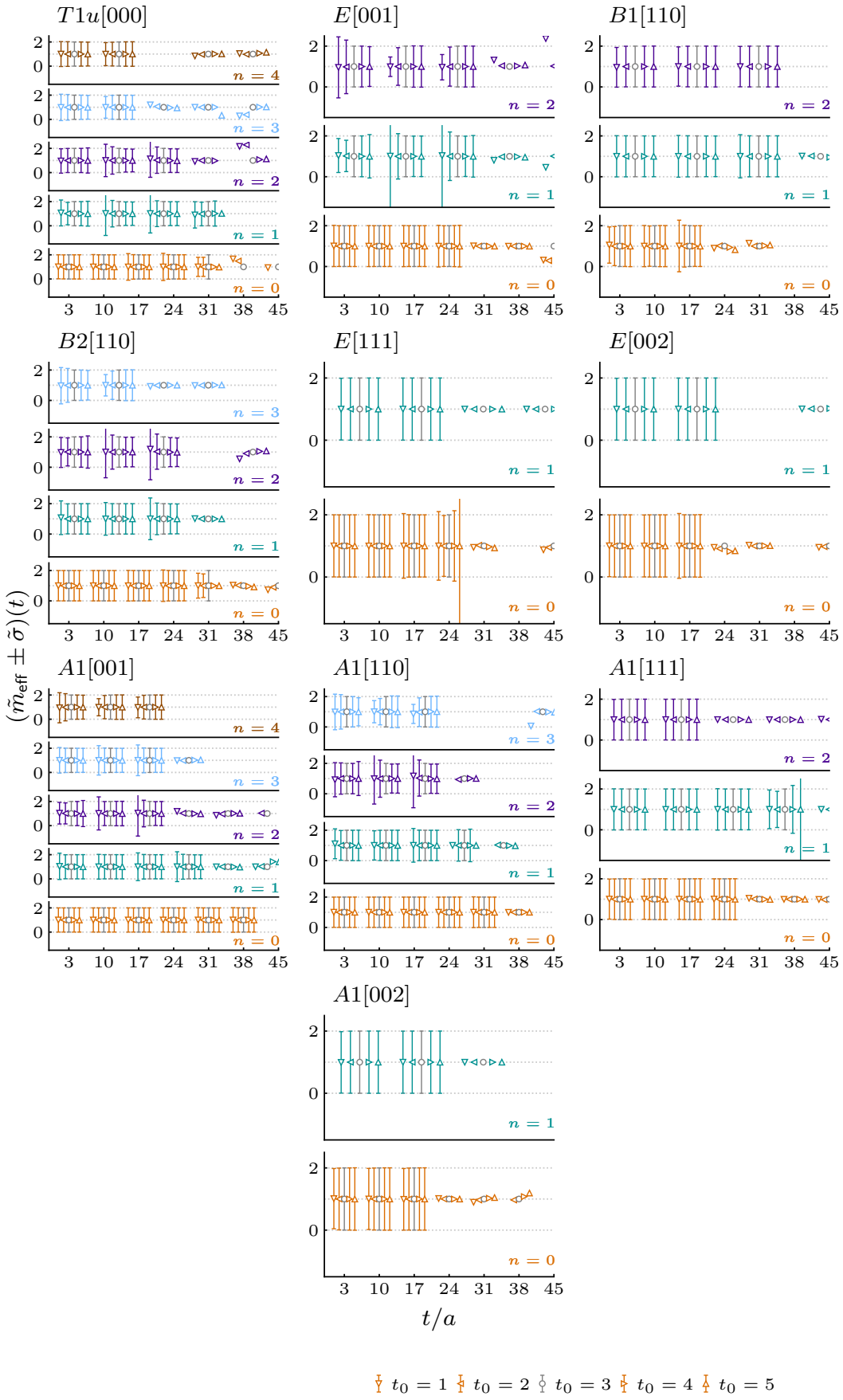

Figure D.12 *Same as Fig.D.11 for* $\pi\pi^{I=1}$.

D.3.4 Group averaging

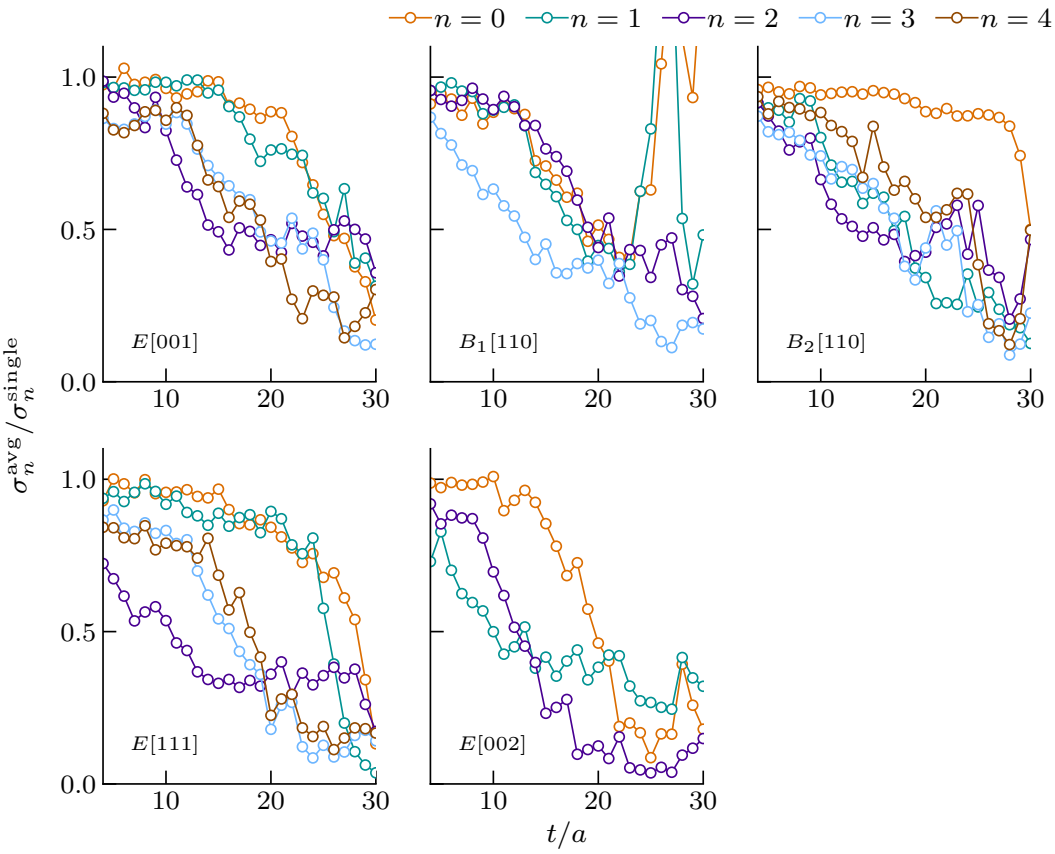

Figure D.13 *Ratio of the standard deviation of eigenvalues before and after group averaging for $K\pi^{I=1/2}$ data.*

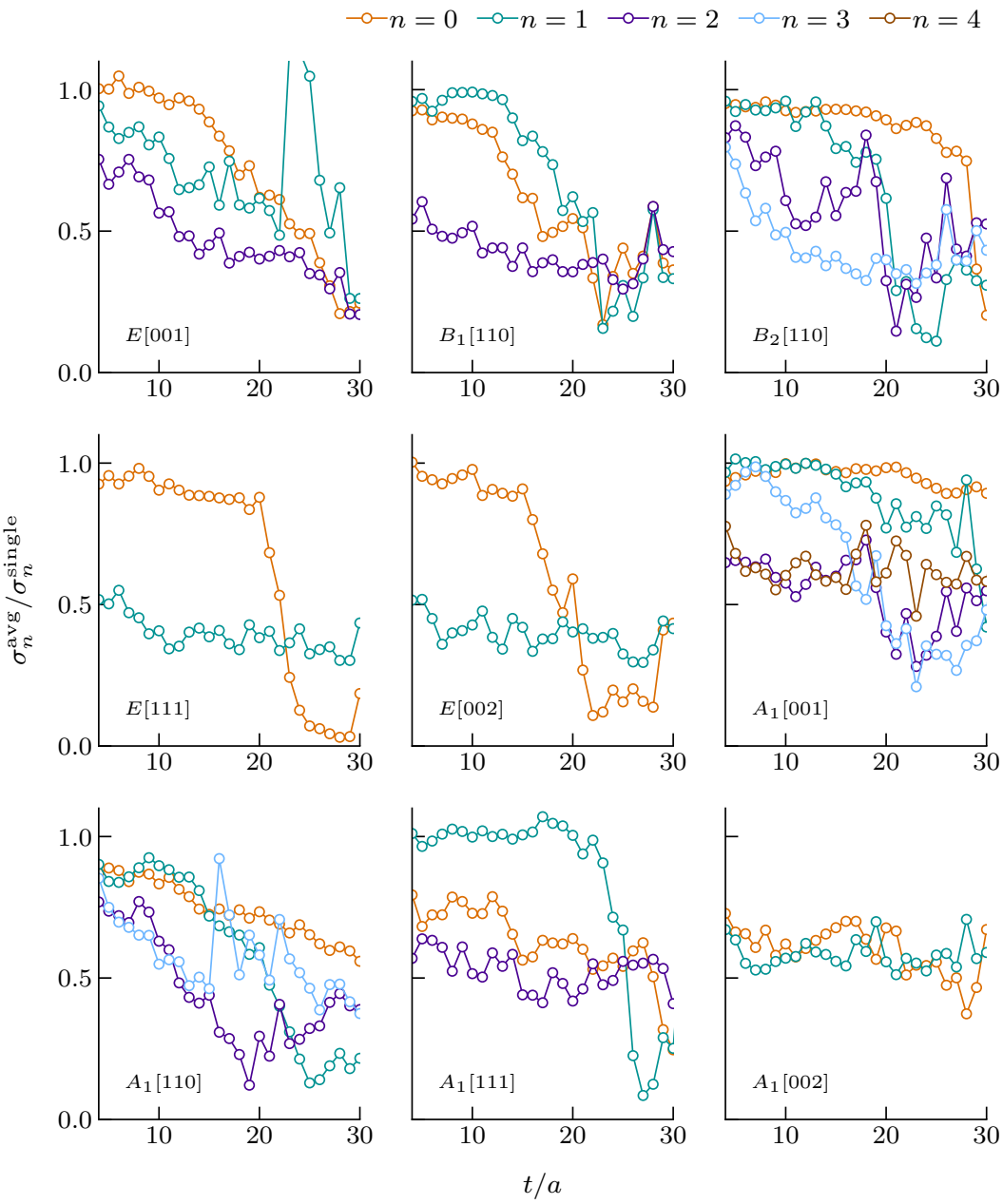

Figure D.14 *Same as Fig.D.13 for* $\pi\pi^{I=1}$.

Bibliography

[1] N. P. Lachini et al. “Kπ scattering at physical pion mass using distillation”. In: *Proceedings of Science* 396 (2022), pp. 1–11. arXiv: 2112.09804.

[2] N. P. Lachini et al. “Towards Kπ scattering with domain-wall fermions at the physical point using distillation”. In: *Proceedings of The 39th International Symposium on Lattice Field Theory — PoS(LATTICE2022).* Trieste, Italy: Sissa Medialab, 2023, p. 076. arXiv: arXiv:2211.16601v1.

[3] F. B. Erben et al. “Exploring distillation at the SU(3) flavour symmetric point”. In: *LATTICE2022, 39th International Symposium on Lattice Field Theory* (2022). arXiv: arXiv:2211.15627.

[4] A. Portelli et al. “aportelli/Hadrons: Hadrons v1.4”. In: *10.5281/zenodo.8023716* (2023).

[5] P. A. Boyle et al. “Physical-mass calculation of $\rho(770)$ and $K^*(892)$ resonance parameters via $\pi\pi$ and $K\pi$ scattering amplitudes from lattice QCD”. In: *In preparation* (2024).

[6] R. L. Workman et al. “Review of Particle Physics (PDG)”. In: *Progress of Theoretical and Experimental Physics* 2022.8 (2022), p. 083C01.

[7] R. L. Workman et al. “15. Quark Model (PDG Review)”. In: *Progress of Theoretical and Experimental Physics* 2022.8 (2022), p. 083C01.

[8] D. Galbraith and C. Burgard. “UX: Standard Model of the Standard Model”. In: *http://davidgalbraith.org/portfolio/ux-standard-model-of-the-standard-model/* (2014).

[9] R. L. Workman et al. “63. Spectroscopy of Light Meson Resonances (PDG Review)”. In: *Progress of Theoretical and Experimental Physics* 2022.8 (2022), p. 083C01.

[10] R. A. Briceño, J. J. Dudek, and R. D. Young. “Scattering processes and resonances from lattice QCD”. In: *Reviews of Modern Physics* 90.2 (2018), p. 25001. arXiv: 1706.06223.

[11] G. Colangelo et al.
"Prospects for precise predictions of a_μ in the Standard Model".
In: *Snowmass 2021* Snowmass (2022), pp. 1–24. arXiv: 2203.15810.

[12] A. Sibidanov et al. "Study of exclusive $B \to X_u \ell \nu$ decays and extraction of $|V_{ub}|$ using full reconstruction tagging at the Belle experiment".
In: *Physical Review D* 88.3 (2013), p. 032005. arXiv: 1306.2781.

[13] F. U. Bernlochner, Z. Ligeti, and S. Turczyk.
"New ways to search for right-handed current in $B \to \rho \ell \bar{\nu}$".
In: *Physical Review D* 90.9 (2014), p. 094003. arXiv: 1408.2516.

[14] A. S. Kronfeld. "Twenty-First Century Lattice Gauge Theory: Results from the Quantum Chromodynamics Lagrangian".
In: *Annual Review of Nuclear and Particle Science* 62.1 (2012), pp. 265–284.

[15] R. L. Workman et al.
"17. Lattice Quantum Chromodynamics (PDG Review)".
In: *Progress of Theoretical and Experimental Physics* 2022.8 (2022), p. 083C01.

[16] Y. Aoki et al. "FLAG Review 2021".
In: *European Physical Journal C* 82.10 (2022). arXiv: 2111.09849.

[17] M. Lüscher. "Computational Strategies in Lattice QCD".
In: *Lectures given at the Summer School on "Modern perspectives in lattice QCD", Les Houches* (2010). arXiv: 1002.4232.

[18] P. A. Boyle et al. "Lattice QCD and the Computational Frontier".
In: *Snowmass 2021*. 2022, pp. 1–21. arXiv: 2204.00039.

[19] Sz. Borsanyi et al. "Leading hadronic contribution to the muon magnetic moment from lattice QCD". In: *Nature* 593.7857 (2021), pp. 51–55. arXiv: 2002.12347.

[20] A. S. Kronfeld et al. "Lattice QCD and Particle Physics".
In: *Snowmass 2021* (2021). arXiv: 2207.07641.

[21] H. Wittig. "Progress on $(g-2)_\mu$ from Lattice QCD". In: *57th Rencontres de Moriond on Electroweak Interactions and Unified Theories* 2 (2023), pp. 1–9. arXiv: 2306.04165.

[22] S. Durr et al. "Ab Initio Determination of Light Hadron Masses".
In: *Science* 322.5905 (2008), pp. 1224–1227. arXiv: 0906.3599.

[23] A. Bazavov et al. "Nonperturbative QCD simulations with 2+1 flavors of improved staggered quarks".
In: *Reviews of Modern Physics* 82.2 (2010), pp. 1349–1417. arXiv: 0903.3598.

[24] Robert G. Edwards et al.
"Excited state baryon spectroscopy from lattice QCD".
In: *Physical Review D* 84.7 (2011), p. 074508. arXiv: 1104.5152.

[25] L. Maiani and M. Testa.
"Final state interactions from euclidean correlation functions".
In: *Physics Letters B* 245.3-4 (1990), pp. 585–590.

[26] M. T. Hansen and Stephen R. Sharpe.
"Lattice QCD and Three-Particle Decays of Resonances".
In: *Annual Review of Nuclear and Particle Science* 69.1 (2019), pp. 65–107.
arXiv: 1901.00483.

[27] M. T. Hansen. "Pushing the Periodic Boundaries".
In: *Proceedings of The 38th International Symposium on Lattice Field Theory — PoS(LATTICE2021)* 396 (2022), p. 024.

[28] M. Peardon et al. "Novel quark-field creation operator construction for hadronic physics in lattice QCD".
In: *Physical Review D* 80.5 (2009), p. 054506.

[29] C. Morningstar et al. "Improved stochastic estimation of quark propagation with Laplacian Heaviside smearing in lattice QCD".
In: *Physical Review D* 83.11 (2011), p. 114505. arXiv: 1104.3870.

[30] A. D. Hanlon.
"Hadron spectroscopy and few-body dynamics from lattice QCD".
In: *Proceedings of The 40th Annual International Symposium on Lattice Field Theory — PoS(LATTICE2023)* (2024). arXiv: 2402.05185.

[31] C. Hanhart, J. R. Peláez, and G. Ríos. "Quark-mass dependence of the ρ and σ mesons from dispersion relations and chiral perturbation theory".
In: *Physical Review Letters* 100.15 (2008). arXiv: arXiv:0801.2871v2.

[32] J. Nebreda and J. R. Peláez.
"Strange and nonstrange quark mass dependence of elastic light resonances from SU(3) unitarized chiral perturbation theory to one loop".
In: *Physical Review D* 81.5 (2010), p. 054035. arXiv: 1001.5237.

[33] R. Molina and J. Ruiz de Elvira.
"Light- and strange-quark mass dependence of the $\rho(770)$ meson revisited".
In: *Journal of High Energy Physics* 2020.11 (2020), p. 17. arXiv: 2005.13584.

[34] J. R. Green et al.
"Weakly Bound H Dibaryon from SU(3)-Flavor-Symmetric QCD".
In: *Physical Review Letters* 127.24 (2021). arXiv: 2103.01054.

[35] C. Lehner et al.
"Opportunities for Lattice QCD in quark and lepton flavor physics".
In: *The European Physical Journal A* 55.11 (2019), p. 195. arXiv: 1904.09479.

[36] V. Cirigliano et al. "The role of Lattice QCD in searches for violations of fundamental symmetries and signals for new physics".
In: *The European Physical Journal A* 55.11 (2019), p. 197. arXiv: 1904.09704.

[37] G. Zweig.
"An SU(3) model for strong interaction symmetry and its breaking".
In: *Developments in the quark theory of hadrons.*
Geneva: Hadronic Press, 1964, pp. 22–101.

[38] M. Gell-Mann. "A schematic model of baryons and mesons".
In: *Physics Letters* 8.3 (1964), pp. 214–215.

[39] C. N. Yang and R. L. Mills.
"Conservation of isotopic spin and isotopic Gauge invariance".
In: *Physical Review* 96.1 (1954), pp. 191–195.

[40] S. Weinberg. "A model of leptons".
In: *Physical Review Letters* 19.21 (1967), pp. 1264–1266.

[41] A. Salam. "Weak and electromagnetic interactions".
In: *Selected Papers of Abdus Salam*. Ed. by A Ali et al.
World scientific series in 20th century physics.
Singapore: World Scientific, 1994, pp. 244–254.

[42] P. W. Higgs. "Broken Symmetries and the Masses of Gauge Bosons".
In: *Physical Review Letters* 13.16 (1964), pp. 508–509.

[43] F. Englert and R. Brout.
"Broken symmetry and the mass of Gauge vector mesons".
In: *Physical Review Letters* 13.9 (1964), pp. 321–323.

[44] G. S. Guralnik, C. R. Hagen, and T. W. B. Kibble.
"Global Conservation Laws and Massless Particles".
In: *Physical Review Letters* 13.20 (1964), pp. 585–587.

[45] O. W. Greenberg. "Spin and Unitary-Spin Independence in a Paraquark Model of Baryons and Mesons".
In: *Physical Review Letters* 13.20 (1964), pp. 598–602.

[46] J. Bulava et al. "String breaking by light and strange quarks in QCD".
In: *Physics Letters B* 793 (2019), pp. 493–498. arXiv: 1902.04006.

[47] J. Greensite. *An Introduction to the Confinement Problem*. Vol. 972.
Lecture Notes in Physics. Cham: Springer International Publishing, 2020.

[48] D. J. Gross and F. Wilczek.
"Ultraviolet behavior of non-Abelian Gauge theories".
In: *Physical Review Letters* 30.26 (1973), pp. 1343–1346.

[49] H. D. Politzer. "Reliable perturbative results for strong interactions?"
In: *Physical Review Letters* 30.26 (1973), pp. 1346–1349.

[50] S. L. Adler. "Axial-Vector Vertex in Spinor Electrodynamics".
In: *Physical Review* 177.5 (1969), pp. 2426–2438.

[51] J. S. Bell and R. Jackiw. "A PCAC puzzle: $\pi^0 \to \gamma\gamma$ in the σ-model".
In: *Il Nuovo Cimento A* 60.1 (1969), pp. 47–61.

[52] R.P. Feynman and A.R. Hibbs. *Quantum Mechanics and Path Integrals*.
New York: McGraw-Hill, 1965.

[53] M. Schwartz. "Quantum Field Theory and the Standard Model". In:
Cambridge: Cambridge University Press, 2014.

[54] C. Alexandrou et al. "Neutron electric dipole moment using lattice QCD simulations at the physical point".
In: *Physical Review D* 103.5 (2021), p. 54501. arXiv: 2011.01084.

[55] M. Lüscher, K. Symanzik, and P. Weisz.
Anomalies of the free loop wave equation in the WKB approximation.
Tech. rep. 1980, pp. 365–396.

[56] M. E. Peskin and D. V. Schroeder. *An Introduction to Quantum Field Theory.*
Frontier of Physics. Boulder: Westview Press, 1995.

[57] S. U. Chung et al. "Partial wave analysis in K-matrix formalism".
In: *Annalen der Physik* 507.5 (1995), pp. 404–430.

[58] C. B. Lang. "The πK Scattering and Related Processes".
In: *Fortschritte der Physik* 26.10 (1978), pp. 509–564.

[59] Y. Aoki et al. "Continuum limit physics from 2+1 flavor domain wall QCD".
In: *Physical Review D* 83.7 (2011), p. 074508. arXiv: 1011.0892.

[60] R. L. Workman et al. "50.Resonances (PDG Review)".
In: *Progress of Theoretical and Experimental Physics* 2022.8 (2022), p. 083C01.

[61] G. Breit and E. Wigner. "Capture of slow electrons".
In: *Phys. Rev.* 49.1935 (1936), p. 519.

[62] L. Fonda, G. C. Ghirardi, and A. Rimini.
"Decay theory of unstable quantum systems".
In: *Reports on Progress in Physics* 41.4 (1978), pp. 587–631.

[63] D. Cocolicchio. "Characterization of unstable particles".
In: *Physical Review D* 57.12 (1998), pp. 7251–7261.

[64] V. I. Kuksa. "Unstable states in quantum theory".
In: *Physics of Particles and Nuclei* 45.3 (2014), pp. 568–608.

[65] R. E. Peierls. "Interpretation and properties of propagators".
In: *Proceedings of the Glasgow Conference on Nuclear and Meson Physics.*
Pergamon Press London, 1954.

[66] M. Lévy. "On the description of unstable particles in quantum field theory".
In: *Il Nuovo Cimento* 13.1 (1959), pp. 115–143.

[67] V. Gribov. *Strong Interactions of Hadrons at High Energies.*
Cambridge: Cambridge University Press, 2008, p. 400.

[68] K. Osterwalder and R. Schrader. "Axioms for Euclidean Green's functions".
In: *Communications in Mathematical Physics* 31.2 (1973), pp. 83–112.

[69] K. G. Wilson. "Confinement of quarks".
In: *Physical Review D* 10.8 (1974), pp. 2445–2459.

[70] M. Lüscher. "Construction of a selfadjoint, strictly positive transfer matrix for Euclidean lattice gauge theories".
In: *Communications in Mathematical Physics* 54.3 (1977), pp. 283–292.

[71] István Montvay and G. Münster. *Quantum fields on a lattice.*
Cambridge Univ. Press, 1994.

[72] E Seiler and D. Zwanziger.
Monte Carlo Simulation of Non-Compact QCD with Stochastic Gauge Fixing.
Tech. rep. 1984, pp. 177–200.

[73] A. Cucchieri and T. Mendes.
"Critical slowing-down in SU(2) Landau gauge-fixing algorithms".
In: *Nuclear Physics B* 471.1-2 (1996), pp. 263–290.

[74] T. Blum et al. "Domain wall QCD with physical quark masses".
In: *Physical Review D* 93.7 (2016), p. 074505. arXiv: 1411.7017.

[75] D. J. Antonio et al.
"Localization and chiral symmetry in three flavor domain wall QCD". In:
Physical Review D - Particles, Fields, Gravitation and Cosmology 77.1 (2008).
arXiv: 0705.2340.

[76] Y. Iwasaki.
"Renormalization Group Analysis of Lattice Theories and Improved Lattice Action. II – four-dimensional non-abelian SU(N) gauge model".
In: 118 (2011). arXiv: 1111.7054.

[77] M. Creutz. *Quarks, Gluons and Lattices.*
Cambridge: Cambridge University Press, 1983.

[78] C. Gattringer and C. B. Lang. *Quantum Chromodynamics on the Lattice.*
Vol. 788. Springer Berlin Heidelberg, 2010.

[79] J. G. Smith. *Introduction to quantum fields on a lattice.* Vol. 15.
Cambridge lecture notes in physics.
Cambridge: Cambridge University Press, 2002.

[80] D. Kaplan. "Chiral Symmetry and Lattice Fermions".
In: *Modern Perspectives in Lattice QCD.* 2011.

[81] H. Neuberger. "A practical implementation of the overlap dirac operator".
In: *Physical Review Letters* 81.19 (1998), pp. 4060–4062.
arXiv: 9806025 [hep-lat].

[82] D. Kaplan. "A method for simulating chiral fermions on the lattice".
In: *Physics Letters B* 288.3-4 (1992), pp. 342–347. arXiv: 9206013 [hep-lat].

[83] V. Furman and Y. Shamir.
"Axial symmetries in lattice QCD with Kaplan fermions".
In: *Nuclear Physics, Section B* 439.1-2 (1995), pp. 54–78.
arXiv: 9405004 [hep-lat].

[84] T. Blum. "Domain wall fermions in vector gauge theories".
In: *Nuclear Physics B - Proceedings Supplements* 73.1-3 (1999), pp. 167–179.
arXiv: 9810017 [hep-lat].

[85] R. C. Brower and H. Neff. "The Mobius Domain Wall Fermion Algorithm".
In: (2012), pp. 1–51. arXiv: arXiv:1206.5214v1.

[86] G. McGlynn. "Algorithmic improvements for weak coupling simulations of domain wall fermions". In: *Proceedings of The 33rd International Symposium on Lattice Field Theory — PoS(LATTICE 2015).* July.
Trieste, Italy: Sissa Medialab, 2016, p. 019.

[87] A. Sokal. “Monte Carlo Methods in Statistical Mechanics: Foundations and New Algorithms”. In: *Lectures at the Cargése Summer Schoolon on "Functional Integration Basics and Applications"*. Ed. by Cecile DeWitt-Morette, Pierre Cartier, and Antoine Folacci. Vol. 361. NATO ASI series B: physics. Boston, MA: Springer US, 1997, pp. 131–192.

[88] N. Metropolis et al. “Equation of state calculations by fast computing machines”. In: *The Journal of Chemical Physics* 21.6 (1953), pp. 1087–1092.

[89] S. Duane et al. “Hybrid Monte Carlo”. In: *Physics Letters B* 195.2 (1987), pp. 216–222.

[90] U. Wolff. “Monte Carlo errors with less errors”. In: *Computer Physics Communications* 156.2 (2004), pp. 143–153.

[91] C. E. Thomas, R. G. Edwards, and J. J. Dudek. “Helicity operators for mesons in flight on the lattice”. In: *Physical Review D* 85.1 (2012), p. 014507. arXiv: 1107.1930.

[92] M. S. Dresselhaus, G. Dresselhaus, and A. Jorio. *Group Theory: Application to the Physics of Condensed Matter*. 2008.

[93] R.C. Johnson. “Angular momentum on a lattice”. In: *Physics Letters B* 114.2-3 (1982), pp. 147–151.

[94] D. C. Moore and G. T. Fleming. “Angular momentum on the lattice: The case of nonzero linear momentum”. In: *Physical Review D - Particles, Fields, Gravitation and Cosmology* 73.1 (2006), pp. 1–5. arXiv: 0507018 [hep-lat].

[95] J. J. Dudek, R. G. Edwards, and C. E. Thomas. “S- and D-wave phase shifts in isospin-2 $\pi\pi$ scattering from lattice QCD”. In: *Physical Review D - Particles, Fields, Gravitation and Cosmology* 86.3 (2012), pp. 1–33. arXiv: 1203.6041.

[96] J. Elliot and P.G.Dawber. *Symmetry in Physics. Vol. 1: Principles and Simple Applications*. 1987.

[97] J. Foley et al. “Group-theoretical construction of finite-momentum and multi-particle operators for lattice hadron spectroscopy”. In: *Proceedings of Science* 139 (2011). arXiv: 1205.4223.

[98] D. C. Moore and G. T. Fleming. “Multiparticle states and the hadron spectrum on the lattice”. In: *Physical Review D - Particles, Fields, Gravitation and Cosmology* 74.5 (2006), pp. 1–6. arXiv: 0607004 [hep-lat].

[99] W. Detmold et al. “Multi-particle interpolating operators in quantum field theories with cubic symmetry”. In: (2024), pp. 1–27. arXiv: 2403.00672.

[100] H. B. Meyer. “Photodisintegration of a Bound State on the Torus”. In: (2012). arXiv: 1202.6675.

[101] M. T. Hansen, A. Lupo, and N. Tantalo.
"Extraction of spectral densities from lattice correlators".
In: *Physical Review D* 99.9 (2019), pp. 1–15. arXiv: arXiv:1903.06476v2.

[102] K. Huang and C. N. Yang.
"Quantum-mechanical many-body problem with hard-sphere interaction".
In: *Physical Review* 105.3 (1957), pp. 767–775.

[103] B. S. DeWitt. "Transition from discrete to continuous spectra".
In: *Physical Review* 103.5 (1956), pp. 1565–1571.

[104] M. Lüscher. "A New Method to Compute the Spectrum of Low-Lying States in Massless Asymptotically Free Field Theories".
In: *Physics Letters* 118.December (1982), pp. 391–394.

[105] G. Münster. "The size of finite size effects in lattice gauge theories".
In: *Nuclear Physics, Section B* 249.4 (1985), pp. 659–671.

[106] M. Lüscher. "Volume dependence of the energy spectrum in massive quantum field theories I".
In: *Communications in Mathematical Physics* 104.2 (1986), pp. 177–206.

[107] M. Lüscher. "Volume dependence of the energy spectrum in massive quantum field theories II".
In: *Communications in Mathematical Physics* 105.2 (1986), pp. 153–188.

[108] A. B. Raposo and M. T. Hansen.
"Finite-volume scattering on the left-hand cut". In: (2023).
arXiv: 2311.18793.

[109] M. T. Hansen, F. Romero-López, and S. R. Sharpe. "Incorporating $DD\pi$ effects and left-hand cuts in lattice QCD studies of the $T_{cc}(3875)^+$".
In: 3875 (2024), pp. 0–54. arXiv: 2401.06609.

[110] C. H. Kim, C. T. Sachrajda, and S. R. Sharpe.
"Finite-volume effects for two-hadron states in moving frames".
In: *Nuclear Physics B* 727.1-2 (2005), pp. 218–243. arXiv: 0507006.

[111] M. Lüscher.
"Two-particle states on a torus and their relation to the scattering matrix".
In: *Nuclear Physics, Section B* 354.2-3 (1991), pp. 531–578.

[112] K. Rummukainen and S. Gottlieb.
"Resonance scattering phase shifts on a non-rest-frame lattice".
In: *Nuclear Physics B* 450.1-2 (1995), pp. 397–436. arXiv: 9503028 [hep-lat].

[113] L. Leskovec and S. Prelovsek. "Scattering phase shifts for two particles of different mass and nonzero total momentum in lattice QCD".
In: *Physical Review D* 85.11 (2012), p. 114507. arXiv: arXiv:1202.2145.

[114] Z. Fu. "Rummukainen-Gottlieb formula on a two-particle system with different masses". In: *Physical Review D* 85.1 (2012), p. 014506.
arXiv: 1110.0319.

[115] Hua-Xing C. and E. Oset. "$\pi\pi$ interaction in the ρ channel in finite volume".
In: *Physical Review D* 87.1 (2013), p. 016014. arXiv: 1202.2787.

[116] M. T. Hansen and S. R. Sharpe.
"Multiple-channel generalization of Lellouch-Lüscher formula".
In: *Physical Review D* 86.1 (2012), p. 016007. arXiv: 1204.0826.

[117] M. T. Hansen and S. R. Sharpe.
"Relativistic, model-independent, three-particle quantization condition".
In: *Physical Review D* 90.11 (2014), p. 116003. arXiv: 1408.5933.

[118] M. Mai and M. Döring. "Three-body unitarity in the finite volume".
In: *European Physical Journal A* 53.12 (2017), pp. 1–9. arXiv: 1709.08222.

[119] H. W. Hammer, J. Y. Pang, and A. Rusetsky. "Three-particle quantization condition in a finite volume: 1. The role of the three-particle force".
In: *Journal of High Energy Physics* 2017.10 (2017), p. 115. arXiv: 1706.07700.

[120] R. A. Briceño.
"Two-particle multichannel systems in a finite volume with arbitrary spin".
In: *Physical Review D - Particles, Fields, Gravitation and Cosmology* 89.7 (2014), pp. 1–13. arXiv: 1401.3312.

[121] L. Lellouch and M. Lüscher.
"Weak transition matrix elements from finite-volume correlation functions".
In: *Communications in Mathematical Physics* 219.1 (2001), pp. 31–44.

[122] R. A. Briceño, M. T. Hansen, and A. Walker-Loud.
"Multichannel $1 \to 2$ transition amplitudes in a finite volume".
In: *Physical Review D* 91.3 (2015), p. 034501. arXiv: arXiv:1406.5965v2.

[123] F. Müller et al.
"Three-particle Lellouch-Lüscher formalism in moving frames".
In: *Journal of High Energy Physics* 2023.2 (2023). arXiv: 2211.10126.

[124] R. Aaij et al. "Study of the doubly charmed tetraquark T_{cc}^{+}".
In: *Nature Communications* 13.1 (2022), pp. 1–19. arXiv: 2109.01056.

[125] Tyler D. Blanton and Stephen R. Sharpe.
"Equivalence of relativistic three-particle quantization conditions".
In: *Physical Review D* 102.5 (2020), p. 054515. arXiv: 2007.16190.

[126] S. Aoki. "Hadron interactions in lattice QCD".
In: *Progress in Particle and Nuclear Physics* 66.4 (2011), pp. 687–726.
arXiv: 1107.1284.

[127] J. J. Sakurai and J. Napolitano. *Modern Quantum Mechanics*.
Cambridge University Press, 2017.

[128] J. Nagata, S. Muroya, and A. Nakamura.
"Lattice study of Kπ scattering in I=3/2 and 1/2 channels".
In: *Physical Review C - Nuclear Physics* 80.4 (2009), pp. 1–14.

[129] S. R. Beane et al.
"The $I = 2\pi\pi$ S-wave Scattering Phase Shift from Lattice QCD".
In: *Physical Review D* 85.3 (2012), p. 034505. arXiv: 1107.5023.

[130] T. Wang and C. Kelly.
"S-wave $\pi\pi$ I=0 and I=2 scattering with physical pion mass".
In: *Proceedings of Science* 363 (2019), pp. 0–6.

[131] J. J. Dudek et al. "Phase shift of isospin-2 $\pi\pi$ scattering from lattice QCD".
In: *Physical Review D - Particles, Fields, Gravitation and Cosmology* 83.7 (2011), pp. 3–7. arXiv: arXiv:1011.6352v2.

[132] V. Bernard et al.
"Resonance properties from the finite-volume energy spectrum".
In: *Journal of High Energy Physics* 2008.8 (2008), pp. 1–26. arXiv: 0806.4495.

[133] P. Guo et al. "Coupled-channel scattering on a torus". In: *Physical Review D - Particles, Fields, Gravitation and Cosmology* 88.1 (2013), pp. 1–12.
arXiv: 1211.0929.

[134] J. J. Dudek, R. G. Edwards, and C. E. Thomas. "Energy dependence of the ρ resonance in $\pi\pi$ elastic scattering from lattice QCD".
In: *Physical Review D* 87.3 (2013), p. 034505. arXiv: arXiv:1212.0830v2.

[135] A. Alexandru et al.
"P -wave $\pi\pi$ scattering and the ρ resonance from lattice QCD".
In: *Physical Review D* 96.3 (2017), pp. 1–22. arXiv: arXiv:1704.05439v2.

[136] J. Bulava et al.
"I = 1 and I = 2 $\pi - \pi$ scattering phase shifts from Nf = 2 + 1 lattice QCD".
In: *Nuclear Physics B* 910.24 (2016), pp. 842–867. arXiv: 1604.05593.

[137] F. B. Erben.
"A Lattice QCD study of the ρ resonance and the timelike pion form factor".
PhD thesis. Johannes Gutenberg-Universität, 2018.

[138] C. Andersen et al. "The I = 1 pion–pion scattering amplitude and timelike pion form factor from $N_f = 2 + 1$ lattice QCD".
In: *Nuclear Physics B* 939 (2019), pp. 145–173. arXiv: arXiv:1808.05007v2.

[139] Z. Fu. "Lattice study on πk scattering with moving wall source".
In: *Physical Review D* 85.7 (2012), pp. 1–18. arXiv: arXiv:1110.1422v2.

[140] Sasa Prelovsek et al.
"$K\pi$ scattering and the K^* decay width from lattice QCD".
In: *Physical Review D* 88.5 (2013), p. 054508. arXiv: 1307.0736.

[141] G. S. Bali et al. "ρ and K* resonances on the lattice at nearly physical quark masses and Nf=2". In: *Physical Review D* 93.5 (2016), pp. 1–15.

[142] D. J. Wilson et al.
"Quark-Mass Dependence of Elastic πk Scattering from QCD".
In: *Physical Review Letters* 123.4 (2019), pp. 1–11.
arXiv: arXiv:1904.03188v1.

[143] Arkaitz Rodas, Jozef J. Dudek, and Robert G. Edwards. "Quark mass dependence of $\pi\pi$ scattering in isospin 0, 1, and 2 from lattice QCD".
In: *Physical Review D* 108.3 (2023), p. 034513. arXiv: 2303.10701.

[144] M. Padmanath. “Hadron Spectroscopy and Resonances : Review”. In: *Proceedings of The 36th Annual International Symposium on Lattice Field Theory — PoS(LATTICE2018)*. Vol. 334. Trieste, Italy: Sissa Medialab, 2019, p. 013. arXiv: 1905.09651.

[145] W. Detmold et al. “Hadrons and nuclei”. In: *The European Physical Journal A* 55.11 (2019), p. 193. arXiv: 1904.09512.

[146] J. Bulava et al. “Hadron Spectroscopy with Lattice QCD”. In: *Snowmass 2021* Snowmass (2022), pp. 1–35. arXiv: 2203.03230.

[147] G. Moir et al. “Excited spectroscopy of charmed mesons from lattice QCD”. In: *Journal of High Energy Physics* 2013.5 (2013). arXiv: 1301.7670.

[148] R. J. Dowdall et al. “Precise heavy-light meson masses and hyperfine splittings from lattice QCD including charm quarks in the sea”. In: *Physical Review D* 86.9 (2012), p. 094510. arXiv: 1207.5149.

[149] J. J. Dudek. “The lightest hybrid meson supermultiplet in QCD”. In: *Physical Review D* 84.7 (2011), p. 074023. arXiv: 1106.5515.

[150] D. Vadacchino. “A review on Glueball hunting”. In: *Proceedings of The 39th Annual International Symposium on Lattice Field Theory — PoS(LATTICE2022)* (2023). arXiv: 2305.04869.

[151] J. J. Dudek et al. “Highly excited and exotic meson spectrum from dynamical lattice QCD”. In: *Physical Review Letters* 103.26 (2009), pp. 2–5. arXiv: 0909.0200.

[152] P. Bicudo et al. “Evidence for the existence of $ud\bar{b}\bar{b}$ and the nonexistence of $ss\bar{b}\bar{b}$ and $cc\bar{b}\bar{b}$ tetraquarks from lattice QCD”. In: *Physical Review D - Particles, Fields, Gravitation and Cosmology* 92.1 (2015), pp. 1–12.

[153] R. J. Hudspith et al. “Lattice investigation of exotic tetraquark channels”. In: *Physical Review D* 102.11 (2020), p. 114506. arXiv: 2006.14294.

[154] C. Morningstar et al. “Progress with excited states in lattice QCD”. In: *Proceedings of Science*. Vol. 139. 2013, pp. 448–450. arXiv: 1112.0212.

[155] M. Lüscher and U. Wolff. “How to calculate the elastic scattering matrix in two-dimensional quantum field theories by numerical simulation”. In: *Nuclear Physics, Section B* 339.1 (1990), pp. 222–252.

[156] B. Blossier et al. “On the generalized eigenvalue method for energies and matrix elements in lattice field theory”. In: *Journal of High Energy Physics* 2009.4 (2009). arXiv: 0902.1265.

[157] C. Gattringer et al. “Derivative sources in lattice spectroscopy of excited light-quark mesons”. In: *Physical Review D* 78.3 (2008), p. 034501. arXiv: arXiv:0802.2020v3.

[158] C. Morningstar et al. “Extended hadron and two-hadron operators of definite momentum for spectrum calculations in lattice QCD”. In: *Physical Review D* 88.1 (2013), p. 014511. arXiv: 1303.6816.

[159] S. Prelovsek, U. Skerbis, and C. B. Lang.
"Lattice operators for scattering of particles with spin".
In: *Journal of High Energy Physics* 2017.1 (2017). arXiv: 1607.06738.

[160] F. Knechtli, M. Günther, and M. Peardon. *Lattice Quantum Chromodynamics*.
SpringerBriefs in Physics. Dordrecht: Springer Netherlands, 2017.

[161] C. J. Morningstar and M. Peardon.
"Analytic smearing of $SU(3)$ link variables in lattice QCD".
In: *Physical Review D* 69.5 (2004), p. 054501. arXiv: 0311018 [hep-lat].

[162] C. R. Allton et al. "Gauge-invariant smearing and matrix correlators using Wilson fermions at β=6.2".
In: *Physical Review D* 47.11 (1993), pp. 5128–5137.

[163] P. A. Boyle. "A novel gauge invariant multistate smearing technique".
In: *Journal of Computational Physics* 179.2 (2002), pp. 349–370.
arXiv: 9903033 [hep-lat].

[164] P. A. Boyle et al. "Isospin-breaking corrections to light-meson leptonic decays from lattice simulations at physical quark masses".
In: *Journal of High Energy Physics* 2023.2 (2023), p. 242. arXiv: 2211.12865.

[165] S. J. Dong and K. F. Liu. "Stochastic estimation with Z2 noise".
In: *Physics Letters B* 328.1-2 (1994), pp. 130–136.
arXiv: 9308015v1 [arXiv:hep-lat].

[166] J. Foley et al. "Practical all-to-all propagators for lattice QCD".
In: *Computer Physics Communications* 172.3 (2005), pp. 145–162.
arXiv: 0505023 [hep-lat].

[167] J. Foley et al. "A novel method for evaluating correlation functions in Lattice hadron spectroscopy." In: *Proceedings of The XXVIII International Symposium on Lattice Field Theory — PoS(Lattice 2010)*. Vol. 105.
Trieste, Italy: Sissa Medialab, 2011, p. 098. arXiv: 1011.0481.

[168] S. Bernardson, P. McCarty, and C. Thron. "Monte Carlo methods for estimating linear combinations of inverse matrix entries in lattice QCD".
In: *Computer Physics Communications* 78.3 (1994), pp. 256–264.

[169] J. J. Dudek et al. "Toward the excited meson spectrum of dynamical QCD".
In: *Physical Review D* 82.3 (2010), p. 034508. arXiv: 1004.4930.

[170] C. Michael and I. Teasdale. "Extracting glueball masses from lattice QCD".
In: *Nuclear Physics B* 215.3 (1983), pp. 433–446.

[171] C. Michael. "Adjoint sources in lattice gauge theory".
In: *Nuclear Physics B* 259.1 (1985), pp. 58–76.

[172] D. Djukanovic. "Quark Contraction Tool — QCT".
In: *Computer Physics Communications* 247 (2020), p. 106950.
arXiv: 1603.01576.

[173] C. Bernard. *Weak Matrix Elements On and Off the Lattice*. Tech. rep. 1989.

[174] C. Pelissier and A. Alexandru.
"Resonance parameters of the rho-meson from asymmetrical lattices".
In: *Physical Review D* 87.1 (2013), p. 014503. arXiv: 1211.0092.

[175] A. Portelli. "Hadrons: a Grid-powered workflow management system for lattice QCD measurements".
In: *37th International Symposium on Lattice Field Theory (LATTICE2019)*. 2019.

[176] P. A. Boyle, Azusa Yamaguchi, and A. Portelli.
"Grid: A next generation data parallel C++ QCD library".
In: *The 33rd International Symposium on Lattice Field Theory*. Sissa, 2015.

[177] M. Fischer et al. "On the generalised eigenvalue method and its relation to Prony and generalised pencil of function methods".
In: *European Physical Journal A* 56.8 (2020), pp. 1–17. arXiv: 2004.10472.

[178] F. B. Erben et al. "Rho resonance, timelike pion form factor, and implications for lattice studies of the hadronic vacuum polarization".
In: *Physical Review D* 101.5 (2020), p. 054504. arXiv: 1910.01083.

[179] G. Rendon et al. "I = 1/2 S-wave and P-wave Kπ scattering and the κ and K* resonances from lattice QCD". In: *Physical Review D* 102.11 (2020), p. 114520. arXiv: 2006.14035.

[180] David J. Wilson et al.
"Resonances in coupled $\pi K, \eta K$ scattering from lattice QCD".
In: *Physical Review D* 91.5 (2015), p. 054008. arXiv: 1411.2004.

[181] R. Brett et al. "Determination of s- and p-wave I = 1/2 Kπ scattering amplitudes in Nf = 2 + 1 lattice QCD".
In: *Nuclear Physics B* 932.20 (2018), pp. 29–51. arXiv: arXiv:1802.03100v2.

[182] X. Feng, K. Jansen, and D. B. Renner.
"Resonance parameters of the ρ-meson from lattice QCD".
In: *Physical Review D* 83.9 (2011), p. 094505. arXiv: arXiv:1011.5288v2.

[183] S. Aoki et al. "ρ meson decay in $2 + 1$ flavor lattice QCD".
In: *Physical Review D* 84.9 (2011), p. 094505. arXiv: arXiv:1106.5365v4.

[184] D. J. Wilson et al. "Coupled $\pi\pi, K\bar{K}$ scatterin gin P-wave and the ρ resonance from lattice QCD". In: *Physical Review D* 92.9 (2015), p. 094502. arXiv: arXiv:1507.02599v2.

[185] Z. Fu and L. Wang.
"Studying the ρ resonance parameters with staggered fermions".
In: *Physical Review D* 94.3 (2016), p. 034505. arXiv: arXiv:1608.07478v1.

[186] D. Guo et al. "Rho resonance parameters from lattice QCD".
In: *Physical Review D* 94.3 (2016), p. 034501. arXiv: arXiv:1605.03993v2.

[187] M. Werner et al. "Hadron-Hadron Interactions from Nf = 2 + 1 + 1 Lattice QCD: The ρ-resonance". In: *The European Physical Journal A* 56.2 (2020). arXiv: 1907.01237.

[188] M. Fischer et al.
"The ρ-resonance from N = 2 lattice QCD including the physical pion mass".
In: *Physics Letters B* 819 (2021), p. 136449. arXiv: 2006.13805.

[189] S. Paul et al. "I = 1 $\pi\pi$ scattering at the physical point".
In: *Proceedings of Science* 396 (2022), pp. 1–9. arXiv: arXiv:2112.07385v1.

[190] Sz. Borsanyi et al.
"Ab initio calculation of the neutron-proton mass difference".
In: *Science* 347.6229 (2015), pp. 1452–1455. arXiv: 1406.4088.

[191] W. I. Jay and E. T. Neil.
"Bayesian model averaging for analysis of lattice field theory results".
In: *Physical Review D* 103.11 (2021), p. 114502. arXiv: 2008.01069.

[192] E. T. Neil and J. W. Sitison. "Improved information criteria for Bayesian model averaging in lattice field theory".
In: *Physical Review D* 109.1 (2024), p. 014510. arXiv: 2208.14983.

[193] E. T. Neil and J. W. Sitison.
"Model averaging approaches to data subset selection".
In: *Physical Review E* 108.4 (2023), p. 045308. arXiv: 2305.19417.

[194] H. J. Rothe. *Lattice Gauge Theories*. Vol. 82.
World Scientific Lecture Notes in Physics. Singapore: World Scientific, 2012.

[195] J. J. Dudek et al. "Charmonium excited state spectrum in lattice QCD".
In: *Physical Review D* 77.3 (2008), p. 034501. arXiv: 0707.4162.

[196] H. A. Bethe. "Theory of the effective range in nuclear scattering".
In: *Physical Review* 76.1 (1949), pp. 38–50.

[197] P. Young. "Everything you wanted to know about Data Analysis and Fitting but were afraid to ask". In: (2012). arXiv: 1210.3781.

[198] M. Albaladejo et al.
"Finite volume treatment of $\pi\pi$ scattering in the ρ channel".
In: 2 (2013), pp. 1–11. arXiv: 1307.5169.

[199] J. A. Nelder and R. Mead. "A simplex method for function minimization".
In: *The Computer Journal* 7 (1965), pp. 308–313.

[200] S. G. Johnson. *The NLopt nonlinear-optimization package*.
https://github.com/stevengj/nlopt. 2007.

[201] J. Wess and B. Zumino. "Consequences of anomalous ward identities".
In: *Physics Letters B* 37.1 (1971), pp. 95–97.

[202] U. G. Meißner. "Low-energy hadron physics from effective chiral Lagrangians with vector mesons".
In: *Physics Reports* 161.5-6 (1988), pp. 213–361.

[203] J. R. Peláez and A. Rodas. "Pion-kaon scattering amplitude constrained with forward dispersion relations up to 1.6 GeV".
In: *Physical Review D* 93.7 (2016), pp. 1–29. arXiv: 1602.08404.

[204] J. R. Peláez, A. Rodas, and J. Ruiz de Elvira.
"Global parameterization of $\pi\pi$ scattering up to 2 GeV".
In: *The European Physical Journal C* 79.12 (2019), p. 1008. arXiv: 1907.13162.

[205] P. Estabrooks et al. "Study of $K\pi$ scattering using the reactions $K^{\pm}p \to K^{\pm}\pi^{\pm}$ and $K^{\pm}p \to K^{\pm}\pi^{-}\Delta^{++}$ at 13 GeV/c *".
In: *Nuclear Physics, Section B* 133.3 (1978), pp. 490–524.

[206] S. D. Protopopescu et al. "$\pi\pi$ Partial-Wave Analysis from Reactions $\pi^{+}p \to \pi^{+}\pi^{-}\Delta^{++}$ and $\pi^{+}p \to K^{+}K^{-}\Delta^{++}$ at 7.1 GeV/c".
In: *Physical Review D* 7.5 (1973), pp. 1279–1309.

[207] J. Bulava and M. T. Hansen.
"Scattering amplitudes from finite-volume spectral functions".
In: *Physical Review D* 100.3 (2019), pp. 1–22. arXiv: 1903.11735.

[208] Z. Fu. "Preliminary lattice QCD calculation of the σ meson decay width".
In: *Journal of High Energy Physics* 2012.7 (2012), pp. 0–20.

[209] R. A. Briceño et al.
"Isoscalar $\pi\pi$ Scattering and the σ Meson Resonance from QCD".
In: *Physical Review Letters* 118.2 (2017).

[210] R. L. Workman et al. "64. Scalar Mesons below 1 GeV (PDG Review)".
In: *Progress of Theoretical and Experimental Physics* 2022.8 (2022), p. 083C01.

[211] R. A. Briceño and M. T. Hansen. "Relativistic, model-independent, multichannel $2 \to 2$ transition amplitudes in a finite volume".
In: *Physical Review D* 94.1 (2016). arXiv: 1509.08507.

[212] A. Baroni et al. "Form factors of two-hadron states from a covariant finite-volume formalism". In: *Physical Review D* 100.3 (2019), p. 34511.

[213] R. A. Briceño et al. "Prospects for $\gamma^{*}\gamma^{*} \to \pi\pi$ via lattice QCD".
In: *Physical Review D* 107.3 (2023), p. 34504.

[214] H. B. Meyer. "Lattice QCD and the Timelike Pion Form Factor".
In: *Physical Review Letters* 107.7 (2011), p. 072002. arXiv: 1105.1892.

[215] R. A. Briceño et al.
"Resonant $\pi^{+}\gamma \to \pi^{+}\pi^{0}$ Amplitude from Quantum Chromodynamics".
In: *Physical Review Letters* 115.24 (2015). arXiv: arXiv:1507.06622v2.

[216] C. Alexandrou et al.
"$\pi\gamma \to \pi\pi$ transition and the ρ radiative decay width from lattice QCD".
In: *Physical Review D* 98.7 (2018), pp. 1–28. arXiv: arXiv:1807.08357v5.

[217] A. Radhakrishnan, J. J. Dudek, and R. G. Edwards. "Radiative decay of the resonant K^{*} and the $\gamma K \to K\pi$ amplitude from lattice QCD".
In: *Physical Review D* 106.11 (2022), p. 114513. arXiv: arXiv:2208.13755v1.

[218] A. Agadjanov et al. "The $B \to K^{*}$ form factors on the lattice".
In: *Nuclear Physics B* 910 (2016), pp. 387–409.

[219] R. A. Briceño et al. "Long-range electroweak amplitudes of single hadrons from Euclidean finite-volume correlation functions".
In: *Physical Review D* 101.1 (2020), p. 14509. arXiv: 1911.04036.

[220] M. Algueró et al. “Emerging patterns of New Physics with and without Lepton Flavour Universal contributions”.
In: *European Physical Journal C* 79.8 (2019), pp. 1–18. arXiv: 1903.09578.

[221] R. Aaij et al. “Test of Lepton Universality in $b \to s\ell^+\ell^-$ Decays”.
In: *Physical Review Letters* 131.5 (2023), p. 51803. arXiv: 2212.09152.

[222] Belle II Collaboration et al. “Reconstruction of $B \to \rho\ell\nu_\ell$ decays identified using hadronic decays of the recoil B meson in 2019 – 2021 Belle II data”.
In: *arXiv* (2022), pp. 1–19. arXiv: 2211.15270.

[223] L. Leskovec et al. “A lattice QCD study of the $B \to \pi\pi\ell\nu$”. In: *The 39th International Symposium on Lattice Field Theory - PoS(LATTICE2022)* (2022). arXiv: arXiv:2212.08833v2.

[224] T. Blum et al. “Nonperturbative renormalization of domain wall fermions: Quark bilinears”. In: *Physical Review D - Particles, Fields, Gravitation and Cosmology* 66.1 II (2002), pp. 145041–1450419.

[225] B. Efron. *The Jackknife, the Bootstrap and Other Resampling Plans.*
Society for Industrial and Applied Mathematics, 1982.

[226] A. Portelli, M. Spraggs, and A. Yong. “aportelli/LatAnalyze: v3.5.1”.
In: *10.5281/zenodo.429* (2020).

[227] P. Kaelo and M. M. Ali. “Some variants of the controlled random search algorithm for global optimization”.
In: *Journal of Optimization Theory and Applications* 130 (2006), pp. 253–264.

[228] H. Dembinski and Et Al. “scikit-hep/iminuit”. In: (2020).

[229] F. James and M. Roos. “Minuit - a system for function minimization and analysis of the parameter errors and correlations”.
In: *Computer Physics Communications* 10.6 (1975), pp. 343–367.

[230] D. Kraft.
“Algorithm 733: TOMP–Fortran modules for optimal control calculations”.
In: *ACM Transactions on Mathematical Software* 20 (1994), pp. 262–281.

[231] H. Akaike. “A new look at the statistical model identification”.
In: *IEEE Transactions on Automatic Control* 19.6 (1974), pp. 716–723.

[232] R. P. Brent. “Chapter 4: An Algorithm with Guaranteed Convergence for Finding a Zero of a Function”.
In: *Algorithms for Minimization without Derivatives.*
Englewood Cliffs, NJ: Prentice-Hall, 1973.

[233] T. J. Dekker. “Finding a zero by means of successive linear interpolation”.
In: *Constructive Aspects of the Fundamental Theorem of Algebra.*
London: Wiley-Interscience, 1969.

[234] M. Galassi. *GNU Scientific Library Reference Manual (3rd Ed.)* 2021.

[235] N. P. Lachini and F. B. Erben. “Distillation documentation - Hadrons”.
In: *https://aportelli.github.io/Hadrons-doc/#/mdistil* (2022).